OCS Study
BOEM 2014-040

Coastal Marine Institute

Analysis of Ocean Current Data from Gulf of Mexico Oil and Gas Platforms

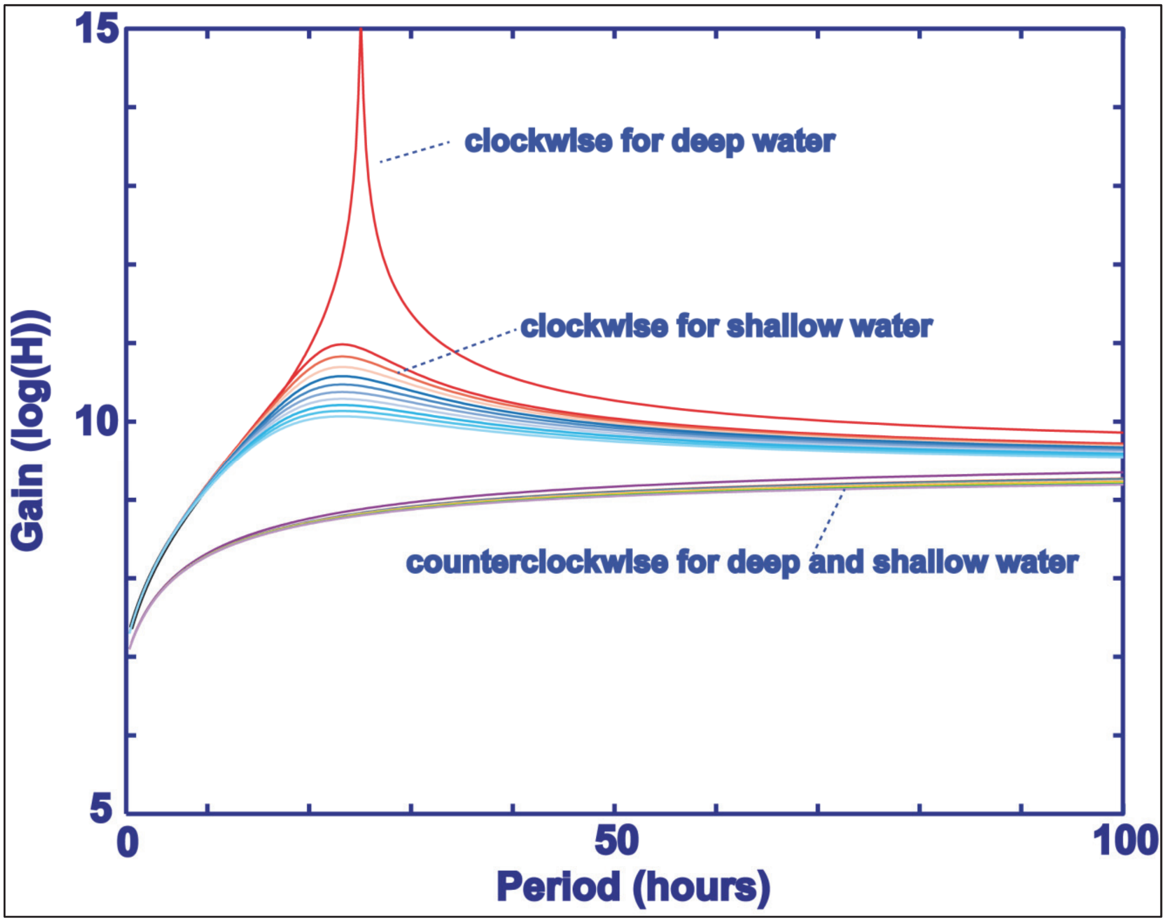

U.S. Department of the Interior
Bureau of Ocean Energy Management
Gulf of Mexico OCS Region

Cooperative Agreement
Coastal Marine Institute
Louisiana State University

OCS Study
BOEM 2014-040

Coastal Marine Institute

Analysis of Ocean Current Data from Gulf of Mexico Oil and Gas Platforms

Authors

Chunyan Li
Lawrence J. Rouse, Jr.

April 2014

Prepared under BOEM Cooperative Agreement
M08AX12686
By
Louisiana State University
Coastal Marine Institute
Baton Rouge, Louisiana 70803

Published by

U.S. Department of the Interior
Bureau of Ocean Energy Management
Gulf of Mexico OCS Region

Cooperative Agreement
Coastal Marine Institute
Louisiana State University

DISCLAIMER

REPORT AVAILABILITY

To download a PDF file of this Gulf of Mexico OCS Region report, go to the U.S. Department of the Interior, Bureau of Ocean Energy Management, Environmental Studies Program Information System website and search on OCS Study BOEM 2014-040.

This report can be viewed at select Federal Depository Libraries. It can also be obtained from the National Technical Information Service; the contact information is below.

U.S. Department of Commerce
National Technical Information Service
5301 Shawnee Rd.
Springfield, Virginia 22312
Phone: (703) 605-6000, 1(800)553-6847
Fax: (703) 605-6900
Website: http://www.ntis.gov/

CITATION

Li, Chunyan, Lawrence J. Rouse, Jr. 2014. Analysis of ocean current data from Gulf of Mexico oil and gas platforms. U.S. Dept. of the Interior, Bureau of Ocean Energy Management, Gulf of Mexico OCS Region, New Orleans, LA. OCS Study BOEM 2014-040. 141 pp.

CONTENTS

LIST OF FIGURES

LIST OF TABLES

1. INTRODUCTION

On April 21, 2005, the Minerals Management Service (MMS), now the Bureau of Ocean Energy Management, of the U.S. Department of Interior issued Notice to Lessees and Operators, NTL No. 2005-G05, in the Gulf of Mexico (GoM) Outer Continental Shelf (OCS) Region. This NTL required that companies report ocean current data to the National Data Buoy Center (NDBC) Internet website for two years effective April 30, 2005. These ocean current data were measured by acoustic Doppler current profilers (ADCPs) installed on oil and gas platforms and all floating MODUs operating in locations with water depth greater than 400 meters.

The NTL No. 2005-G05 stipulates that for the floating MODUs, real time ADCP data should be collected between 30 m and 1000 m in the water column at 20 minute intervals. For the floating MODUs in depths greater than 1100 m, an additional ADCP should be installed at near the bottom (100 m from the seabed) to collect data at 20-minute intervals. These observations are not required when the rigs are moving from one location to another. It is also required that prior to the installation of any new facilities for oil and gas production, a time series data of at least one year needs to be collected in the water column between 30 m below the surface and 100 m above the bottom. For single point current meters they cannot be separated by more than 500 m. The data are not required if a nearby facility within 30 km range can provide similar data unless it is near steep topography where the range is reduced to 8 km. For any additional current data or other data (such as weather and wave data), the MMS requested voluntary reporting.

These ADCP were required to be put online through the NDBC web pages starting from April – June 2005. These web based data files are open to the public[1]. Data are recorded in waters with a total depth greater than 400 m at 10-20 minute intervals from near surface (~ 30 m) to ~ 500 - 1000 m. In places with depth greater than 1100 m, two ADCPs may be used. Hurricanes Katrina and Rita damaged some of the instruments and interrupted the data reporting on the NDBC web site, but many were quickly restored and the rest gradually resumed data collection.

The benefit for this collective monitoring effort is obvious. It has been known that ocean current velocity values in the Gulf of Mexico area might have been underestimated according to oil and gas industries. These velocity values are used by the industry in design, operation, and function of mobile offshore drilling units and floating production platforms and their ancillary equipment such as the drilling and production risers, tendons, and mooring systems. An overlook of large velocity events can impact the cost and operation. A proper estimate of the ocean current velocity under different conditions at different sites is thus needed for structural design, fatigue criteria, as well as routine operations. Additionally, a better understanding of the circulation is important for a proper handling of spills and pollution. Furthermore, both hindcasting and forecasting of the ocean current using numerical models require reliable flow field measurements. The long-term measurements from numerous locations in the deep ocean provide useful database for model validation.

One of the major concerns of the oil and gas companies with deep water oil and gas rigs in the Gulf of Mexico is the energy and momentum input from the Loop Current (LC), Loop Current

---

[1] Available at this NOAA web site: http://www.ndbc.noaa.gov/maps/ADCP_WestGulf.shtml.

Eddies (LCE) (e.g. Welsh and Inoue, 2000), and associated cross slope flows. Strong deepwater currents or jets may occur, contrary to "intuition." These deepwater jets have a time scale of a few hours to one day with a maximum subsurface velocity magnitude between 0.4 m/s and 2 m/s at a depth between 150 and 350 m below the surface with little or no energetic surface expression. The large velocity can affect the deep ocean drilling and oil and gas production in the northern Gulf of Mexico by the associated extreme loads, causing structural fatigues, thus affecting the daily operations. Extensive studies have been conducted on about a dozen of incidents of strong subsurface jets in the area using historic hydrographic and current meter data (DiMarco et al., 2004; Hamilton et al., 2001, 2003). Several plausible mechanisms are discussed in this study, which include the baroclinic frontal instability (e.g. Tang, 1975; Hart, 1975; Hogg, 1985; Dimas and Triantafyllou, 1995; Robinson and McWilliams, 1974; Pedlosky, 1975; Qiu et al, 1988; Meacham, 1988; Tanaka and Alkitomo, 2001; Olascoaga, 2001; Meacham and Stephens, 2001; Lozier et al., 2002; Walker and Pedlosky, 2002, etc.), inertial wave train, reversed geostrophic flow, interactions between eddies (Frolov et al, 2004a,b), or between slope-shelf and eddies (Vukovich and Crissman 1986; Kirwan et al. 1988; Lewis et al. 1989; Vukovich and Waddel 1991; Vidal et al. 1992; Hamilton et al. 1999), wind-driven flow under the influence of undulating seabed, internal solitons, and other motions such as filament and meanders associated with Loop Current or Loop Current Eddies. Some unlikely mechanisms such as the internal solitary waves and bathymetric influences are also discussed. Some instrument issues and effects of inhomogeneous flow field are investigated. It is important to note that several numerical models (DiMarco et al., 2004) could reproduce the strong currents but the temporal duration of the subsurface jets found in the model are usually longer (2-6 days or longer) than those seen in observations (one-third to 2 days). In addition, the high-speed core (~ 70 cm/s) in the models is generally higher in the water column (150-250 m) than in observations (150-350 m). Many unknowns are present on this subject.

The availability of these current data in deep-water from dozens of real time, oil-rig-based ADCPs opens a great opportunity for the study of the three dimensional flow structures in the northern Gulf of Mexico, specifically waters over the outer continental shelf and slope area between 480 and 2400 m. For the first time in history, we are able to use dozens of ADCPs in deep water concurrently to "see" the inside of the ocean with a synoptic large picture (constructed by these current profilers) as the ocean moves under the influence of different mechanisms such as the LC, LCE, inertial motion, frontal instability, filaments, internal soliton, internal waves, geostrophic motion, and extreme weather (i.e. hurricanes and tropical storms) induced motion, to name a few. In general, the Gulf of Mexico is strongly affected by the LC and LCE which are one of the key sources of energy and momentum in most part of the GoM. LC and LCE have a range of spatial and temporal scales and they may be related to complex flow features such as filaments and rings of different horizontal and vertical structures and scales [e.g. Berger et al., 2000a,b].

The main objectives of this study are to determine the three-dimensional characteristics of the deep-water flow in the area by a systematic analysis of the current data from the dozens of ADCPs based on the oil and gas platforms and discuss the mechanisms that drive the flow fields. More specifically, the analysis is conducted for all data available from April 2005 or earlier (if data files are available) to 2008.

We will discuss the basic statistics of the current velocity profiles and their vertical and horizontal variations. The basic statistics includes the mean and standard deviation of the vector flow records at different depths, in different regions, and during different times. The flow velocity vectors are examined in a way similar to the general analysis to wind data, such that predominant flow directions, if any, are identified and discussed. We also discuss the spectra of the flow speed as functions of time, depth, and location. Rotary spectra of the velocity fields are also discussed. Since 2005, several hurricanes and tropical storms impacted the northern Gulf of Mexico. Among them are Hurricanes Katrina and Rita of 2005, and Hurricanes Gustav and Ike of 2008. Near inertial oscillations induced by hurricane and non-hurricane wind events are discussed in a separate chapter.

2. DATA COLLECTION AND DESCRIPTION

2.1 GEOGRAPHIC AREA OF MEASUREMENTS

The rigs that are reporting velocity profile data to the National Data Buoy Center (NDBC, http://www.ndbc.noaa.gov/maps/ADCP_WestGulf.shtml) are located off the coast of Alabama, Mississippi, Louisiana, and Texas (Figure 2.1). These rigs can be permanent or mobile. The rigs are identified by a five-digit station number associated. Identification numbers starting with 423, denote a fixed rig. If the number starts with either 428 or 429, the rig is mobile. Mobile rigs may stay at one location for a few months or longer than a year. The geographic positions of the mobile rigs are included in the ADCP data files.

These rigs with ADCP data reporting to NDBC are within a relatively narrow band over the slope of the northern Gulf of Mexico, south of the continental shelf and mostly off the Louisiana and Texas coasts, between 26° N and 29.2°° N, and 94.9° W and 87.8° W. The southwestern-most fixed rig with ADCP data reporting to NDBC has an NDBC station number 42390, at 26.129°° N and 94.898° W; while the northeastern-most fixed rig is station 42376 at 29.108° N and 87.944° W. Figure 2.1 shows the locations of the rigs in May of 2006. The ones marked with red are fixed and the blues are mobile ones. The mobile ones move at intervals of a few months and are mostly within the above region. These stations are mostly in water depth between 200 and 2000 m.

Most of the ADCPs of these stations are setup to look downward during measurements with vertical bins at 8, 16, 20, and 32 m recorded every 20 minutes. The data cover between a near-surface position to a mid-depth or near bottom up to close to 2000 m, depending on the actual instrument. Table 2.1 and Figure 2.2 show an example of the data coverage in the vertical for 2006, with the minimum, maximum depths covered by the measurements and the vertical bin size. The negative values for bin size in Table 2.1 indicate an upward looking ADCP. There are only two upward looking ADCPs shown in Table 2.1, with data from 2006. Figure 2.3 shows the range of data (the maximum bin depth minus the minimum bin depth) which has a mean value of 861 m and a standard deviation of 263 m. Since the mobile platforms may move, these values may change with time as well. For the ADCPs on the fixed platforms the mean depth range is 894 m, with a standard deviation of 303 m, using the 2006 data as an example. At each site, measurements cover, on average, more than 800 m of the water column, yielding many velocity time series. Thus a large amount of data is available to study the vertical structure and variability of horizontal velocity in the northern Gulf of Mexico.

Table 2.1

The range of data coverage in the vertical by the ADCPs (negative bin size indicates an upward looking ADCP)

Station Number	Top Bin (m)	Bottom Bin (m)	Bin Size (m)
42361	51.0	0803.0	16.0
42362	79.0	1023.1	16.0
42364	51.0	0995.1	16.0
42365	60.0	1004.0	16.0
42366	114.8	0610.9	16.0
42367	94.7	1024.8	30.0
42368	66.9	1123.0	32.0
42370	61.8	1316.3	-20.0
42373	103.6	0596.8	15.9
42374	44.4	0541.2	16.0
42375	48.0	0992.1	16.0
42376	53.1	0984.0	30.0
42377	21.3	0998.9	30.0
42380	52.1	1685.2	-16.0
42381	57.5	0681.5	16.0
42861	54.6	0838.8	16.0
42862	63.0	1007.1	16.0
42863	73.3	1321.4	32.0
42864	77.5	0621.6	16.0
42865	66.9	1123.0	32.0
42867	46.0	0750.0	16.0
42868	72.9	1161.0	32.0
42869	52.9	0548.9	16.0
42870	72.9	1097.0	32.0
42871	63.0	1007.1	16.0
42872	56.7	0760.7	16.0
42873	71.9	1160.0	32.0
42874	68.8	1157.6	32.0
42875	57.0	1081.1	16.0
42876	58.0	1002.1	16.0
42877	26.8	0498.8	8.0
42878	58.6	0522.7	16.0
42879	54.6	0998.7	16.0
42880	62.5	0606.6	16.0
42881	72.9	1000.9	32.0
42882	63.6	0767.7	16.0
42883	57.2	0585.2	16.0
42884	57.0	0553.0	16.0
42886	42.7	0986.7	16.0
42887	72.9	1161.0	32.0
42889	15.2	0627.3	30.0
42892	74.3	1066.4	32.0
42894	74.3	0746.4	32.0
42896	71.9	1320.0	32.0
42897	61.9	1086.0	16.0

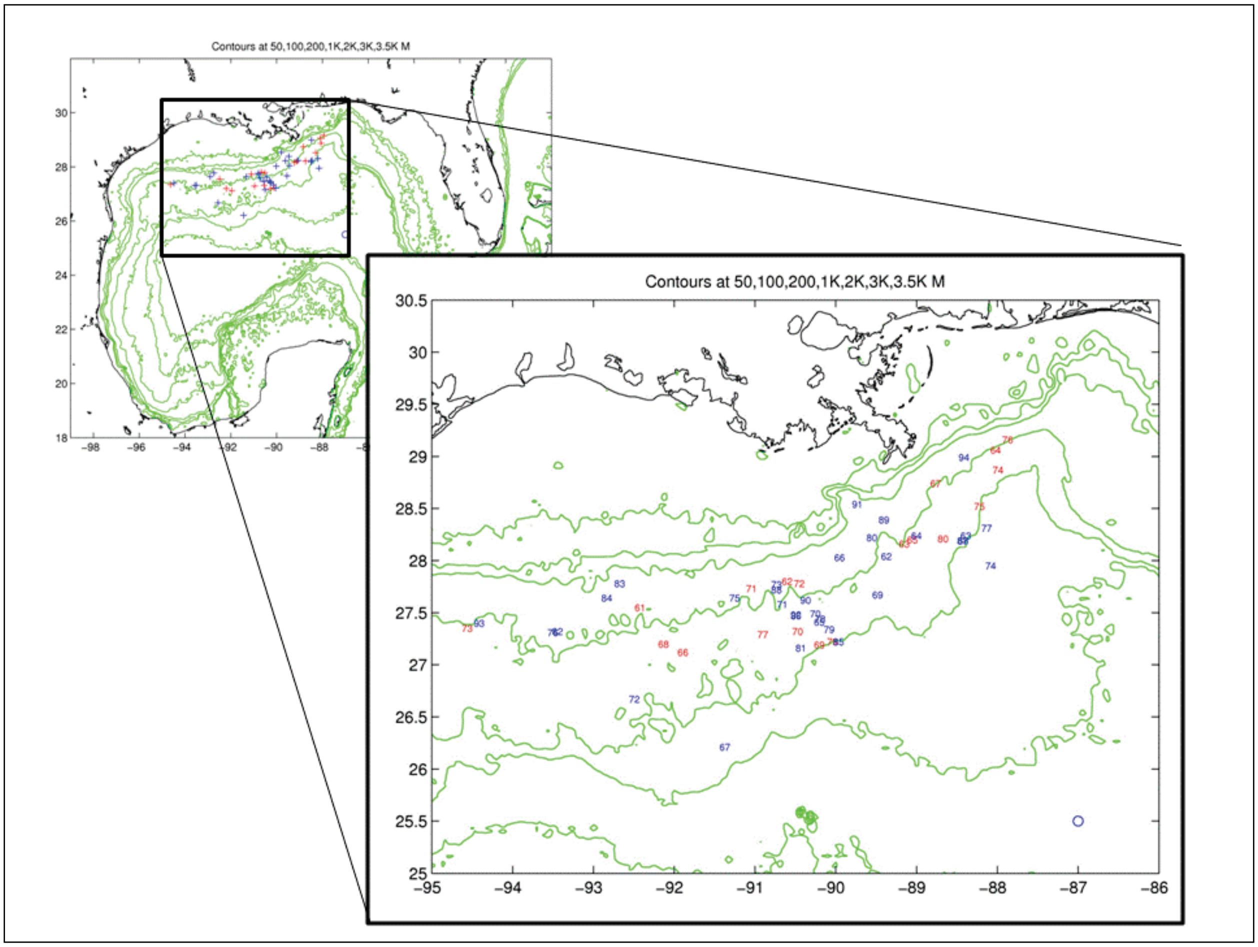

Figure 2.1. Locations of the oil and gas rigs equipped with ADCP and reporting data to NDBC.

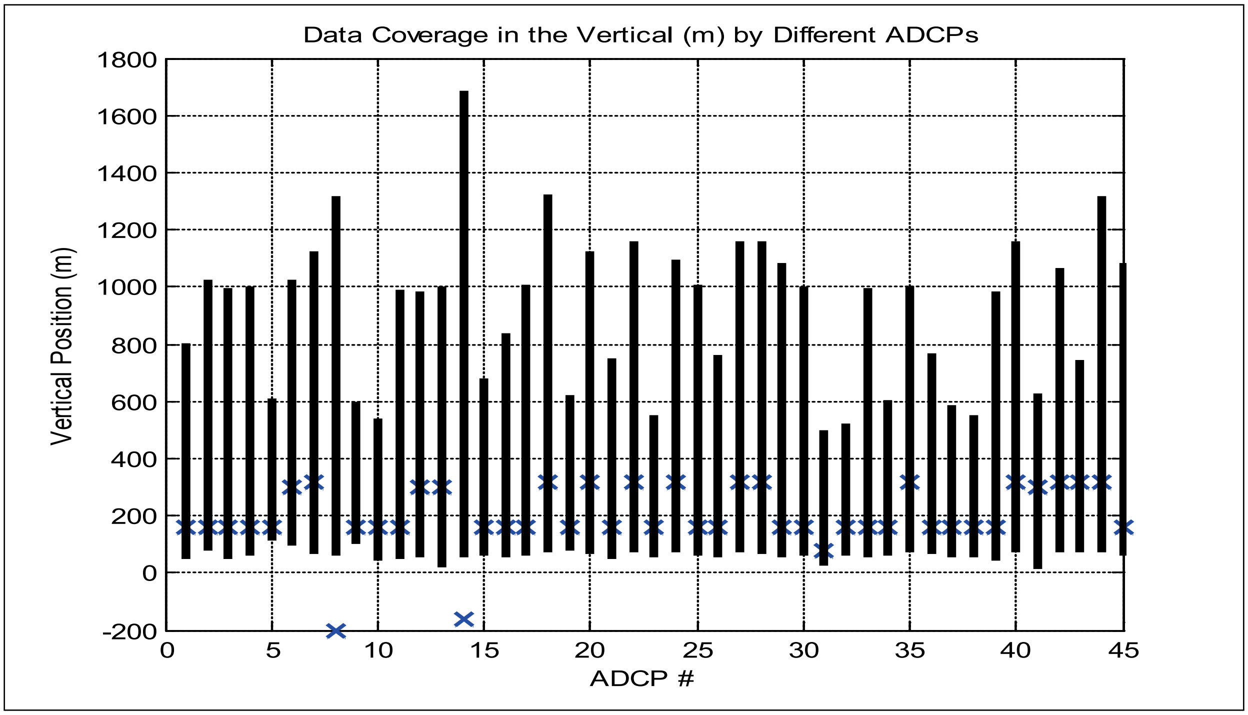

Figure 2.2. Data coverage in the vertical for different ADCPs in 2006 (The x's indicate the bin size as in Table 2.1).

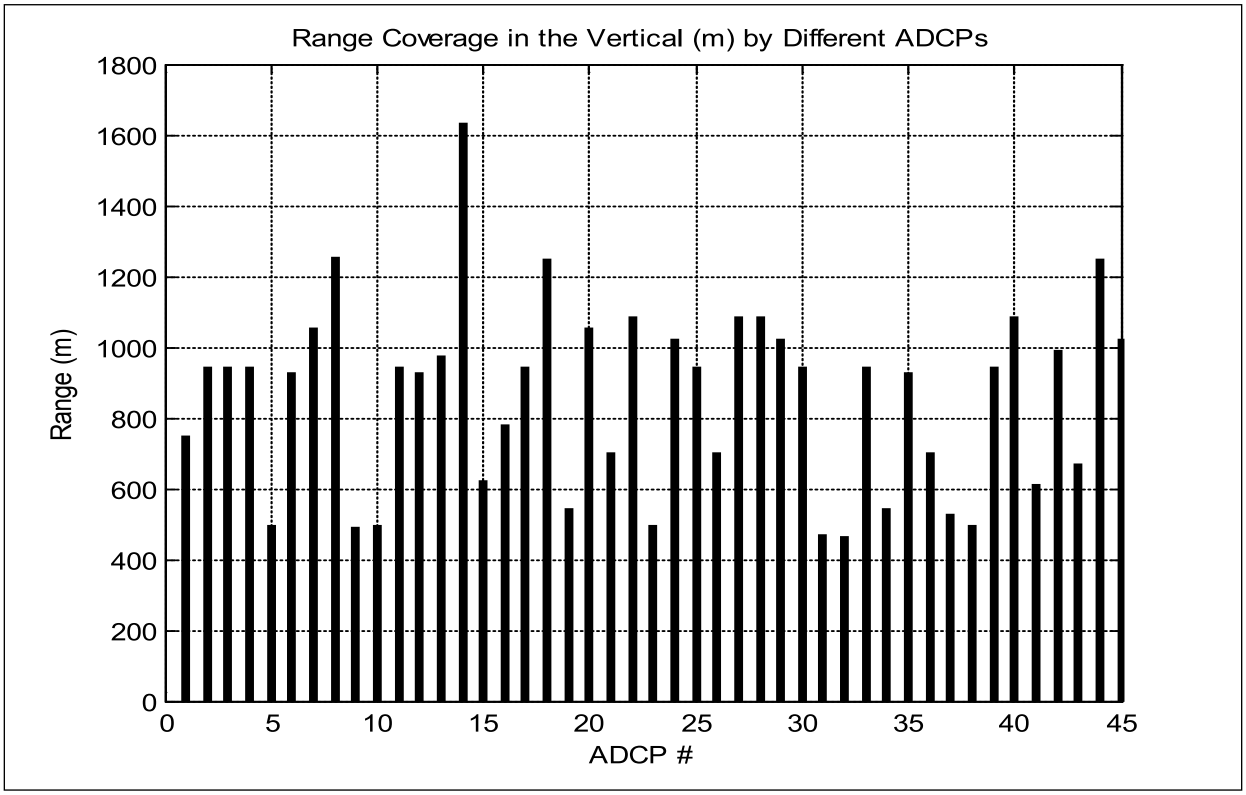

Figure 2.3. Vertical range for different ADCPs in 2006.

2.2 DATA INVENTORY

The temporal coverage of almost all of the ADCPs is quasi-continuous, with mostly continuous record lasting for a few weeks to a few months separated by gaps (sometimes significant gaps of more than a few months). Figure 2.4 shows the temporal coverage of data from 23 fixed-platform based ADCPs from April 2005 to Feb. 2008. Figure 2.5 shows the temporal coverage of data from 38 mobile-platform based ADCPs from April 2005 to Feb. 2008.

Figure 2.4. Temporal coverage of data for fixed stations.

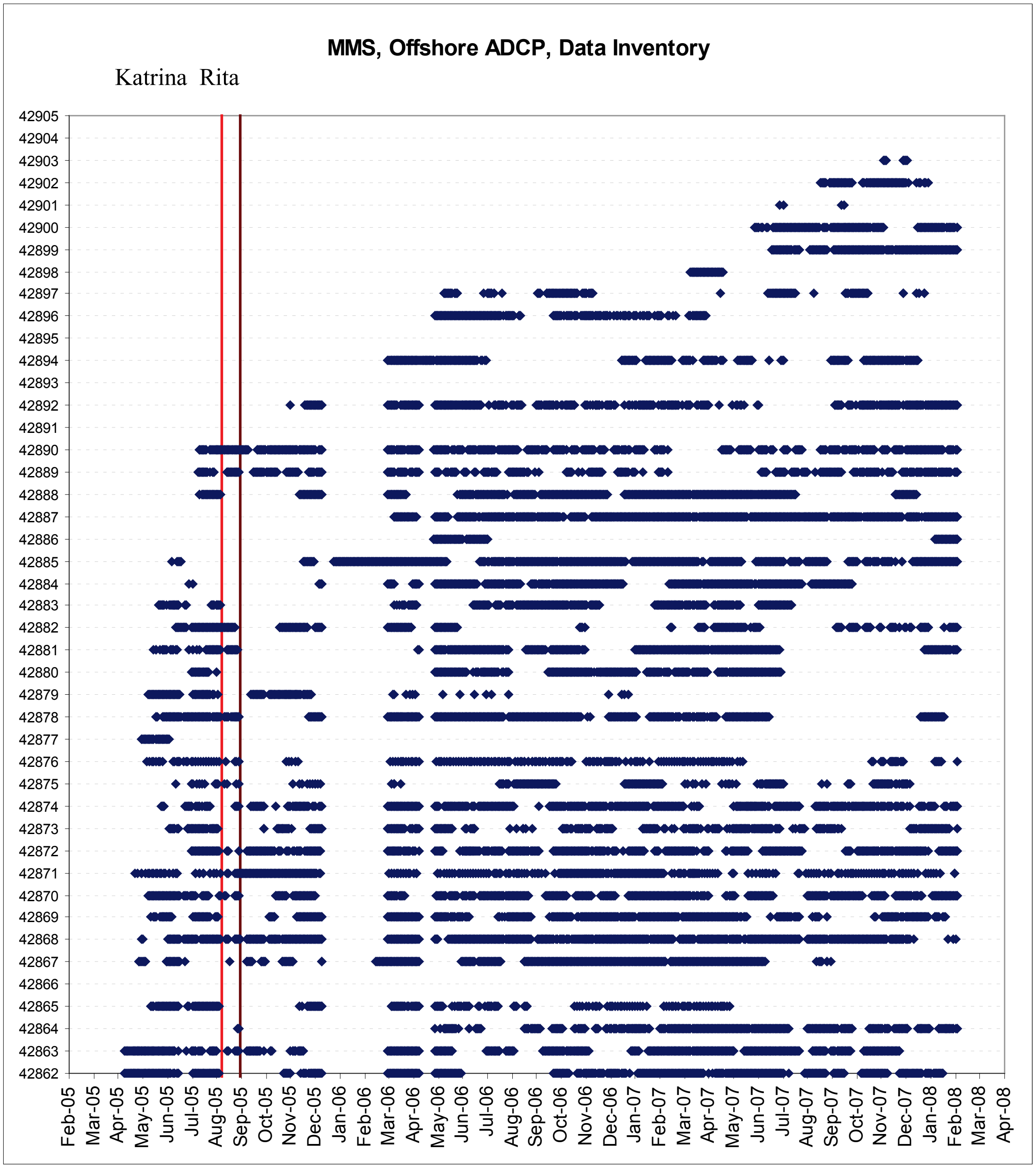

Figure 2.5. Temporal coverage of data for the fixed stations.

3. BASIC STATISTICS OF CURRENTS MEASURED BY ADCPS

3.1 DATA RETURN

The amount of data returned from each instrument varies quite a lot. This is shown by Figure 3.1 which shows the percentage of time during the years 2005, 2006, and 2007 for each of the 60 ADCPs operating in the Gulf of Mexico. The data return varies from near 0% (stations 42383 and 42905) to over 60% with a maximum not exceeding 65% (stations 42367, 42372, 42374, 42375, 42376, 42871, 42872, 42877, 42879, 42882, and 42890). Most of the stations reported data 30%-60% of the time. While Figure 3.1 is just for the depth of 100 m, it is representative of the dataset regarding the relative amount of data returned. The actual percentage, however, generally decreases with depth.

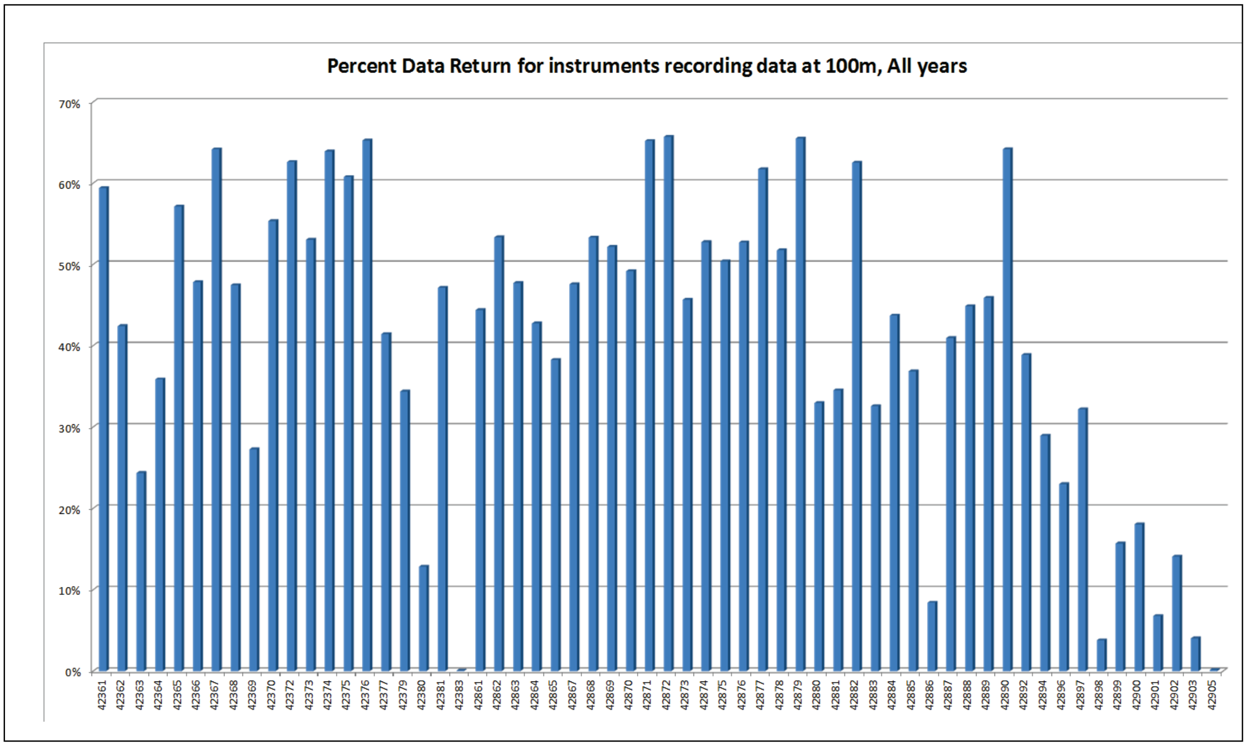

Figure 3.1. Data return from all 60 ACDP operating during 2005-2007 for the 100 m depth.

3.2 OVERALL MEAN AND STANDARD DEVIATION OF THE VELOCITY MAGNITUDE

3.2.1 All Data

In the ADCP data files, there is a field for "Percentage Good" of the data return. This "Percentage Good" is not the same as the above percentage data return in time. The "Percentage Good" is an indication of the data quality. We use 75% with this field as our criteria of data selection: we reject any data point that has a Percentage Good value lower than 75%. Usually, when this value is below 75%, it is generally much lower than 75%: the data either has relatively high Percentage Good (such as 100%) or a low value (such as 40%, 50%, or 0%). According to our experience, choosing 75% as the cut off appears to be appropriate.

Because of the large volume of data, it is desirable that to have a general view of what the data provide. The first statistics are the average and standard deviation of the velocity magnitude for the whole dataset, or as a function of the vertical location in the water column, or for different years, or for different geographic locations. The results are shown in Figures 3.2-3.7, and Tables 3.1.-3.7. As shown in Table 3.1, the averaged velocity magnitude for all available data within the three year period for all locations and all depths is 12.8 cm/s. The standard deviation is 13.2 cm/s, comparable to the mean value. This indicates that the variability of the flow is relatively large. The total number of data points used to obtain these values is 4,640,044, including some data from 2008. When we exclude the 2008 data, the results are very close. The total number of data points without the 2008 data is 4,354,778.

When comparing among different years, we can see that the mean velocity magnitude and associated deviation are similar for different years (Table 3.1): the mean velocity for 2005, 2006, and 2007 are 13.5, 12.7, and 12.7 cm/s, respectively. The standard deviations for these three years are 15.5, 13.7, and 12.1 cm/s, respectively. The total numbers of good data points used to obtain these statistical values are 714,729, 1,616,232, and 2,023,817, respectively. The smaller number of data points for the year 2005 is because data collection started in April or later, with many starting much later than April, 2005.

To examine the vertical variations, the data were vertically averaged with 50 m bins and shown at 50 m intervals. Table 3.2 shows the results from 50 to 2300 m every 50m. The left column is for all data from all stations. The central column is for the data from fixed platforms. The right column is for data from the movable platforms. Since some of the movable platforms (those station numbers starting with 428 or 429) were in deeper water, only the left and right columns cover results to 2300 m. The central column can only cover up to 1900 m. The general trend is such that (1) the mean velocity magnitude decreases with depth, (2) the standard deviation decreases with depth, and (3) the standard deviations are comparable in magnitude to the mean values. More specifically, the mean velocity magnitude at the “surface” (50 m below surface) is 28.0 cm/s for the three–year mean with a standard deviation of 23.8 cm/s (Table 3.1). The mean velocity magnitude at the “surface” (50 m below surface) for the year 2005 is 33.7 cm/s with a standard deviation of 30.6 cm/s, which are much larger than the overall mean and standard deviation, respectively. The year 2005 appears to be the most energetic year. It should be noted again that the 2005 data have a smaller ensemble (only about half of that from 2006 and a third of that from 2007). The year 2006 shows the second largest mean velocity on the surface and throughout the water column (30.1 cm/s mean velocity and 24.3 cm/s standard deviation at 50 m below the surface); while 2007 shows the smallest mean velocity and standard deviation of the three years (25.4 cm/s mean velocity and 21.4 cm/s standard deviation). These results are shown in Table 3.2 and reproduced in the four panels, showing the mean velocity magnitude (the blue curve) and the mean plus or minus the standard deviation as functions of the vertical position in the water column, of Figure 3.2. The deepest point may not be the actual bottom of the water. As we already stated, an individual ADCP may not cover the entire water column.

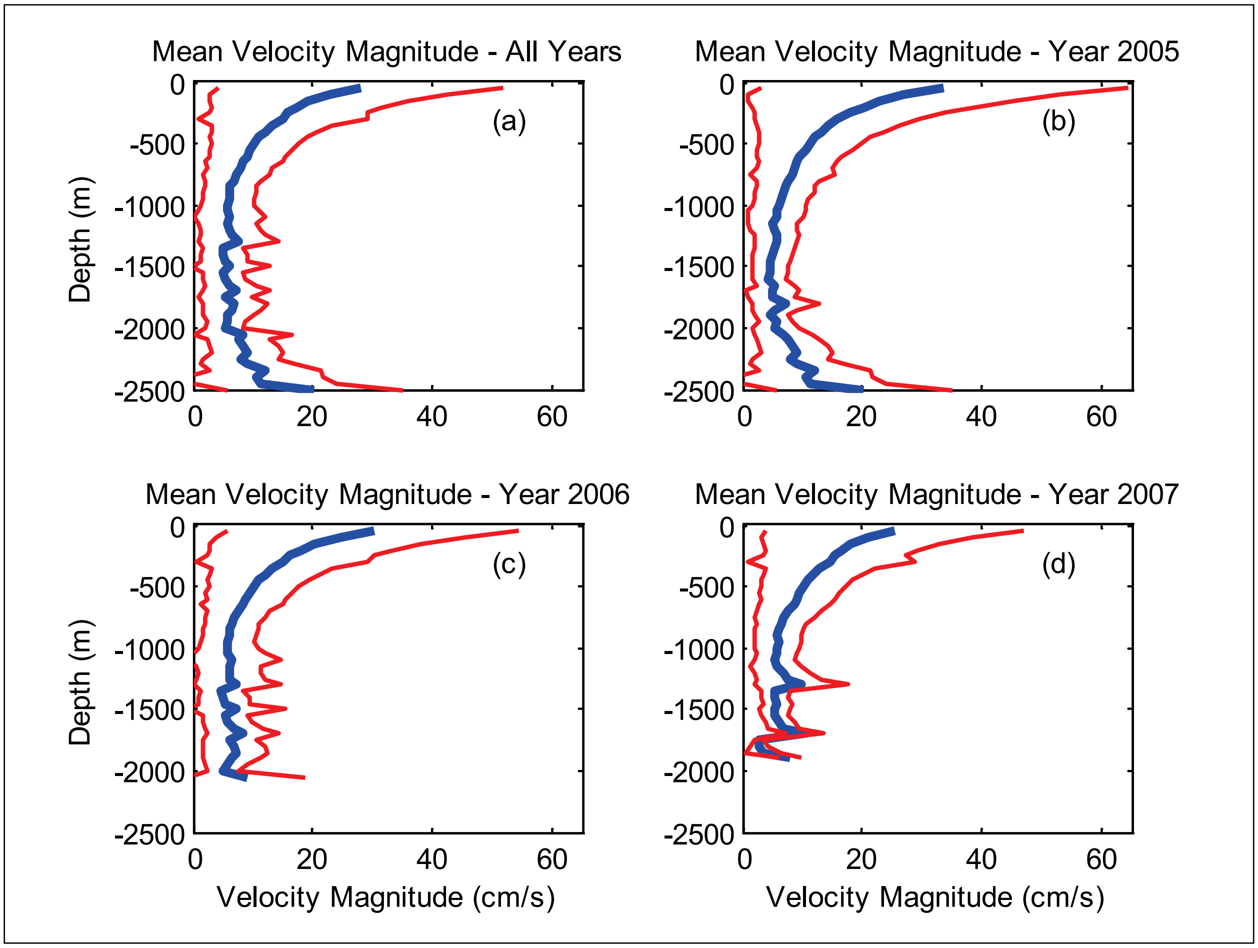

Figure 3.2. Mean velocity magnitude and its standard deviation as functions of water depth for all 60 instruments for (a) all years, (b) 2005, (c) 2006, and (d) 2007.

The rates of decrease of both the velocity magnitude and standard deviation with depth are pretty rapid. The decrease of mean values appears to be exponential and smooth above 1000 m below the surface. Below the 1000 m, velocity becomes weak with a mean value around 5-7 cm/s and variable (not smooth). Near the bottom below 2000 m, the mean velocity magnitude and standard deviation may show some increase. This appears to be coincident with the dramatic drop in the number of data points (Figure 3.3). Below 1300 m, there is only a small fraction of the data points compared to the top 1000 m. This is partly because most of the ADCPs are located at a location where the total water depth is less than 1200 m. A second reason for the dramatic drop in the number of data points is the fact that the ADCPs measure the velocity values at various depths through the backscattering of ultrasonic acoustic signal from suspended particles in the water column but the water at deep ocean is usually very clean with small velocities and high clarity such that there is fewer particles for backscattering to measure the velocity. The increase of the near-bottom velocity may be a result of biased samplings: for faster flows, there is better chance that the water is stirred up more with more particles and stronger return signal from the ADCPs. This however is pure speculation and not verified in anyway by this study. The vertical distribution of the number of data points is similar for the three years but with a general trend of increase from 2005 to 2007 at all depth. This just reflects the fact that more data are reported in 2006 and 2007.

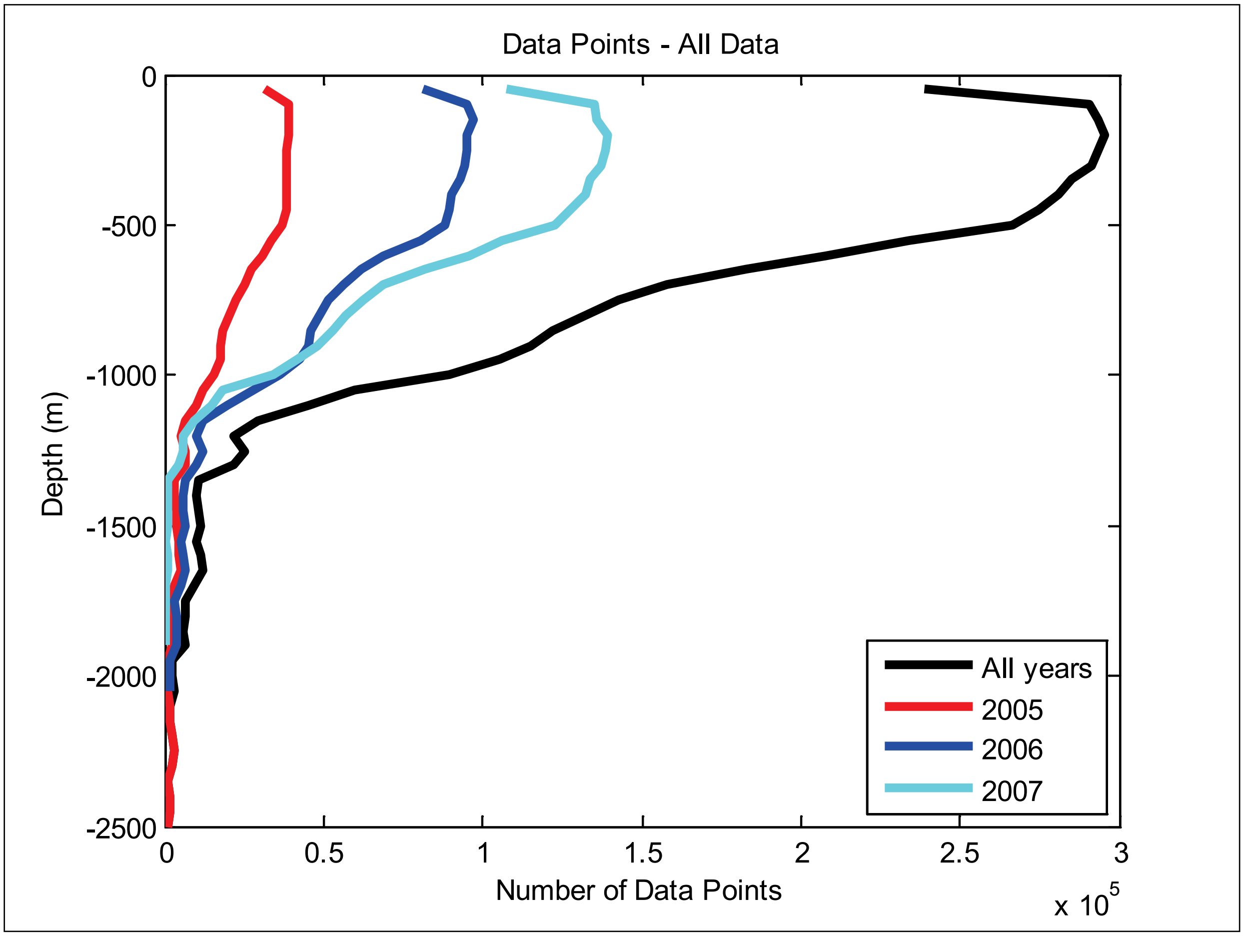

Figure 3.3. Number of data points used for the statistics calculations as a function of water depth for all the ADCPs and for all years (black), the year 2005 (red), the year 2006 (the blue), and the year 2007 (light blue).

3.2.2 The 423* Data

In this section, we discuss the basic statistics results for data measured from fixed platforms (ADCPs numbered with 423 as their first three digits). We present similar calculations as discussed in Section 3.2.1. These stations will potentially provide longer time series than those that move from place to place (428 or 429 as their first three digits in their station identification numbers). It is therefore reasonable and useful to separate data from these fixed ADCPs from those in moving platforms in the discussion of the results.

Similar to the results for all the data, when comparing among different years, we can see that the mean velocity magnitude and associated deviation from the fixed ADCPs (from 423-stations) are also similar for different years (top of Table 3.1): the mean velocity for 2005, 2006, and 2007 are 9.6, 10.1, and 11.5 cm/s, respectively. The standard deviations for these three years are 10.9, 9.0, and 9.8 cm/s, respectively. The total numbers of good data points used to obtain these statistical values are 189,361, 585,696, and 650,420, respectively. The total is 1,425,477 points. Again, the smaller number of data points for the year 2005 is because the data started in April or later, with many starting much later than April of 2005. For all the three years, the mean speed for all depths is 10.7 cm/s with a standard deviation of 9.6 cm/s.

Again, to examine the variation with vertical location, the data were vertically averaged with 50 m bins and shown at 50 m intervals. Table 3.2 shows the results from 50 to 1900 m every 50 m. The deepest measurements from these ADCPs were around 1900, which is shallower than the deepest of those installed on movable drilling units. The general trend is again (1) the mean velocity magnitude decreases with depth, (2) the standard deviation decreases with depth, and (3) the standard deviations are comparable in magnitude to the mean values. More specifically, the mean velocity magnitude at the "surface" (50 m below surface) is 18.8 cm/s for all the three years with a standard deviation of 13.1 cm/s (Table 3.2). The mean velocity magnitude at the "surface" (50 m below surface) for the fixed stations in year 2005 is 14.2 cm/s with a standard deviation of 9.6 cm/s, which are smaller compared to the overall mean and standard deviation, respectively (Table 3.3, Table 3.4). Data from the fixed platforms show that the year 2005 is the least energetic period. The apparent contradiction may be due to the fact that the movable drilling units occupied deeper waters where the influence of Loop Current and Loop Current Eddies are much stronger. The year 2006 shows the largest mean velocity on the surface and throughout the water column (19.6 cm/s mean velocity and 12.8 cm/s standard deviation at 50 m below the surface); while 2007 shows intermediate mean velocity and standard deviation of for these fixed ADCPs (18.8 cm/s mean velocity and 13.8 cm/s standard deviation). These results are shown in Table 3.4 and reproduced visually in Figure 3.3. The number of data points for the fixed platforms are shown in Figure 3.4.

Not surprisingly, the rates of decrease of both the velocity magnitude and standard deviation with depth from the fixed ADCPs are also rapid and smooth above 1000 m below the surface. Below the 1000 m, velocity becomes weak with a mean value around 5-7 cm/s and variable (not smooth). Near the bottom below 2000 m, the mean velocity magnitude and standard deviation start to increase. This is coincident with the dramatic drop in the number of data points (Figure 3.4). Below 1300 m, there is only a small fraction of the data points. Unlike the results for all the data or movable ADCPs (see next section), the fixed ADCP data do not show an increase at near the bottom. One of the reasons for this is that the ADCPs are not as deep as some of those mounted on movable platforms.

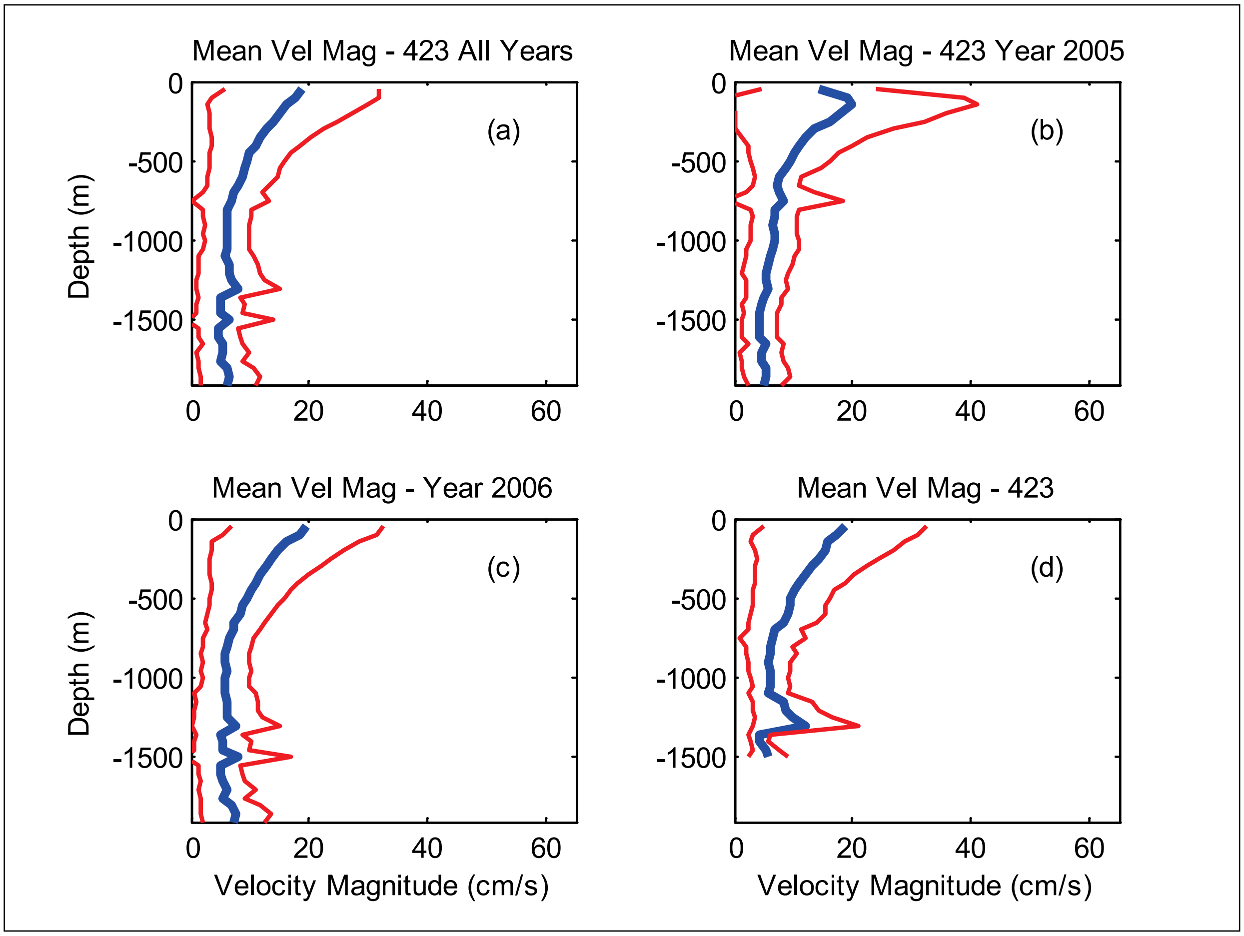

Figure 3.4. Mean velocity magnitude and its standard deviation as functions of water depth for all the 423* stations (on fixed platforms) for (a) all years, (b) 2005, (c) 2006, and (d) 2007.

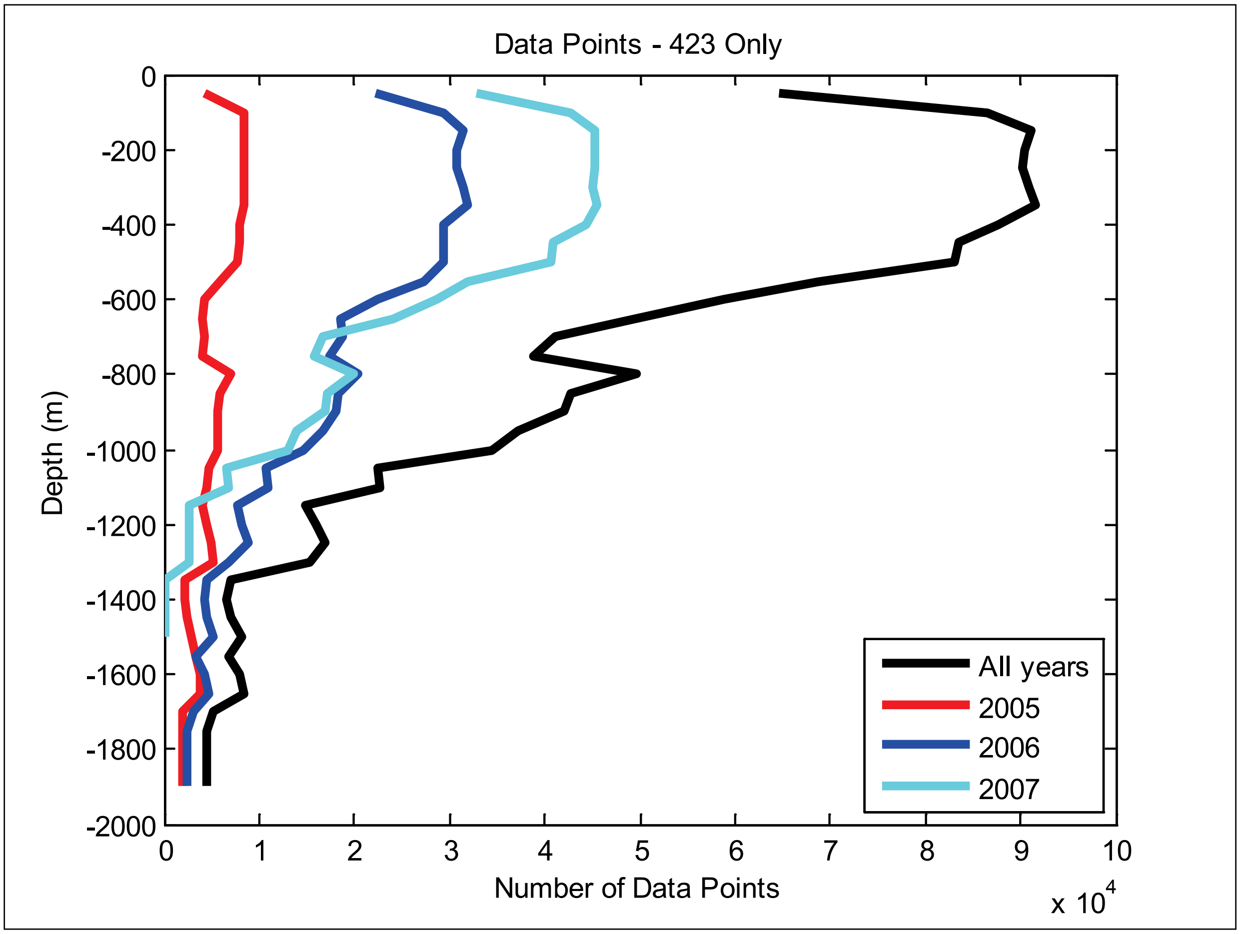

Figure 3.5. Number of data points used for the statistics calculations as a function of water depth for the 423* ADCPs (i.e. those on fixed platforms) and for all years (black), the year 2005 (red), the year 2006 (blue), and the year 2007 (light blue).

3.2.3 The 428* and 429* Data

The movable platform stations with ADCPs are numbered with 428 or 429 as their first three digits. We performed similar calculations to those discussed in Sections 3.2.1 and 3.2.2 for these ADCPs. These have shorter time series at each location than those that are fixed. These moving platforms can also occupy deeper water. Therefore, stronger influence from the Loop Current and associated Loop Current eddies, is expected. These movable platforms usually stay at one place for months if not the entire year. They may move in shorter intervals nevertheless.

Similar to the results for all the data, when comparing among different years, we can see that the mean velocity magnitude and associated deviation from the movable ADCPs are also similar for different years (top of Table 3.1): the mean velocity for 2005, 2006, and 2007 are 14.8, 14.2, and 13.3 cm/s, respectively. The standard deviations for these three years are 16.6, 15.5, and 13.0 cm/s, respectively. The total numbers of good data points used to obtain these statistical values are 525,368, 1,030,536, and 1,373,397, respectively. The total is 2,929,301 points. Again, the smaller number of data points for the year 2005 is because the data started in April or later, with many starting much later than April of 2005. For all the three years, the mean velocity magnitude for all depths is 13.8 cm/s with a standard deviation of 14.5 cm/s.

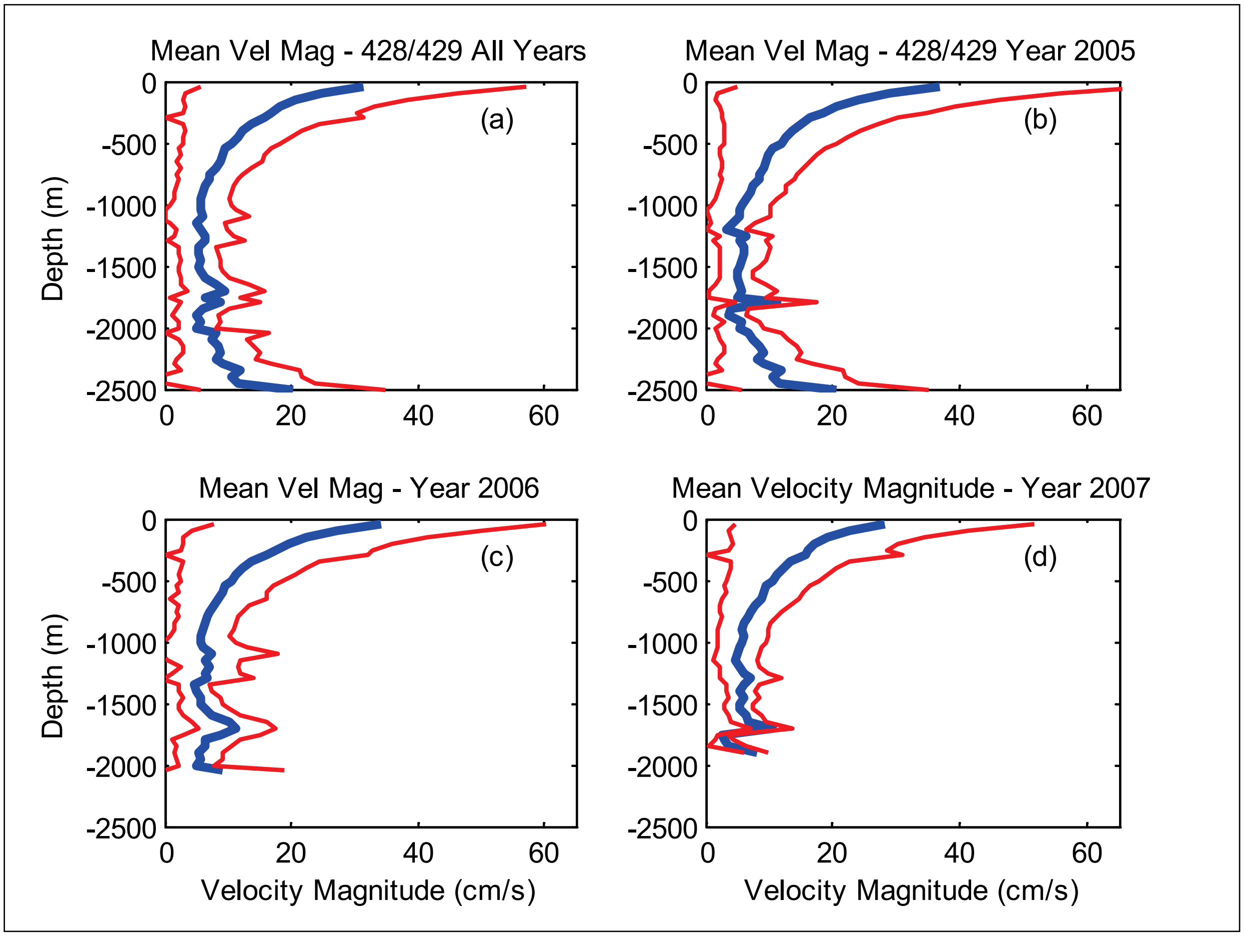

Figure 3.6. Mean velocity magnitude and its standard deviation as functions of water depth for all the 428* and 429* stations (movable platforms) for (a) all years, (b) 2005, (c) 2006, and (d) 2007.

Again, to examine the vertical variation, the data were vertically averaged with 50 m bins and shown at 50 m intervals. The right column of Table 3.2 shows the results from 50 to 2300 m every 50 m. The deepest measurements from these ADCPs were around 2500, which is deeper than the deepest of those installed on fixed platforms. The general trend is again (1) the mean velocity magnitude decreases with depth, (2) the standard deviation decreases with depth, and (3) the standard deviations are comparable in magnitude to the mean values. More specifically, the mean velocity magnitude at the "surface" (50 m below surface) is 31.5 cm/s for all the three years with a standard deviation of 25.8 cm/s (Table 3.2). These values are significantly larger than those from the fixed platforms (> 50% of increase). The mean velocity magnitude at the "surface" (50 m below surface) for the year 2005 is 36.7 cm/s with a standard deviation of 31.6 cm/s, which are the largest compared to the other two years (Table 3.5). The data from the movable platforms show that 2005 had the most energetic currents and more influenced by the Loop Current. Interestingly, 2005 was a year of unusually high hurricane activity. There may be some linkage between stronger and warmer Loop Current and more frequent hurricanes and tropical storms. The year 2006 shows intermediate mean velocity on the surface and throughout the water column (34.1 cm/s mean velocity and 26.3 cm/s standard deviation at 50 m below the surface); while 2007 shows the smallest mean velocity and standard deviation of the three years for these fixed ADCPs (28.2 cm/s mean velocity and 23.4 cm/s standard deviation). These results are shown in Table 3.5 and reproduced visually in Figure 3.5. The vertical structures (Figure 3.5) are very similar to the overall results (Figure 3.2). The number of data points drop dramatically below 1300 m (Figure 3.7).

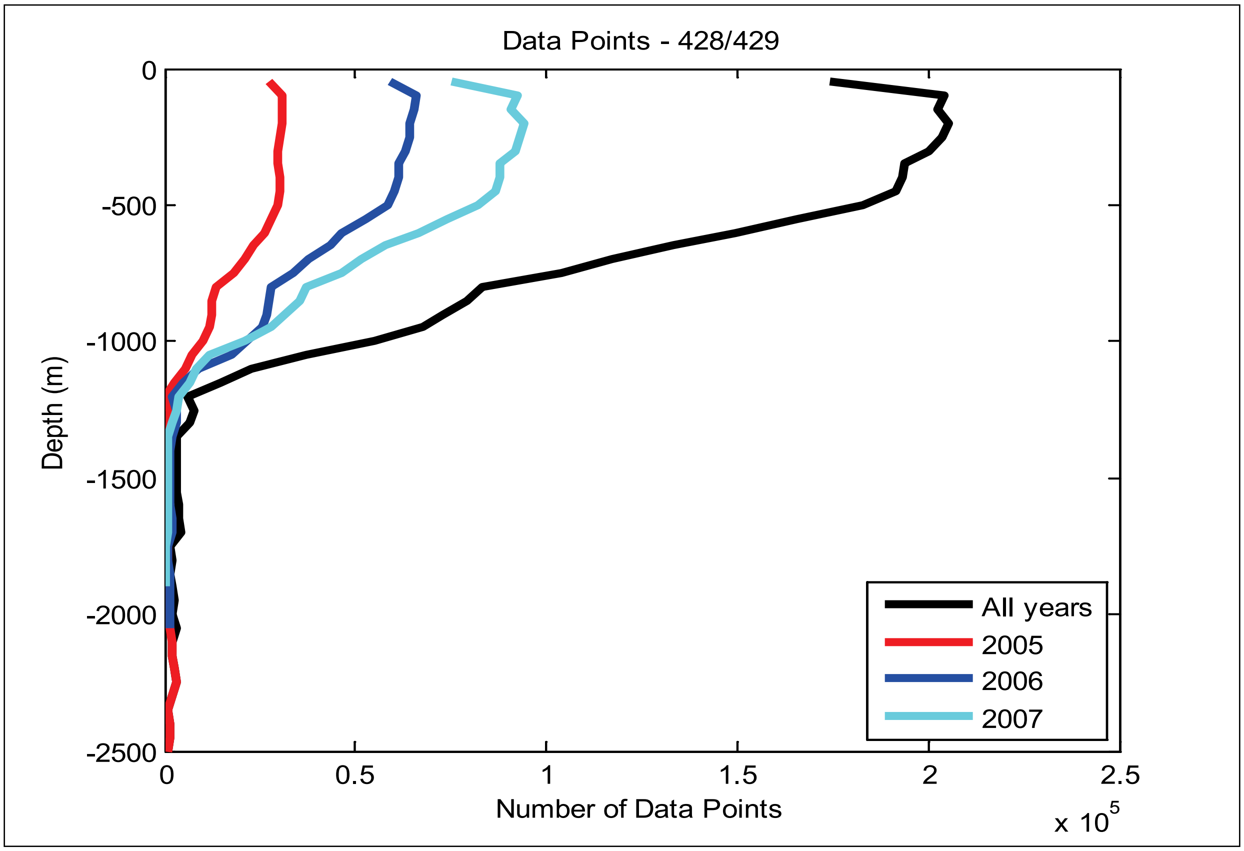

Figure 3.7. Number of data points used for the statistics calculations as a function of water depth for the 428* and 429* ADCPs (i.e. those on movable platforms) and for all years (black), the year 2005 (red), the year 2006 (blue), and the year 2007 (light blue).

To demonstrate how much movements the 428*/429* movable drilling units may have, we plotted the stations and their tracks in Figure 3.8. The red color positions are the fixed platforms, while the blue ones are movable (although some of them did not move during the time of data coverage).

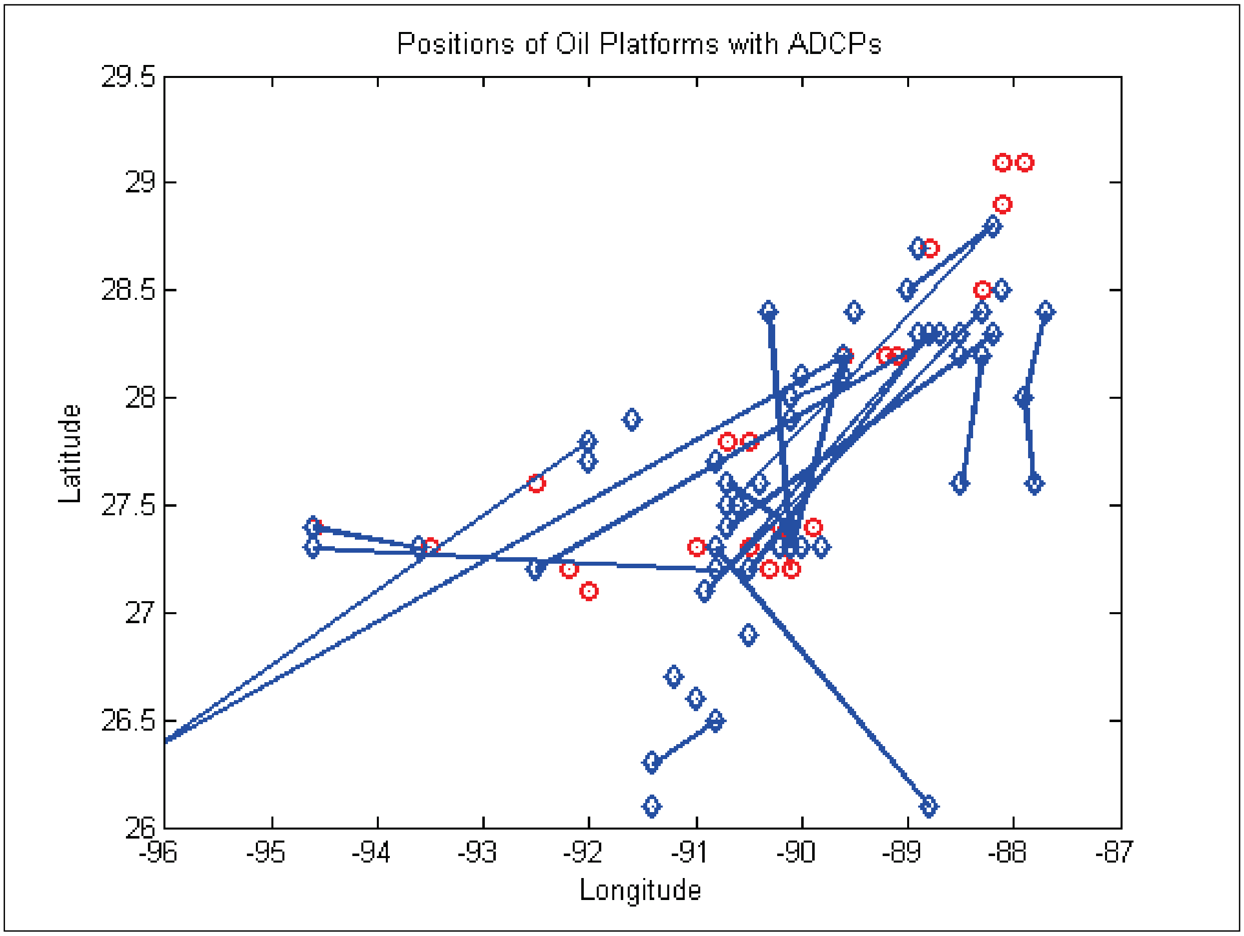

Figure 3.8. Locations and tracks of the study platforms. Red circles are fixed platforms and the blue diamonds are the movable platforms.

3.3 TEMPORAL AND VERTICAL CHANGES OF THE MEAN VELOCITY AND STANDARD DEVIATIONS

The above statistical characteristics of the flow field provide a very crude picture which does not have much information of spatial variations (except the vertical structure) and temporal variations (except the comparison among the three years). In this section, we examine the spatial and temporal variations in more detail by the spatially averaging speed as a function of time for all stations, and by the spatially averaging speed as a function of time for stations from three regions – the western, central, and eastern regions.

These three regions are defined rather arbitrarily for convenience and with consideration of the cluster of ADCPs. As can be seen on Figure 3.9, the West region contains about 12 ADCPs, while the Central and East regions have 24 and 20 ADCPs, respectively. In the following, we will present the results for all the ADCPs, as well as for the ADCPs from the three different regions.

By examining the data, it can be seen that the magnitude of the horizontal velocity as a function of vertical position has a long term variation. This variation does not seem to have a clear periodicity. As shown in Figure 3.10, the large velocity values occur mostly in the top layer above 200 m. When a large velocity occurs, it may last for a few months (note these are averaged and low-pass filtered data and exclude inertial oscillations). The central area seems to have the most energetic speeds, with mean speeds of 15.0, 15.8, 12.4, and 13.3 cm/s for 2005, 2006, 2007, and 2008, respectively; the total number of data points are 150,000 (the year 2008, with partial data) to 819,000 (2007, with full year of coverage). The eastern area has less energetic speeds but stronger flows than the western region, with mean speeds of 13.6, 10.6, 15.3, and 10.5 cm/s for 2005, 2006, 2007, and 2008, respectively; the total number of data points are 84,000 (the year 2008, with partial data) to 782,000 (2007, with full year of coverage). The western area has the least energetic speeds with means of 10.3, 11.1, 8.6, and 12.6 cm/s for 2005, 2006, 2007, and 2008, respectively;, the total number of data points are 43,000 (the year 2008, with partial data) to 422,000 (2007, with full year of coverage, Figure 3.10, Table 3.6).

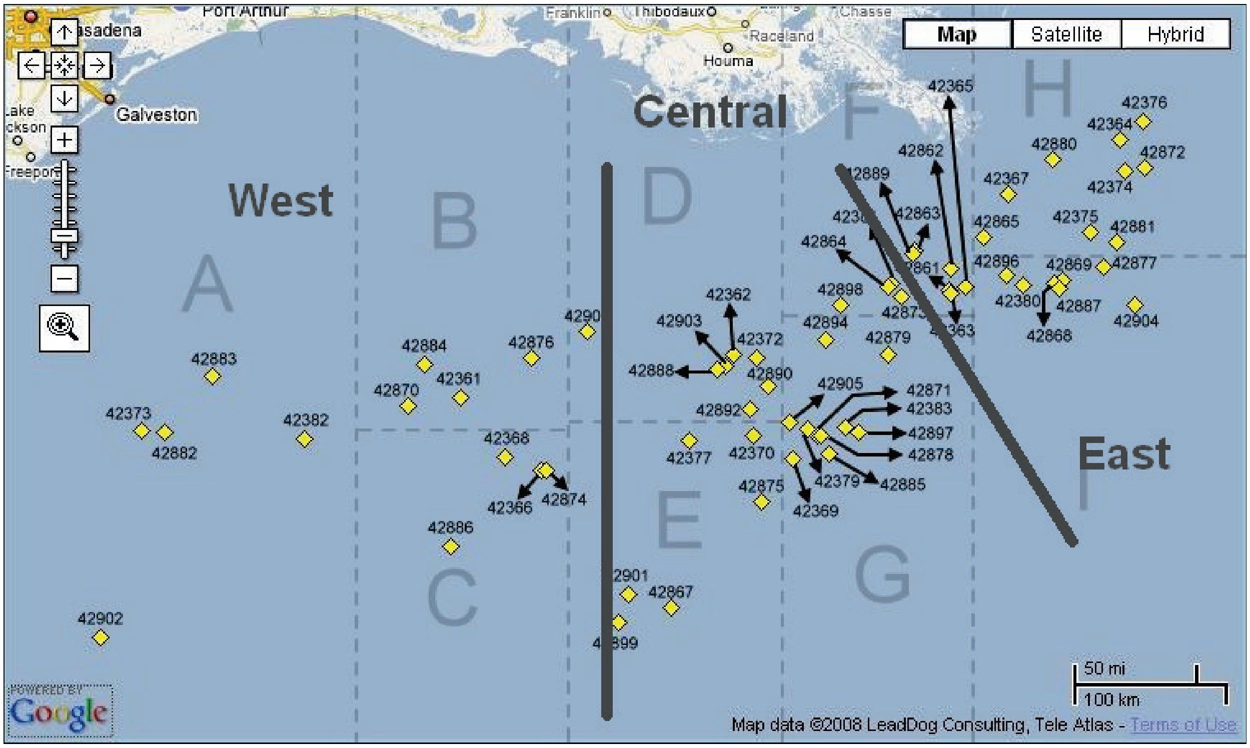

Figure 3.9. Division of the study area into the east, central, and west regions.

The west area and central area can have similarities sometimes but may still be quite different. The maximum flow is mostly on the surface but can extend downward. The depth at which the maximum velocity magnitude reaches also varies, which suggests a result of eddies coming through the area. The central area velocity seems to lead that of the western area most of the time. This is consistent with a westward propagation of eddies. In contrast, the eastern region however has much less similarity to the central and western regions. This suggests that the eastern region is not the "upstream" region of the central and western regions.

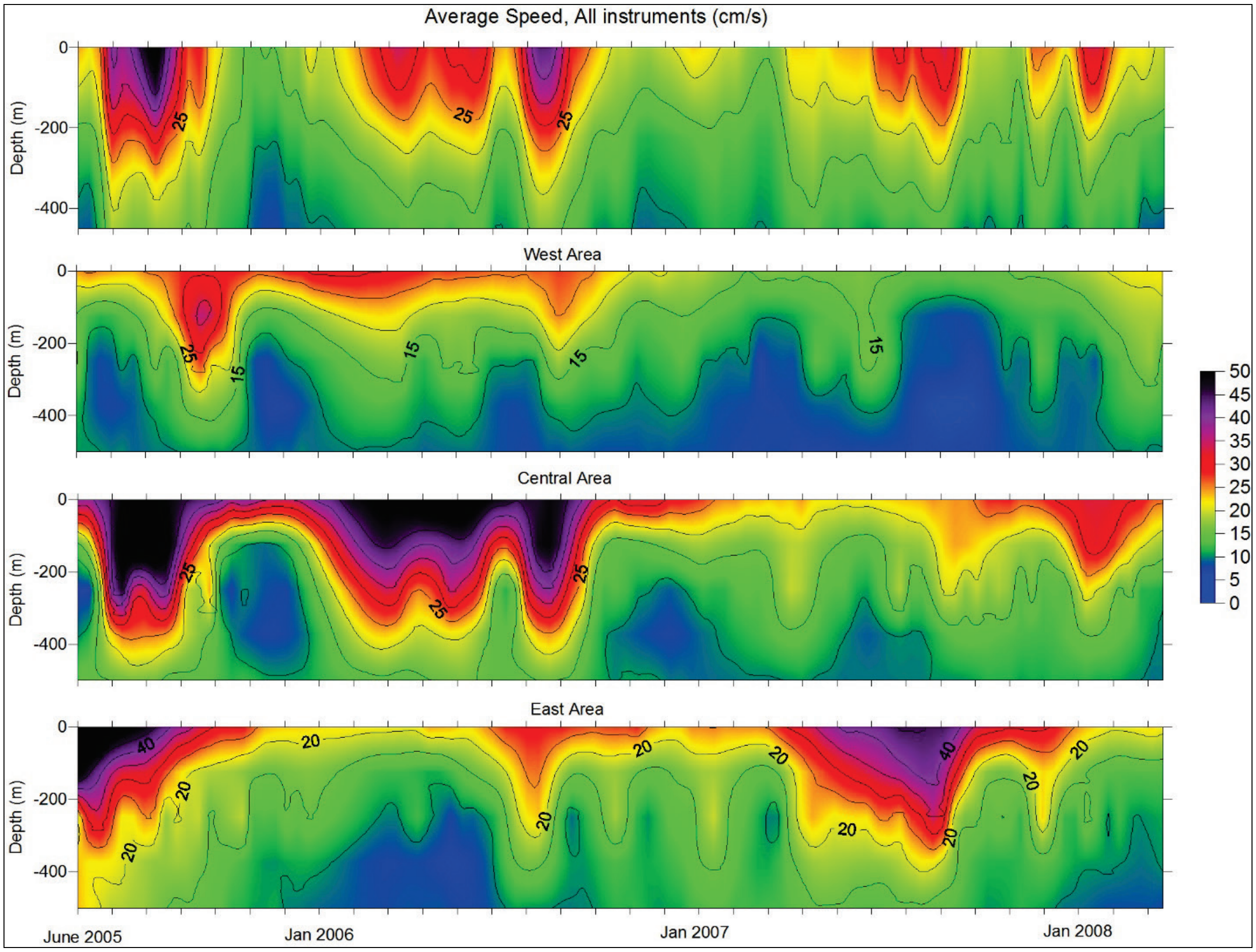

Figure 3.10. Averaged speed as a function of time and depth.

Table 3.1

Flow Statistics for All ADCPS or Different Groups of ADCPs at All Depths and All Years or Different Years.

All ADCPs

Mean (cm/s)	**STD**	**n**
12.8	13.2	4354778

Year	**Mean (cm/s)**	**STD**	**n**
2005	13.5	15.5	714729
2006	12.7	13.7	1616232
2007	12.7	12.1	2023817

423* ADCPs Only

Mean (cm/s)	**STD**	**n**
10.7	9.6	1425477

Year	**Mean (cm/s)**	**STD**	**n**
2005	9.6	10.9	189361
2006	10.1	9.0	585696
2007	11.5	9.8	650420

428*/429* ADCPs Only

Mean (cm/s)	**STD**	**n**
13.8	14.5	2929301

Year	**Mean (cm/s)**	**STD**	**n**
2005	14.8	16.6	525368
2006	14.2	15.5	1030536
2007	13.3	13.0	1373397

Table 3.2

Mean and standard deviation of horizontal speed (cm/s) for all years.

All Stations

Depth	Mean	STD	n
50	28.0	23.8	238728
100	22.8	19.9	290892
150	19.3	16.7	293514
200	17.3	14.2	295724
250	15.9	13.1	293657
300	14.9	14.1	291193
350	13.1	10.1	285379
400	11.9	8.8	280992
450	11.0	8.1	274978
500	10.3	7.3	266133
550	9.6	6.9	234301
600	9.1	6.4	207986
650	8.5	6.4	182986
700	7.8	5.5	158267
750	7.1	5.6	142863
800	6.7	4.5	132516
850	6.3	4.4	121813
900	6.1	4.3	115054
950	6.0	4.3	105199
1000	5.8	4.4	89314
1050	5.8	5.0	59901
1100	6.0	6.1	45429
1150	5.7	4.7	29572
1200	6.3	4.9	21939
1250	6.6	5.3	24891
1300	7.6	6.8	21693
1350	5.1	3.4	10410
1400	5.1	3.9	10056
1450	5.2	3.8	10403
1500	6.2	6.6	11560
1550	5.0	3.4	10105
1600	5.2	3.7	11559
1650	6.3	4.3	12233
1700	7.3	5.6	9162
1750	5.4	4.3	6257
1800	6.9	5.4	6618
1850	6.5	4.9	5869
1900	5.8	4.3	6533
1950	5.6	3.3	2478
2000	5.2	3.1	2162
2050	8.3	8.1	2882
2100	7.6	5.3	1772
2150	8.5	5.7	2045
2200	9.0	6.0	2441
2250	8.1	6.3	2949
2300	9.1	7.7	2298

423* Stations Only

Depth	Mean	STD	n
50	18.8	13.1	64684
100	17.7	14.1	86475
150	16.3	13.6	91089
200	15.2	12.0	90327
250	13.9	10.8	90303
300	12.8	9.7	90965
350	11.8	8.4	91693
400	10.9	7.5	87648
450	10.0	6.8	83439
500	9.5	6.3	83029
550	9.2	6.0	68841
600	8.7	5.9	58760
650	7.9	5.3	49432
700	7.1	4.9	41170
750	6.7	6.5	38808
800	6.1	4.0	49551
850	6.2	4.1	42705
900	6.0	3.7	42096
950	6.1	3.9	37314
1000	6.1	3.7	34510
1050	6.0	3.9	22575
1100	5.9	4.5	22797
1150	6.4	5.0	14898
1200	6.4	5.2	15933
1250	6.7	5.6	17015
1300	8.0	7.1	15234
1350	4.9	3.6	6964
1400	5.0	4.2	6604
1450	4.9	4.0	6965
1500	6.5	7.5	8157
1550	4.6	3.3	6729
1600	4.7	3.5	8013
1650	5.4	3.3	8396
1700	5.4	4.4	5116
1750	5.1	3.7	4548
1800	6.0	4.6	4545
1850	6.6	5.1	4541
1900	6.3	4.5	4537

428*/429* Stations Only

Depth	Mean	STD	n
50	31.5	25.8	174044
100	24.9	21.6	204417
150	20.7	17.8	202425
200	18.2	15.0	205397
250	16.7	13.8	203354
300	15.8	15.6	200228
350	13.8	10.7	193686
400	12.4	9.2	193344
450	11.5	8.5	191539
500	10.7	7.7	183104
550	9.7	7.3	165460
600	9.3	6.6	149226
650	8.7	6.7	133554
700	8.1	5.6	117097
750	7.2	5.2	104055
800	7.0	4.7	82965
850	6.4	4.5	79108
900	6.1	4.6	72958
950	5.9	4.4	67885
1000	5.7	4.8	54804
1050	5.7	5.5	37326
1100	6.1	7.3	22632
1150	5.1	4.4	14674
1200	5.9	3.9	6006
1250	6.3	4.6	7876
1300	6.6	6.2	6459
1350	5.3	3.0	3446
1400	5.4	3.0	3452
1450	5.8	3.1	3438
1500	5.5	3.3	3403
1550	5.7	3.4	3376
1600	6.4	3.8	3546
1650	8.1	5.4	3837
1700	9.6	6.1	4046
1750	6.4	5.5	1709
1800	8.8	6.3	2073
1850	6.1	4.3	1328
1900	4.9	3.6	1996
1950	5.6	3.3	2478
2000	5.2	3.1	2162
2050	8.3	8.1	2882
2100	7.6	5.3	1772
2150	8.5	5.7	2045
2200	9.0	6.0	2441
2250	8.1	6.3	2949
2300	9.1	7.7	2298

Table 3.3

Mean and standard deviation of horizontal speed (cm/s) for all stations in different years.

2005			
Depth	**Mean**	**STD**	**n**
50	33.7	30.6	31622
100	26.9	25.9	38959
150	23.0	22.1	39168
200	20.1	18.3	39355
250	18.1	16.0	38598
300	15.8	13.8	38298
350	14.3	11.9	38151
400	13.1	10.4	38124
450	12.1	9.4	38126
500	11.3	8.5	37235
550	10.4	7.9	33565
600	9.6	7.1	30717
650	9.2	6.6	27490
700	8.8	6.4	25138
750	8.3	7.1	22349
800	7.7	5.2	20436
850	7.2	4.8	18499
900	7.0	5.0	17775
950	6.5	4.5	17526
1000	6.0	4.5	15611
1050	5.7	4.7	11762
1100	5.7	4.6	9755
1150	5.1	4.0	6560
1200	5.2	3.9	4868
1250	5.6	3.7	6294
1300	5.6	3.6	6618
1350	5.4	3.5	3284
1400	5.1	3.4	3396
1450	4.8	3.2	3581
1500	4.6	3.1	4019
1550	4.5	3.0	4514
1600	4.4	2.9	4796
1650	5.5	3.2	4900
1700	5.0	4.4	3219
1750	4.9	4.0	3114
1800	7.2	5.6	3094
1850	5.4	3.7	2124
1900	4.8	2.9	2606
1950	5.6	2.7	920
2000	5.4	3.9	691
2050	6.9	4.9	1181
2100	7.6	5.3	1772
2150	8.5	5.7	2045
2200	9.0	6.0	2441
2250	8.1	6.3	2949
2300	9.1	7.7	2298
2350	12.1	9.4	1089
2400	10.5	11.3	1579
2450	11.5	12.4	1585
2500	20.4	14.7	930

2006			
Depth	**Mean**	**STD**	**n**
50	30.1	24.3	81390
100	24.6	20.8	95282
150	20.3	17.6	96816
200	17.9	15.2	95194
250	16.3	13.8	94873
300	15.0	14.3	94356
350	13.1	10.0	93252
400	11.9	9.2	90449
450	11.0	8.5	89735
500	10.2	7.4	87952
550	9.3	7.1	80287
600	8.8	6.5	68986
650	8.2	7.0	62149
700	7.6	5.2	56194
750	6.9	5.0	51179
800	6.6	4.5	48440
850	6.3	4.5	45829
900	6.0	4.4	45114
950	5.7	4.5	42486
1000	5.8	5.0	36423
1050	5.9	6.0	28129
1100	6.5	8.0	19661
1150	6.1	5.4	12397
1200	6.3	5.2	10307
1250	6.3	5.7	12014
1300	7.3	7.3	10071
1350	4.8	3.5	6346
1400	5.1	4.2	5921
1450	5.3	4.2	6079
1500	7.3	8.1	6802
1550	5.4	3.7	4979
1600	5.7	4.2	6018
1650	6.8	4.9	6631
1700	8.3	6.0	5331
1750	6.0	4.5	3129
1800	6.7	5.2	3510
1850	7.1	5.4	3731
1900	6.5	4.9	3915
1950	5.6	3.6	1558
2000	5.0	2.7	1471
2050	9.2	9.7	1701

2007			
Depth	**Mean**	**STD**	**n**
50	25.4	21.4	107737
100	20.8	17.6	135244
150	18.1	14.6	136091
200	16.6	12.6	139245
250	15.5	11.8	138516
300	14.8	13.8	137184
350	12.9	9.1	133489
400	11.8	8.1	132438
450	10.9	7.6	127878
500	10.2	7.0	122622
550	9.5	6.6	105780
600	9.2	6.2	95448
650	8.6	5.9	82117
700	7.7	5.3	68447
750	6.9	5.0	62337
800	6.5	4.2	57219
850	6.2	4.0	52618
900	5.9	3.8	48251
950	6.0	3.8	41566
1000	5.8	3.7	34151
1050	5.7	3.4	18622
1100	5.4	3.5	15038
1150	5.6	4.2	9441
1200	6.8	4.7	6182
1250	7.7	5.4	6001
1300	10.0	7.8	4422
1350	5.5	2.5	780
1400	5.3	2.3	739
1450	5.9	2.3	743
1500	5.3	2.5	739
1550	5.3	2.3	612
1600	6.3	2.5	745
1650	6.8	2.7	702
1700	10.4	3.2	612
1750	2.7	0.8	14
1800	2.9	1.5	14
1850	3.5	3.0	14
1900	8.1	1.9	12

Table 3.4

Mean and standard deviation of horizontal speed (cm/s) for all fixed stations. (423* stations) at Different Depths during Different Years

2005				2006				2007			
Depth	**Mean**	**STD**	**n**	**Depth**	**Mean**	**STD**	**n**	**Depth**	**Mean**	**STD**	**n**
50	14.2	9.6	4232	50	19.6	12.8	22299	50	18.8	13.8	32758
100	19.1	19.6	8399	100	18.4	13.0	29462	100	17.1	14.0	42801
150	20.0	21.1	8396	150	16.0	12.5	31430	150	15.9	13.0	45336
200	18.0	17.7	8369	200	14.6	11.1	30742	200	15.4	11.7	45295
250	16.1	16.1	8441	250	13.5	10.2	30727	250	14.2	10.3	45214
300	13.7	13.4	8427	300	12.7	9.5	31517	300	13.0	9.4	45128
350	11.9	10.6	8358	350	11.6	8.3	31806	350	12.0	8.4	45475
400	11.1	8.7	7885	400	10.8	7.3	29290	400	11.1	7.6	44435
450	10.1	7.6	7847	450	10.1	6.7	29263	450	10.1	6.8	40944
500	9.3	6.7	7747	500	9.5	6.2	29388	500	9.6	6.4	40560
550	8.9	5.6	5869	550	8.9	5.8	27379	550	9.3	6.2	31865
600	7.5	4.0	4364	600	8.2	5.4	22572	600	9.0	6.4	28789
650	7.1	4.0	4011	650	7.4	4.9	18450	650	8.2	5.7	24161
700	7.7	5.8	4257	700	7.1	4.5	18710	700	6.9	4.6	16691
750	8.3	10.1	4115	750	6.4	4.3	17473	750	6.4	5.6	15741
800	6.7	4.1	7126	800	6.1	4.1	20319	800	6.0	3.9	20010
850	6.8	3.8	5857	850	5.9	4.1	18321	850	6.3	4.1	17128
900	6.6	3.8	5553	900	5.9	3.9	18158	900	5.9	3.6	17005
950	6.7	4.0	5625	950	6.0	4.2	16625	950	6.0	3.5	13825
1000	6.7	4.1	5652	1000	5.9	3.9	14680	1000	6.0	3.2	12975
1050	6.5	4.3	4617	1050	5.6	4.1	10808	1050	6.3	3.3	6568
1100	6.1	4.2	4450	1100	5.7	5.2	11003	1100	5.8	3.4	6744
1150	5.7	4.1	3966	1150	6.0	5.2	7724	1150	8.2	5.0	2625
1200	5.3	3.9	4575	1200	6.0	5.4	8169	1200	8.8	5.6	2607
1250	5.4	3.5	5044	1250	6.2	5.8	8807	1250	9.9	6.5	2582
1300	5.6	3.4	5254	1300	7.6	7.3	6825	1300	12.0	8.8	2573
1350	5.0	3.1	2200	1350	4.9	3.8	4581	1350	4.3	1.9	183
1400	4.6	3.2	2273	1400	5.3	4.8	4197	1400	4.3	1.6	134
1450	4.4	2.9	2452	1450	5.2	4.5	4379	1450	5.3	2.3	134
1500	4.3	2.9	2906	1500	7.9	9.0	5117	1500	5.8	3.4	134
1550	4.4	3.0	3436	1550	4.9	3.6	3293				
1600	4.3	2.9	3708	1600	5.0	3.8	4305				
1650	5.4	2.9	3767	1650	5.4	3.6	4629				
1700	4.6	3.5	2028	1700	6.0	4.8	3088				
1750	4.8	3.6	2040	1750	5.3	3.7	2508				
1800	5.2	3.8	2039	1800	6.7	5.1	2506				
1850	5.5	3.8	2036	1850	7.6	5.8	2505				
1900	5.1	2.8	2038	1900	7.2	5.3	2499				

Table 3.5

Mean and standard deviation of horizontal speed in cm/s for all movable stations (428*/429* stations) at different depths during different years

2005			
Depth	**Mean**	**STD**	**n**
50	36.7	31.6	27390
100	29.0	27.0	30560
150	23.9	22.3	30772
200	20.7	18.4	30986
250	18.6	16.0	30157
300	16.4	13.8	29871
350	15.0	12.1	29793
400	13.7	10.7	30239
450	12.7	9.7	30279
500	11.8	8.9	29488
550	10.7	8.3	27696
600	9.9	7.5	26353
650	9.6	6.9	23479
700	9.0	6.5	20881
750	8.3	6.1	18234
800	8.3	5.7	13310
850	7.4	5.2	12642
900	7.2	5.4	12222
950	6.4	4.8	11901
1000	5.6	4.7	9959
1050	5.2	4.9	7145
1100	5.4	4.9	5305
1150	4.3	3.6	2594
1200	3.3	3.1	293
1250	6.5	4.2	1250
1300	5.4	4.2	1364
1350	6.2	3.9	1084
1400	6.0	3.7	1123
1450	5.8	3.6	1129
1500	5.4	3.2	1113
1550	4.9	2.7	1078
1600	4.9	2.6	1088
1650	5.5	4.0	1133
1700	5.8	5.4	1191
1750	5.0	4.5	1074
1800	11.1	6.3	1055
1850	4.1	2.5	88
1900	3.8	2.7	568
1950	5.6	2.7	920
2000	5.4	3.9	691
2050	6.9	4.9	1181
2100	7.6	5.3	1772
2150	8.5	5.7	2045
2200	9.0	6.0	2441
2250	8.1	6.3	2949
2300	9.1	7.7	2298

2006			
Depth	**Mean**	**STD**	**n**
50	34.1	26.3	59091
100	27.4	23.0	65820
150	22.3	19.3	65386
200	19.5	16.6	64452
250	17.6	15.1	64146
300	16.2	16.1	62839
350	13.8	10.8	61446
400	12.4	9.9	61159
450	11.4	9.2	60472
500	10.6	7.9	58564
550	9.6	7.6	52908
600	9.1	6.9	46414
650	8.6	7.7	43699
700	7.9	5.5	37484
750	7.2	5.3	33706
800	6.9	4.8	28121
850	6.5	4.8	27508
900	6.1	4.7	26956
950	5.6	4.7	25861
1000	5.6	5.7	21743
1050	6.0	6.9	17321
1100	7.5	10.4	8658
1150	6.3	5.7	4673
1200	7.2	4.6	2138
1250	6.6	5.5	3207
1300	6.9	7.3	3246
1350	4.6	2.4	1765
1400	4.9	2.6	1724
1450	5.8	3.0	1700
1500	5.7	3.6	1685
1550	6.3	3.9	1686
1600	7.4	4.6	1713
1650	10.1	5.9	2002
1700	11.4	6.1	2243
1750	9.0	6.2	621
1800	6.5	5.4	1004
1850	6.3	4.4	1226
1900	5.3	3.8	1416
1950	5.6	3.6	1558
2000	5.0	2.7	1471
2050	9.2	9.7	1701

2007			
Depth	**Mean**	**STD**	**n**
50	28.2	23.4	74979
100	22.5	18.8	92443
150	19.1	15.2	90755
200	17.2	12.9	93950
250	16.1	12.4	93302
300	15.6	15.4	92056
350	13.4	9.4	88014
400	12.2	8.3	88003
450	11.3	7.8	86934
500	10.6	7.3	82062
550	9.6	6.7	73915
600	9.3	6.1	66659
650	8.7	6.0	57956
700	7.9	5.5	51756
750	7.0	4.8	46596
800	6.8	4.3	37209
850	6.1	4.0	35490
900	5.8	3.9	31246
950	5.9	4.0	27741
1000	5.7	3.9	21176
1050	5.4	3.4	12054
1100	5.1	3.5	8294
1150	4.6	3.4	6816
1200	5.4	3.2	3575
1250	6.0	3.7	3419
1300	7.2	4.9	1849
1350	5.9	2.5	597
1400	5.5	2.3	605
1450	6.0	2.3	609
1500	5.2	2.2	605
1550	5.3	2.3	612
1600	6.3	2.5	745
1650	6.8	2.7	702
1700	10.4	3.2	612
1750	2.7	0.8	14
1800	2.9	1.5	14
1850	3.5	3.0	14
1900	8.1	1.9	12

Table 3.6

Mean and standard deviation of horizontal speed in cm/s for different regions for all years.

West			Central			East		
Mean	STD	n	Mean	STD	n	Mean	STD	n
9.966	8.561	999114	14.02	14.8	1900064	13.18	13.26	1740866

Mean	STD	n	Year	Mean	STD	n	Year	Mean	STD	n	Year
10.30	9.88	160172	2005	15.04	17.75	296187	2005	13.59	15.29	258370	2005
11.06	9.69	373322	2006	15.78	17.44	627507	2006	10.65	10.38	615403	2006
8.60	6.52	422137	2007	12.44	11.32	819389	2007	15.31	14.31	782291	2007
12.56	8.42	43483	2008	13.28	11.95	156981	2008	10.52	11.43	84802	2008

Table 3.7

Mean and standard deviation of horizontal speed in cm/s for different regions at different depths for All Years

West				Central				East			
Depth	Mean	STD	n	Depth	Mean	STD	n	Depth	Mean	STD	n
50	19.2	14.3	44195	50	31.7	26.0	102964	50	28.3	23.6	91569
100	15.7	11.6	66749	100	26.8	22.4	115747	100	22.9	19.9	108396
150	13.9	10.2	71106	150	22.1	18.9	116088	150	19.9	16.7	106320
200	12.7	9.3	71128	200	19.1	15.6	119672	200	18.4	14.7	104924
250	11.5	8.3	70917	250	17.8	14.6	118226	250	16.7	13.2	104514
300	10.7	7.5	69877	300	16.9	16.8	117575	300	15.4	13.4	103741
350	9.8	6.8	68360	350	14.2	10.3	113717	350	14.1	11.1	103302
400	9.0	6.2	68011	400	12.9	9.3	114231	400	12.8	9.2	98750
450	8.4	5.7	67358	450	11.9	8.6	112595	450	11.9	8.4	95025
500	8.2	5.7	64012	500	10.8	7.5	109910	500	11.1	7.9	92211
550	7.8	6.4	54653	550	10.1	6.6	91230	550	10.1	7.4	88418
600	7.9	6.3	48441	600	9.4	5.9	76176	600	9.5	6.9	83369
650	7.8	8.0	38816	650	8.5	5.4	69248	650	8.8	6.2	74922
700	6.9	5.4	37282	700	7.7	5.4	63445	700	8.5	5.6	57540
750	5.7	5.1	33489	750	7.1	6.1	57077	750	8.0	5.2	52297
800	5.2	3.8	29726	800	7.0	4.4	54083	800	7.3	4.8	48707
850	6.0	4.2	21399	850	6.3	4.2	53133	850	6.6	4.6	47281
900	5.6	3.6	17006	900	5.8	4.0	52069	900	6.6	4.7	45979
950	5.4	3.6	16311	950	5.6	3.8	46866	950	6.6	4.9	42022
1000	5.2	3.7	14892	1000	5.5	3.8	40427	1000	6.5	5.2	33995
1050	5.4	3.6	11741	1050	5.4	3.9	28954	1050	6.6	6.7	19206
1100	5.2	4.6	11538	1100	5.5	4.1	20104	1100	7.4	8.7	13787
1150	3.9	3.0	1766	1150	6.3	4.9	16680	1150	5.2	4.6	11126
1200	3.3	4.4	120	1200	6.7	5.1	16659	1200	5.1	3.9	5160
1250	3.8	5.1	90	1250	7.4	5.9	16435	1250	5.2	3.6	8366
1300	4.0	5.1	84	1300	9.5	7.8	13041	1300	4.7	3.3	8568
1350	12.3	2.7	13	1350	5.4	4.3	2667	1350	4.9	3.0	7730
1400	13.2	5.2	11	1400	6.1	5.5	2630	1400	4.8	3.0	7415
1450	15.3	8.6	11	1450	6.3	5.3	2551	1450	4.8	3.0	7841
1500	15.8	8.2	11	1500	10.4	10.6	3108	1500	4.7	3.0	8441
				1550	7.2	4.7	637	1550	4.8	3.2	9468
				1600	8.8	5.8	703	1600	5.0	3.4	10856
				1650	9.9	7.0	1009	1650	5.9	3.8	11224
				1700	11.1	7.5	1144	1700	6.7	5.0	8018
				1750	8.6	6.1	683	1750	5.0	3.8	5574
				1800	6.3	5.3	1067	1800	7.0	5.4	5551
				1850	6.1	4.3	1314	1850	6.6	5.1	4555
				1900	4.9	3.6	1984	1900	6.3	4.5	4549
				1950	5.6	3.3	2478				
				2000	5.2	3.1	2162				
				2050	8.3	8.1	2882				
				2100	7.6	5.3	1772				
				2150	8.5	5.7	2045				
				2200	9.0	6.0	2441				
				2250	8.1	6.3	2949				
				2300	9.1	7.7	2298				
				2350	12.1	9.4	1089				
				2400	10.5	11.3	1579				
				2450	11.5	12.4	1585				
				2500	20.4	14.7	930				

3.4 FLOW DIRECTION STATISTICS

This section presents the statistics of the flow directions using current roses. Flow direction represents as to where the water flows and the number of data points for a given direction is represented by the length of the rose radii. To better illustrate the spatial and temporal variability of the flows, we constructed a map with a current rose for each fixed platforms and each year (2005, 2006, and 2007). Data from movable units are more difficult to characterize and were not displayed. At a given station, different years may exhibit different flow directions. Some of them are "unidirectional" meaning that the most of the flow is in the same direction. Others are "bidirectional" with the majority of the flows alternating in two different directions, either opposite directions or at angles different than 180 degrees. Still others are "omnidirectional" with no apparent preferred direction.

Station 42361 (Auger - Garden Banks 426), Figures 3.11-3.13, is operated by Shell International E&P. It is on a fixed platform at 27.550 N 92.490 W with a water depth of 872 m, covering between 51 and 803 m below the surface. At Station 42361, the flow direction is quite consistent during 2005 to 2007. The flow is mostly westward with a secondary direction of eastward for 2005. For 2006, the flow is mainly westward with perhaps secondary directions of southwest and northwest. For 2007, the results are similar to 2006.

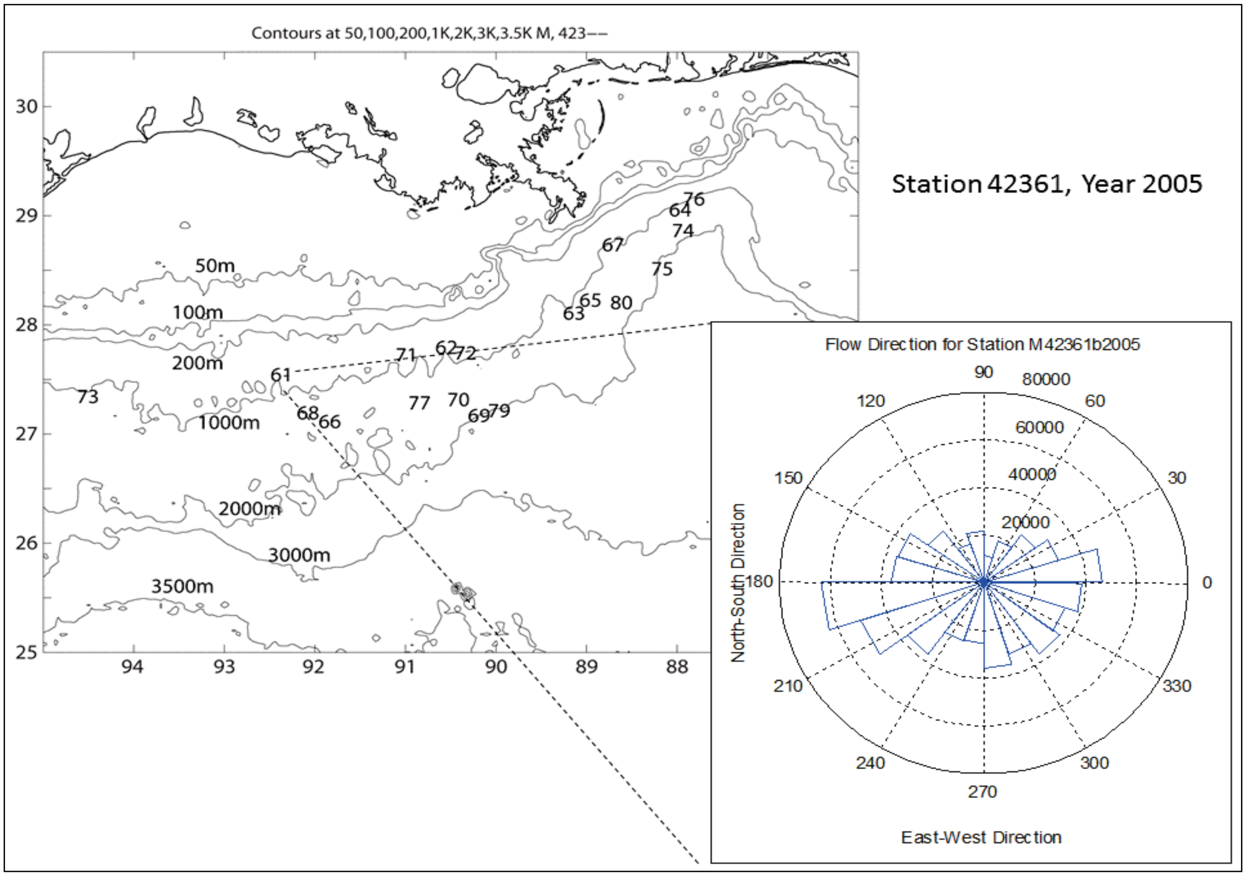

Figure 3.11. Current direction rose plot for Station 42361 in year 2005.

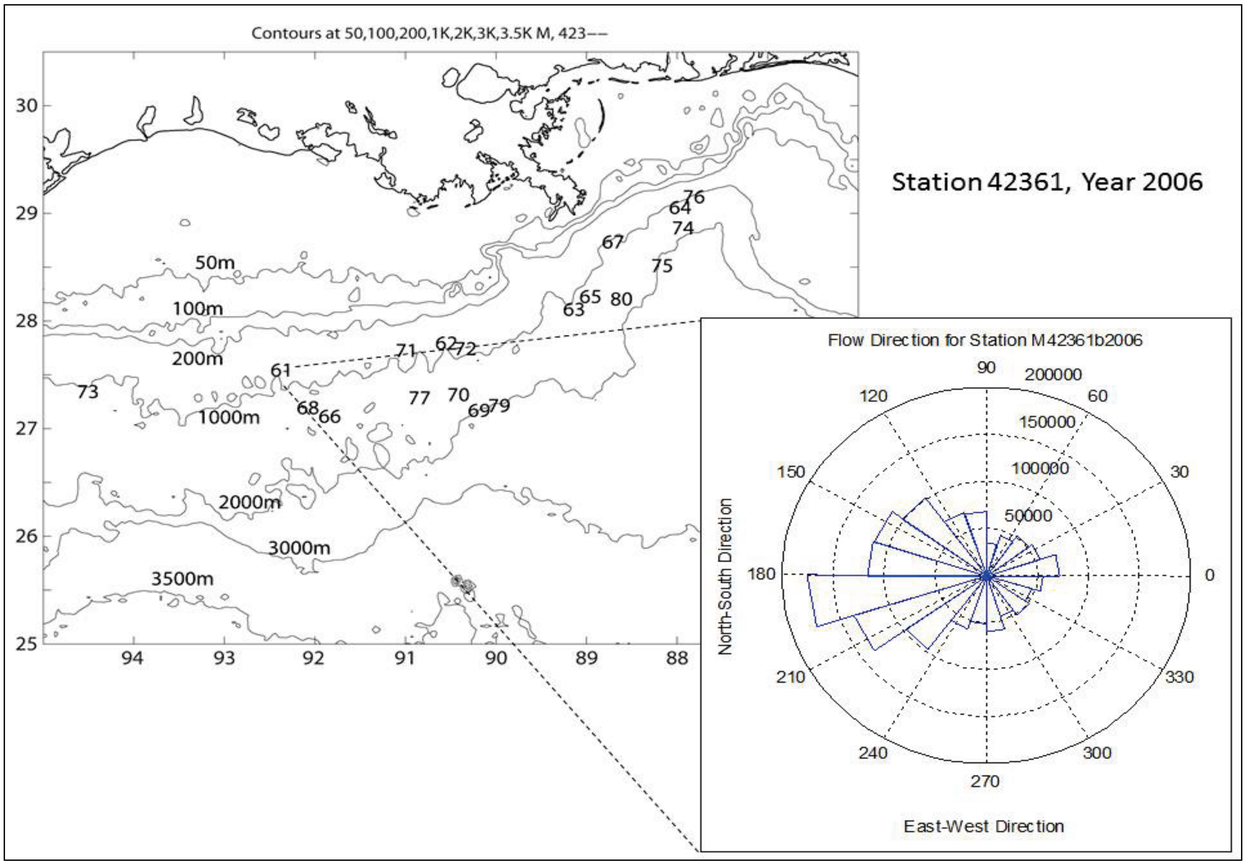

Figure 3.12. Current direction rose plot for Station 42361 in year 2006.

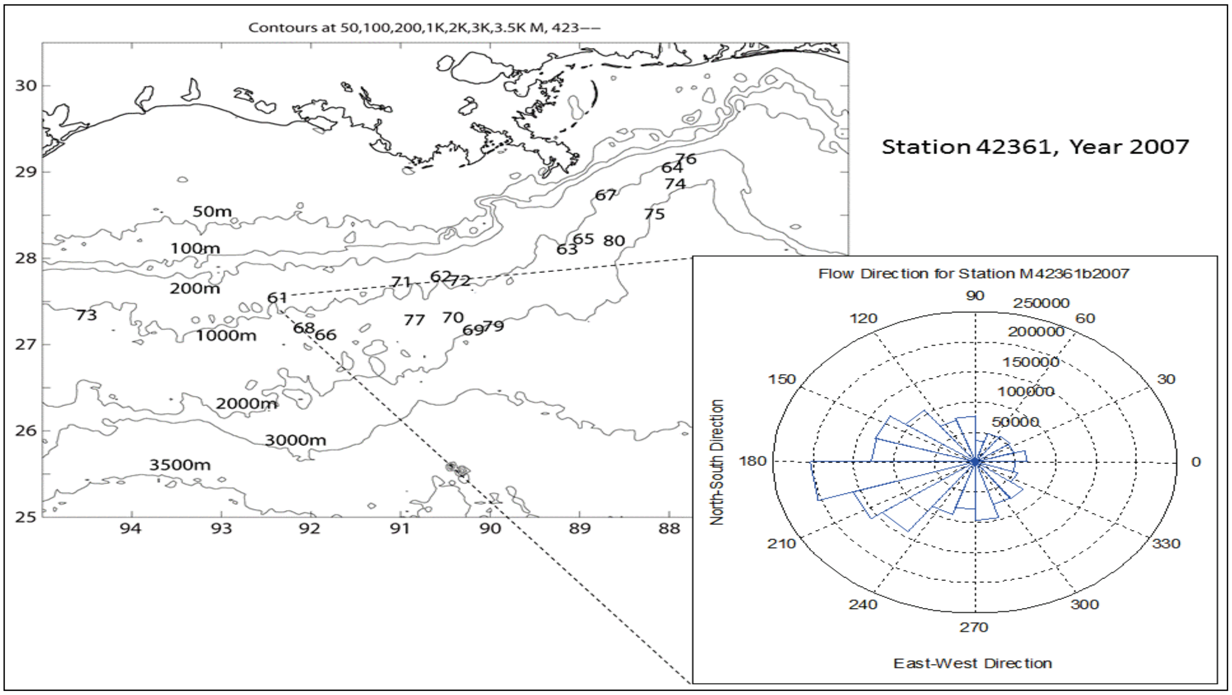

Figure 3.13. Current direction rose plot for Station 42361 in year 2007.

Station 42362 (Brutus – Green Canyon 158), Figures 3.14-3.15, is operated by Shell International E&P and located at 27.8 N, 90.67 W at 910 m water depth, covering between 79 m and near bottom. The site only has data from 2006 and 2007. It is almost two degrees in longitude (or 197 km) due east of Station 42361. The flow is quite different from Station 42361: it is mostly toward the northeast and north in 2006, and northwest in 2007.

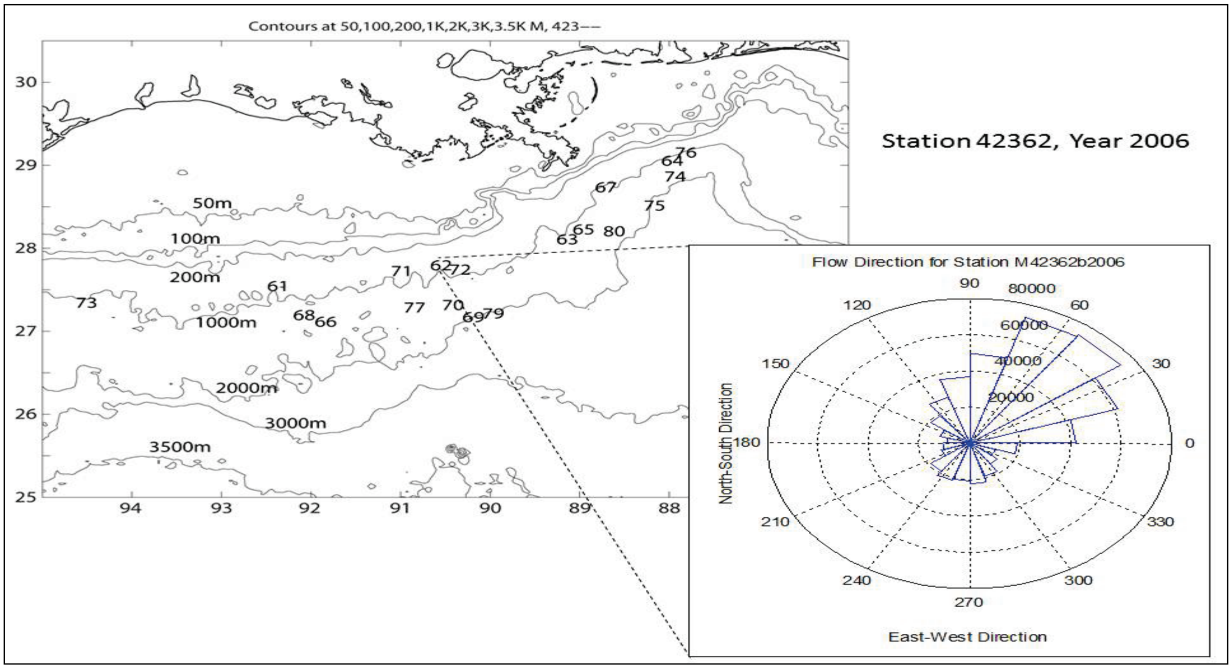

Figure 3.14. Current direction rose plot for Station 42362 in year 2006.

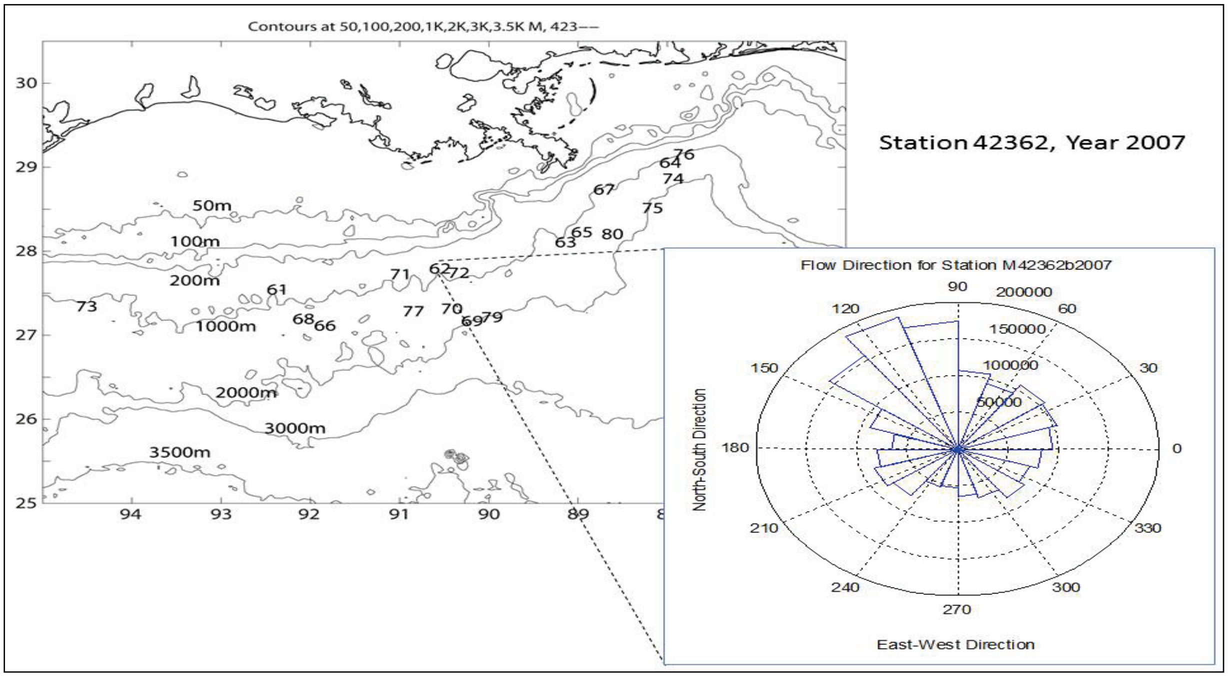

Figure 3.15. Current direction rose plot for Station 42362 in year 2007.

Station 42363 (Mars - Mississippi Canyon 807), Figures 3.16- 3.18, is 150 km east of Station 42362 and is operated by Shell International E&P. This fixed platform is located at 28.160 N 89.220 W. The water depth there is 894 m and the data expands almost the entire water column from 61 m below the surface. Again this site there is large variability of the flow directions from 2005 to 2007. The predominant flow direction in 2005 is eastward with some variability (from northeast to southwest), and a secondary northwest flow direction. This is changed in 2006, which shows mostly southward flows and secondary direction of northwest. The 2007 flow is changed again to be mostly toward the northeast. This suggests that a large component of the flow in within the low frequency band with a strong inter-annual variability. The main dynamical systems there are the Loop Current and associated eddies. Apparently, the predominant flow directions change as eddies and Loop Current sweep through the area. The Loop Current and eddies have their typical time scales of a few months and thus are low-frequency motions.

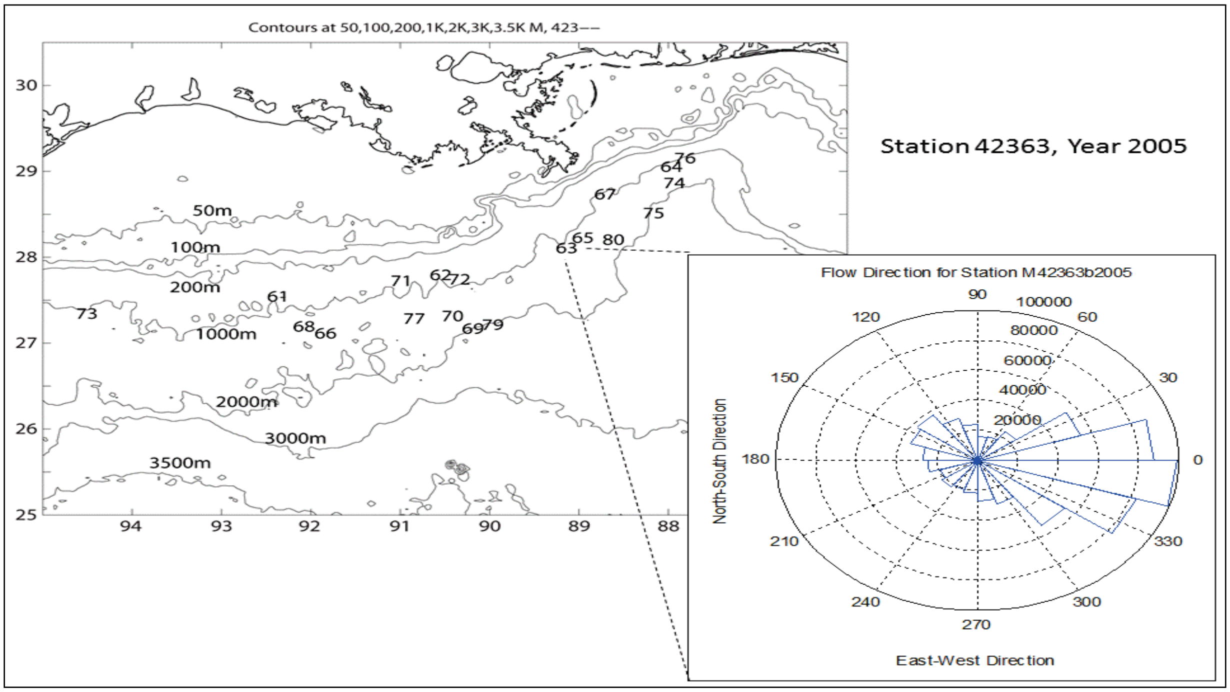

Figure 3.16. Current direction rose plot for Station 42363 in year 2005.

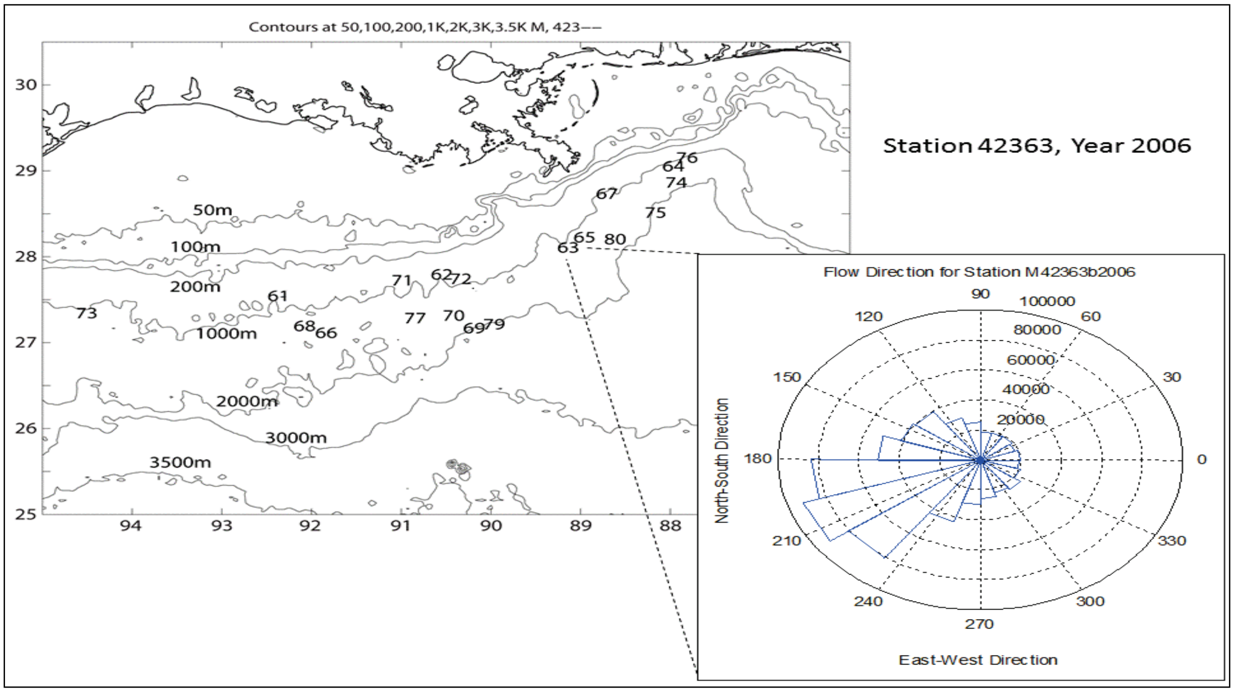

Figure 3.17. Current direction rose plot for Station 42363 in year 2006.

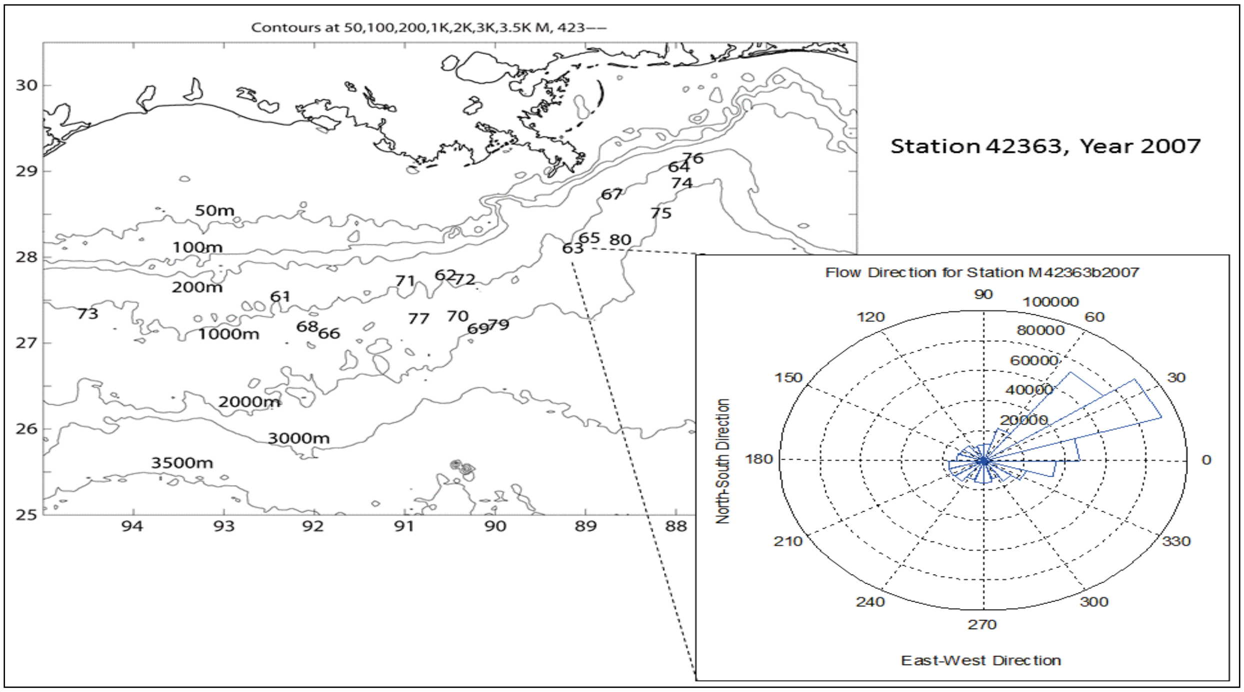

Figure 3.18. Current direction rose plot for Station 42363 in year 2007.

Operated by Shell International E&P, Station 42365 (Ursa - Mississippi Canyon 809), Figures 3.19-3.21 is located at 28.200 N 89.120 W, northeast of and very close to Station 42363, in 1158 m water depth. Figure 3.18 is very similar to Figure 3.21; showing that the predominant flow direction in 2005 and 2007 is eastward with some variability (from northeast to southwest). In 2006 the flow directionality changed, and the flow is going mostly.

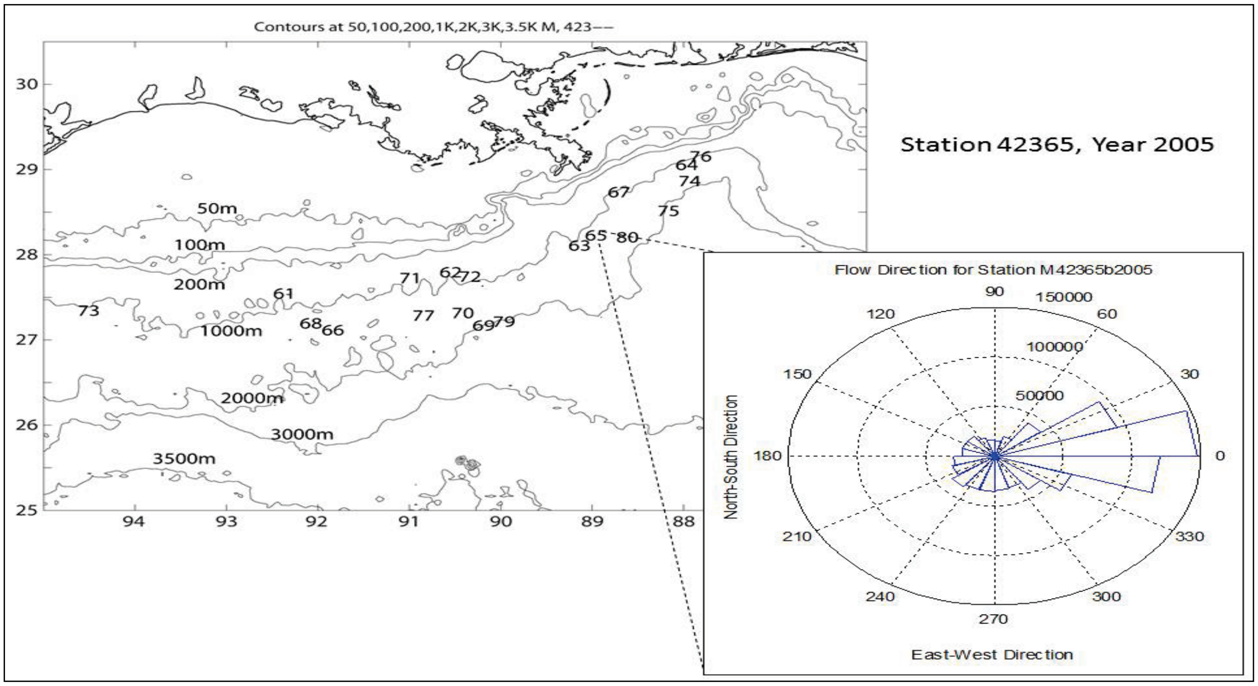

Figure 3.19. Current direction rose plot for Station 42365 in year 2005.

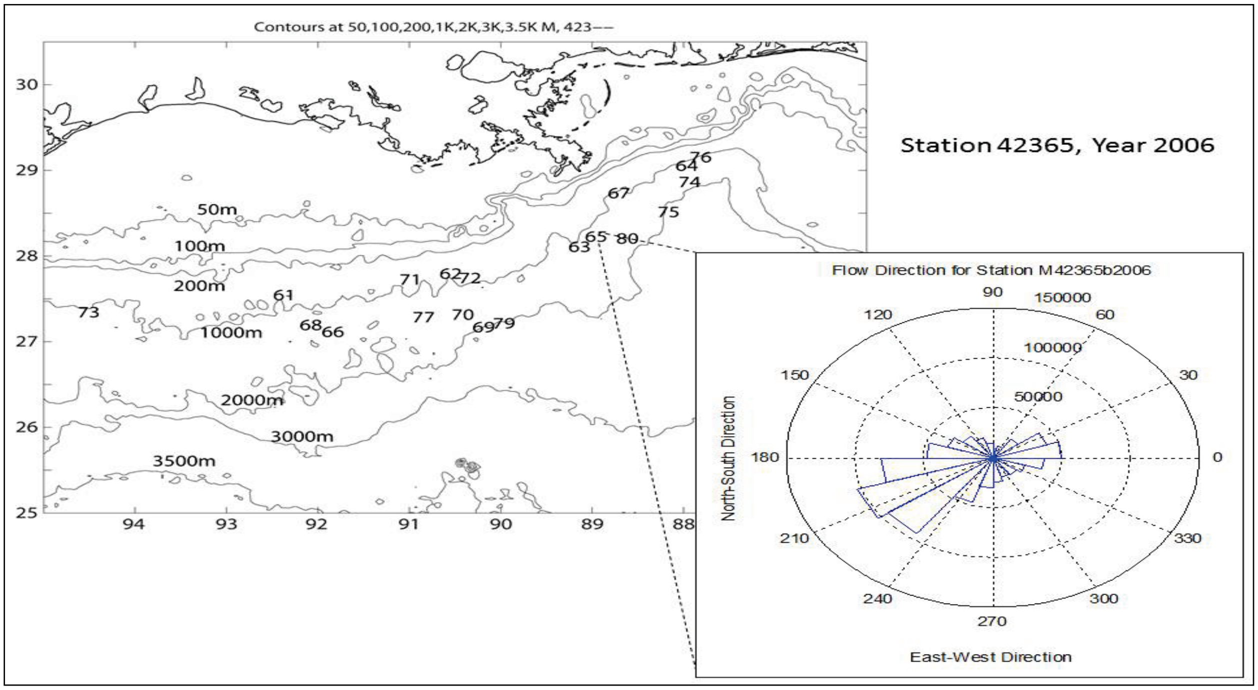

Figure 3.20. Current direction rose plot for Station 42365 in year 2006.

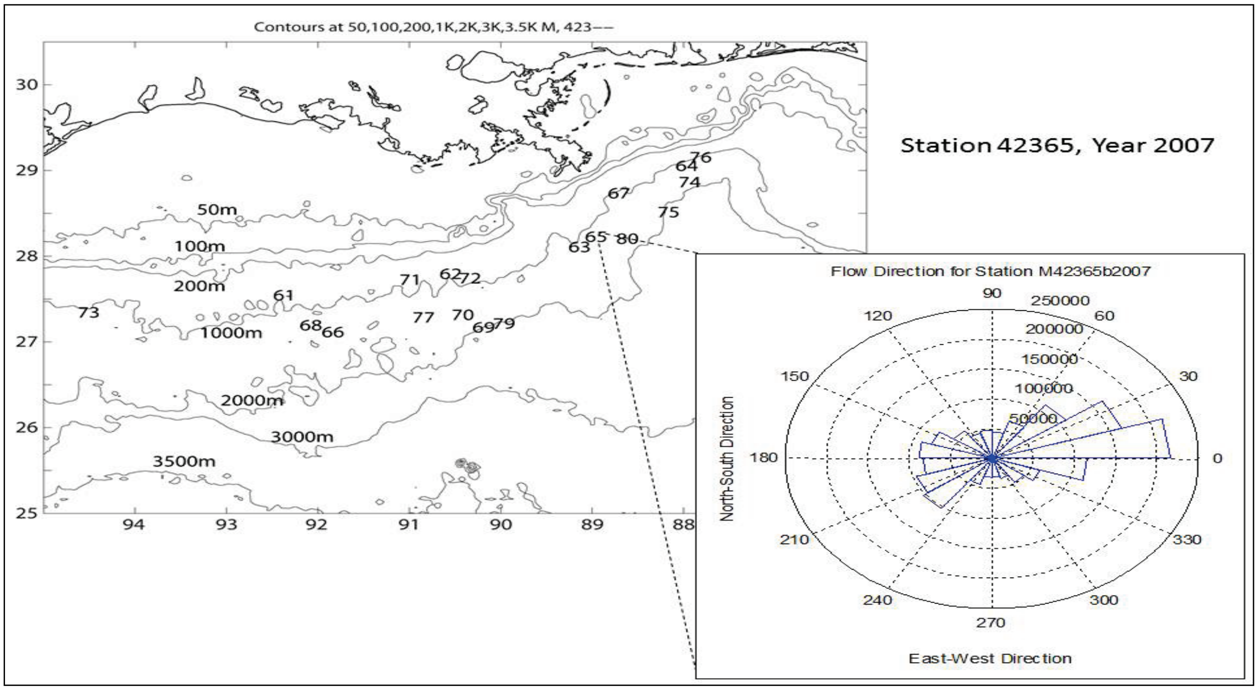

Figure 3.21. Current direction rose plot for Station 42365 in year 2007.

Station 42366 (Red Hawk - Garden Banks 877), Figures 3.22 – 3.24, is operated by Kerr-McGee Oil and Gas Corporation and located at 27.122 N 91.959 W, southeast of Station 42361 for more than 50 km. The water depth at this station is 872 m. The flow at this site is very different, even though it is close to the Station 42361. The year-to-year variability is very little, in contrast to other stations and the predominant flow direction is northward.

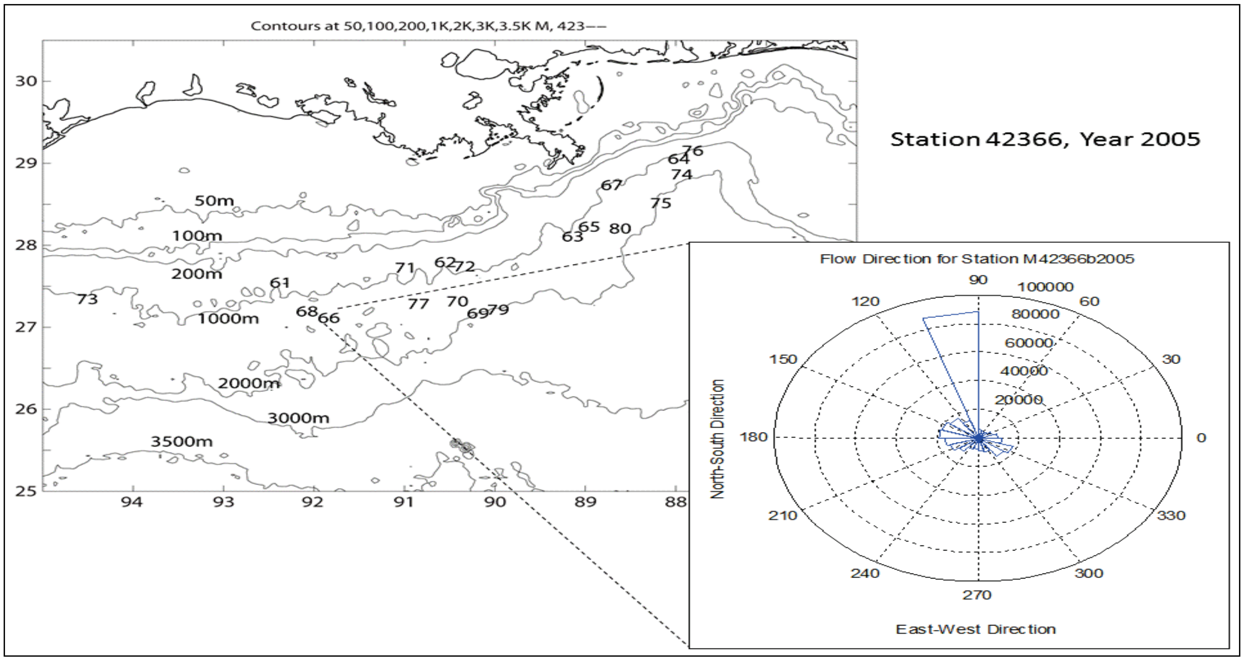

Figure 3.22. Current direction rose plot for Station 42366 in year 2005.

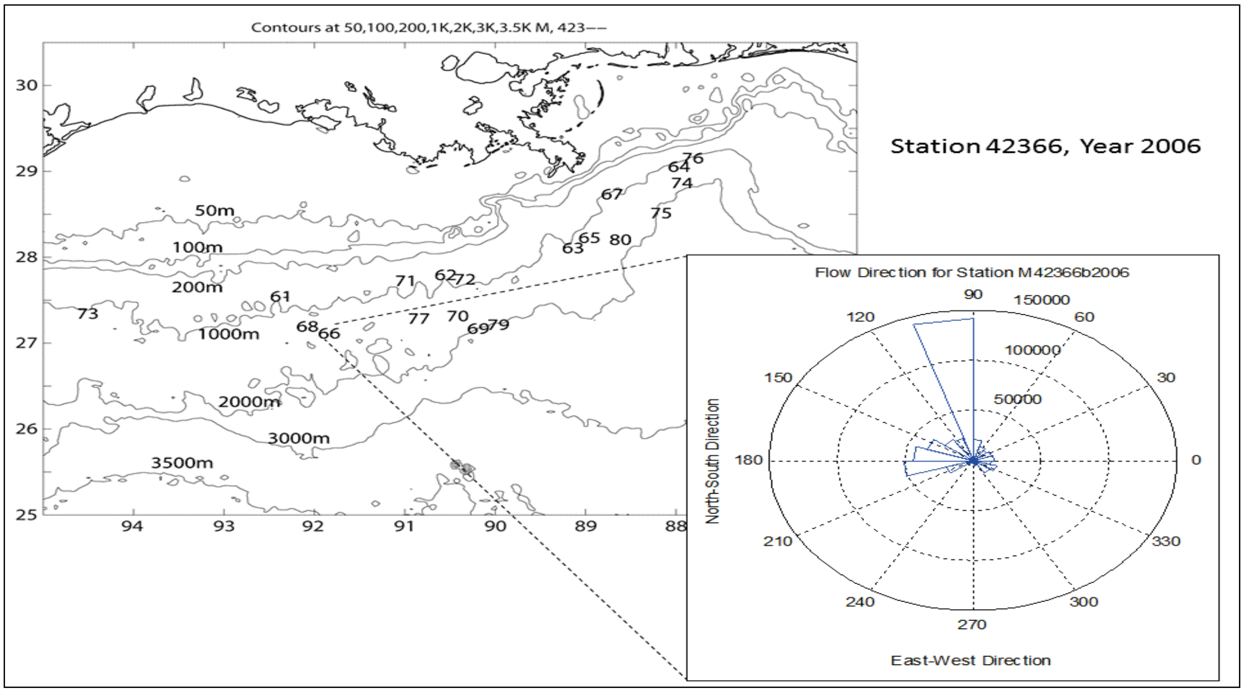

Figure 3.23. Current direction rose plot for Station 42366 in year 2006.

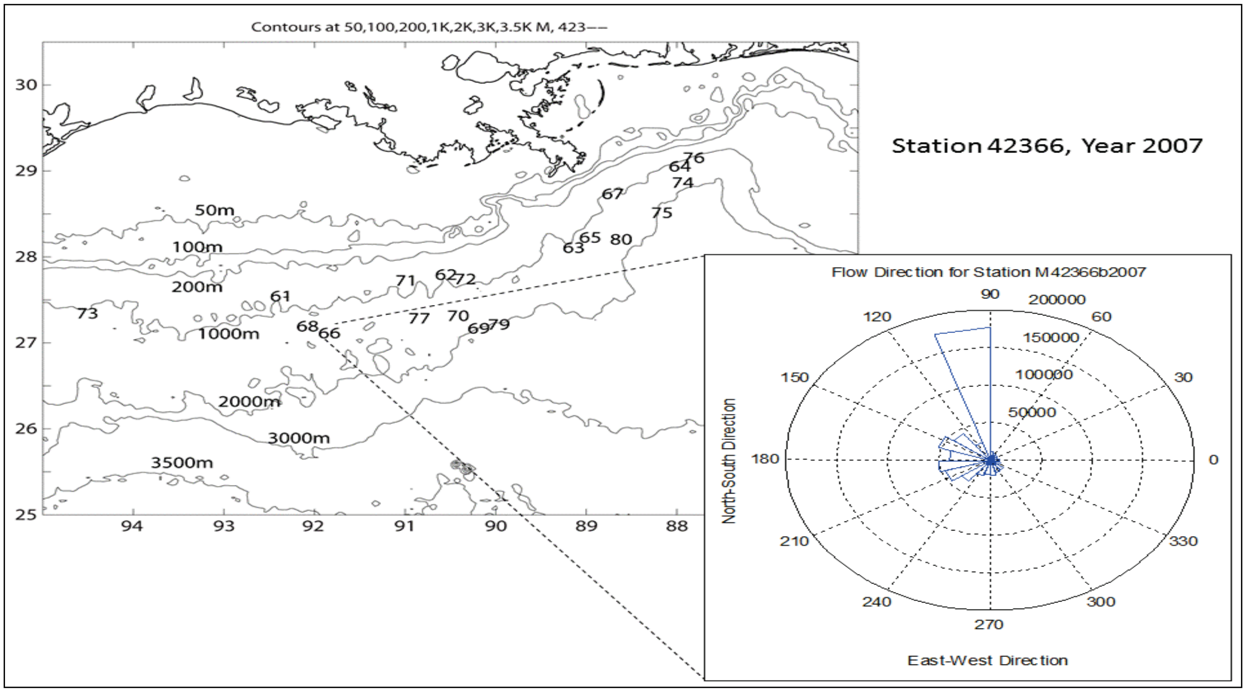

Figure 3.24. Current direction rose plot for Station 42366 in year 2007.

Station 42367 (Matterhorn - Mississippi Canyon 243), Figures 3.25-3.27, is operated by Total USA, Inc. and located at 28.743 N 88.826 W in water depths of 860 m. The data cover between 95 and 1025 m. It is located southeast of the Birdfoot's Delta. The flow at this site appears to be quite consistent from 2005 to 2007. The predominant flow direction is toward the southwest, with some secondary flows in the northwest (2005) direction and northeast directions (2006 and 2007). Although Stations 42363 and 42365 are similar in flow directions, Station 42367 appears to be quite different. This could be due to the fact that the former two stations are closer to the Loop Current and associated eddies.

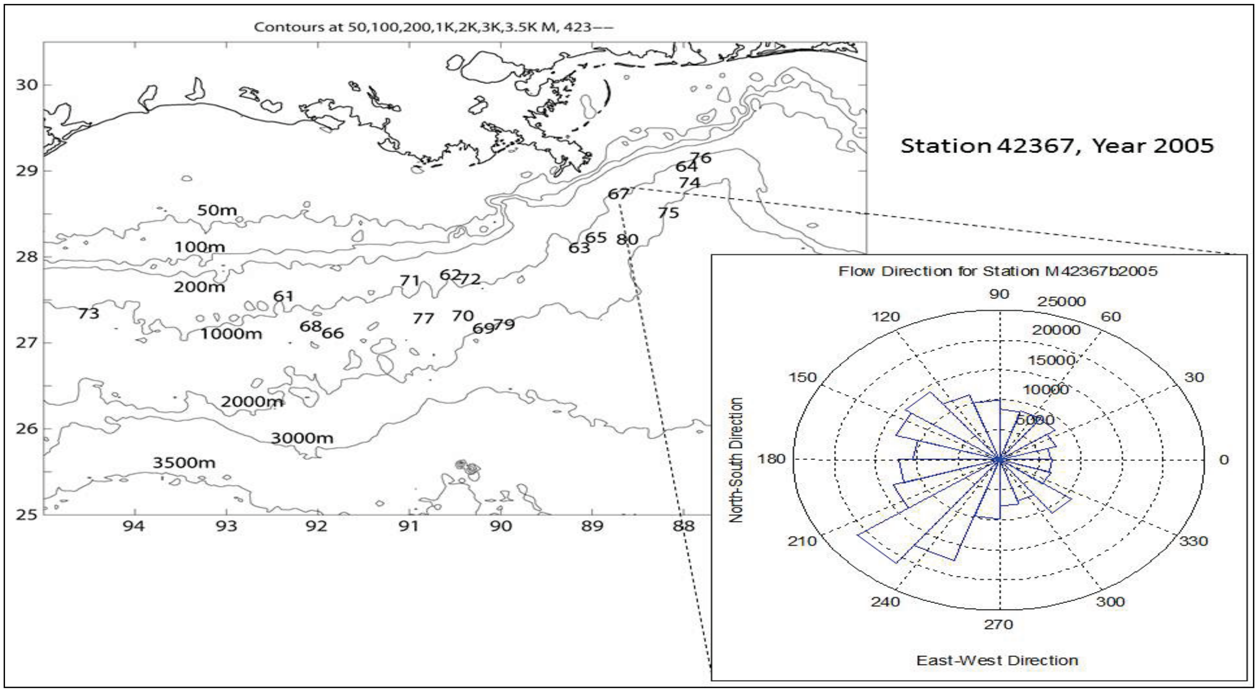

Figure 3.25. Current direction rose plot for Station 42367 in year 2005.

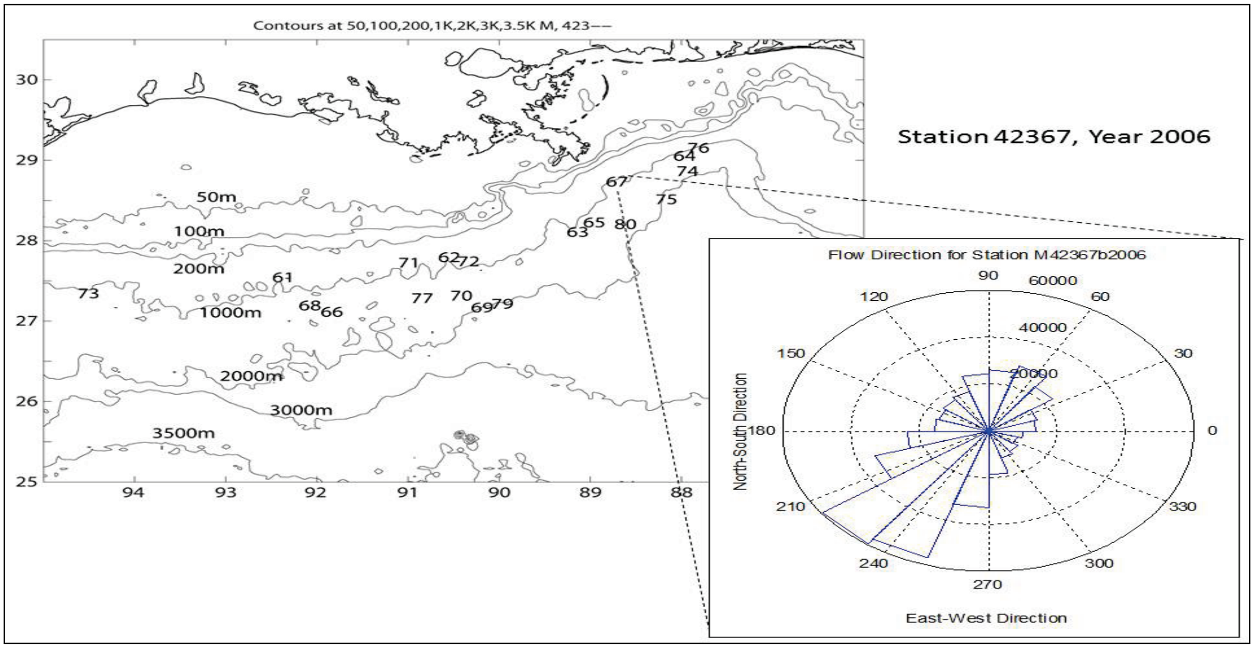

Figure 3.26. Current direction rose plot for Station 42367 in year 2006.

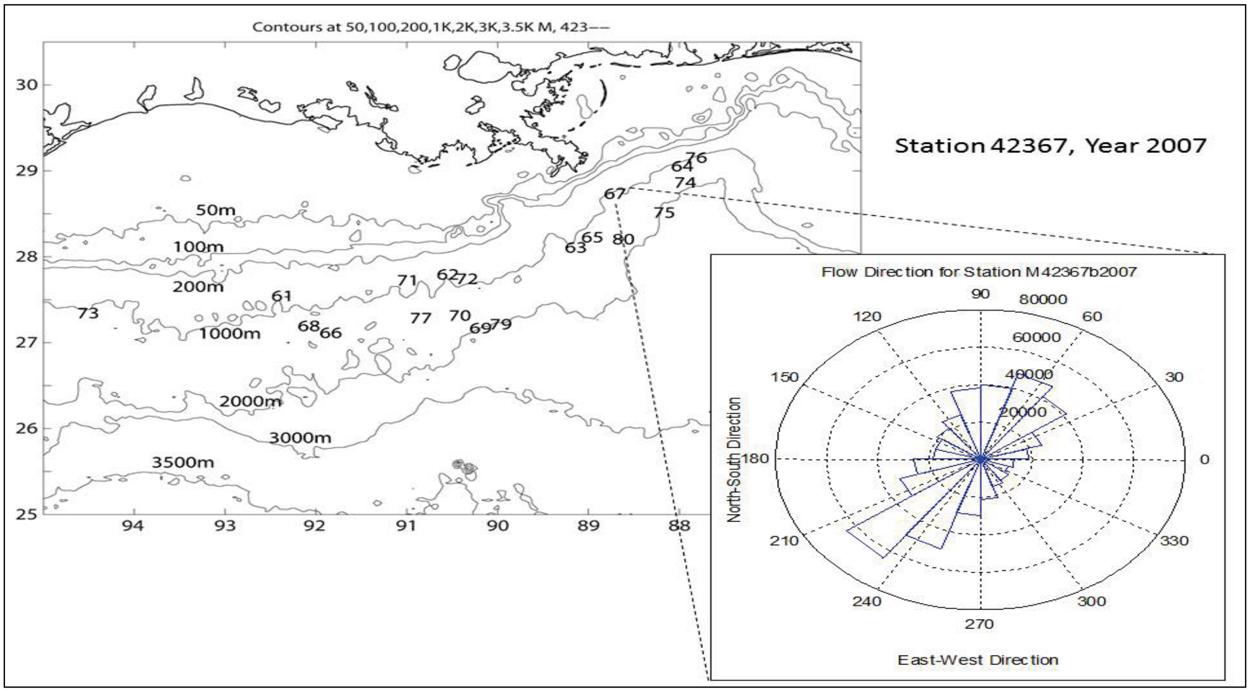

Figure 3.27. Current direction rose plot for Station 42367 in year 2007.

Station 42368 (Magnolia - Garden Banks 783), Figures 3.28- 3.30, is operated by ConocoPhillips and located at 27.204 N 92.203 W in water depths of 1424 m. It is very close to Station 42366 (about 20 km west-northwest of Station 42366). The flow however is very different from that nearby station. At this station, the flow is mostly toward the southern quadrants (southwesterly directed but with secondary directions such as south and northwest. The difference between Stations 42366 and 42368 is partly due to the difference in data coverage in the vertical. Station 42366 covers the vertical from 115 to 610 m, while Station 42368 covers between 67 and 1123 m.

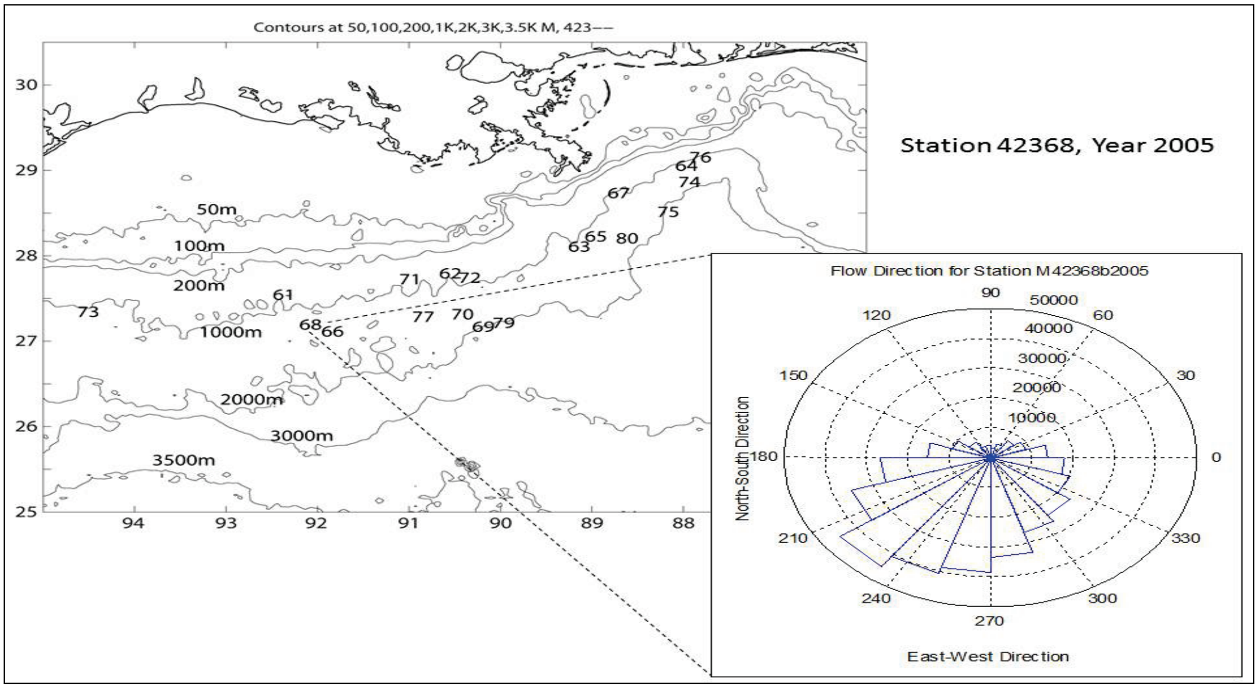

Figure 3.28. Current direction rose plot for Station 42368 in year 2005.

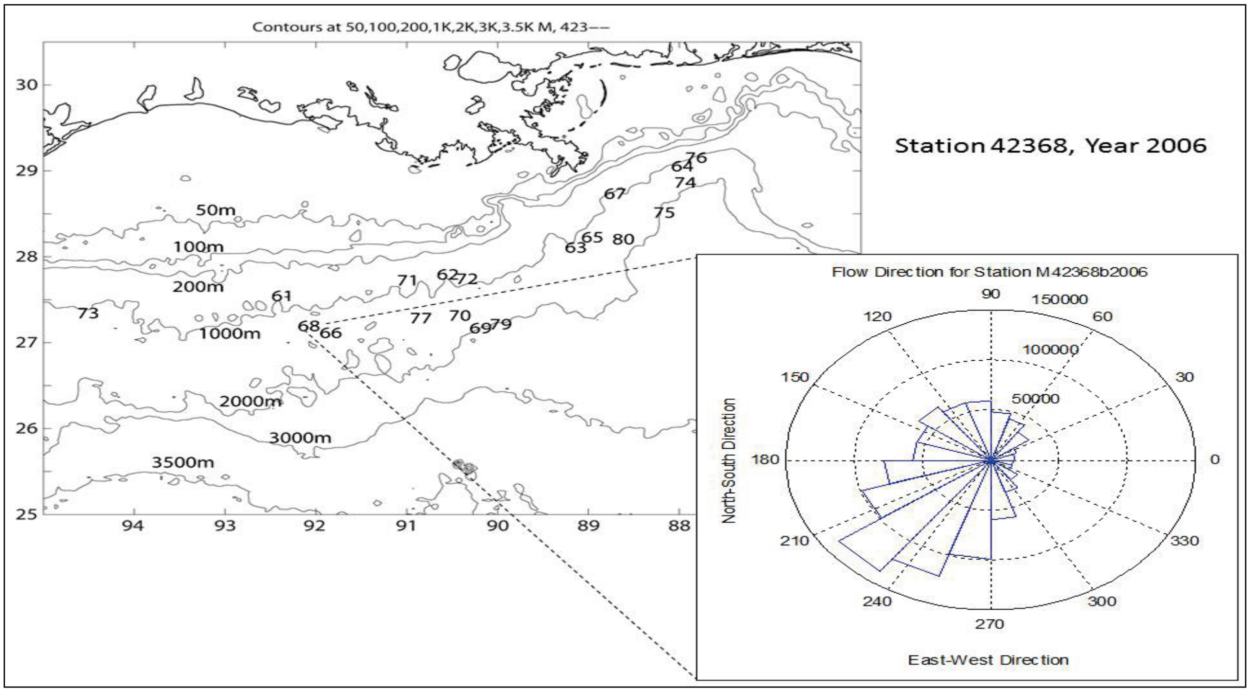

Figure 3.29. Current direction rose plot for Station 42368 in year 2006.

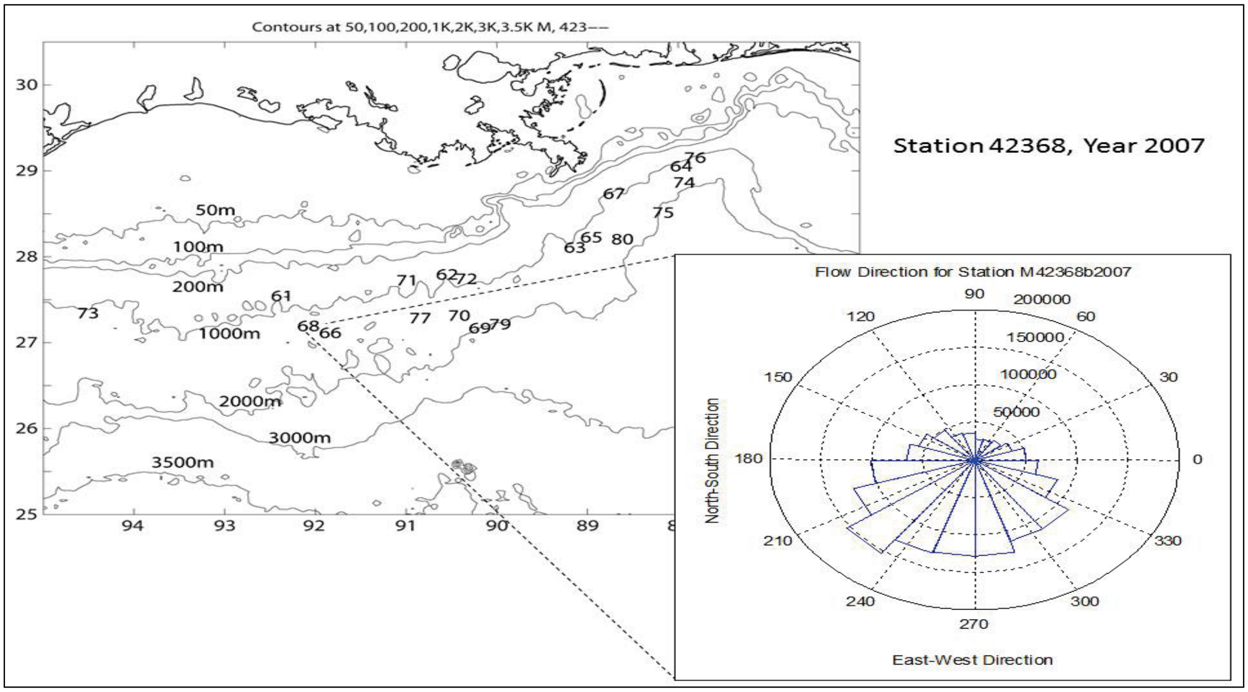

Figure 3.30. Current direction rose plot for Station 42368 in year 2007.

Station 42369 (Mad Dog - Green Canyon 782), Figures 3.31-3.33 is operated by BP, Inc., located at 27.189 N 90.269 W in water depths of 1372 m. The data cover 124 to 868 m. The flow direction exhibits large variation from time to time. The 2005 data shows a predominant direction of northeast, while the 2006 data added a southeast direction. The 2007 data shows a direction of south and southwest, with secondary directions of northwest and southeast.

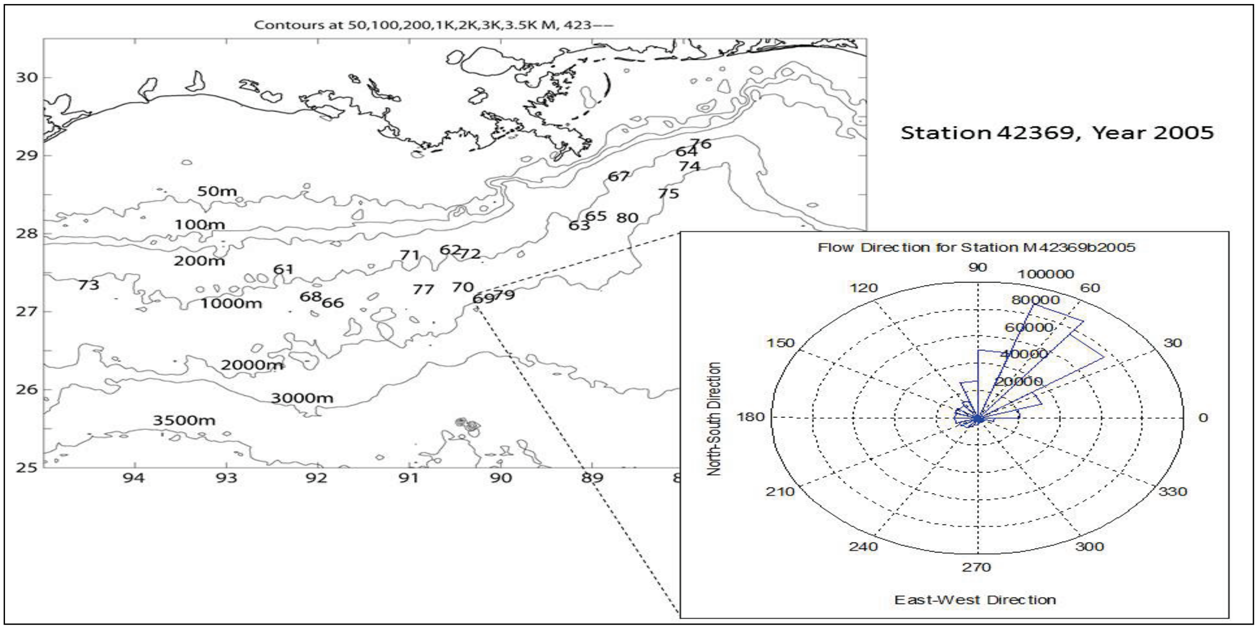

Figure 3.31. Current direction rose plot for Station 42369 in year 2005.

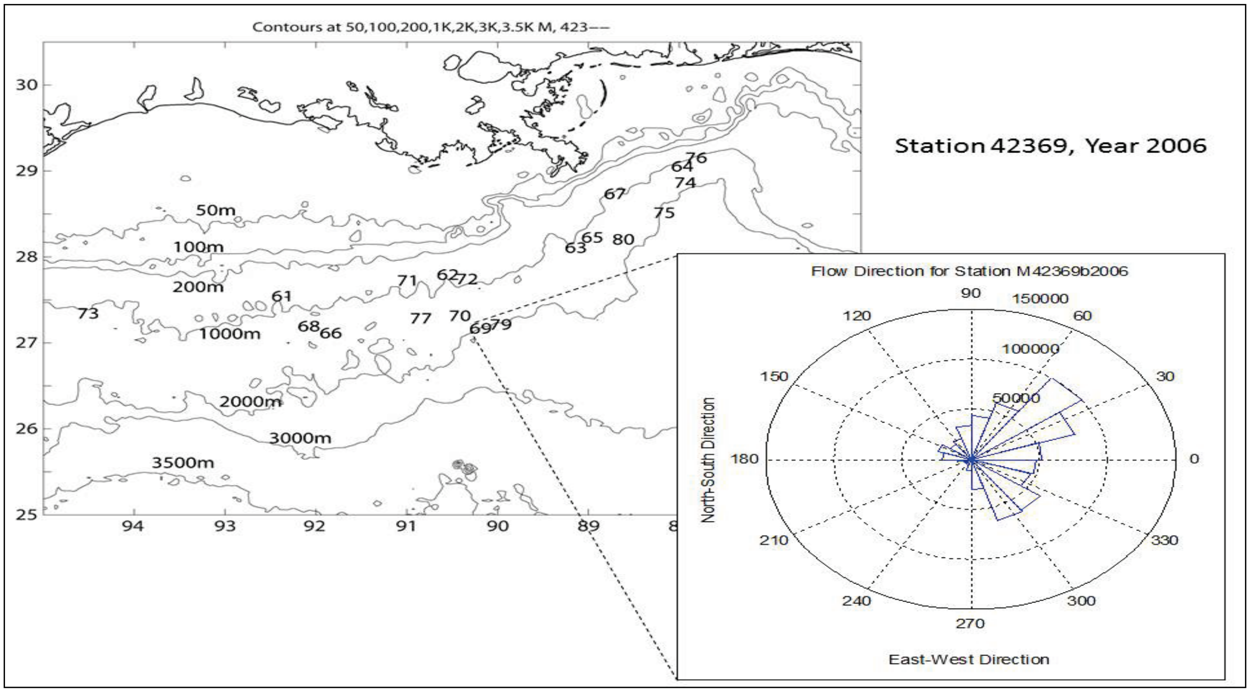

Figure 3.32. Current direction rose plot for Station 42369 in year 2006.

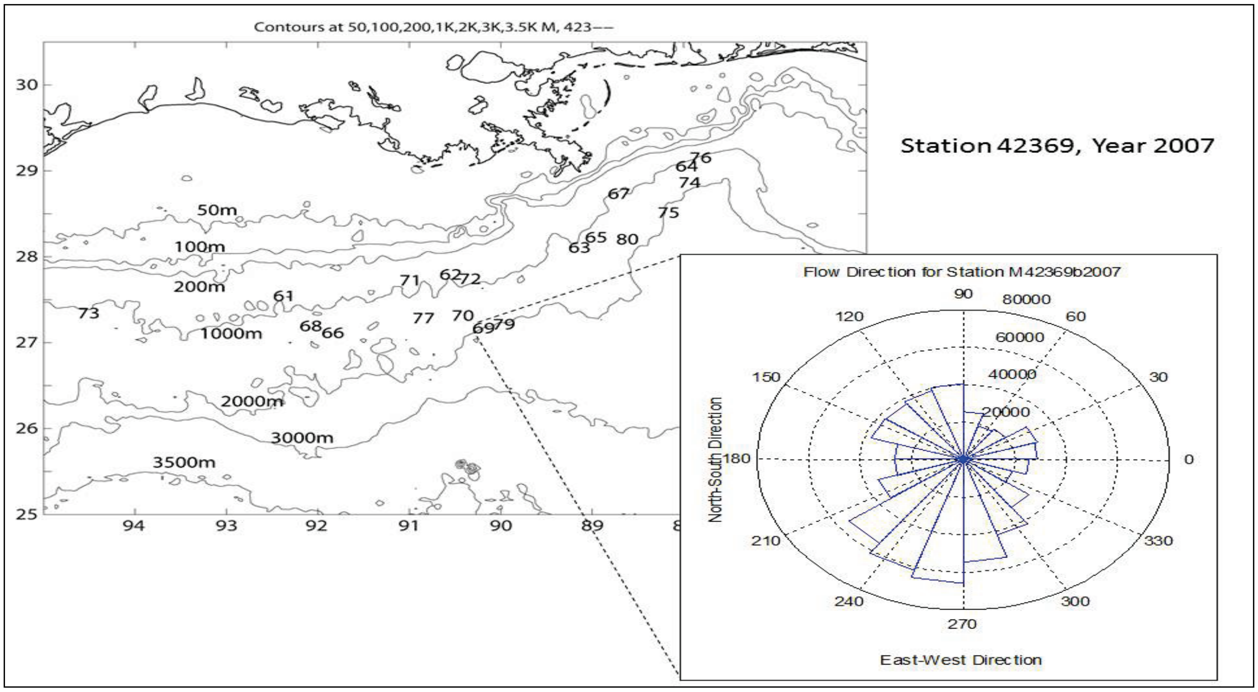

Figure 3.33. Current direction rose plot for Station 42369 in year 2007.

Station 42370 (Holstein - Green Canyon 645), Figures 3.34-3.36, is operated by BP, Inc., and located at 27.321 N 90.536 W in water depths of 1311 m. The data cover 62 to 992 m. The flow direction exhibits large variation from time to time. The 2005 data shows bi-directional with northeast and southwest as the main directions and large variability, while the 2006 data is also bi-directional with southeast and northeast directions. The 2007 data is almost omnidirectional with more emphasis on the southwest directions. This station is very close to 42369 but the results seem to be quite different. The depths covered are similar. It is not known what caused the difference in flow directions.

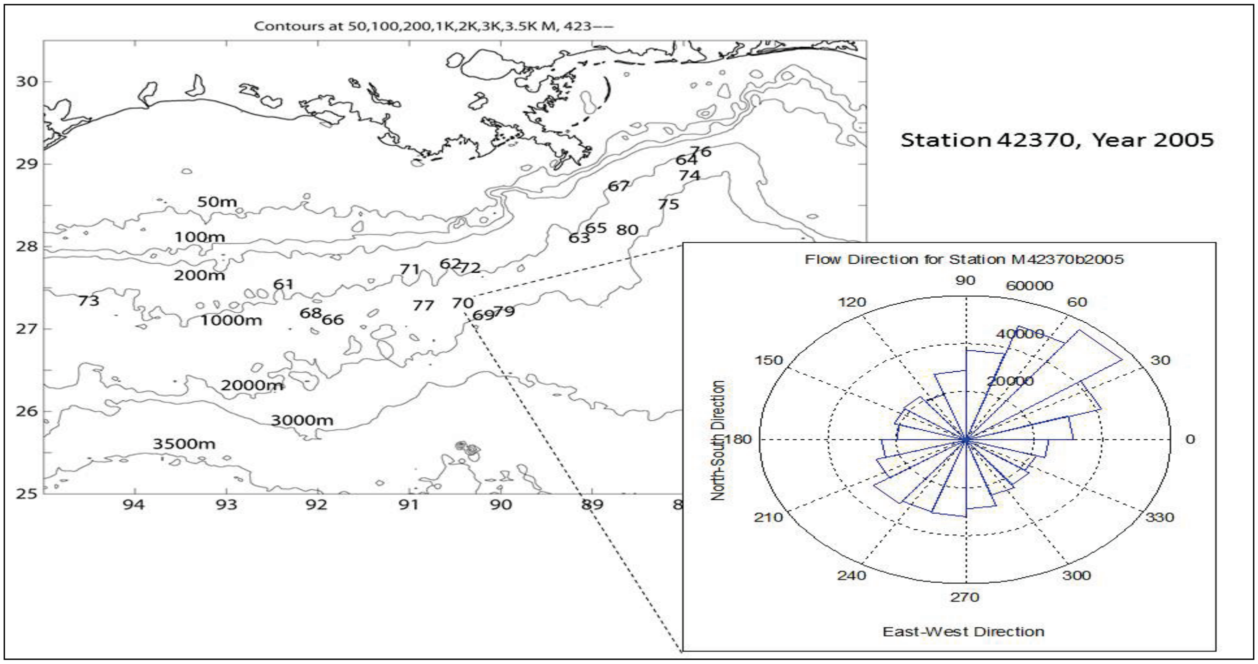

Figure 3.34. Current direction rose plot for Station 42370 in year 2005.

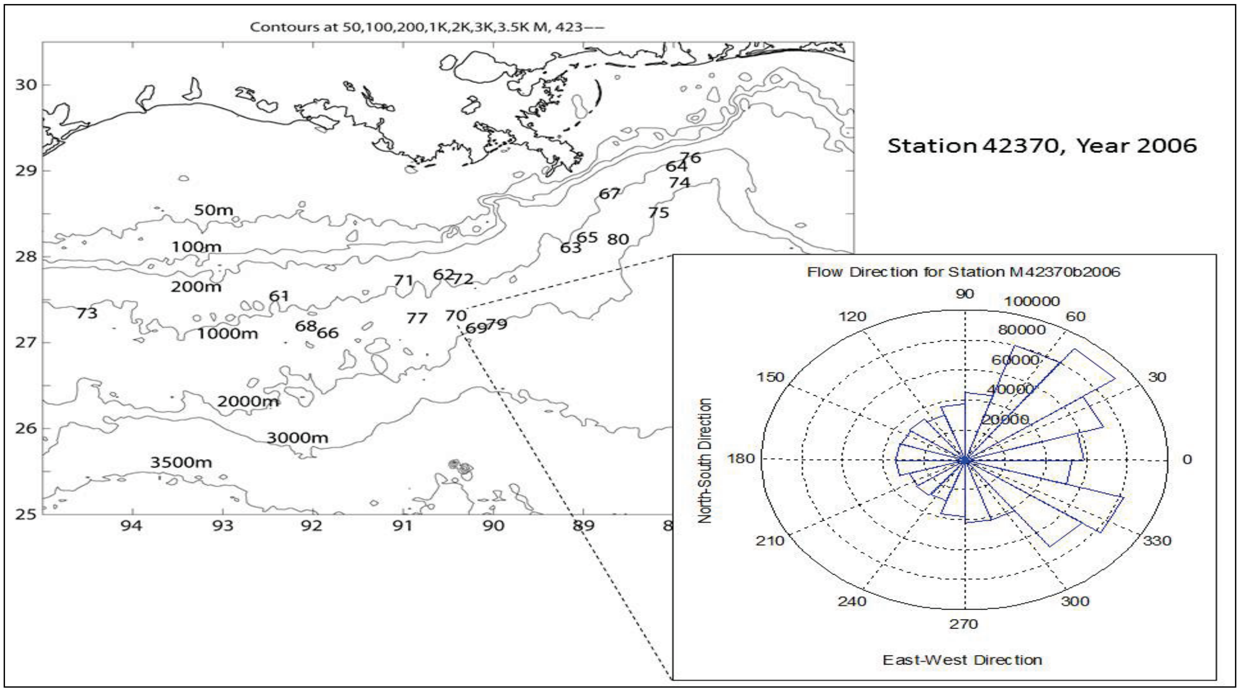

Figure 3.35. Current direction rose plot for Station 42370 in year 2006.

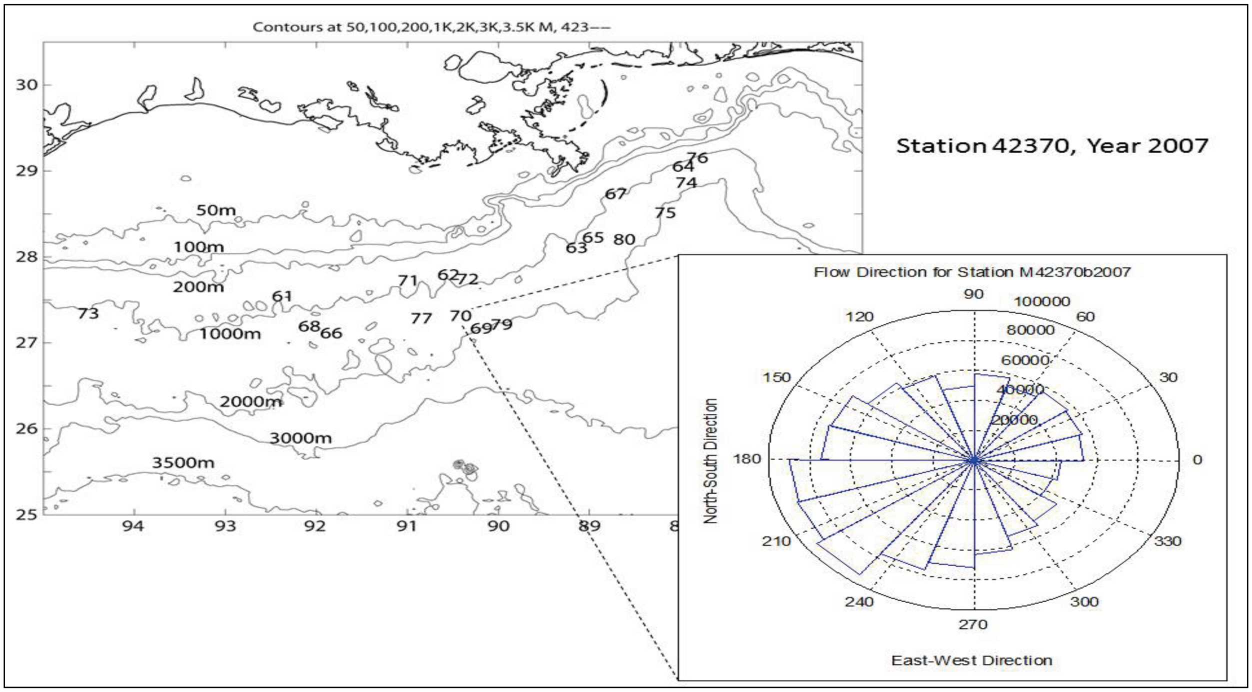

Figure 3.36. Current direction rose plot for Station 42370 in year 2007.

Station 42372 (Genesis - Green Canyon 205), Figures 3.37- 3.39, is operated by Chevron and located at 27.779 N 90.519 W in water depths of 789 m. The data cover 28 to 660 m. It is very close to Station 42362. The flow directions however are quite different. The 2005 data for Station 42372 is mostly eastward and northeastward, with a weak secondary northwestward flow direction. The Station 42362 does not have 2005 data. The 2006 flow at Station 42372 is predominantly eastward; while the Station 42362 shows mainly northeast preference. The 2007 data for Station 42372 is bimodal with southwest and northeast preference, while the Station 42362 shows north and northwest preference. This variation between two adjacent stations may be caused by the gradient between the two stations: this may happen when they are at the edge of certain features (such as Loop Current or an eddy).

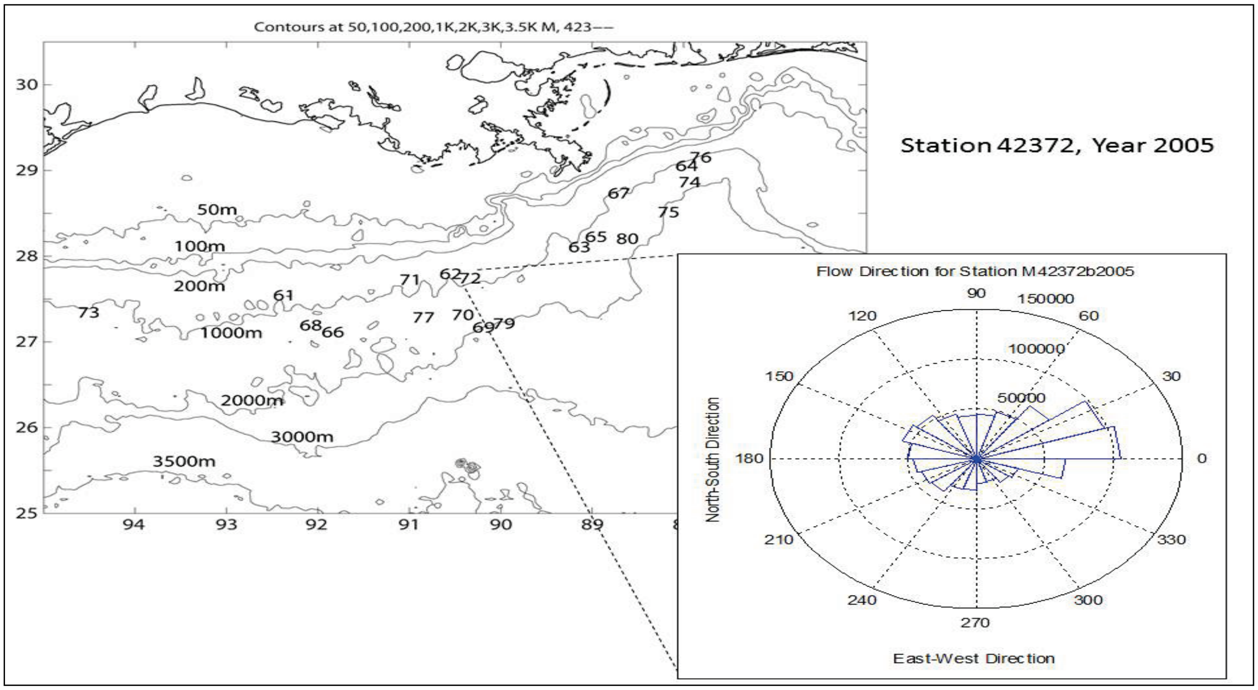

Figure 3.37. Current direction rose plot for Station 42372 in year 2005.

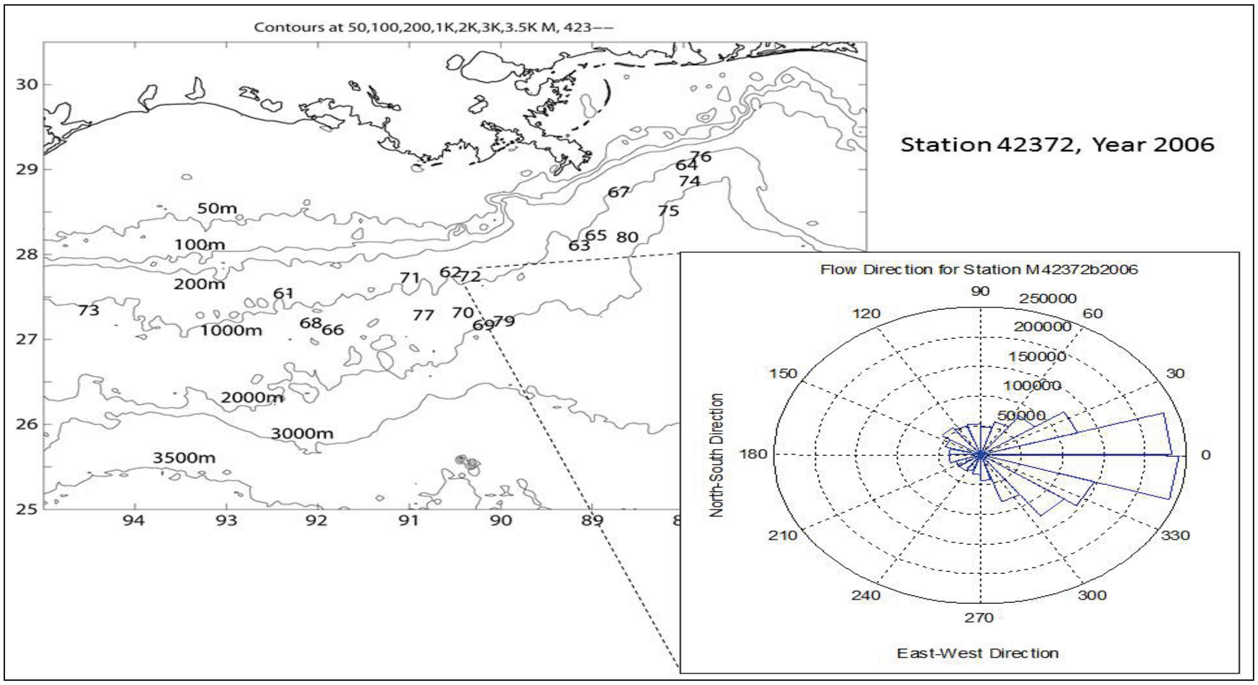

Figure 3.38. Current direction rose plot for Station 42372 in year 2006.

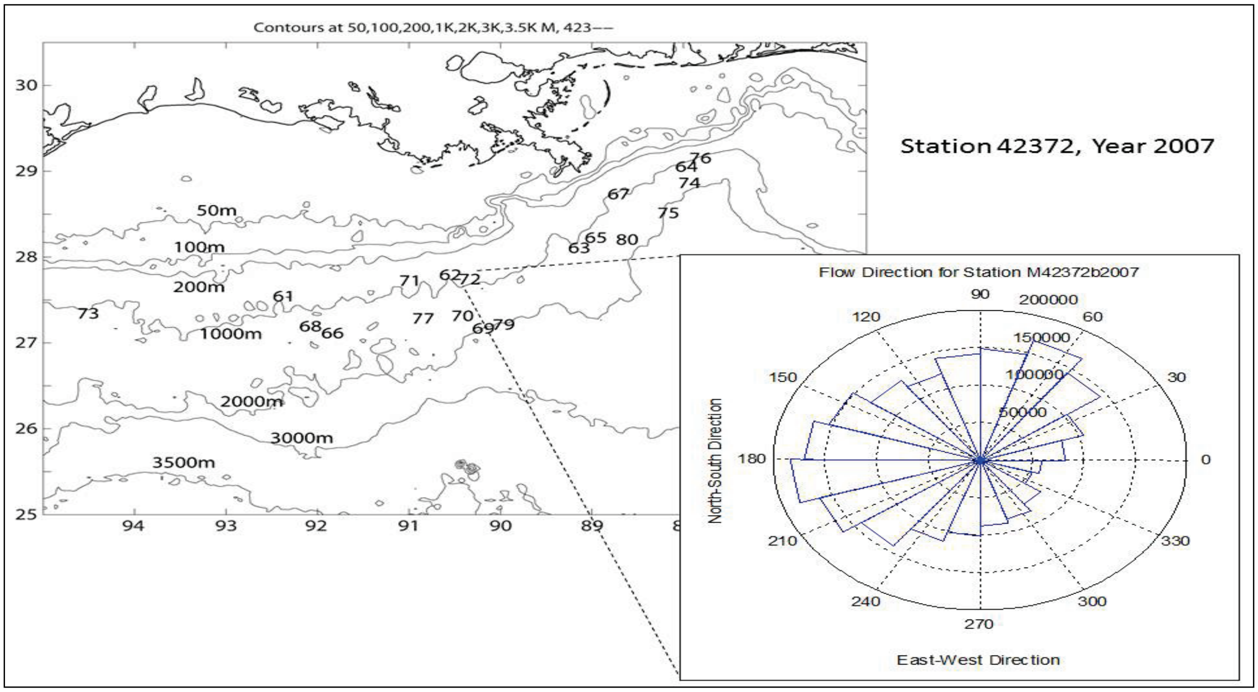

Figure 3.39. Current direction rose plot for Station 42372 in year 2007.

Station 42373 (Boomvang - East Breaks 643), Figures 3.40 - 3.42, is operated by Kerr-McGee Oil and Gas Corporation and located at 27.354 N 94.625 W in water depths of 1,113 m. The data only cover 104 to 597 m. The station is at the far west of the area. The flow direction is very persistent between 2005 and 2007: mostly northward, with much weaker secondary flow directions of various degrees.

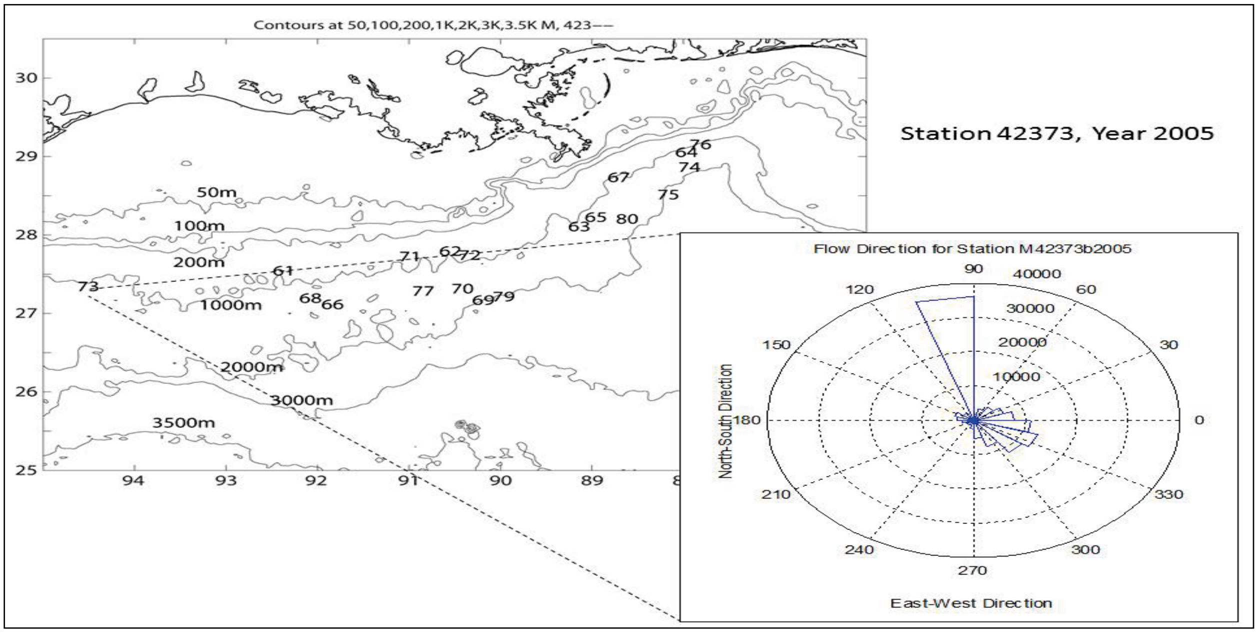

Figure 3.40. Current direction rose plot for Station 42373 in year 2005.

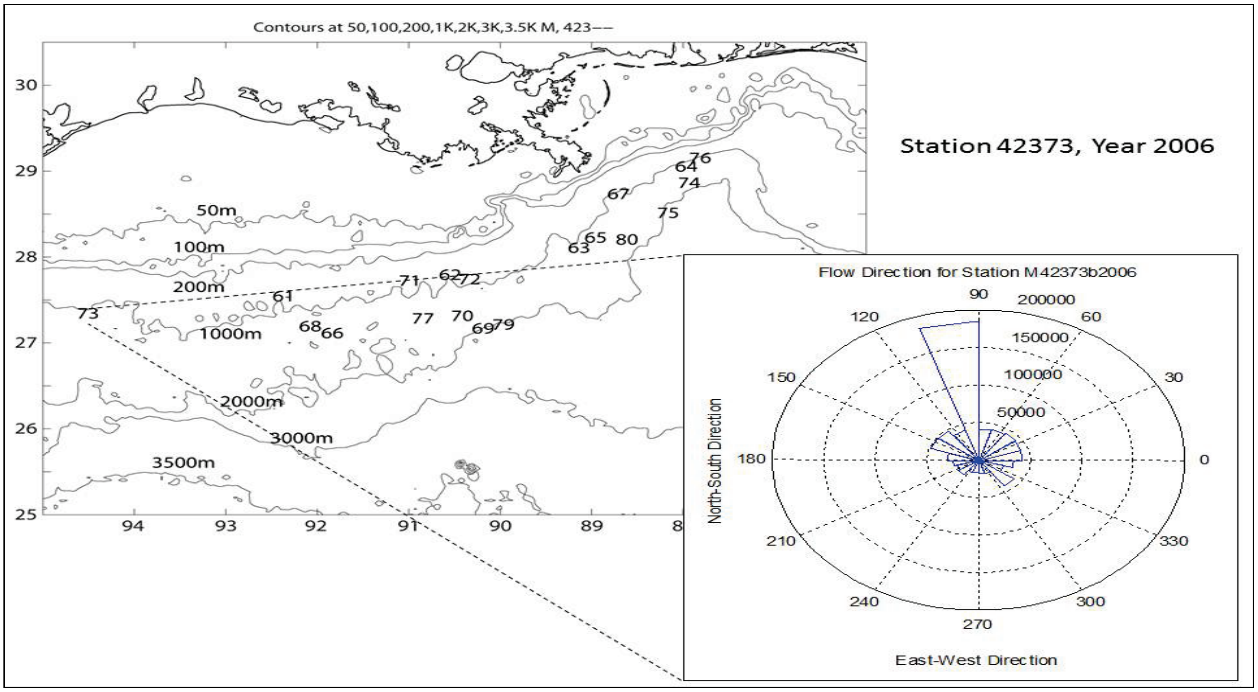

Figure 3.41. Current direction rose plot for Station 42373 in year 2006.

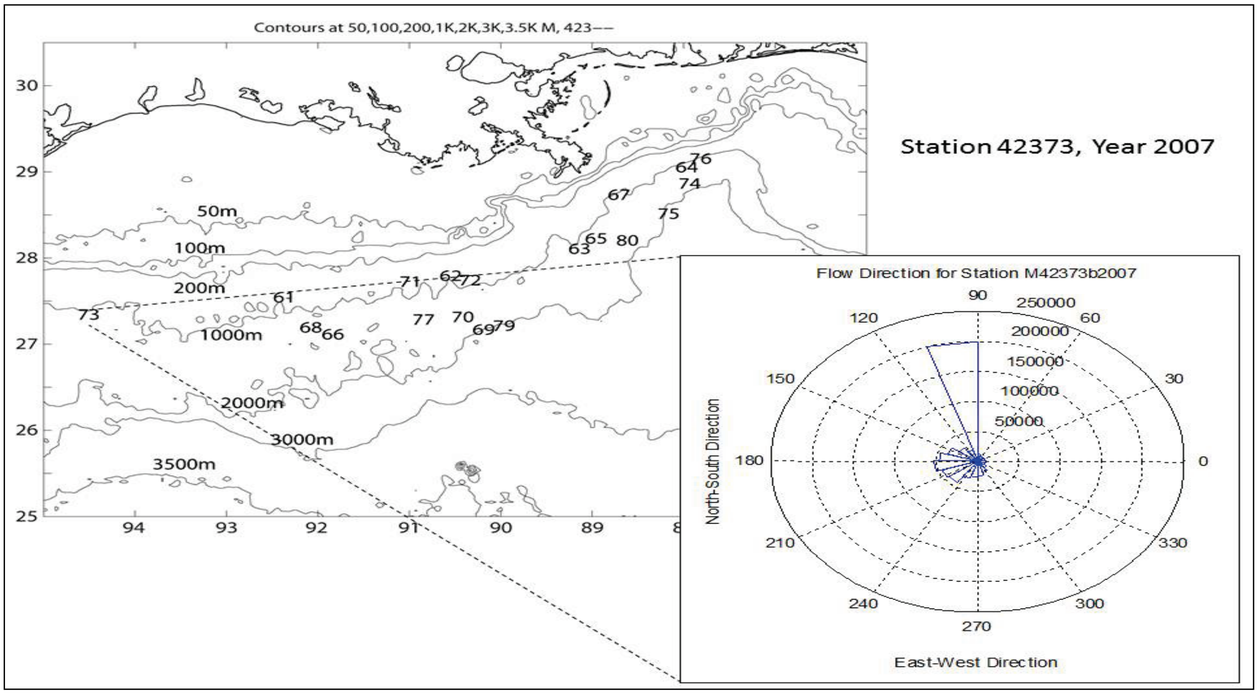

Figure 3.42. Current direction rose plot for Station 42373 in year 2007.

Station 42374 (Horn Mountain - Mississippi Canyon 126 and 127), Figures 3.43 – 3.45, is operated by BP, Inc. and located at 28.866 N 88.056 W, in water depths of 1646 m. The data only cover 45 to 541 m. The station is at the far east of the area. The flow direction varies a lot: although the 2005 data has northeast and northwest directions for the most part, the variation covers the northern quadrants. The 2006 data is almost omnidirectional with slight preference to the northeast and southwest directions; whereas the 2007 data is more like bimodal with eastward and westward or southwestward preferences. There is a deeper ADCP at this site looking upward covering 1646 to 1150 m. The flow direction in 2005 is mostly southwestward, very different from the upper level condition (Figure 3.84 compared with Figure 3.81).

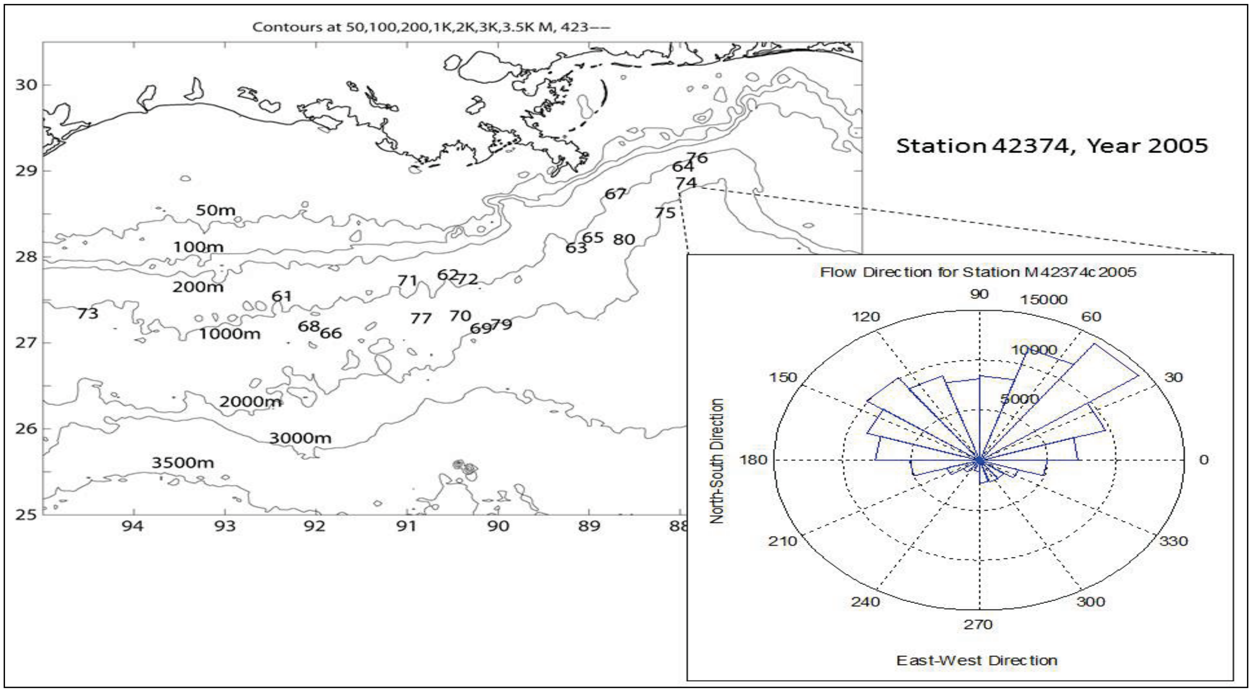

Figure 3.43. Current direction rose plot for Station 42374 in year 2005.

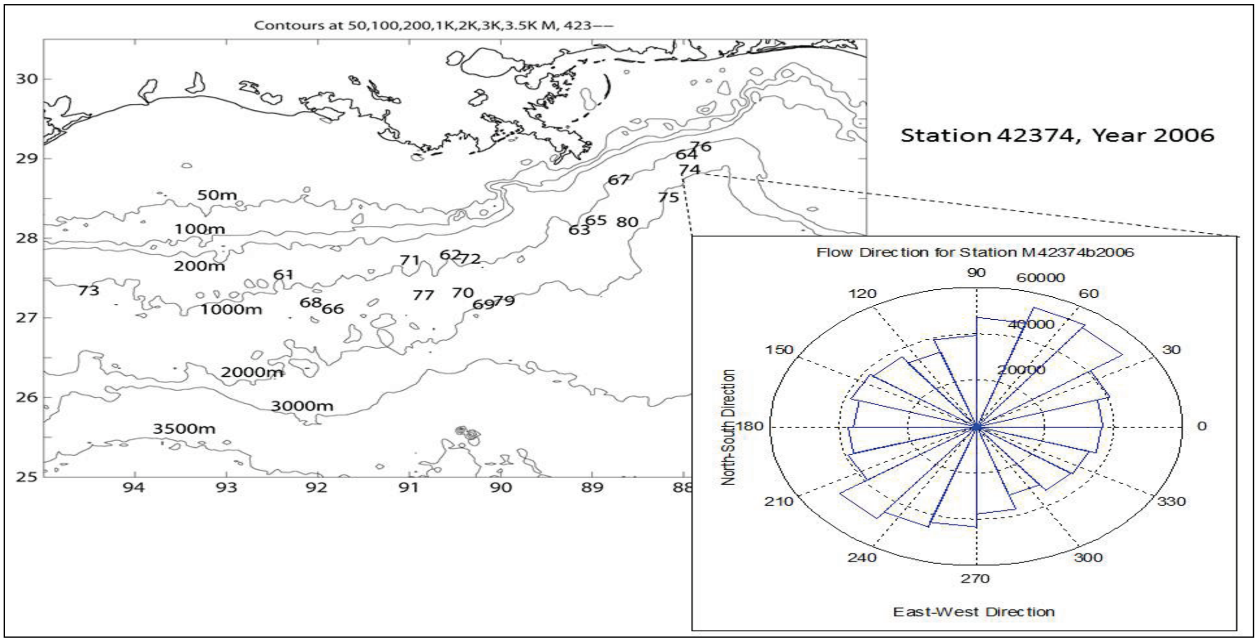

Figure 3.44. Current direction rose plot for Station 42374 in year 2006.

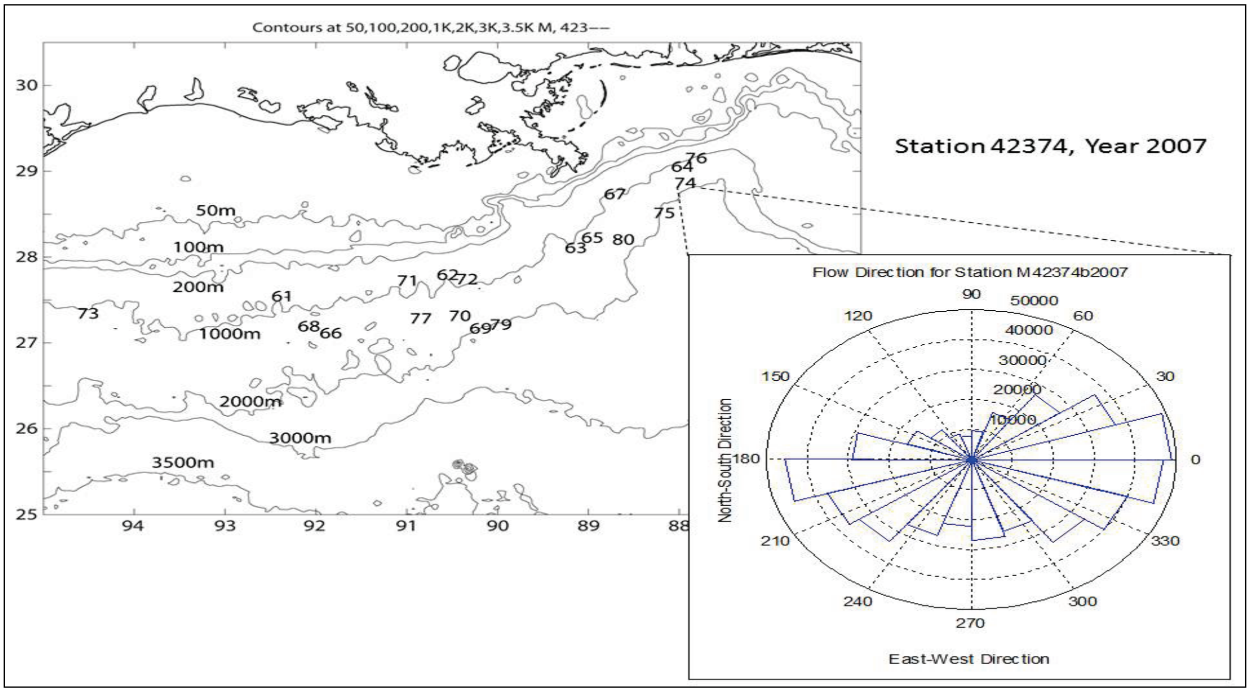

Figure 3.45. Current direction rose plot for Station 42374 in year 2007.

Station 42375 (Na Kika - Mississippi Canyon 474), Figures 3.46 – 3.48, is operated by BP, Inc. and located at 28.521 N 88.289 W in water depths of 1920 m. There are two ADCPs at this station. The data from the first ADCP cover 1912 to 1416 m (with the instrument looking upward). Data from the second ADCP cover depth from 48 to 992 m. These data display strong near-inertial oscillations and thus the flow direction is mostly omnidirectional with some preference perhaps as a result of superposition of larger-scale motions caused by the influence of Loop Current and eddies. The 2005 data is omnidirectional plus a southwestward emphasis. The 2006 data is omnidirectional with westward, northwestward, and southwestward preferences. The 2007 data show more emphasis on the northeast, south, and west directions. Even though this station is close to Station 42374, their directionalities are somewhat different.

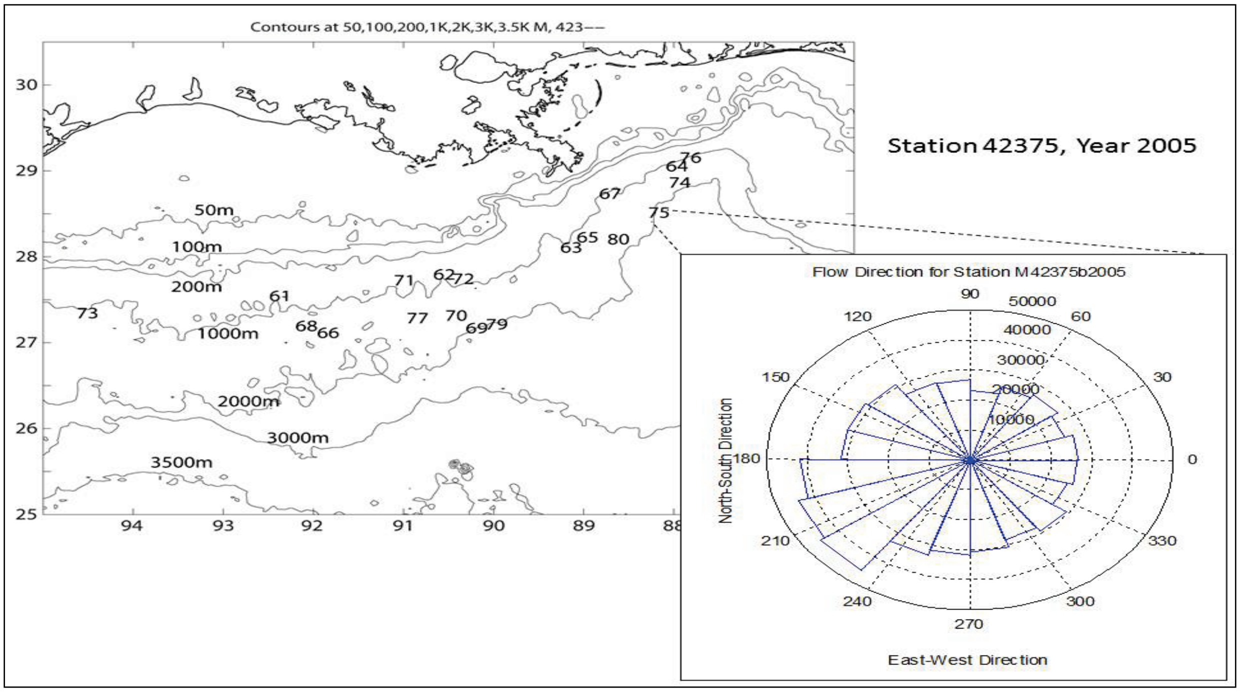

Figure 3.46. Current direction rose plot for Station 42375 in year 2005.

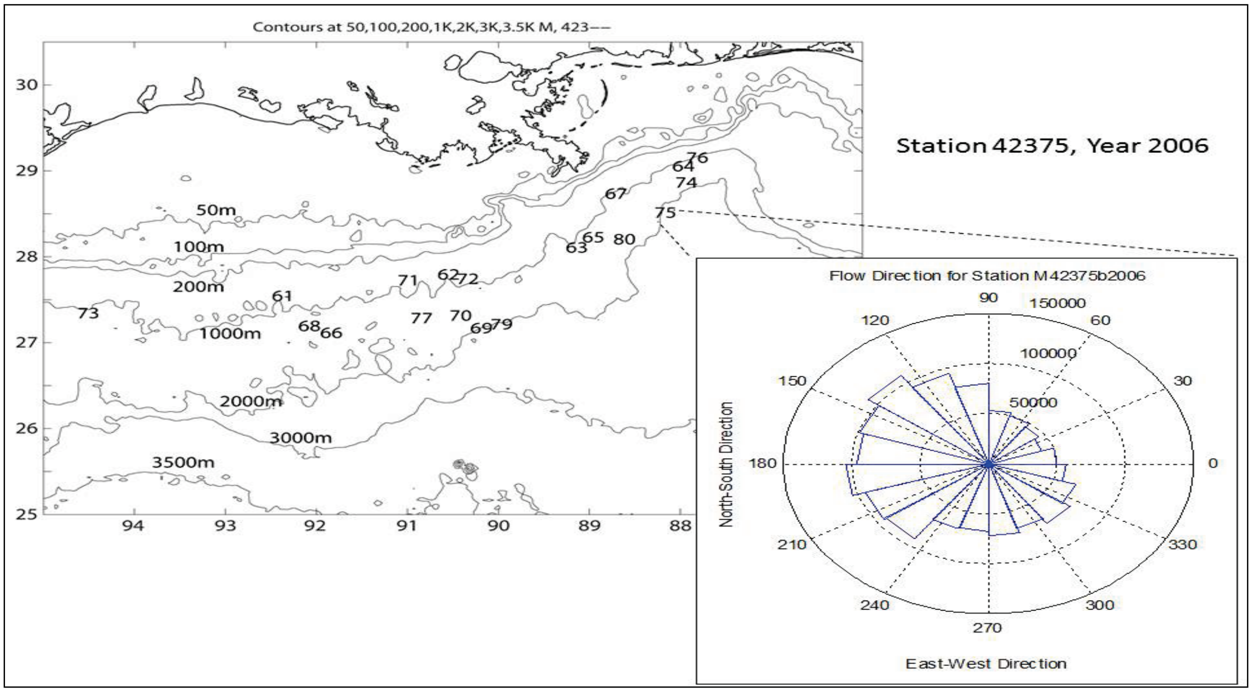

Figure 3.47. Current direction rose plot for Station 42375 in year 2006.

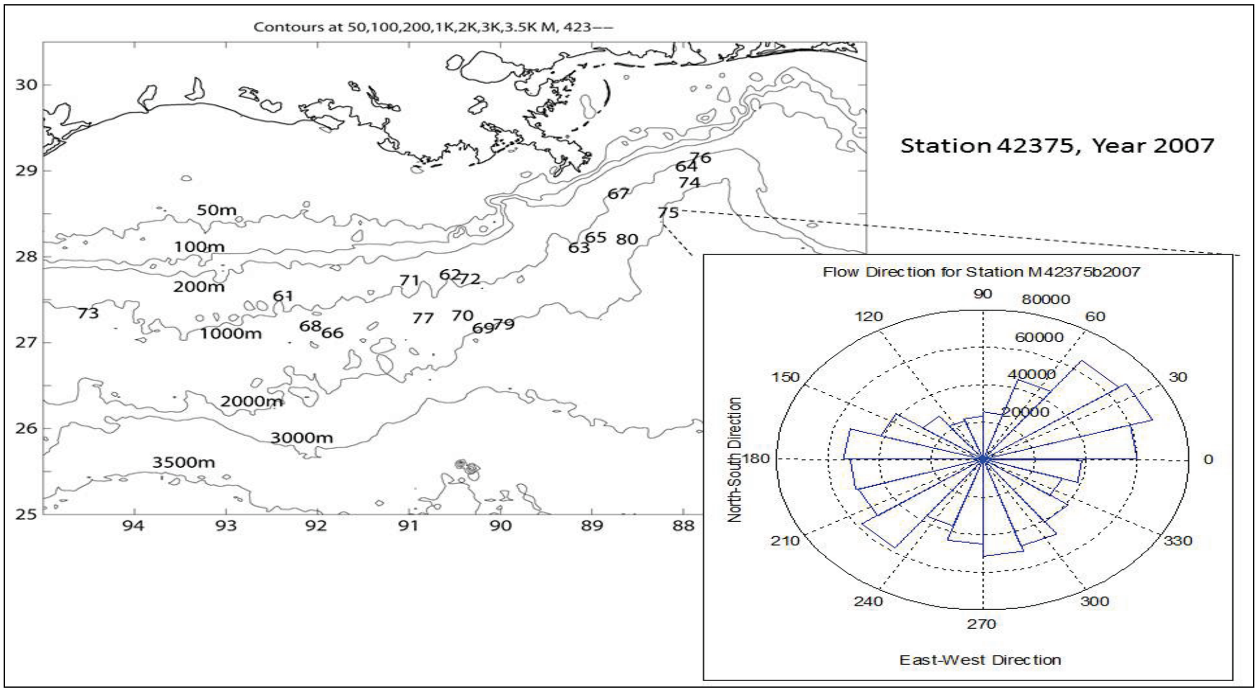

Figure 3.48. Current direction rose plot for Station 42375 in year 2007.

Station 42376 (Marlin - Viosca Knoll 915), Figures 3.49- 3.51, is operated by BP, Inc. and located at 29.108 N 87.944 W, in water depths of 986 m. The data from the ADCP cover 54 to 984 m. This station is close to Station 42364 but covers deeper water and has different directional preferences. The majority of the data in 2005 shows a predominant direction of south and southwest. This is in contrast to the directionality of Station 42374 in 2005 (Figure 3.81). The other two years (2006 and 2007) show some similarity between data from Station 42374 and Station 42376. Station 42376 in 2006 shows almost omnidirectional except it lacks the southeast flow. The bimodal flow in 2007 at Station 42376 is much more similar to that at Station 42374.

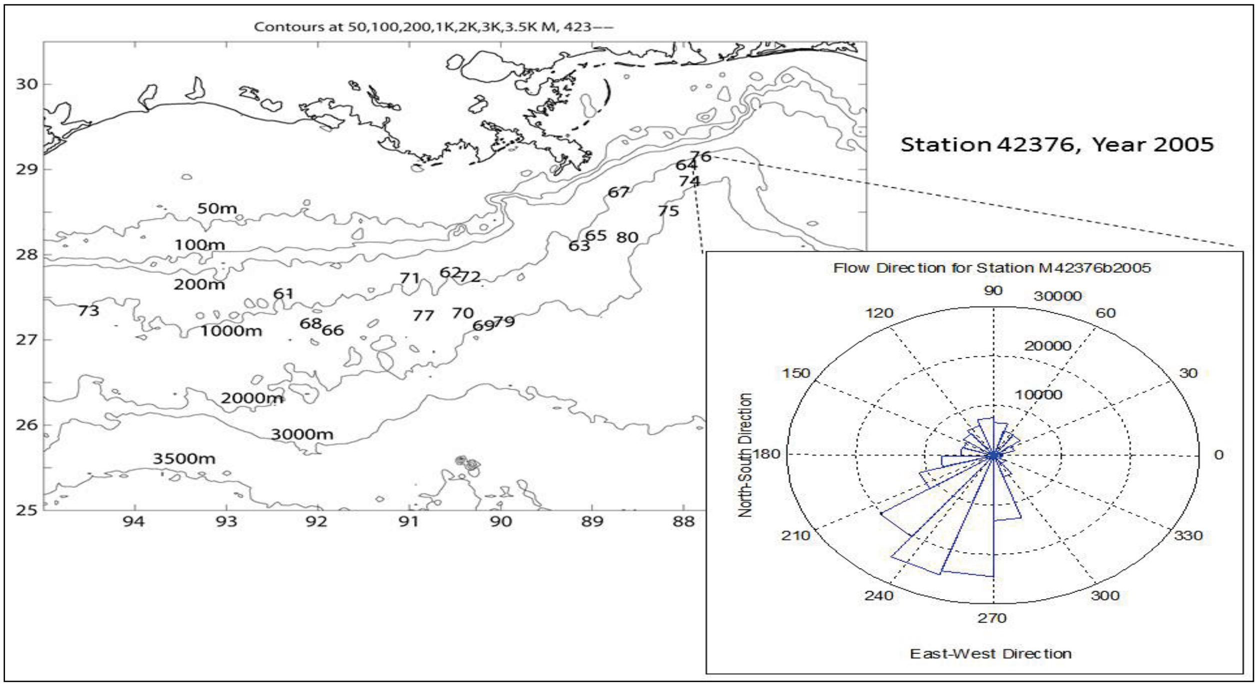

Figure 3.49. Current direction rose plot for Station 42376 in year 2005.

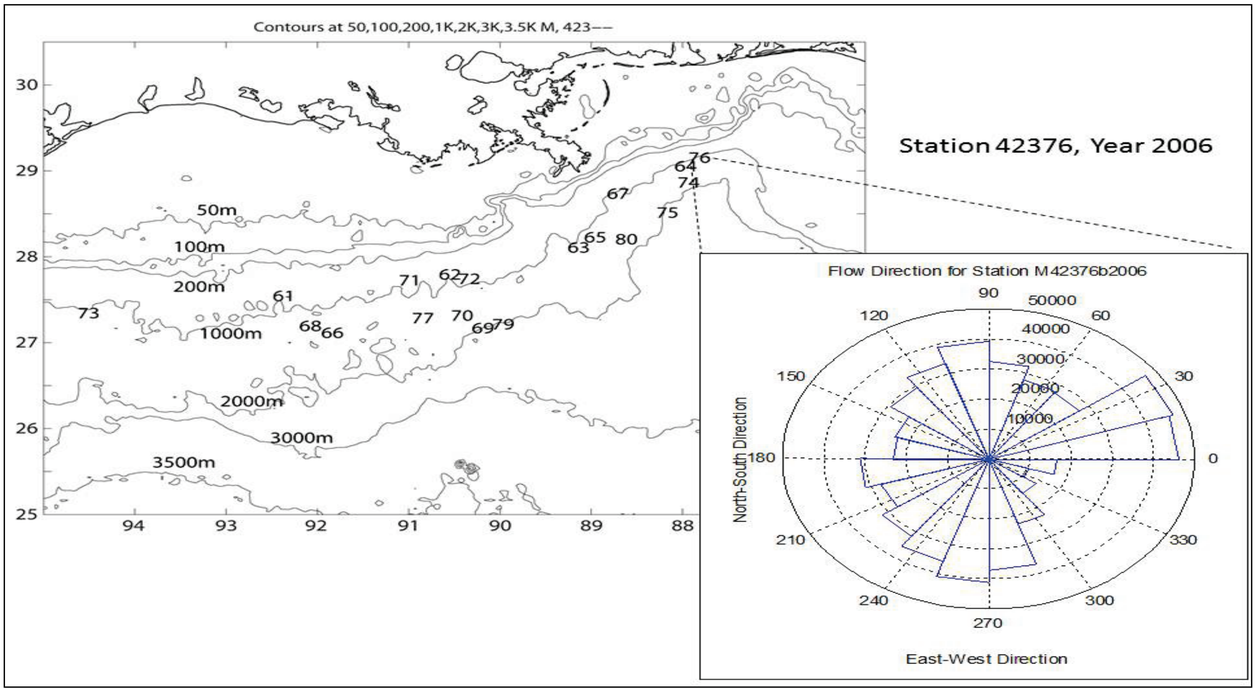

Figure 3.50. Current direction rose plot for Station 42376 in year 2006.

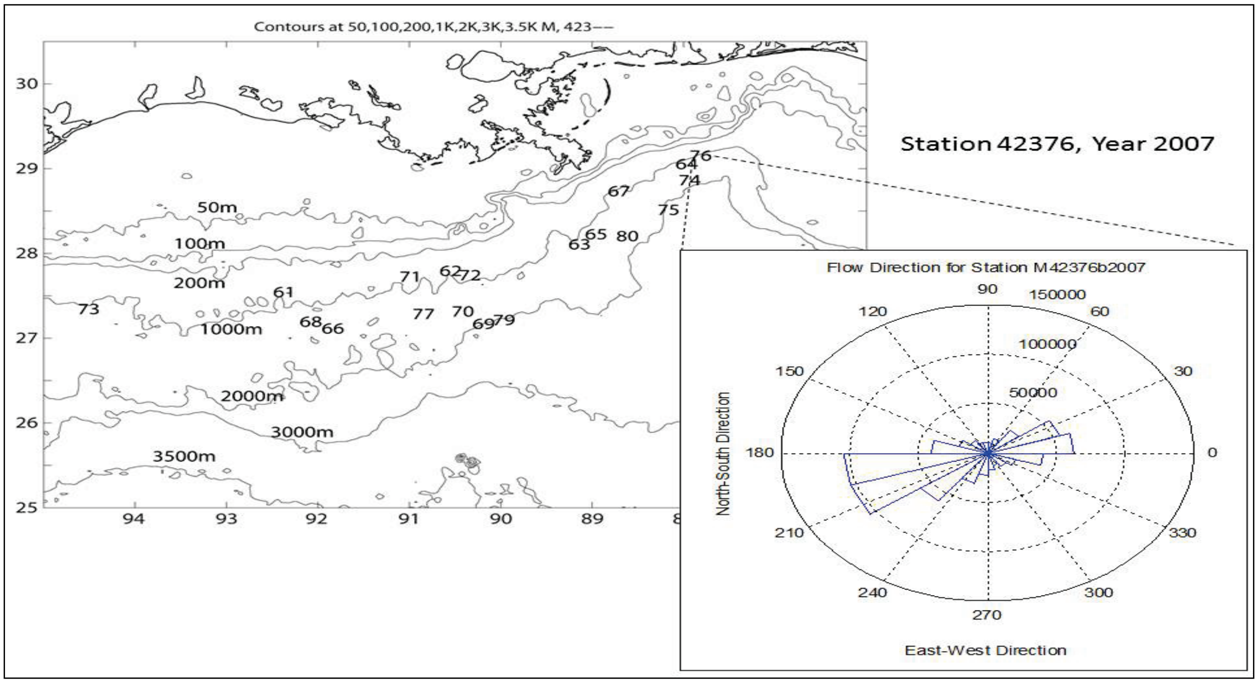

Figure 3.51. Current direction rose plot for Station 42376 in year 2007.

Station 42377 (Constitution - Green Canyon 680), Figures 3.52- 3.53, is operated by Kerr-McGee Oil and Gas Corporation and located at 27.293 N 90.968 W, in water depths of 1524 m. The data cover 2006 and 2007 and between 69 and 999 m. The 2006 data shows bimodal directions – northeast and southwest. This is different from two nearby stations (42369 and 42370, which are similar for 2006). The 2007 data also shows bimodal directions but with east and west preferences. This is also very different from the two nearby stations (42369 and 42370, which are different themselves for 2007).

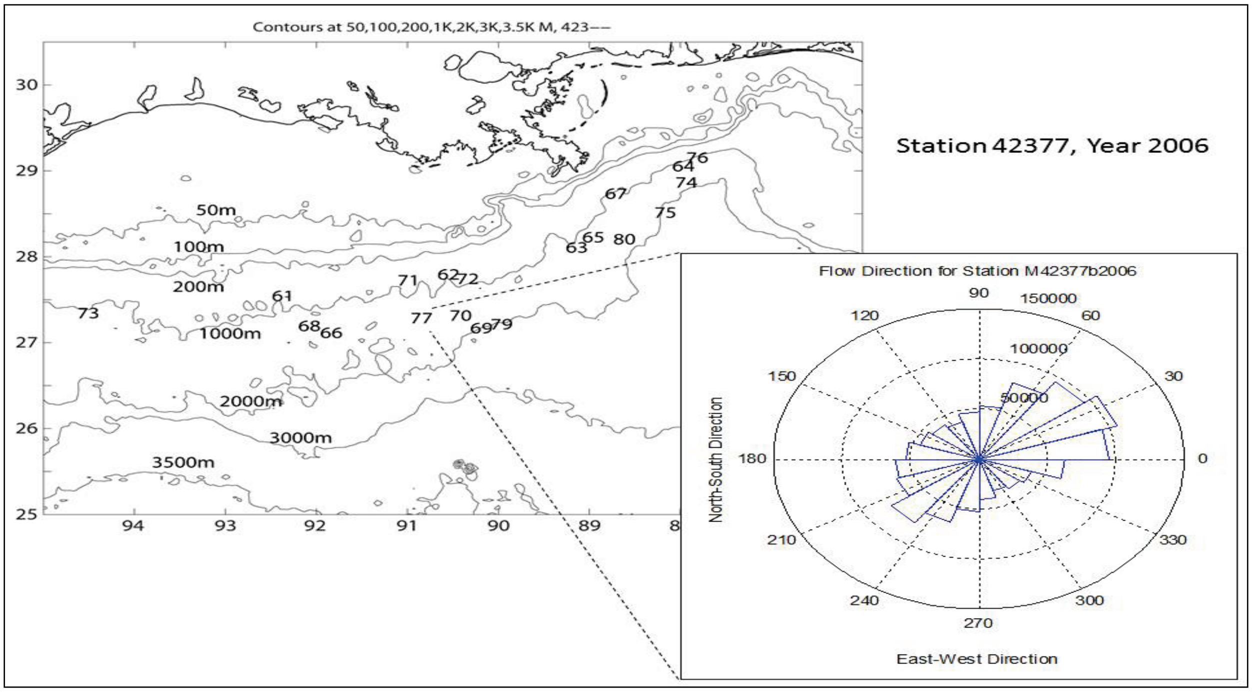

Figure 3.52. Current direction rose plot for Station 42377 in year 2006.

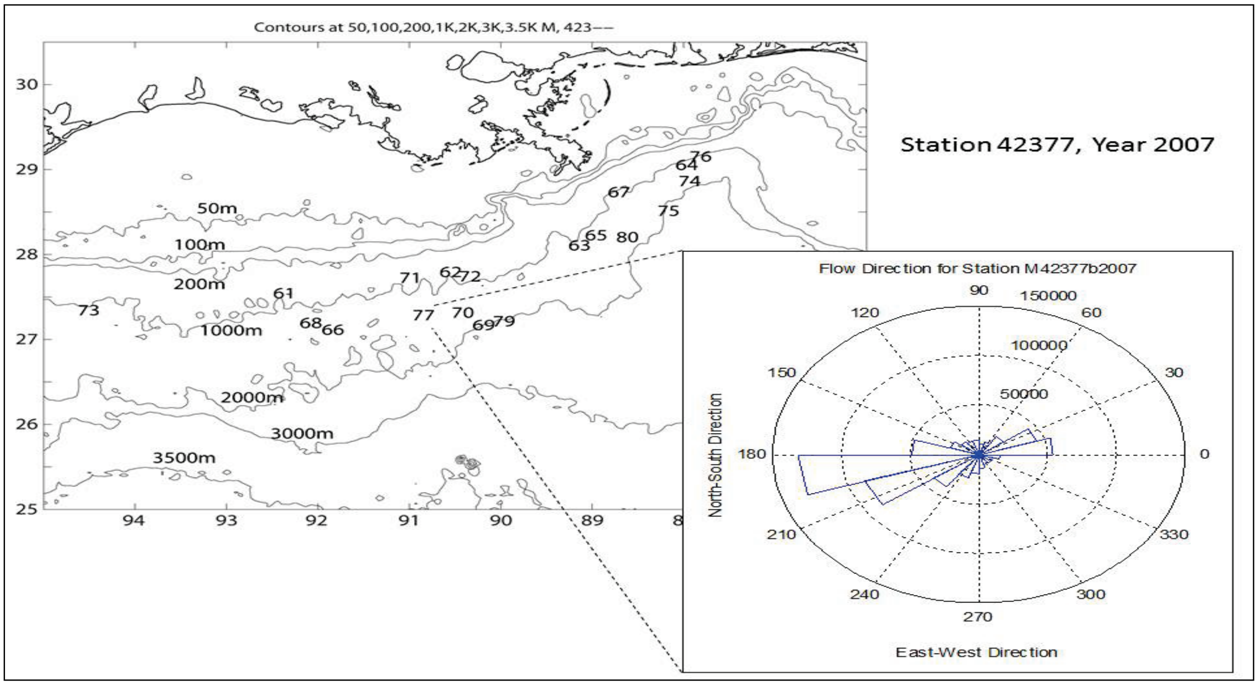

Figure 3.53. Current direction rose plot for Station 42377 in year 2007.

Station 42379 (Marco Polo - Green Canyon 608), Figures 3.54 – 3.55, is operated by Anadarko Petroleum Corporation and located at 27.362 N 90.181 W, in water depths of 1286 m. The data cover 2006 and 2007 and between 1259 and 683 m (upward looking). This station is very close to Station 42369. The 2006 data shows an eastward–northeastward and some southeastward preferences. Although this is somewhat different from 42369 and 42370, which are similar for 2006, but these two other stations also have northeast and southeast preferences for 2006, the three stations have some similarities. The 2007 data shows directions from southwest to northwest. This covers some of the predominant directions of Station 42370.

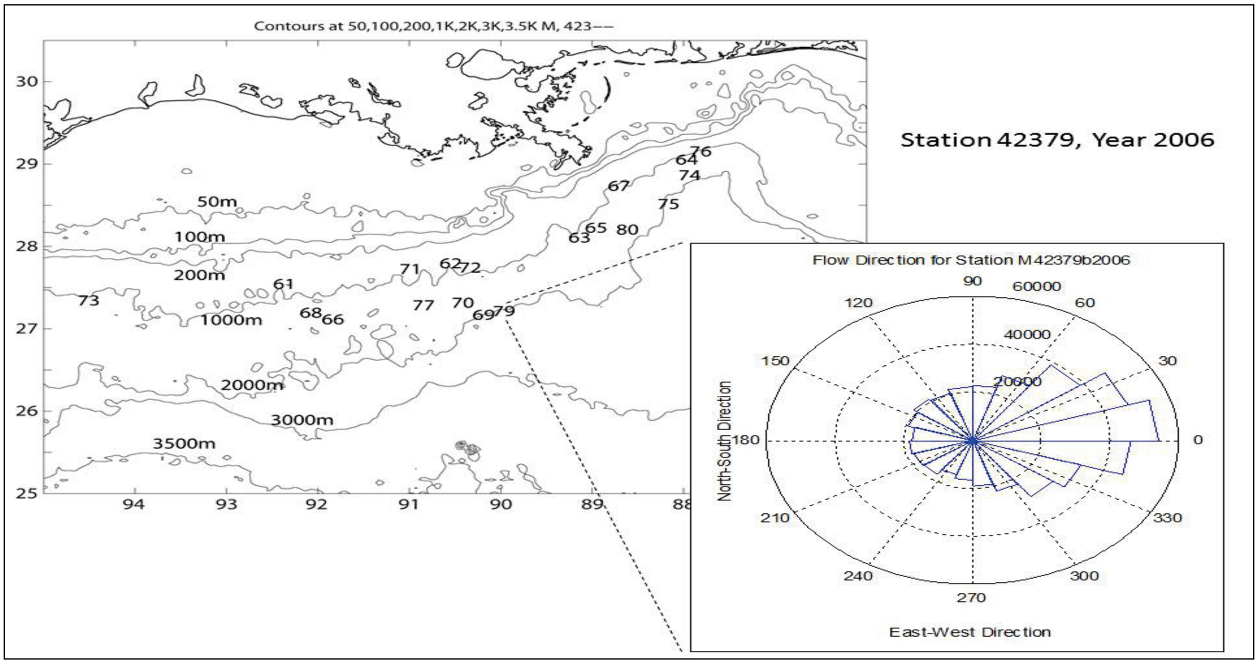

Figure 3.54. Current direction rose plot for Station 42379 in year 2006.

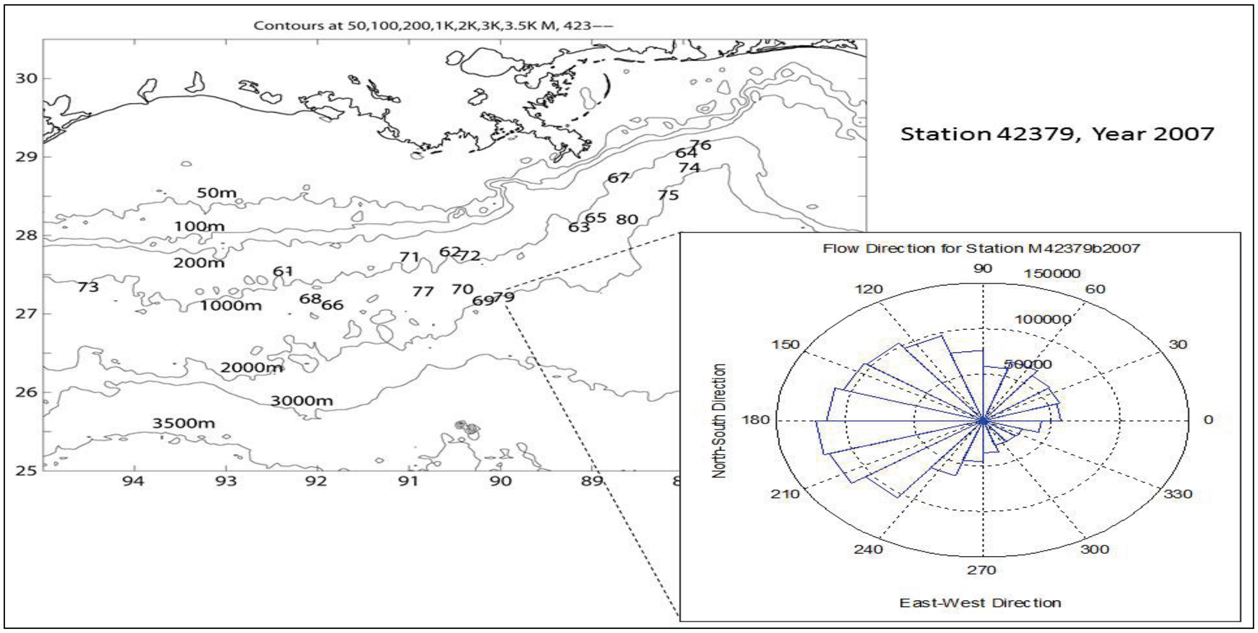

Figure 3.55. Current direction rose plot for Station 42379 in year 2007.

4. VERTICAL VARIATIONS OF HORIZONTAL VELOCITY

The previous chapter describes basic statistics of the flow velocity. Here we will examine the velocity time series as function of time and vertical position. Below we provide discussions of selected data, emphasizing their variability and other characteristics. Due to the large volume of data, these discussions are necessarily based on a few representative examples.

4.1 VELOCITY VECTORS FROM STATION 42361 IN 2005

As discussed in Chapter 3, Station 42361 (Auger - Garden Banks 426) is operated by Shell International E&P, located at 27.550 N 92.490 W in water depths of 872 m, covering between 51 and 803 m below the surface. Note that the first data bins shown in the following figures are not necessarily consistent with the actual first bin of the data. This is because of the QA/QC may take out some of the nearsurface data if the "percentage good" field is less than 75% value. The near-surface values are often times contaminated by the surface reflection of sidelobes of the ADCP signal, sidelobe effect, and are often excluded. The time series of the vertical profiles of the velocity vectors show quite large variations. For instance, the near-surface flow on May 1, 2005 was southwestward. The flow appears to have a thickness of 350-400 m below the surface, although the flow magnitude decreases with depth (Figure 4.1). This appears to be quite consistent with what the satellite images reveal. Here we only mention a few variations related to the movement of the Loop Current that can be verified by the satellite images. We will not discuss changes of smaller magnitude.

From May 1, 2005, the near-surface flow decreases and on May 6 the thick layer of flow has decrease substantially (Figure 4.1). This is agrees with what satellite images suggest, although the satellite images do not show much of the details and there is not enough resolution to quantitatively compare with the in situ data.

The vertical structure of the flow appears to suggest a few layers, each with its own characteristics. These layers however are changing with time and related features of flows can propagate upward and downward. The layered flows suggest that there are strong vertical shears of horizontal velocity at some levels during certain time periods. Strong velocity can also occur between layers: local maximum can be in the middle of a water column.

After May 9, the near-surface flow started to increase again in the southwest direction. It then increased in a layer of up to 450 to 500 m below the surface. It is obvious that the daily oscillations are strong for most of the data. This appears to be near-inertial oscillation. On May 11 and 12 there was a relatively strong deep water strong flow between 500 m and 770 m below the surface. The magnitude can be larger than 20 cm/s. The direction of the flow is mainly southward (Figure 4.2). During this time period, the Loop Current is quite strong. Its tip reached to relatively north and west, almost to 29N and 91W. On May 19, 2005, the Loop Current was still quite strong.

The speed of the flow significantly decreased before June 9 (due to data gap we do not have flow data between May 21 and June 8. This speed reduction is apparently a result of the southward retreat of the tip of the Loop Current. The near-inertial oscillations are however still obvious.

Sometimes such oscillations (of roughly 24 hour period) are in a layer of the water column for some time. The thickness of the layer does not appear to be regular. Between June 9 and 13, there was a 5 day persistent daily oscillation between 500 and 600 meters. This oscillation appears to be propagating downward. From the way it varies over time, it is obvious that it has a clockwise rotation with time of the flow vector, although there was a mean flow going toward the north (Figure 4.3). During the last three days of this period, the flow below 625 m shows a southward flow, opposite of the upper layer flows. Between 500 and 700 m, the flow of June 18 and 19 shows a relatively strong northward spike. It then gradually decreased even though the oscillation lasted for a few days. Between 250 and 450 m, there was a relatively strong and clear daily oscillation clearly propagated downward at a speed of about 200 m per day.

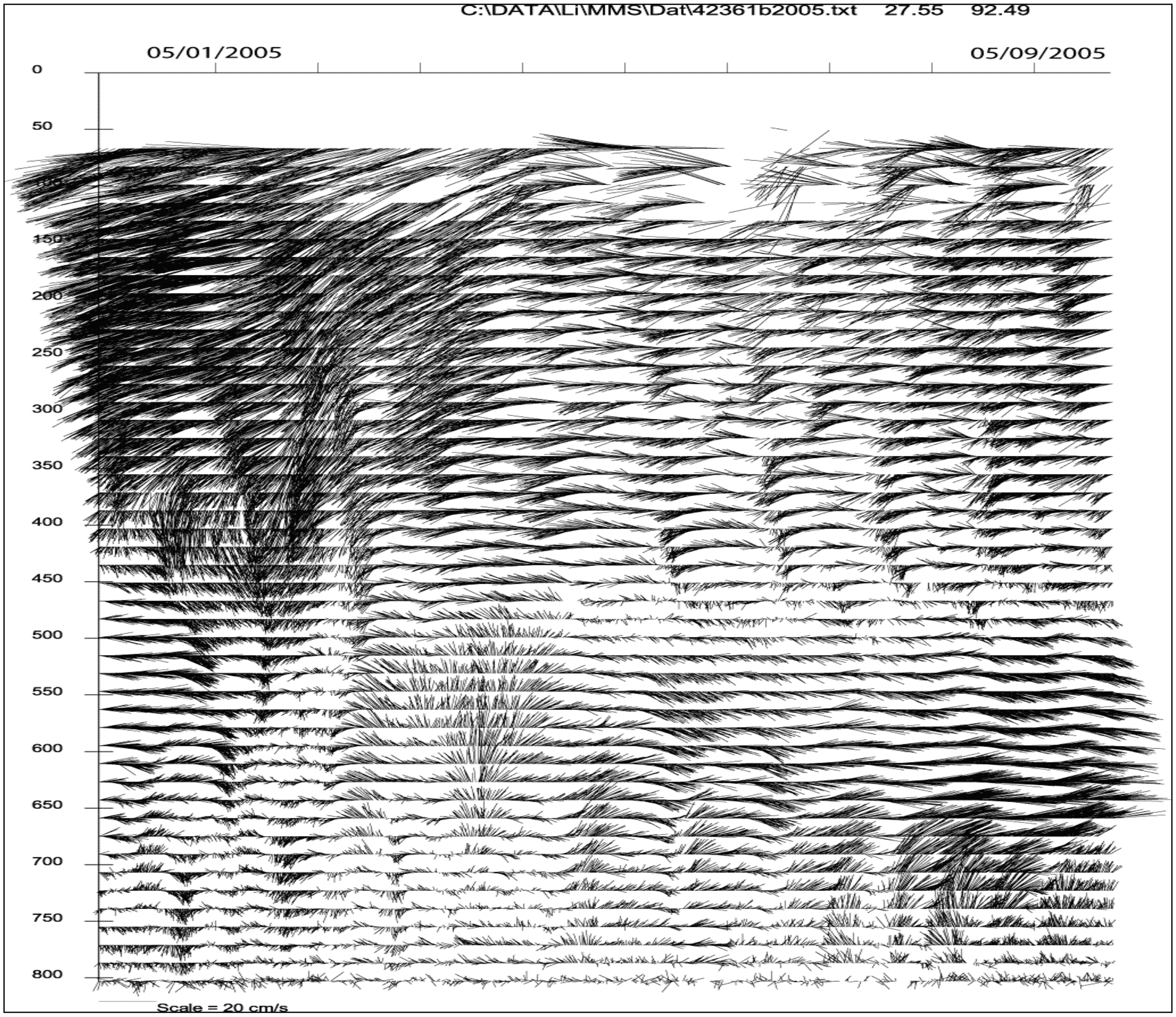

Figure 4.1. Vertical profiles of horizontal velocity at Station 42361, May 1-10, 2005.

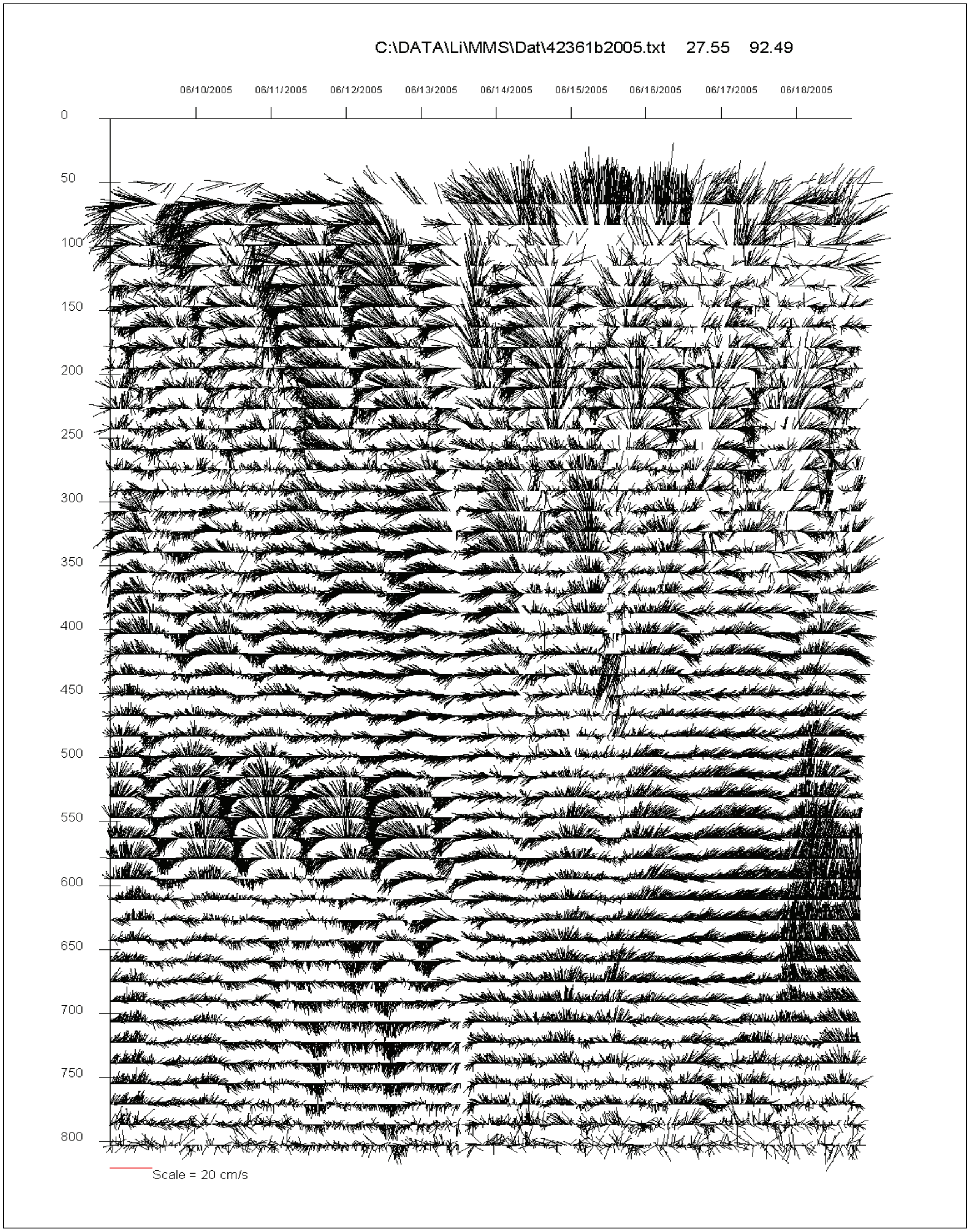

Figure 4.2. Vertical profiles of horizontal velocity at Station 42361, May 12-19, 2005.

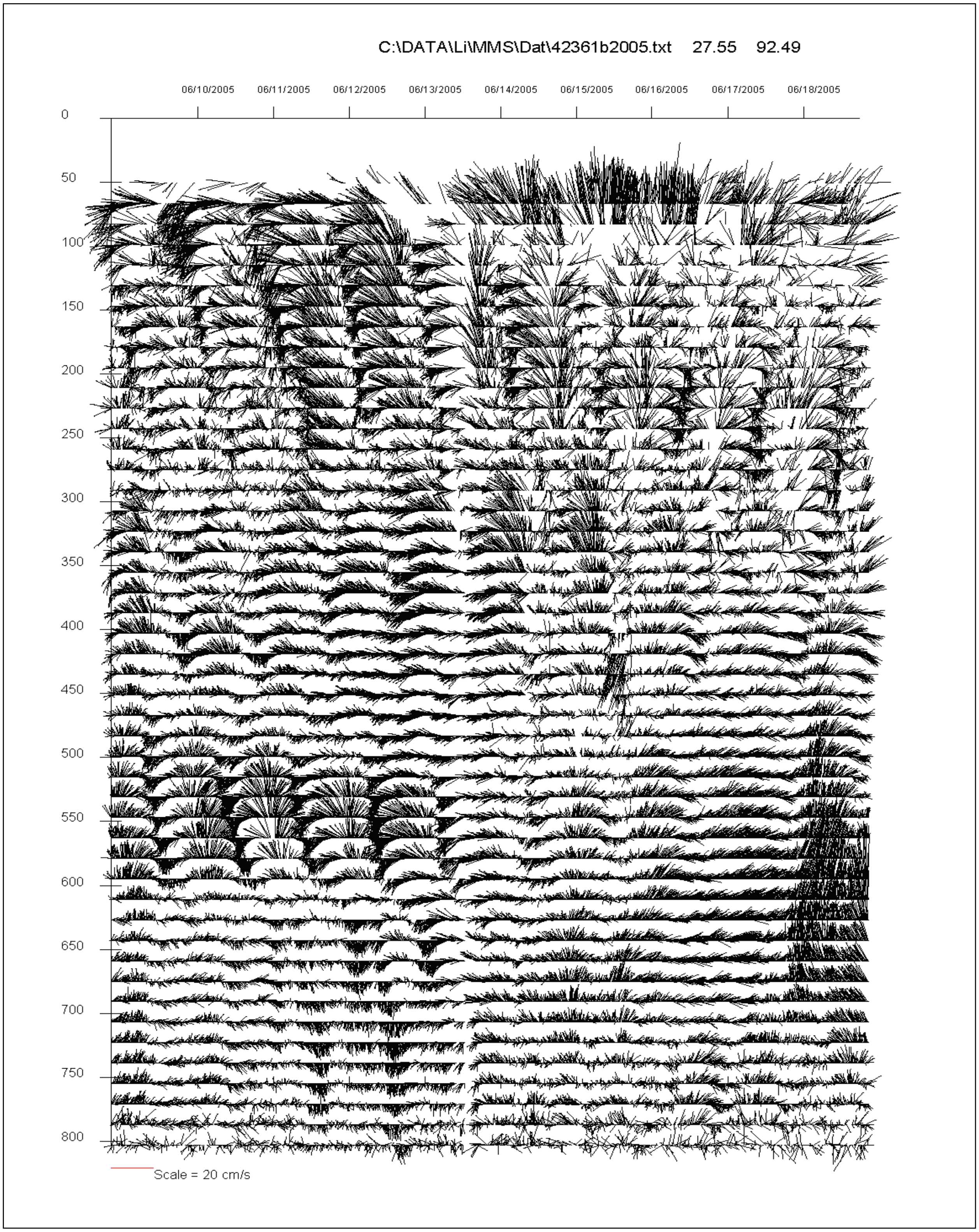

Figure 4.3. Vertical profiles of horizontal velocity at Station 42361, June 9-19, 2005.

4.2 VELOCITY VECTORS FROM STATION 42363 IN 2005

Station 42363 (Mars - Mississippi Canyon 807) is 150 km east of Station 42362. This station is operated by Shell International E&P and located at 28.160 N 89.220 W, in water depths of 894 m. The data cover almost the entire water column from 61 m below the surface. This is a place where the Loop Current sweeps through quite often. When this station is within the Loop Current, the flow velocity is very strong. Between May 13 and 23, 2005, there was first a strong southeastward or eastward before May 20, Figure 4.4. After May 20, the flow switched to northeastward until about June 29 when it decreased, Figure 4.5. It then increased again and changed to northward. It then decreased as the direction changed to northwestward. On June 10, the flow velocity magnitude had decreased to its minimum followed by a change of flow direction to southward on June 11 and June 12, Figure 4.6. Before June 13, the flow changed to northeast again followed by another change in flow direction for many days starting from June 16, Figure 4.7. This persistent southward flow started to increase its magnitude and another swing of flow direction on July 2, Figure 4.8, when the flow started to become southeastward. This strong flow lasted until August 10 when it decreased significantly.

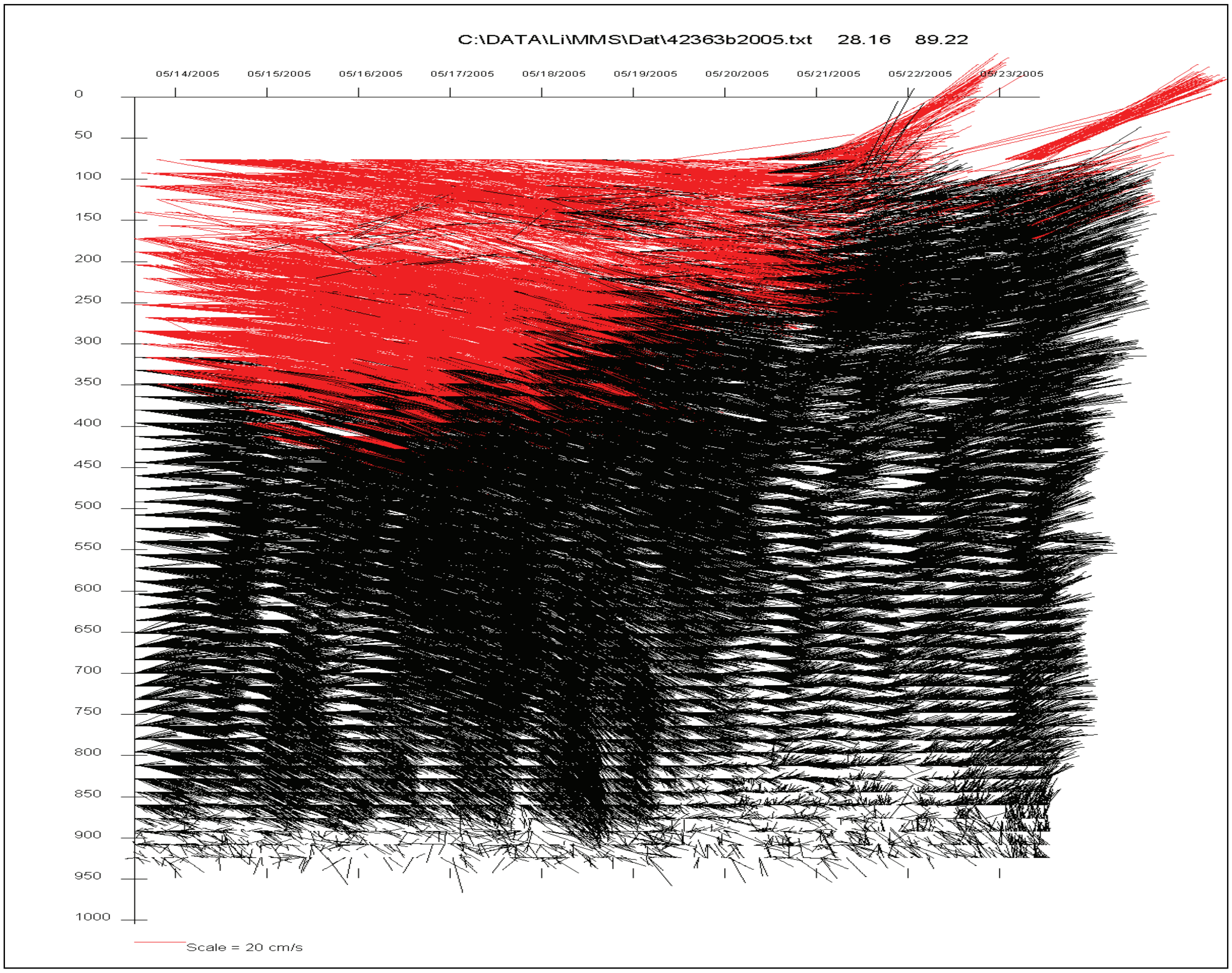

Figure 4.4. Vertical profiles of horizontal velocity at Station 42363, May 13-23, 2005.

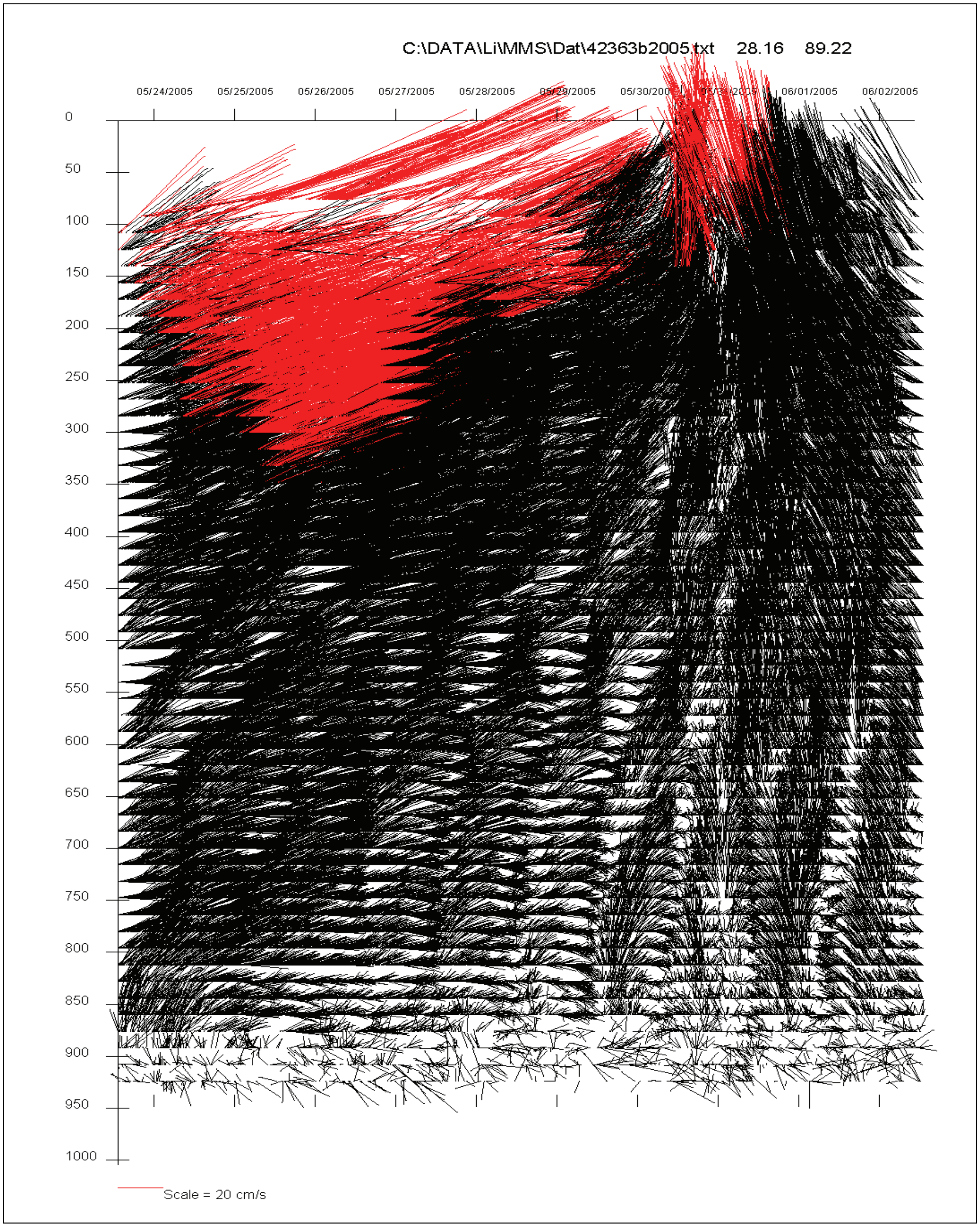

Figure 4.5. Vertical profiles of horizontal velocity at Station 42363, May 24-June 2, 2005.

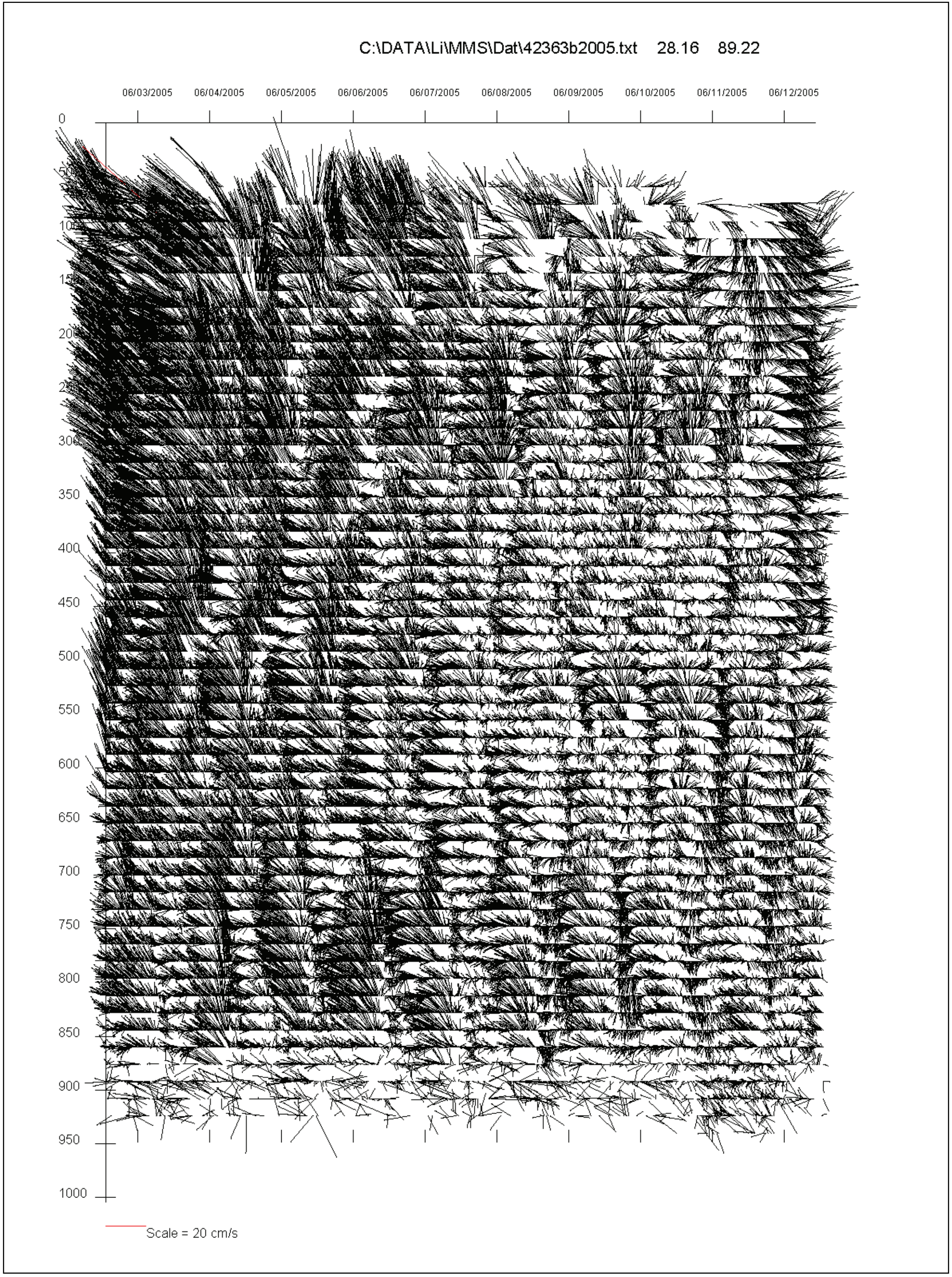

Figure 4.6. Vertical profiles of horizontal velocity at Station 42363, June 3-12, 2005.

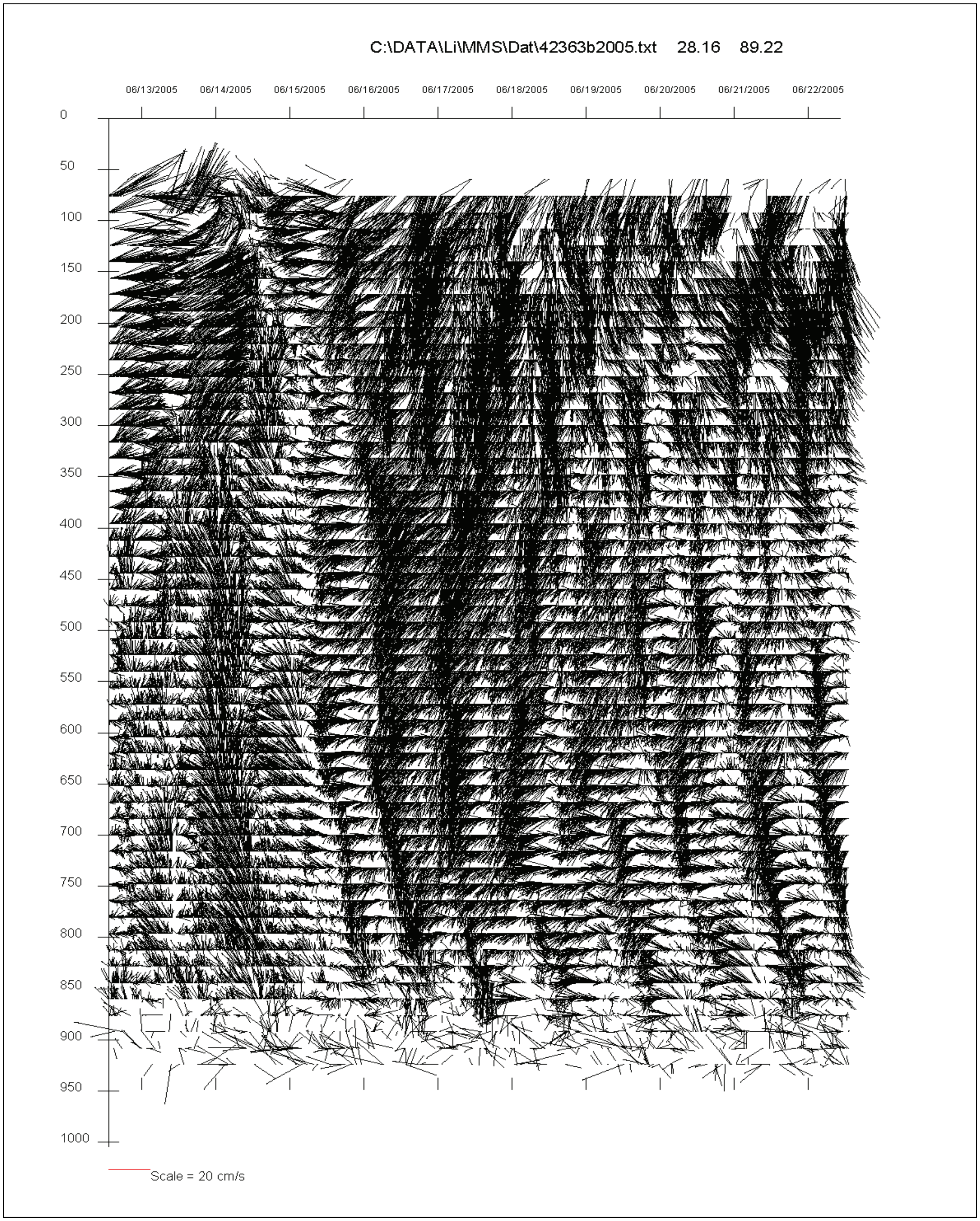

Figure 4.7. Vertical profiles of horizontal velocity at Station 42363, June 13-22, 2005.

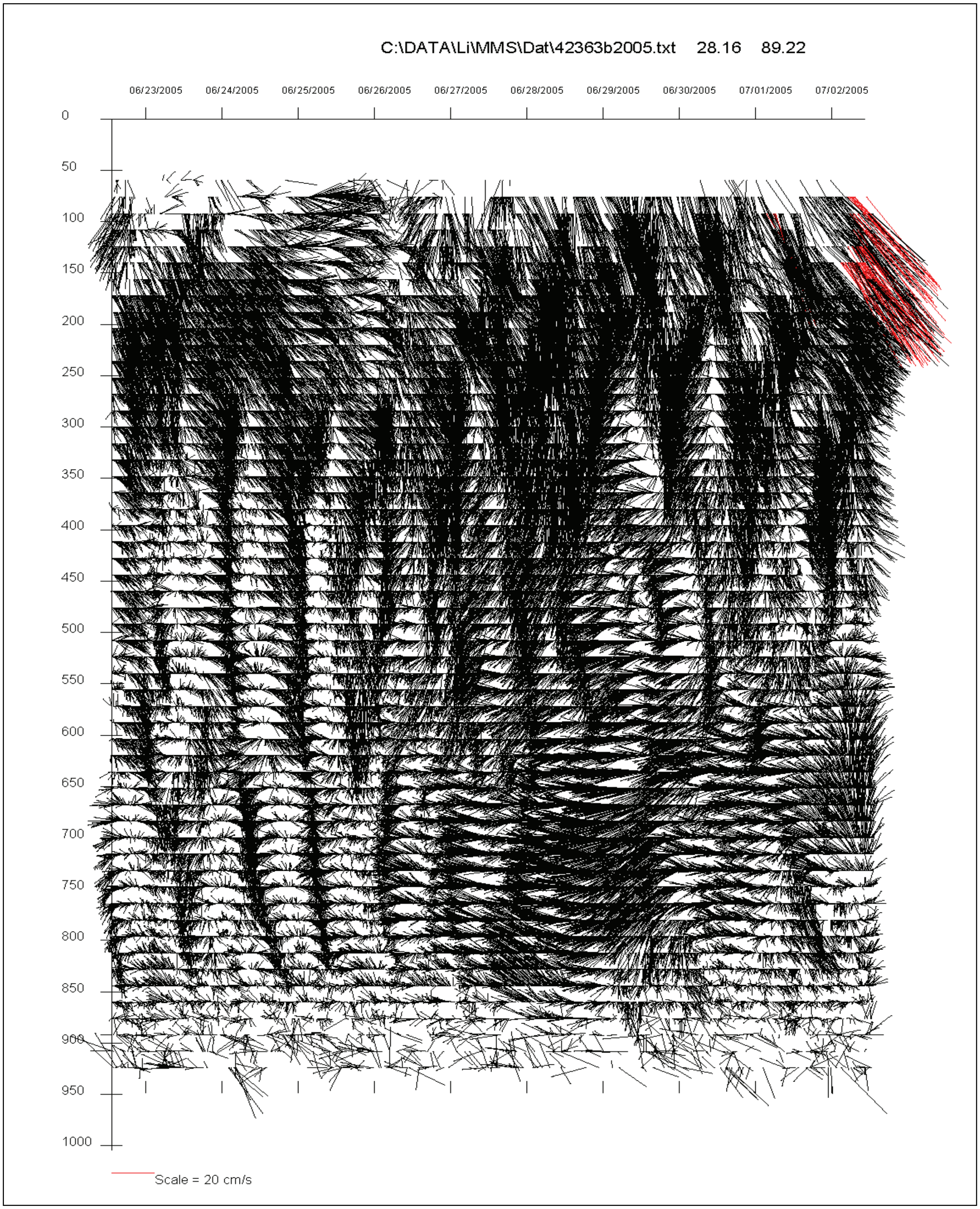

Figure 4.8. Vertical profiles of horizontal velocity at Station 42363, June 23-July 2, 2005.

4.3 VELOCITY VECTORS FOR STATION 42366 IN 2005

Station 42366 (Red Hawk - Garden Banks 877) is operated by Kerr-McGee Oil and Gas Corporation at 27.122 N 91.959 W, southeast of Station 42361 by more than 50 km. The water depth at this station is 1615 m.

The May 2005 data showed oscillations between northward and southward flows until early September, when the flow magnitude started to increase in the southeast direction for about a month. This is the time when the Loop Current was deforming, extending to the west, and developing an eddy that eventually separated from the Loop Current. The separated anti-cyclonic eddy subsequently moved to the west.

4.4 VELOCITY VECTORS FOR STATION 42368 IN 2005

Station 42368 (Magnolia - Garden Banks 783) is operated by ConocoPhillips at 27.204 N 92.203 W in water depths of 1424 m. It is about 20 km west-northwest of Station 42366. The flow however is very different from that nearby station. At this station, the flow is mostly toward the southern quadrants (southwesterly directed but with secondary directions such as south and northwest. The difference between Stations 42366 and 42368 is partly due to the difference in data coverage in the vertical. Station 42366 covers the vertical from 115 to 610 m, while Station 42368 covers between 67 and 1123 m.

At this station, there was a persistent southerly flow from mid-May until mid-June of 2005, during which the velocity profile was quite consistent throughout the lower 1000 m of the water column. Daily variations are very obvious, suggesting strong near inertial oscillations. The NIO, however, are smaller than the mean southerly flow such that the overall flow was in the same direction. For a few days in mid-June (June 14 – 18), the near-surface flow reversed direction. A few days before this time period, the vertical profiles started to show some variations and vertical propagation of the NIO. While the wave form propagates upward, the energy propagates downward. During this time period, the near-bottom flow also appeared to have reversed its direction from mid-June to late June (June 12-26). Mid-depth reversal of flow also occurred during June 26 and July 2 between 650 and 1000 m, with apparent upward propagation of the NIO at a rate of about 300 m/day. Throughout much of July, the flow becomes southern again all the way to the bottom, with a decrease in magnitude downward. The data has a long gap until Dec. 9, 2005. From Dec. 9 (when measurements resumed) to Dec. 23, 2005 (when measurements stopped) the flow was southerly with some more randomness (noisier than the summer data).

4.5 VELOCITY VECTORS FOR STATION 42370 IN 2005

Station 42370 (Holstein - Green Canyon 645) is operated by BP, Inc., at 27.321 N 90.536 W in water depths of 1311 m. The data covered 62 to 992 m. This station had two ADCPs in 2005. The data from 2005 covered from May 5 to August 3 for the upper level ADCP. From August 4 to Sept. 20, the top level ADCP only covered down to 250 m. The lower level ADCP covered most of 2005 with some minor gaps. Because of the proximity of this station to station 42369, the flow patterns and variations at both stations are more or less similar.

The flow started with roughly a northerly direction (similar to Station 42369) and an increasing trend that peaked in May 13, instead of May 12. This change coincided with a westward bulging of the Loop Current over this station.
Obviously, Station 42370 had about a one-day time lag compared to Station 42369. The flow then became southerly gradually. At this location, it appears to be from the mid-depth upward, i.e. there was an upward vertical propagation of the southerly flow as early as May 7 at 1300 m depth. By May 14, the southerly flow was at about 1000 m. By May 20th, the southerly flow had risen to 650 m, and by May 23, the southerly flow reached the surface. Daily oscillations are again imbedded in the predominant flow signal. This southerly flow lasted until June 4 when the flow started to reverse again to northward. This flow lasted pretty much unchanged (only minor changes) until June 25 when the flow speed increased rapidly. When this happened, there was a downward propagation of the speed increase. It was then followed by an upward propagation of the speed reduction, which was mostly flowing toward the northern quadrants. In the lower layer, there was a downward propagation of the near inertial oscillation. From June 28 to 30, there appears to be a strong reversed flow at the deep lower layer. The near-surface flow wax and wane but remained significantly high (> 50 cm/s) for much of the time until the end of August and early September. Again, this dramatic and lasting speed increase resulted from the large bulge of the Loop Current attempting to separate and becoming an eddy. The strong flow was mostly northeastward. A big anti-cyclonic eddy finally detached from the Loop Current on September 29. The lower layer ADCP continued to show near inertial oscillations with vertical propagation of the daily variations.

4.6 VELOCITY VECTORS FROM STATION 42373

Station 42373 (Boomvang - East Breaks 643) is operated by Kerr-McGee Oil and Gas Corporation at 27.354 N 94.625 W, in water depths of 1113 m. The station is at the far west end of the study area. Two ADCPs operated at this station; the first ADCP cover 104 to 597 m and the second unit cover from about 550 to near bottom. Data from the upper ADCP spanned from August 20 to December 10 with a few short gaps lasting a few days each. Data from the second ADCP covered from October 28 until the year’s end.

Between August 20 and 29 of 2005 the flow was strong and southerly from 100 to 250 m. Between 250 and 400 m vertical propagation of near inertial oscillation was observed. The upward propagation was about 200 m per day. Below 400 m, the near-inertial oscillations seemed to be vertically uniform. After August 29, the strong southerly flow was replaced by northward flow throughout the entire water column. There may be a downward phase propagation of near-inertial oscillation between 300 and 400 m and between Sept. 2 and 3. Measurements stopped on September 6 and resumed October 28, 2005. The flow velocity varied in direction and magnitude along the vertical such that the flow direction reversed along the water column. For example, between October 28 and November 7, the velocity between 100 and 350 m had a persistent strong southerly flow. This flow either decreased in speed or even reversed direction below 400 to 450 m. The northerly flow in the deep water then increased its speed between 600 m and near the bottom. Vertical propagation of phase occurred but the most obvious one was between 600 and 900 m during November3 and 6, and between 250 to 450 m during November 1 and 4. The upper layer flow reversed its direction again on November 6 when some of the deep water velocity reversed direction for 3 days (600 – 800 m on Nov. 6-9) or

4 days (750 m, on November 10-14). The near-surface northerly flow peaked before November 18 followed by a sudden reversal of the flow on November 20 throughout the entire water column vertical phase propagation can be seen at places. Upward propagation can be seen between 700 and 1050 m to be at about 700 m in 12 hours. This southerly flow started to reverse from the bottom. This near-bottom reversal kept below 600 m till December 12 after which the water column was once again occupied by southerly flows throughout the bottom layer for 2-3 days before we see once again some near-bottom reversal (northerly flow) during which (December 15-16) the lower layer southerly flow is strengthened for a few days, until December 18 when a strong northeasterly developed which subsequently decreased in magnitude.

4.7. VELOCITY VECTORS FROM STATION 42374

Station 42374 (Horn Mountain - Mississippi Canyon 126 and 127) is operated by BP, Inc., at 28.866 N 88.056 W, in water depths of 1646 m. There were two ADCPs at this site; the first ADCP covered 45 to 541 m. The deeper ADCP was looking upward covering 1646 to 1150 m. This station is at the far east of the area.

The 2005 data covered from June 29 until the year's end for the lower level, while the upper ADCP data ended after August 28. Before June 29 and July 10, 2005, the upper layer (0 – 350 m) was dominated by a northerly flow. The bottom layer velocity was weak from June 29 to July 7. While the surface flow started to change from northward to westward with strong vertical shear on July 12, the lower layer flow reversed direction and increased its speed. A strong lower layer flow reversal occurred again on July 14. The strong flows were all quite uniform from 1150 to 1600 m. The lower layer flow then turned to southwestward. A northward flow developed from the bottom on July 19 which expanded from 1600 m to 1250 m, two or three days later. A near-inertial oscillation was seen on July 23, 2005, near the bottom and propagating upward in about 5 days, with strong southerly flows. This oscillation lasted until August 1.

5. DEEP WATER OSCILLATIONS UNDER NORMAL AND EXTREME WEATHER

Near-Inertial Oscillations (NIOs) in the deep ocean are motions initiated by external forcing such as winds and under the influence of earth rotation (e.g. Gill, 1982; Apel, 1988). The NIOs can be viewed as Poincare waves regardless of whether they are internal (baroclinic) or external (barotropic) (Gill, 1982). A major feature of this kind of motion is that the two velocity components, u and v are close in magnitude and the particles' trajectories are almost circular, rotating clockwise (counter-clockwise) in the northern (southern) hemisphere. Under ideal conditions, inertial oscillations propagate vertically without a horizontal wave number component (Gill, 1982; Alpel 1988). In the northern Gulf of Mexico, the NIOs are particularly strong because the inertial frequencies are close to those of the diurnal tides, and thus resonance tends to occur (e.g. Chen et al., 1996; Hamilton, 1990; Nowlin et al., 2004). Tides in the deep ocean are usually very small, but they are amplified in shallow waters. In the northern Gulf, separating diurnal tides from NIOs may require a relatively long time series because of the proximity of the frequencies which depend on the latitude.

The study of NIOs has a long history. Pollard (1970) proposed a modified model of Veronis (1956) for the ocean response to a transient wind stress, in which a continuous stratification is added. The wind-generated NIOs appear to decrease with depth rapidly. However, the amount of energy transferred to NIOs does not really depend on the stratification and the horizontal scale of the wind but rather on the transient nature or the temporal variation of wind forcing, which is found to be responsible for both generating and destroying the NIOs. The model of Pollard (1970) cannot explain the deeper water NIOs because the force applied to the model is rather peculiar: the wind stress is applied as a body force that is non-zero only within the mixed layer.

In a study with observations (Schott, 1970), data from instruments on four moorings are analyzed: three of the moorings form an equilateral triangle with 4.5 km on each side, around the fourth mooring. Temperature and currents are measured for about 13 days at depths between 18 and 70 m. The NIO is out of phase between upper and lower layers. The inertial temperature variations are in phase throughout the thermocline. Perkins (1972) shows that, with measurements at five depths between 200 and 2200 m at 500 m intervals, the NIO frequency is 3% higher than the local inertial frequency. The velocity magnitudes are 2-12 cm/s at 200 m, less than 5 cm/s at 700 m, less than 3 cm/s at 1200 m, and 2-3 cm/s at 2200 m. The model of Kroll (1975) uses an arbitrarily stratified β-plane model with a viscous boundary layer at the surface and an inviscid interior to determine the NIOs in deep water. The wind produces Ekman suction in the surface boundary layer and NIO propagates into the interior. Perkins (1976) tries to explain the observation of two peaks around the local inertial frequency by the existence of an anticyclonic eddy which can cause the shift in the frequency peaks from the local inertial frequency. A simple expression of the new frequency is

$$f_e = \sqrt{f(f+\zeta)}$$

where ζ is the vertical component of the relative vorticity due to advection, and is non-zero for an eddy. This can be verified by the dispersion relationship when the nonlinear advection is included for a mean flow. Some studies use a slightly different expression for f_e, e.g. (Kunze, 1985)

$$f_e = f + \zeta/2$$

which is a commonly used form and essentially the same as the first equation above when relative vorticity is “small”. However $f_e = \sqrt{f(f+\zeta)}$ is more general and does not require that that vorticity be small. An even more general form is $f_e = \sqrt{f(f+\zeta)+\delta}$ in which δ is a “higher order” term consisting of velocity gradients. This can be readily shown by the dispersion relationship when the advective acceleration is included by only considering the importance of the mean flow: the nonlinear terms due to perturbation of the mean flow are all considered negligible. The formula by Mooers (1975) is very similar, i.e. $f_e = \sqrt{f(f+v_x)}$, here the cross stream flow shear for a long straight jet is used in place of the more general vorticity term.

Weller (1982) also confirms that vorticity in quasi-geostrophic flow shifts the frequency to either larger or smaller values than the local inertial frequency. In a simple barotropic model, Pollard and Millard (1970) show realistic-looking NIOs in the surface layer with large depth. Similar models are used to produce results that match observations reasonably well (e.g. Chen et al., 1996). Though many studies have found that the NIOs are surface- or sub-surface intensified (e.g. Chen, 1996; Qi et al., 1995; D’Asaro et al., 1995; D’Asaro, 1995; Tintore et al., 1995), or with a 180-degree phase shift in surface and lower layers, some studies also show highly coherent oscillations throughout the water column, e.g. Brooks (1983) show such characteristics in a depth of 732 m using sensors deployed 200 m below the surface and 32 m above the bottom. Numerous numerical model studies of NIOs have also been conducted throughout the last decade (e.g. Chen et al., 1996; Xing and Davies, 2004a,b, 2005).

Gill (1984) provides a frictionless, baroclinic model showing the vertical propagation of internal waves caused by storms. The barotropic flow was found weak. However, this conclusion was based on an assumption that the surface slope was too small compared to the interface displacements such that the rigid lid approximation would hold. This, however, can be problematic because the rigid lid approximation effectively filters out all surface gravity (barotropic shallow water) waves that have an immediate response at the bottom. The baroclinic motion shows a very long time scale (several days to 150 days) for the propagation of the storm-induced inertial waves to transfer to the bottom of the ocean. Observations show that the deep water inertial oscillations are almost instantaneous, right after the passage of the storm. This is quite contradictory and also indicates that the use of a rigid lid approximation may not be appropriate for the problems. In this chapter, we will examine the NIOs in the GoM under normal and extreme weather conditions especially immediately following three major hurricanes of 2005. In the analysis, we will present an analytic barotropic model and a Laplace Transform method to demonstrate the response of the ocean to surface atmospheric forcing and the dependence on water depth.

5.1 NEAR INERTIAL OSCILLATIONS UNDER NON-SEVERE WEATHER CONDITIONS

As we have seen in previous chapters that near-inertial oscillations are very common in the ADCP record. The difference between NIOs and ocean tide is that the former depends on local inertial frequency (function of latitude) and external forcing which is much less predictable than tides. As a result, NIOs happen randomly with largely variable magnitude that is also not predictable. This can be seen clearly from our data. It should be noted that most NIOs exist with background flows varying mostly at much lower frequencies.

Figures 5.1.1 through 5.1.10 are examples of time series plots of the north and east components of velocity at the very first bin of the velocity profile, usually a point closet to the surface of the ocean. These are randomly selected and they are representative of the variations of velocity components of the entire dataset. Despite the wide range of variability, there are some common features that are worth mentioning. The first of which is the variation at roughly daily period. This daily period variation appears to be quite irregular in terms of the magnitude. This appears to be mainly due to a larger irregular magnitude low-frequency variation which can be a result of eddies, Loop Current, and other background low frequency circulation. Another feature is that the north and east components have similar magnitudes. Clearly, this indicates that these daily oscillations are inertial oscillations. This can be verified by rotary spectrum analysis (which is presented later). It should also be noted that the NIOs are always excited by an external forcing, whether wind stress, atmospheric pressure gradient, or a water pressure gradient due to waves or other distances. The data suggests that the disturbances may be quite frequent; otherwise, the oscillations wouldn't be so common. It is not the objective of this project to identify each of these external forcing for all the NIOs in this dataset. Nor is it realistic to do that. However, we can verify and examine NIOs after major hurricanes, which is the subject of the next sub-section. In 2005, there were several tropical storms and hurricanes, see Figure 5.1.11 They are (1) Tropical Storm Arlene, which landed on Jun 11 at 5:00PM, at 30.7 N, 87.4 W, (2) Tropical Storm Cindy which made landfall on July 5 2005 at 11:00PM, at 29.0 N, 90.1 W, 60; (3) Hurricane Dennis which made landfall at 5 PM on July 10 at 30.8 N, 87.2 W; (4) Hurricane Emily, which made landfall at 5 PM on July 20 at 24.7 N, 97.2 W; (5) Hurricane Katrina, which made landfall at 5 AM on Aug 29 at 28.8 N, 89.6 W, and (6) Hurricane Rita which made landfall at 5 AM on Sep 24 at 29.9 N, 93.9 W. These landfall times correspond to Julian days of 2005 (Jan. 1 is Day 1) of 162, 186, 191, 202, 241, and 267, respectively. When the tropical storms come close to a station, the record may show increased NIOs. For example, Figure 5.1.3 shows that when Tropical Storm Cindy passed, before Day 186, NIO started to increase. Figure 5.1.8 shows that when Hurricane Rita passed, before Day 267, NIO started to increase as well. These NIOs appear to be mixed with the normal condition NIOs and did not seem to show much difference except some increase in oscillation magnitude. More detailed examination for stations with stronger response will be given later.

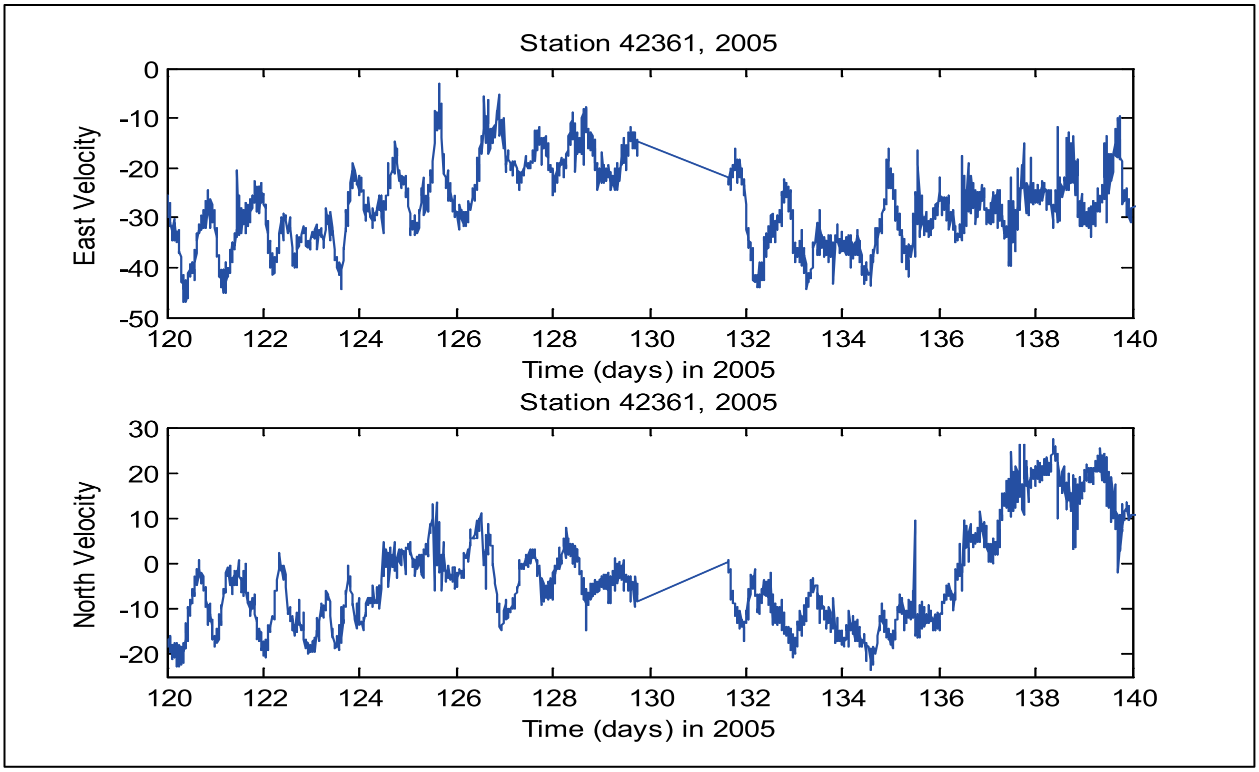

Figure 5.1.1. Time series of the eastward (upper panel) and northward (lower panel) velocity components in 2005 at Station 42361. Horizontal axis is Julian time with day 1 equals January 1, 2005.

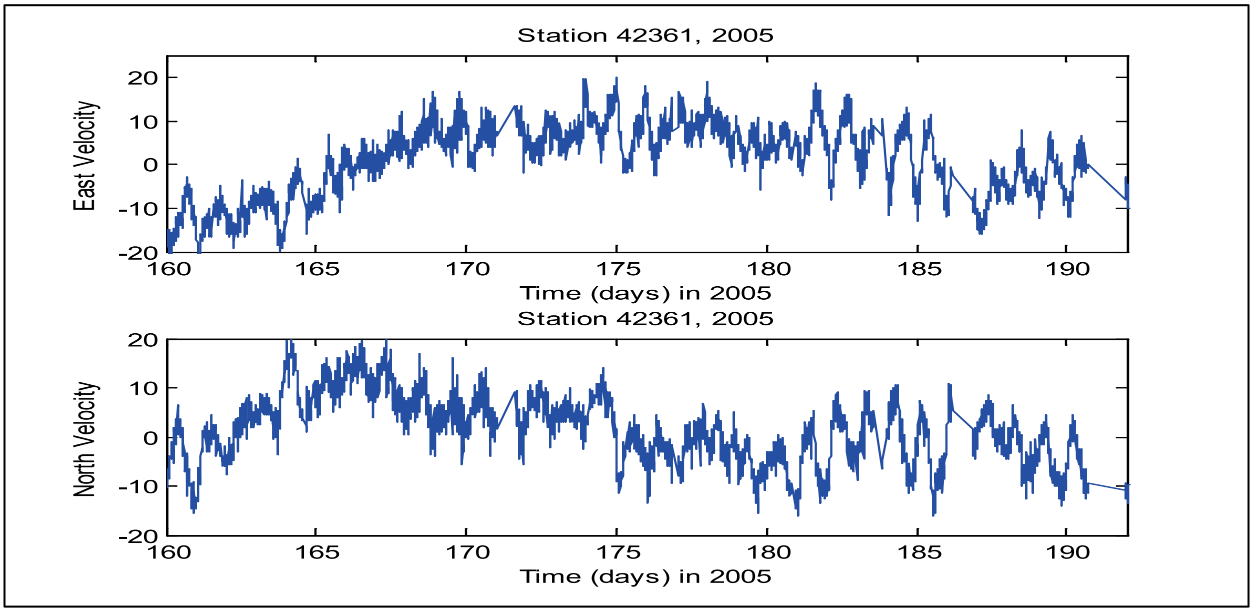

Figure 5.1.2. Time series of the eastward (upper panel) and northward (lower panel) velocity components in 2005 at Station 42361. Horizontal axis is Julian time with day 1 equals January 1, 2005.

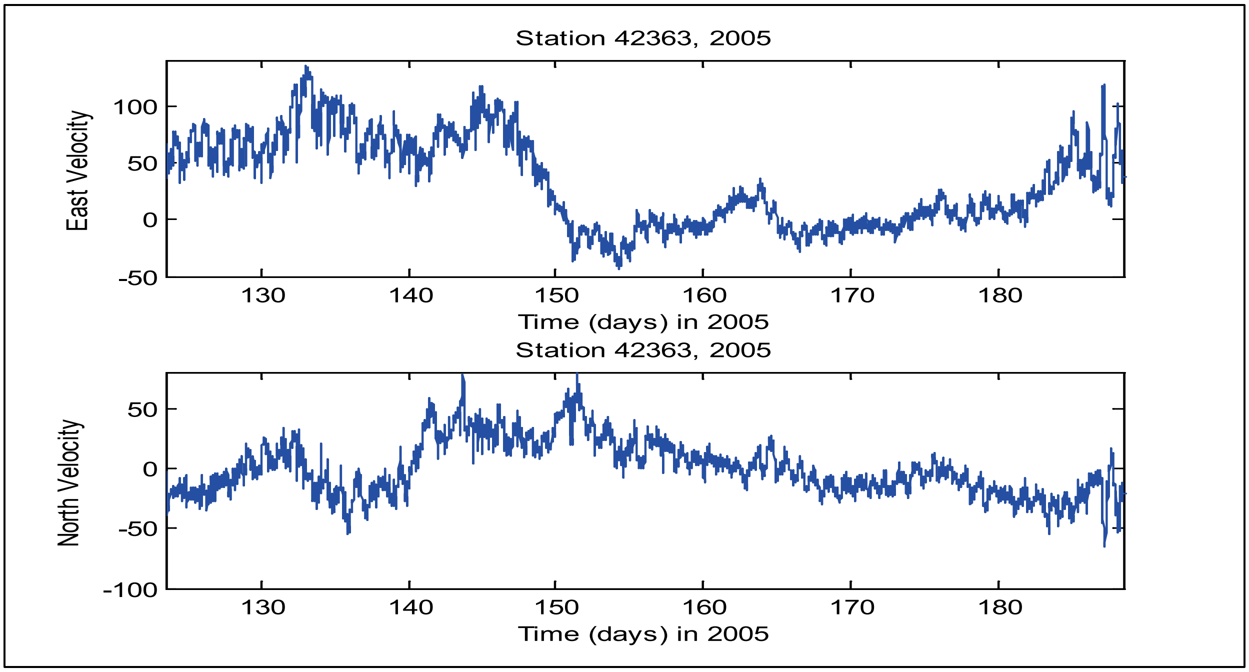

Figure 5.1.3. Time series of the eastward (upper panel) and northward (lower panel) velocity components in 2005 at Station 42363. Horizontal axis is Julian time with day 1 equals January 1, 2005.

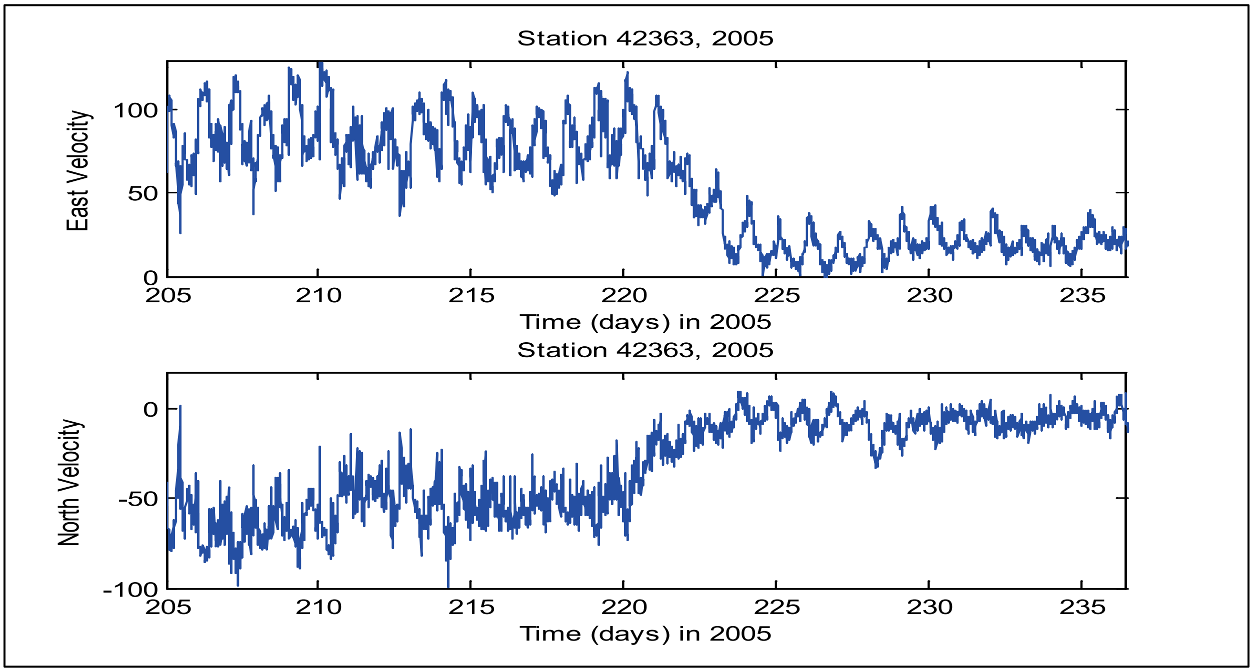

Figure 5.1.4. Time series of the eastward (upper panel) and northward (lower panel) velocity components in 2005 at Station 42363. Horizontal axis is Julian time with day 1 equals January 1, 2005.

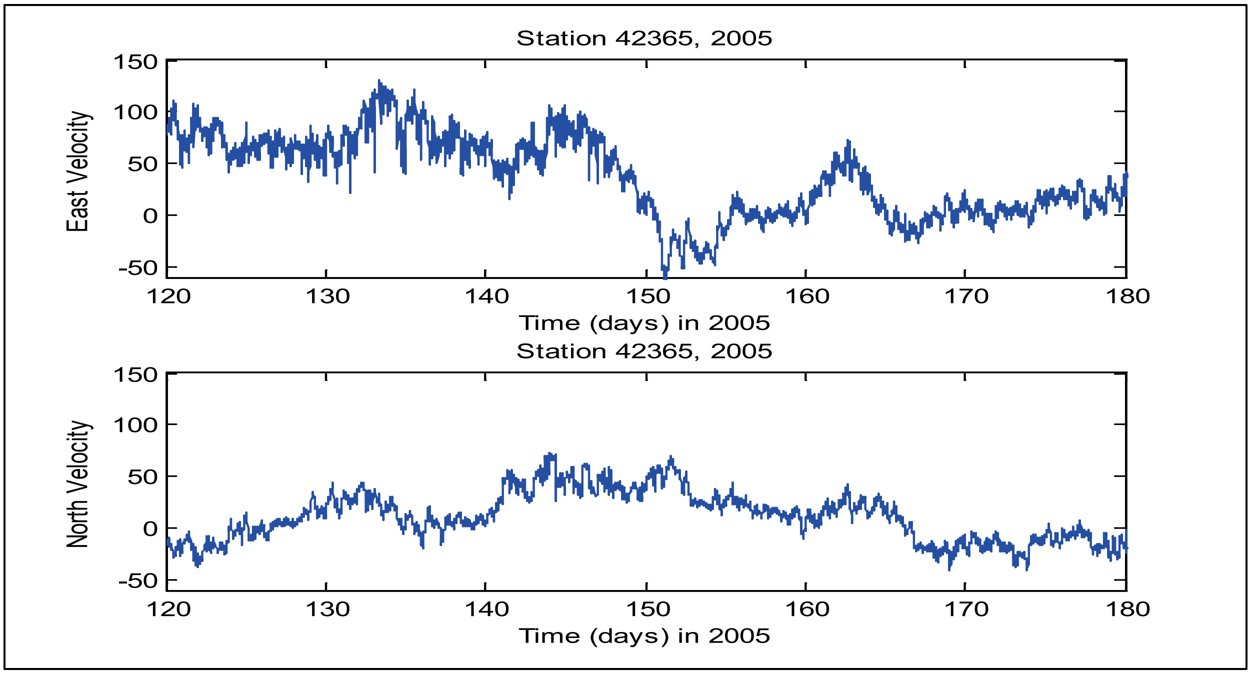

Figure 5.1.5. Time series of the eastward (upper panel) and northward (lower panel) velocity components in 2005 at Station 42365. Horizontal axis is Julian time with day 1 equals January 1, 2005.

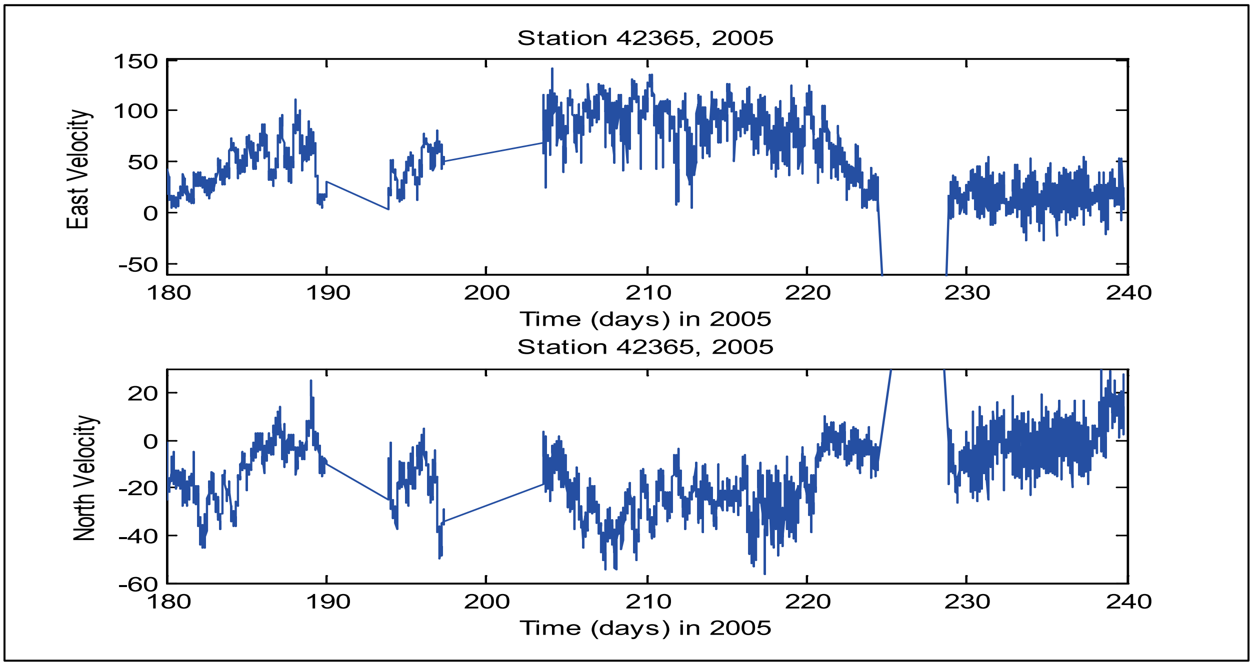

Figure 5.1.6. Time series of the eastward (upper panel) and northward (lower panel) velocity components in 2005 at Station 42365. Horizontal axis is Julian time with day 1 equals January 1, 2005.

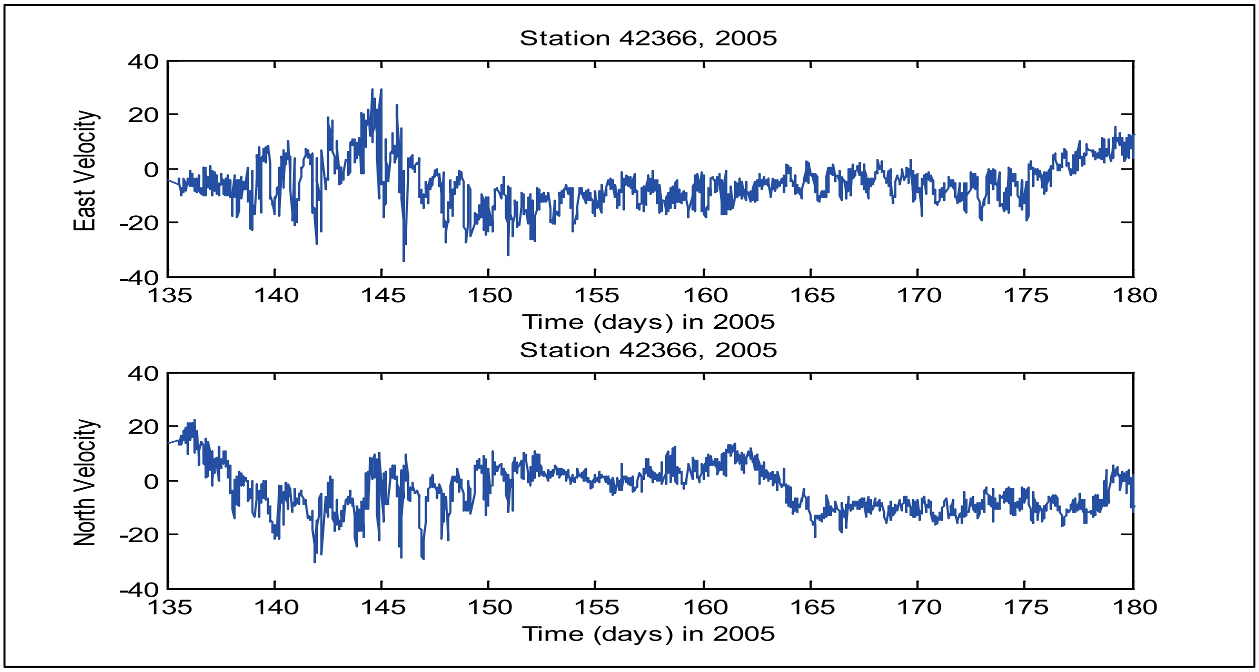

Figure 5.1.7. Time series of the eastward (upper panel) and northward (lower panel) velocity components in 2005 at Station 42366. Horizontal axis is Julian time with day 1 equals January 1, 2005.

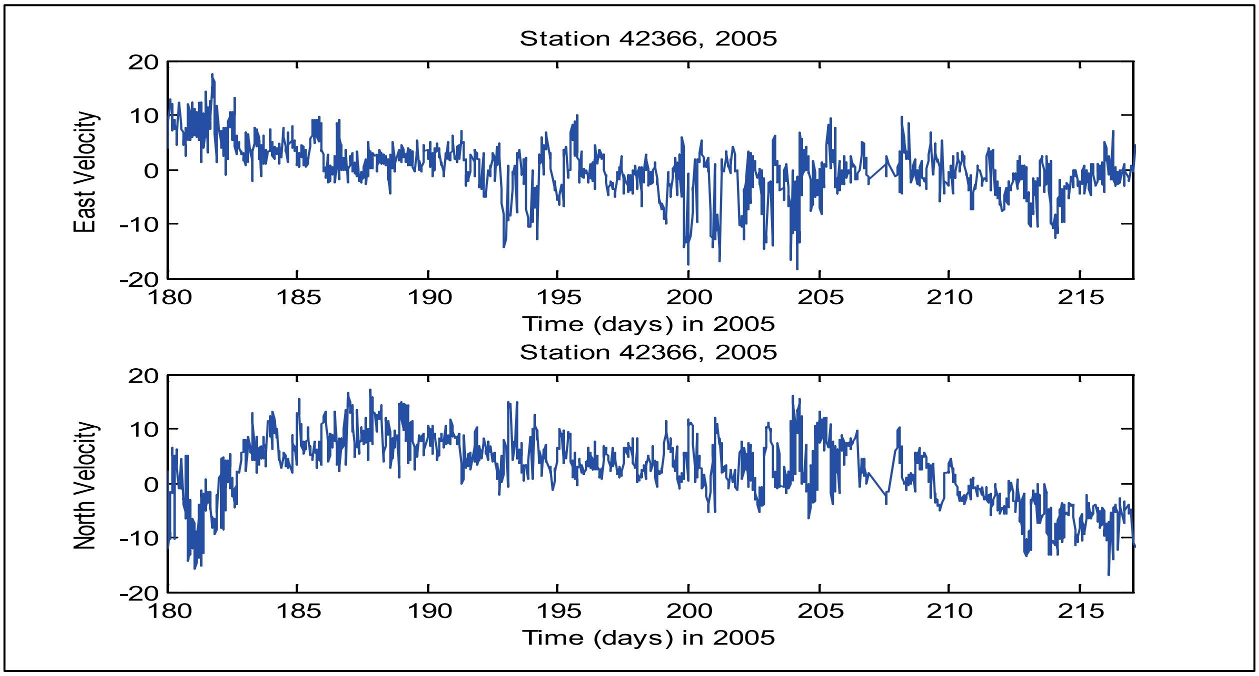

Figure 5.1.8. Time series of the eastward (upper panel) and northward (lower panel) velocity components in 2005 at Station 42366. Horizontal axis is Julian time with day 1 equals January 1, 2005.

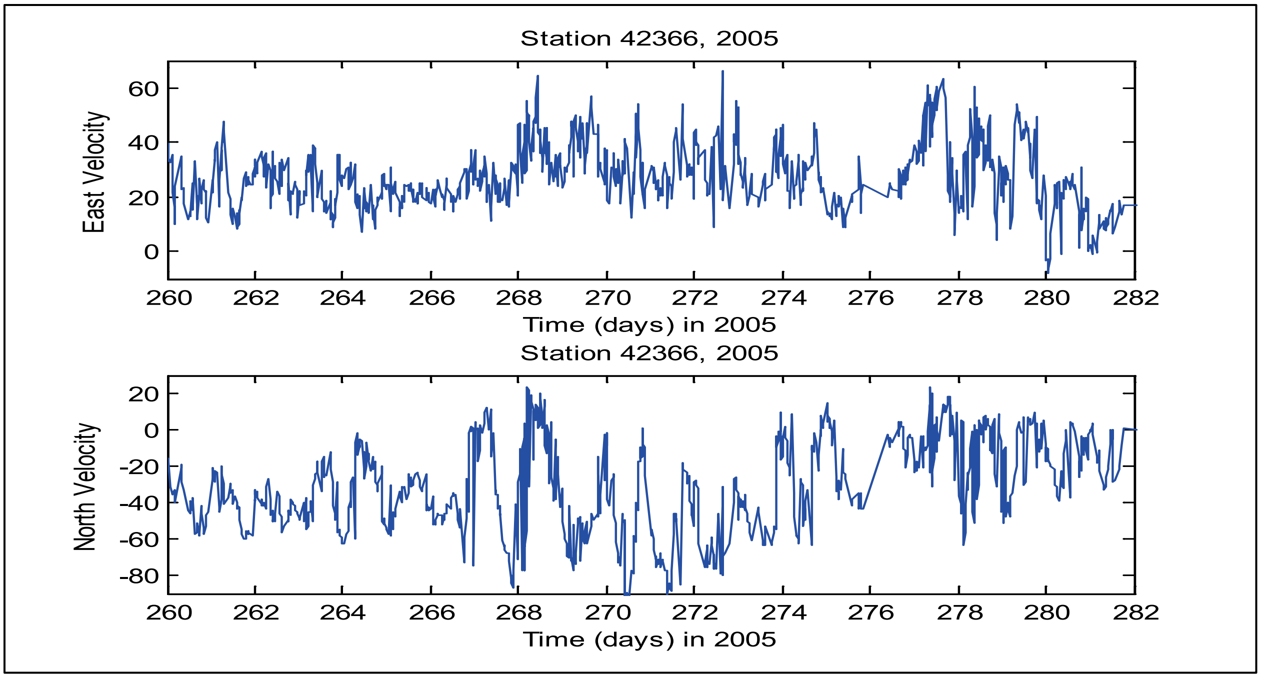

Figure 5.1.9. Time series of the eastward (upper panel) and northward (lower panel) velocity components in 2005 at Station 42361. Horizontal axis is Julian time with day 1 equals January 1, 2005.

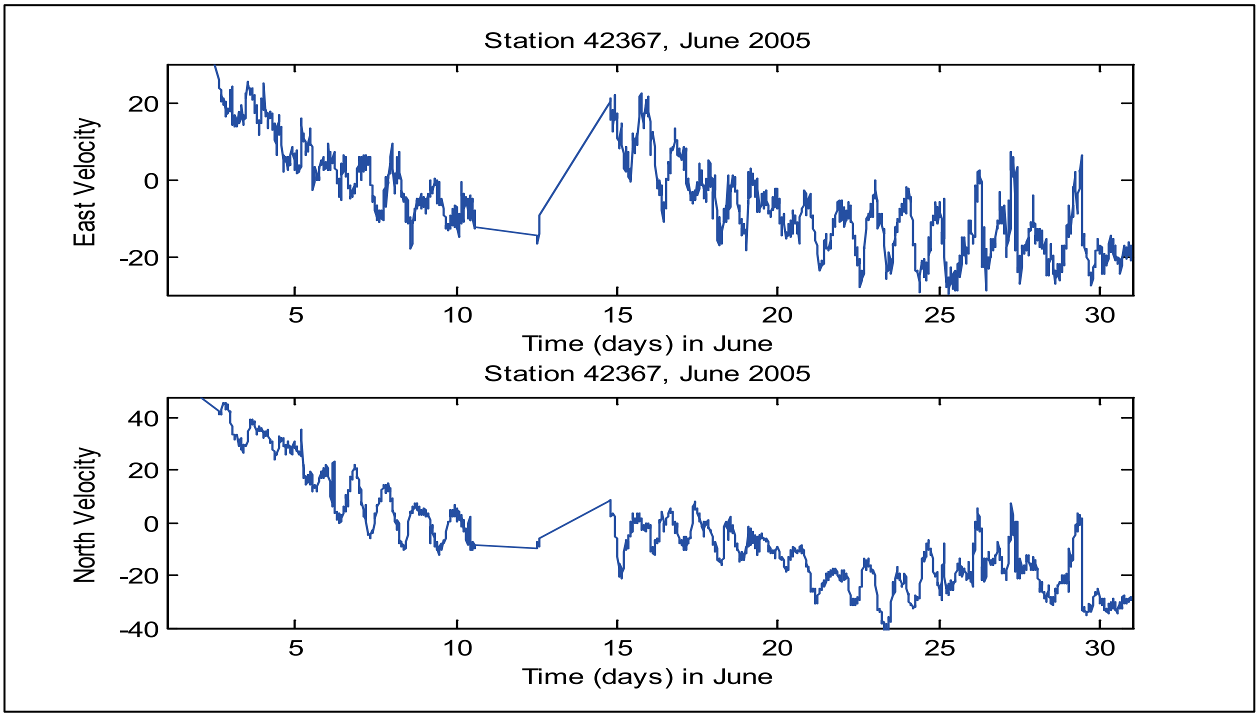

Figure 5.1.10. Time series of the eastward (upper panel) and northward (lower panel) velocity components in 2005 at Station 42367. Horizontal axis is Julian time with day 1 equals January 1, 2005.

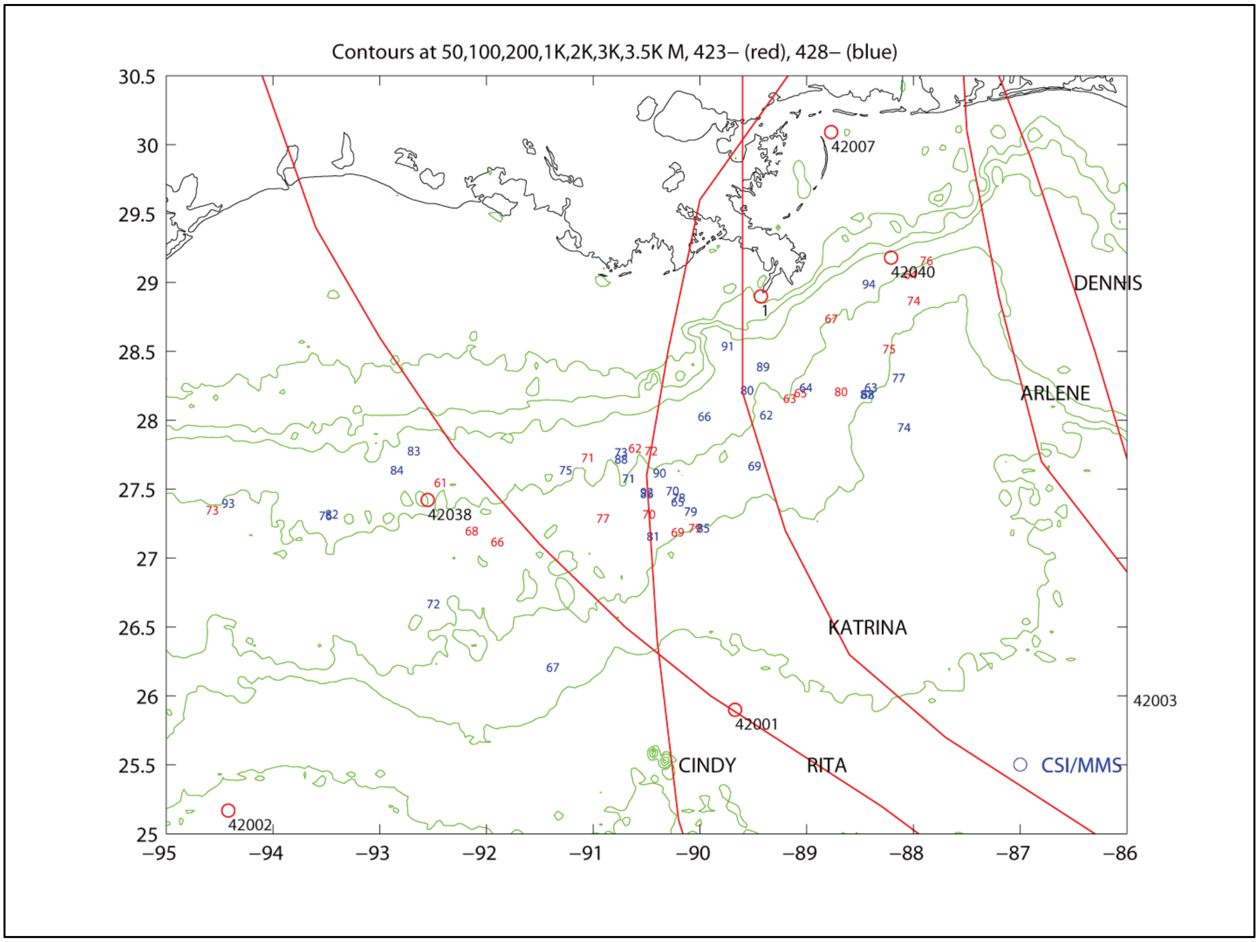

Figure 5.1.11. The 2005 hurricane and tropical storm tracks for (1) Tropical Storm Arlene, (2) Tropical Storm Cindy, (3) Hurricane Dennis, (4) Hurricane Emily, (5) Hurricane Katrina, and (6) Hurricane Rita.

Figures 5.1.12-5.1.40 show some examples of progressive vector diagrams for May 2006. These plots provide a different view point for the NIOs, their temporal (from time to time) and horizontal spatial variability (from station to station), and vertical variations.

Figure 5.1.12 shows progressive vector diagram plot for Station 42361 at various vertical locations in May of 2006. It should be noted that all the “trajectories” start from the origin of the coordinate, i.e. (0, 0) – this makes it easy to identify where the “trajectory” starts and where it is moving. It is clear that the flows at different levels appear to be similar but with some variations such that over time, the “trajectories” are separated. This indicates strong vertical shears and perhaps also layered flows in which different layers behave differently. To better view this, we zoom in and plotted the progressive vector diagram at a few depths for improved resolution (Figure 5.1.13). The top bin was at 51 m below the surface. The next selected bin was at 195 m below the surface, which showed quite similar flow 144 m above but with a reduced magnitude – the flows at the two levels appear to have same directions but with a reduced magnitude downward such that the progressive vectors appear to be rough parallel to each other. The next selected vertical location for the plot was at 355 m below the surface and it shows much different “trajectory”, suggestion that we are looking at a different layer. The last selected vertical location is at 515 m below the surface and had opposite flow directions at times. To further examine how the water particles moved in the top layer, we further zoom in and selected 6 vertical locations about 131 m (Figure 5.1.14). The selected vertical levels are 51, 67, 83, 99, 115, and 131 m, respectively. This gives an amazing picture of vertical variation of flow condition that is roughly consistent with the surface boundary layer Ekman spiral. On top of the long term “trajectories”, it is also equally striking to see the NIOs (in a clockwise direction).

Figure 5.1.15 shows progressive vector diagram plot for Station 42364 at various vertical locations in May of 2006. Again, the flows at different levels appear to be similar for some vertical positions but with some variations such that over time, the “trajectories” are separated. This indicates strong vertical shears and perhaps also layered flows in which different layers behave differently. To better view this, we zoom in and plotted the progressive vector diagram at a few depths to improved resolution (Figure 5.1.16). The top bin was at 51 m below the surface. The next selected bin was at 195 m below the surface. Differences are obvious between the 144 m levels in addition to being with a reduced magnitude downward although the progressive vectors appear to be roughly parallel to each other. The next selected vertical location for the plot was at 355 m below the surface and it shows a similar “trajectory” in direction. The last selected depth was 515 m below the surface and had very different trajectory.

Figure 5.1.17 shows progressive vector diagram plot for Station 42368 at various vertical locations in May of 2006. It is clear that the flows at different levels appear to be similar but with some variations such that over time, the “trajectories” are separated. This again indicates some vertical shears and perhaps also layered flows in which different layers behave differently. To better view this, we zoom in and plotted the progressive vector at a few depths to improved resolution (Figure 5.1.18). The top bin was at 51 m below the surface. The next selected bin was at 67 m below the surface, which showed quite similar flow. The next levels are 83, 99, 115, and 131 m below the surface, respectively. This again gives an amazing picture of vertical variation of flow condition that is roughly consistent with the surface boundary layer Ekman spiral. On top of the long term “trajectories”, it is also equally striking to see the NIOs (in a clockwise direction). These features are remarkably similar to those shown earlier in Figures 5.1.12 and 5.1.13 for Station 42361. By consulting the locations of these stations, we know that they are very close geographically (about 50 km apart), so is no surprise that the vertical structure of the flow is similar.

Figure 5.1.19 shows progressive vector diagram plot for Station 42375 at various vertical locations in May of 2006. It is clear that the flows at different levels appear to be very similar but with a decrease of flow magnitude with depth such that over time, the “trajectories” are separated. This indicates strong vertical shears and but no apparent layered flows such that different layers behave differently (e.g. with opposite flow directions, which does not appear here). To better view this, we zoom in and plotted the progressive vector at a few depths to improved resolution (Figure 5.1.20). The top bin was at 48.1 m below the surface. The next selected bin was at 192.1 m below the surface, which showed similar flow more than 140 m above but with a reduced magnitude – the flows at the two levels appear to have same directions but with a reduced magnitude downward such that the progressive vectors appear to be rough parallel to each other. The next selected vertical location for the plot was at 352.1 m below the surface and it still shows similar “trajectory”, suggesting that we are still looking at the same layer. The last selected vertical location is at 512.1 m below the surface and still has the same flow directions for the entire time period. The overall flow is toward northeast first and then turn southeast, with the entire top water column (surface to 500 m). It is interesting to note that the flow at different levels was first quite uniform and then strong shear showed during the latter portion of the data.

Figure 5.1.21 shows progressive vector diagram plot for Station 42863 at various vertical locations in May of 2006. Again, the flows at different levels appear to be very similar with some indication of a decrease of flow magnitude with depth. Over time, the “trajectories” are separated. The overall flow seemed to be mostly eastward first and then turned to the northwest. To better show this, we zoom in and plotted the progressive vectors at selected depths to improved resolution (Figure 5.1.22). The top bin was at 73.3 m below the surface. The next selected bin was at 361.3 m below the surface. The next selected vertical location for the plot was at 681.3 m below the surface. The last selected vertical location is at 1001.3 m below the surface. Again, and indeed, this is amazing to have the entire water column to move together. This suggests that the motion is probably not local wind-driven. It may have been a result of much larger scale atmospheric forcing or large scale oceanic process (Loop Current and eddies) or the oscillation within the Gulf of Mexico. These are speculations not even hypothesis but more analysis is needed for a holistic picture of the underlining dynamics.

Figure 5.1.23 shows progressive vector diagram plot for Station 42865 at various vertical locations in May of 2006. It is clear that the flows at different levels appear to be very similar but with a decrease of flow magnitude with depth such that over time, the “trajectories” are separated. However, they kept being parallel to each other. This indicates vertical shears but with no apparent layered of flows going in different directions. To better view this, we zoomed in and plotted the progressive vectors at a few selected depths to improved resolution (Figure 5.1.24). The top bin was at 67 m below the surface. The next selected bin was at 355 m below the surface. The last selected vertical location is at 675 m below the surface and still has the same flow directions for the entire time period. No NIOs are obvious for this station during this time period.

Figure 5.1.25 shows progressive vector diagram plot for Station 42869 at various vertical locations in May of 2006. The flows at different levels appear to be similar and with a decrease of flow magnitude. Again, as at the previous station, they kept being parallel to each other. This indicates vertical shears but with no apparent layered of flows going in different directions. The decrease of the flows, as in other cases, must be due to frictional effect. To better view this, we zoomed in and plotted the progressive vectors at a few selected depths to improved resolution (Figure 5.1.26). The top bin was at 52.9 m below the surface. The next selected bin was at 196.9 m below the surface. The last two selected vertical locations are at 356.9 and 516.9 m below the surface, respectively. Overall, they are very consistent (perhaps the most vertically consistent flow example) along the same flow directions for the entire time period. The flow throughout the entire 500 water column was moving northeastward, and then westward, then northward, and final westward again. All levels exhibit this same pattern. No NIOs are obvious for the entire record at this station during this time period.

Figure 5.1.27 shows progressive vector diagram plot for Station 42873 at various vertical locations in May of 2006. The flows at different levels appear to be mostly similar and with a decrease of flow magnitude. In addition, there seems to be a veering of the flow direction toward the right as the flow decreases during the early period of the record. This is consistent with an upper layer surface boundary layer Ekman Spiral. To better view this plot, we zoom in (Figure 5.1.28). Now we can see quite a lot of NIOs, perhaps throughout the water column. We further selected a few depths and re-plotted the progressive vectors in Figure 5.1.29. Over the 1000 m water column, the flow varied quite a lot – perhaps the most variable flow compared to the other stations discussed earlier.

Figure 5.1.30 shows progressive vector diagram plot for Station 42875 at various vertical locations in May of 2006. The flows at different levels appear to be similar and with a decrease of flow magnitude. In addition, there seems to be a veering of the flow direction toward the right as the flow decreases during the early period of the record. This is consistent with an upper layer surface boundary layer Ekman Spiral. Overall, during the entire the record, the flow is consistent in direction at all levels (all going southeast). To better view this plot, we zoom in (Figure 5.1.31). Now we can see quite a lot of NIOs. We further selected a few vertical locations and re-plotted the progressive vectors in Figure 5.1.32. The top bin was at 57 m below the surface. The next selected bin was at 201 m below the surface. The last two selected vertical locations are at 361 and 521 m below the surface, respectively. No NIOs are obvious for these levels, indicating that the NIOs are all at deeper levels.

Figure 5.1.33 shows a progressive vector diagram plot for Station 42880 at various vertical locations in May of 2006. The flows at different levels appear to be bi-modal – one goes toward the east, one to the west, northwest or north. In addition, there are no observable NIOs. To better view this plot, we zoomed in (Figure 5.1.34). Now we can see the NIOs clearly but the mean flows have opposite directions. We further selected a few depths and re-plotted the progressive vectors in Figure 5.1.35. The top bin was at 62.5 m below the surface. The next selected bin was at 206.5 m below the surface, which shows consistent direction with the upper level for the early time but much smaller magnitude. The last two selected vertical locations are at 366.5 and 526.5 m below the surface, respectively. Some NIOs are observable. The flow directions of the last two layers are about 90 degrees different from the first two levels. Down to the last level, the selected levels still do not show the flow opposite of the upper levels, i.e. the westward flow levels must be at lower levels. So in this case, we see three entirely different vertical layers: the upper layer, middle layer, and bottom layer, all going in different directions.

Figure 5.1.36 shows progressive vector diagram plot for Station 42881 at various vertical locations in May of 2006. The flows at different levels appear to be very similar and with a decrease of flow magnitude. In addition, there is a veering of the flow direction toward the right as the flow decreases during the early period of the record. This is consistent with an upper layer surface boundary layer Ekman Spiral. During the latter portion of the record, the flows are consistent in directions such that they mostly go to the east and then southeast. To better view this plot, we zoom in (Figure 5.1.37). There is no obvious NIOs except at what appears to be lower levels (where flow magnitude reduced so the lines shorter). We further selected a few vertical locations and re-plotted the progressive vectors in Figure 5.1.38. The top bin was at 72.9 m below the surface. The next selected bin was at 360.9 m below the surface. It can be seen that the flow direction has a right veering tendency. This right veering and decrease in magnitude extended toward the lower layer as well at 680.9 and 1000.9 m, respectively.

Figure 5.1.39 shows a zoomed in progressive vector diagram plot for Station 42884 at various vertical locations in May of 2006. The flows at different levels appear to be quite persistent, mostly in the east and west directions. To better view this plot, we selected a few depths and zoomed in (Figure 5.1.40). The top bin was at 42.7 m below the surface. The next selected bin was at 186.7 m below the surface. The last two selected depths were at 346.7 and 506.7 m below the surface. The near-surface flow was southward all the time, while the rest moved westward first and then eastward and then northward.

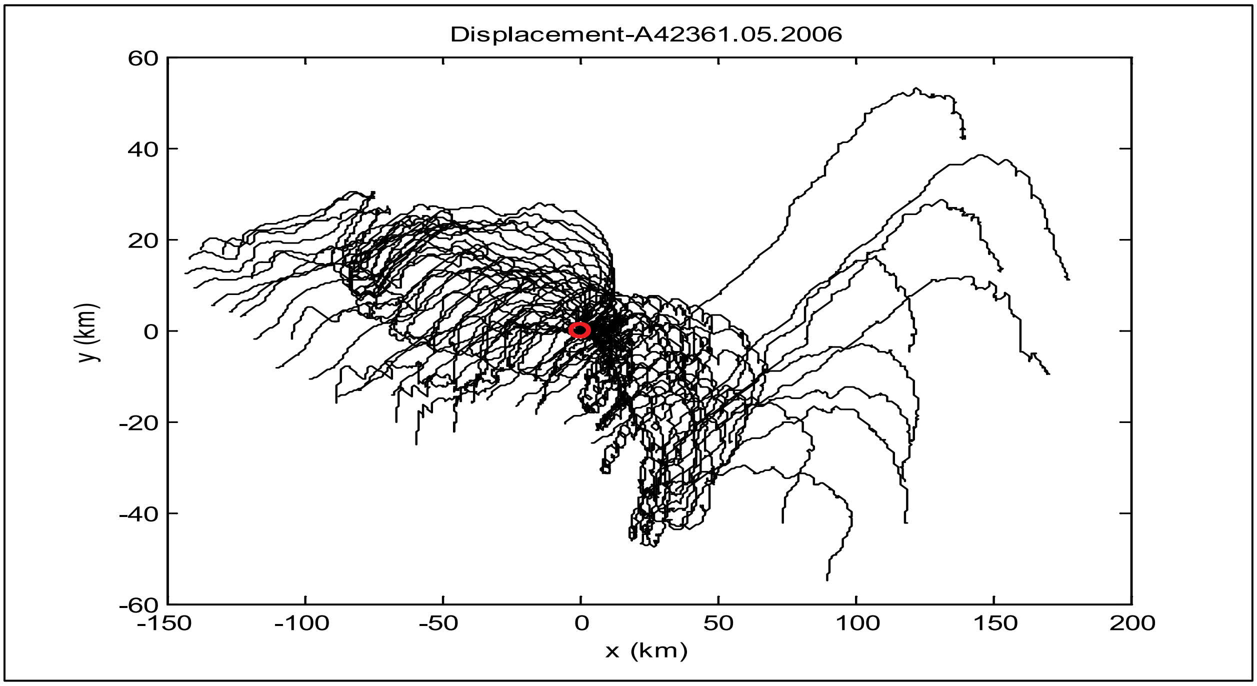

Figure 5.1.12. Progressive vector diagram at different depths for May 2006 at Station 42361.

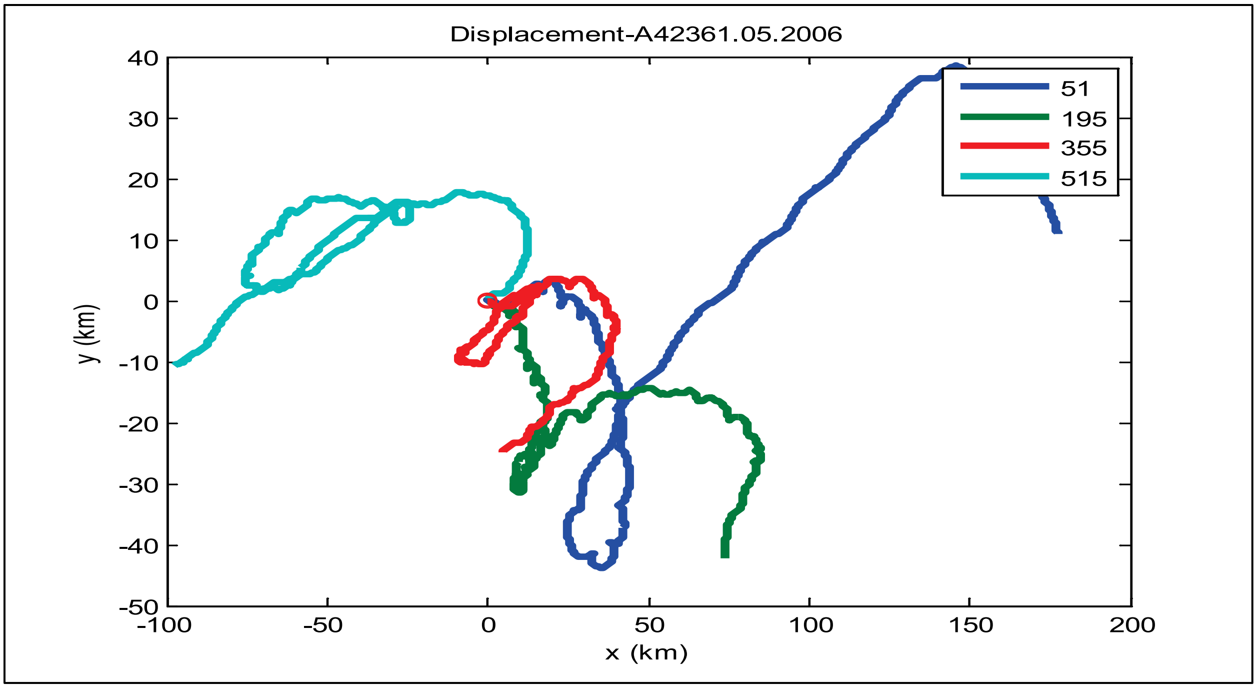

Figure 5.1.13. Progressive vector diagram at Station 42361 for different depths in May 2006.

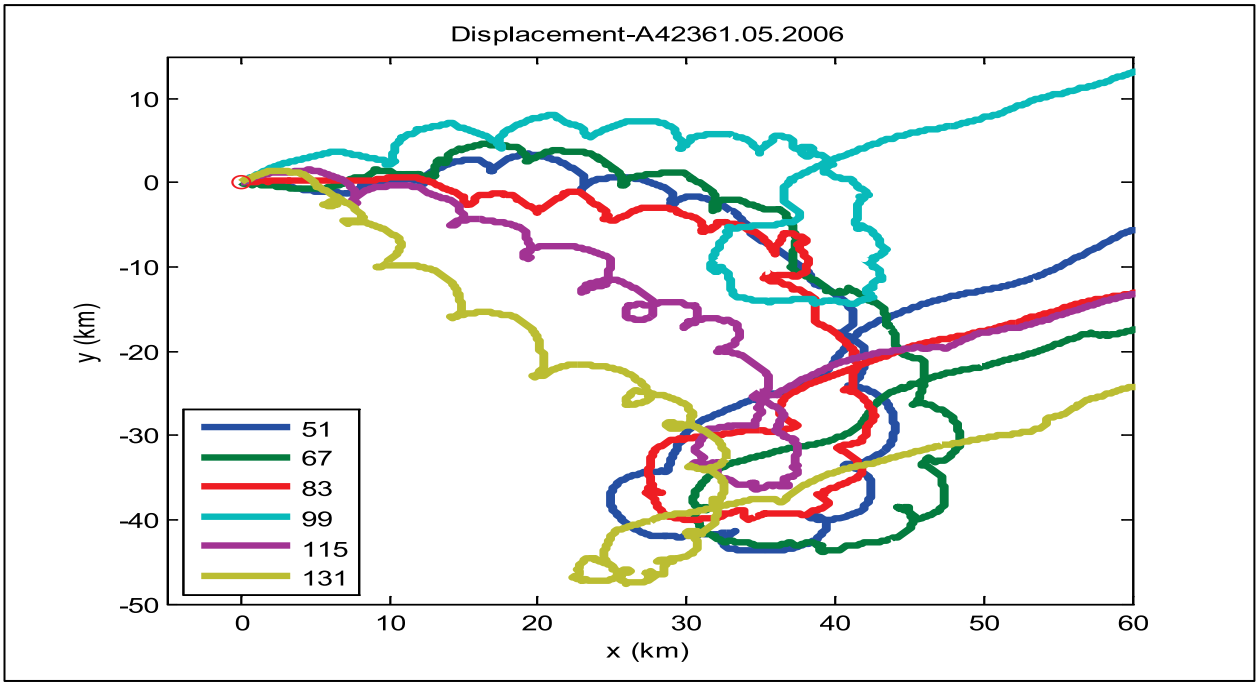

Figure 5.1.14. Progressive vector diagram at Station 42361 focusing in shallow depths in May 2006.

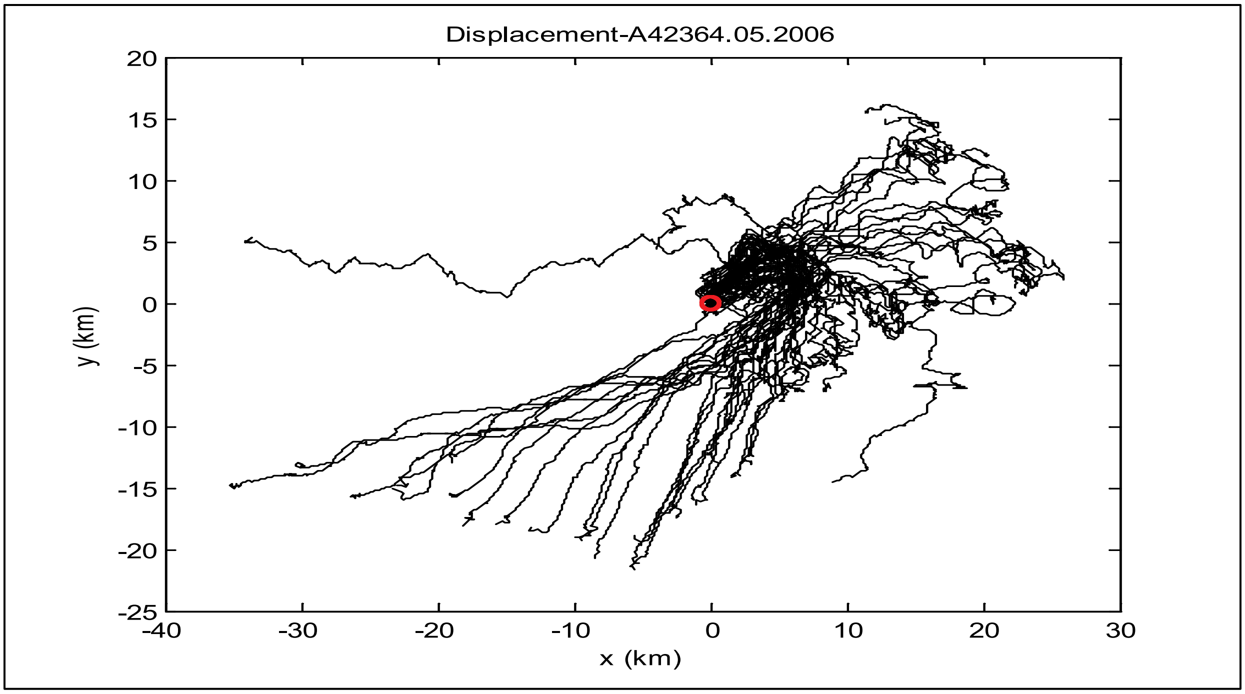

Figure 5.1.15. Progressive vector diagram at different depths for May 2006 at Station 42364.

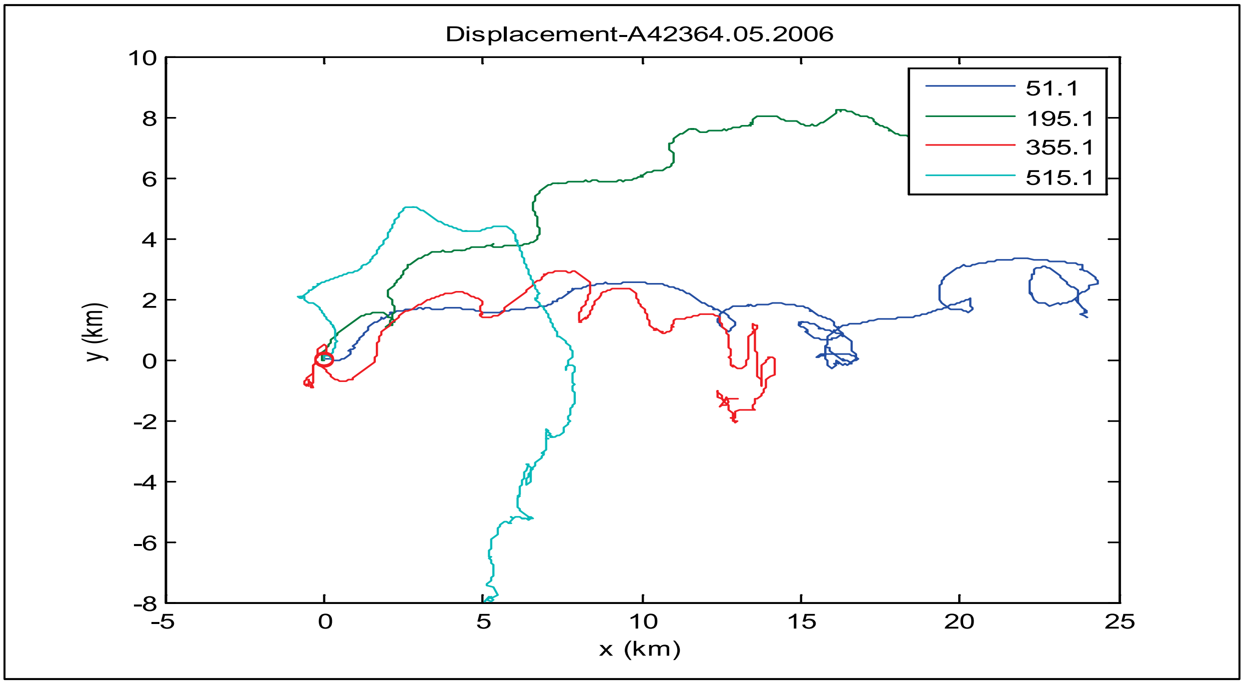

Figure 5.1.16. Progressive vector diagram at Station 42364 for different depths in May 2006.

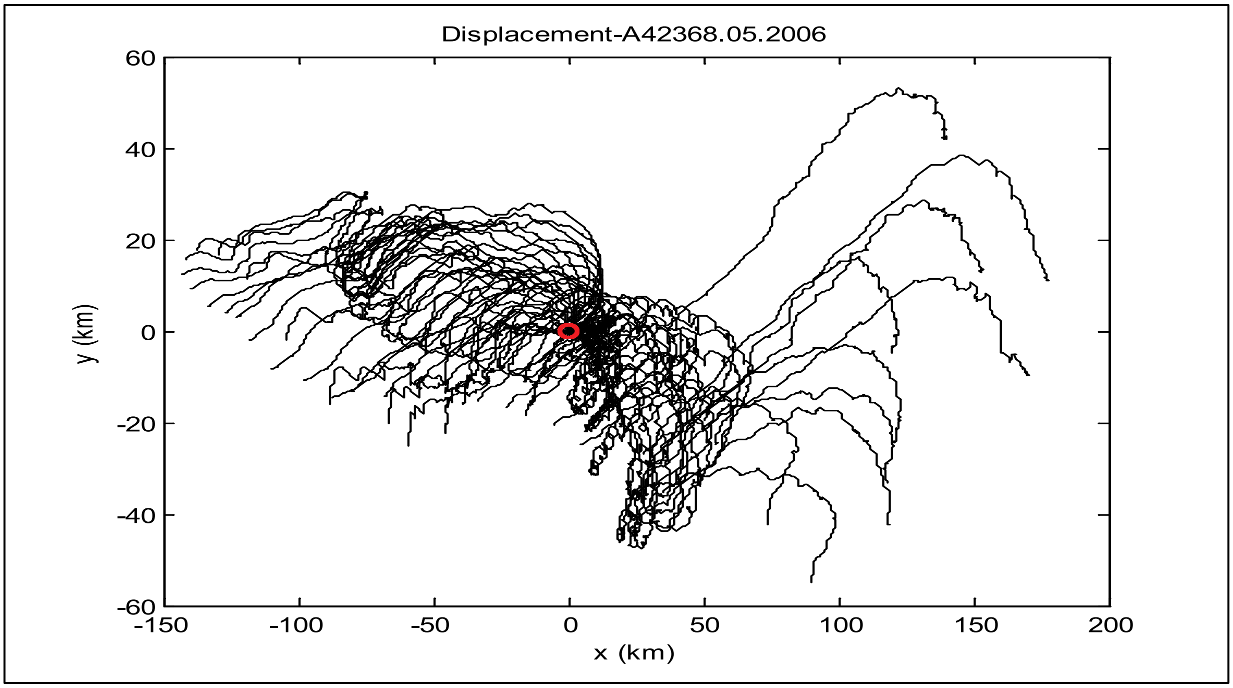

Figure 5.1.17. Progressive vector diagram at different depths for May 2006 at Station 42368.

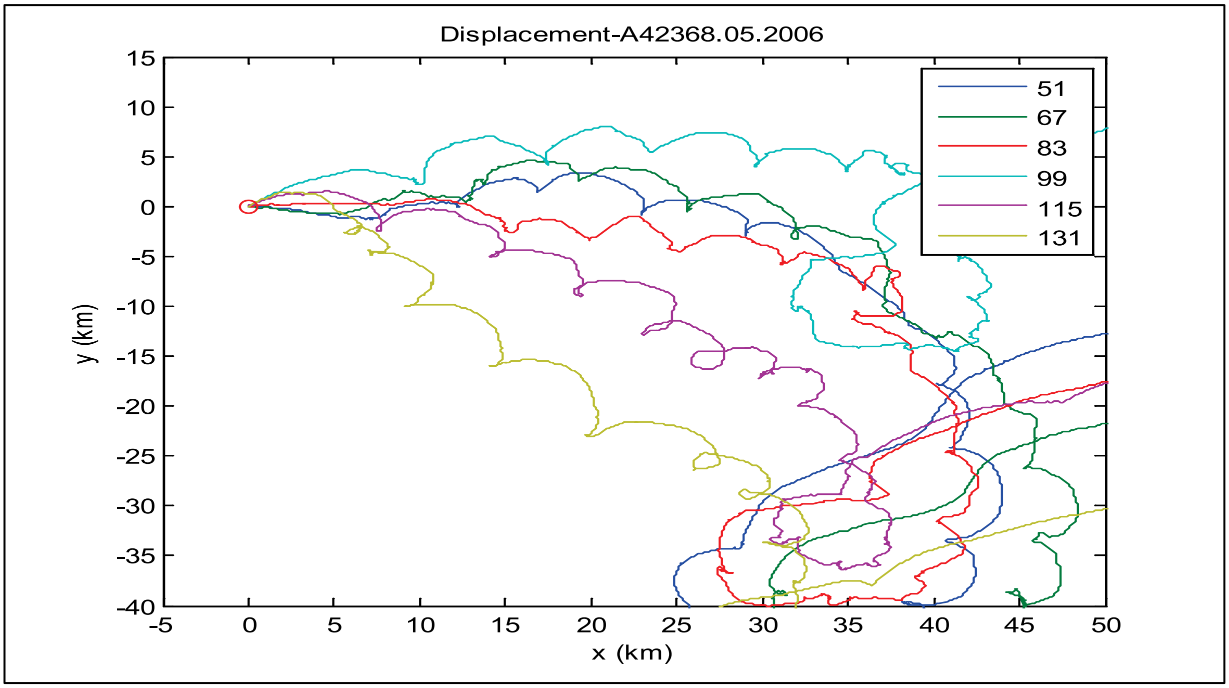

Figure 5.1.18. Progressive vector diagram at selected depths for May 2006 at Station 42368.

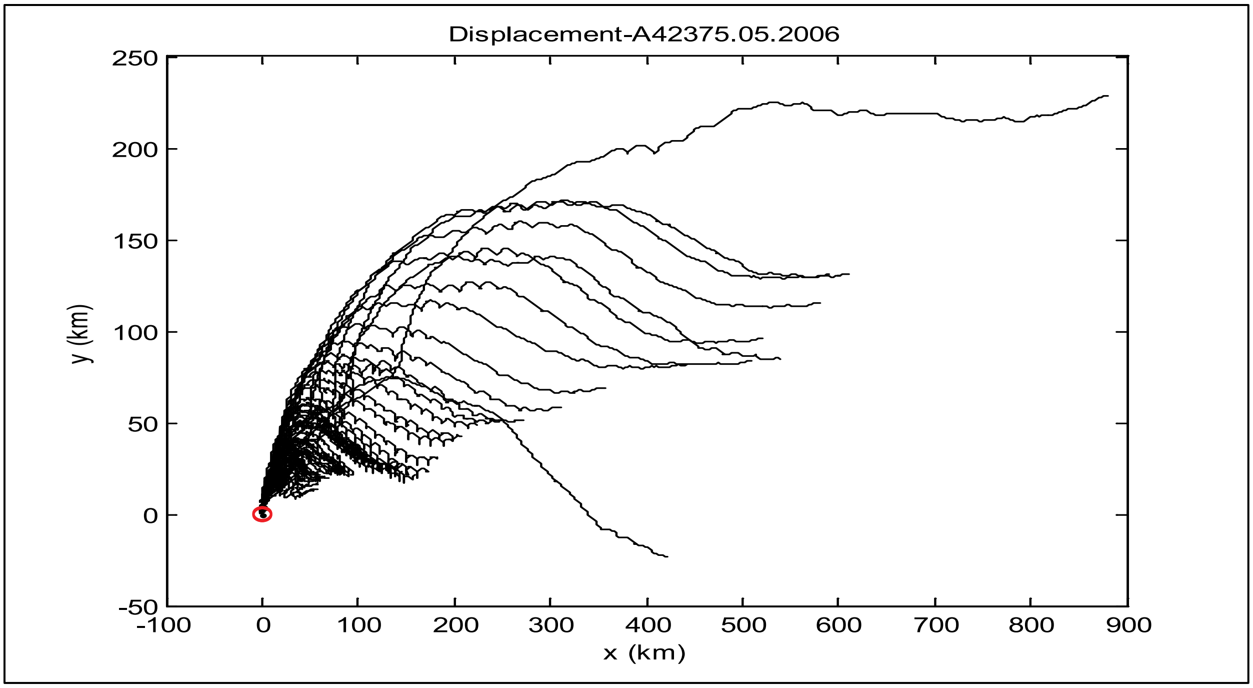

Figure 5.1.19. Progressive vector diagram at different depths for May 2006 at Station 42375.

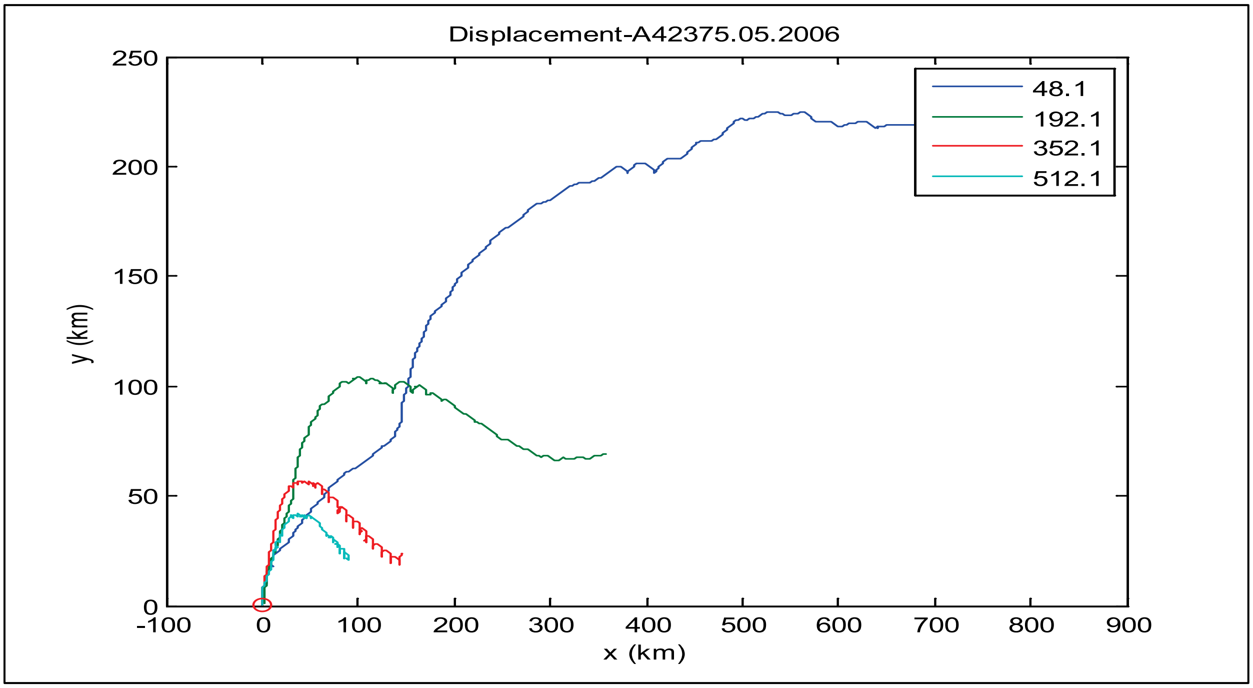

Figure 5.1.20. Progressive vector diagram at selected depths for May 2006 at Station 42375.

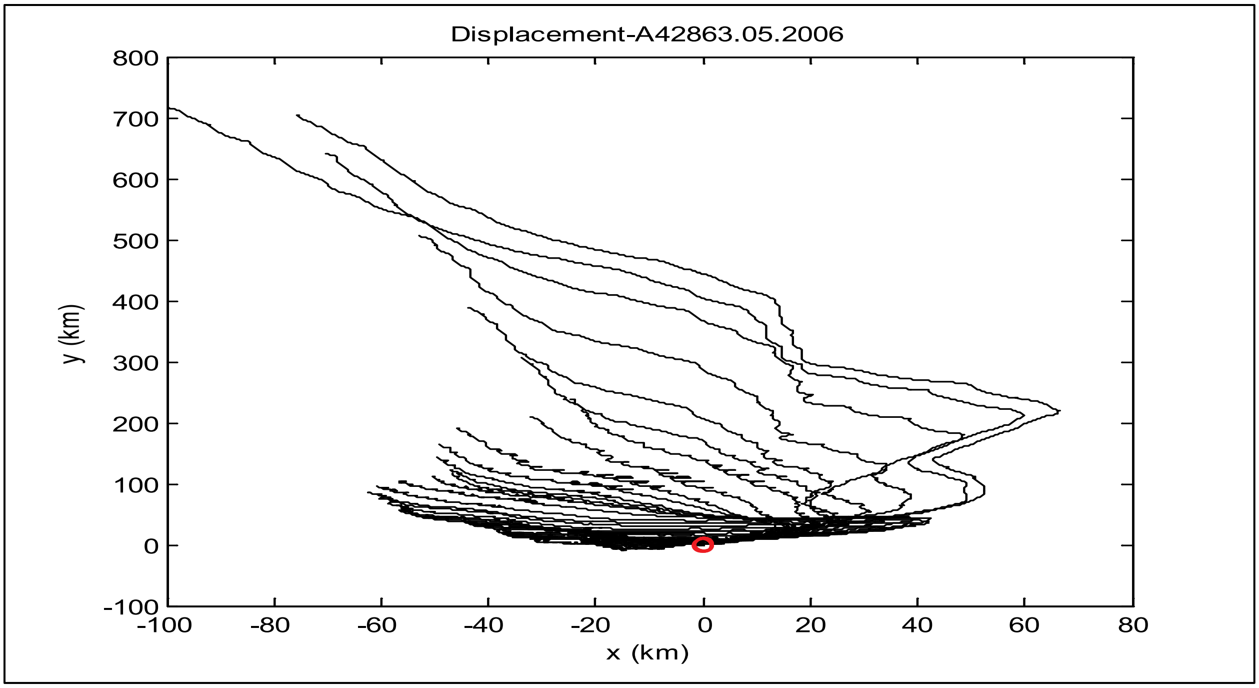

Figure 5.1.21. Progressive vector diagram at different depths for May 2006 at Station 42863.

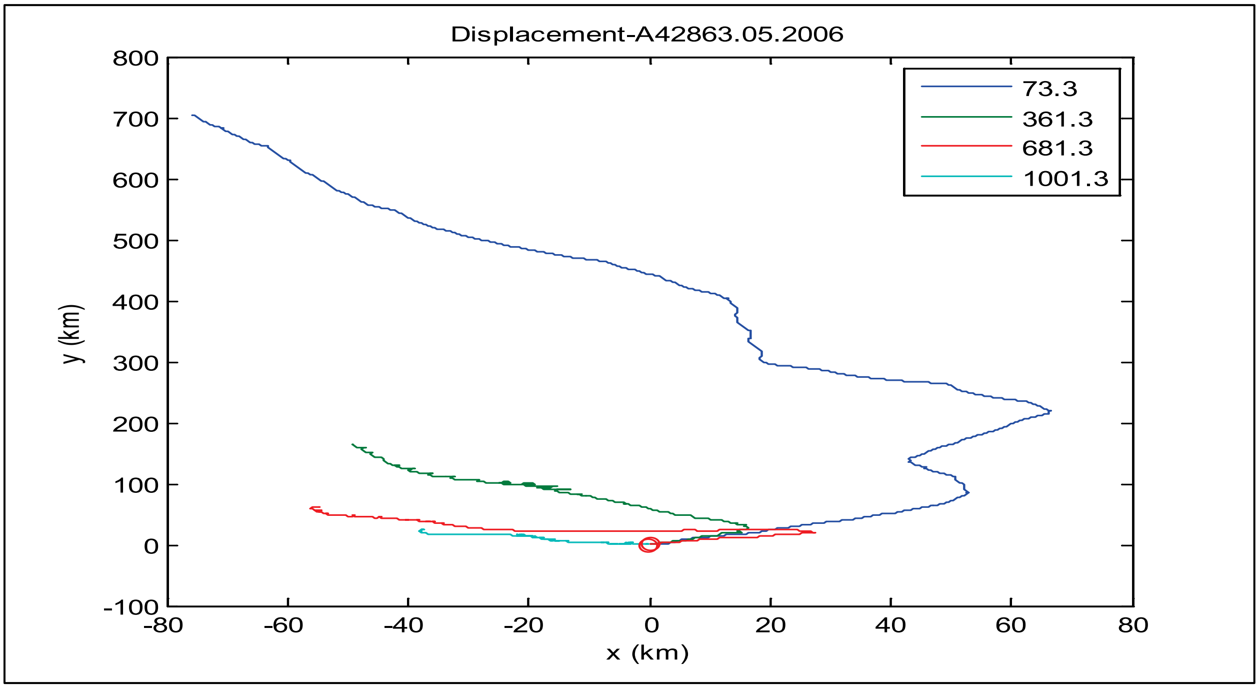

Figure 5.1.22. Progressive vector diagram at selected depths at Station 42863 in May 2006 zooming in to show the NIOs.

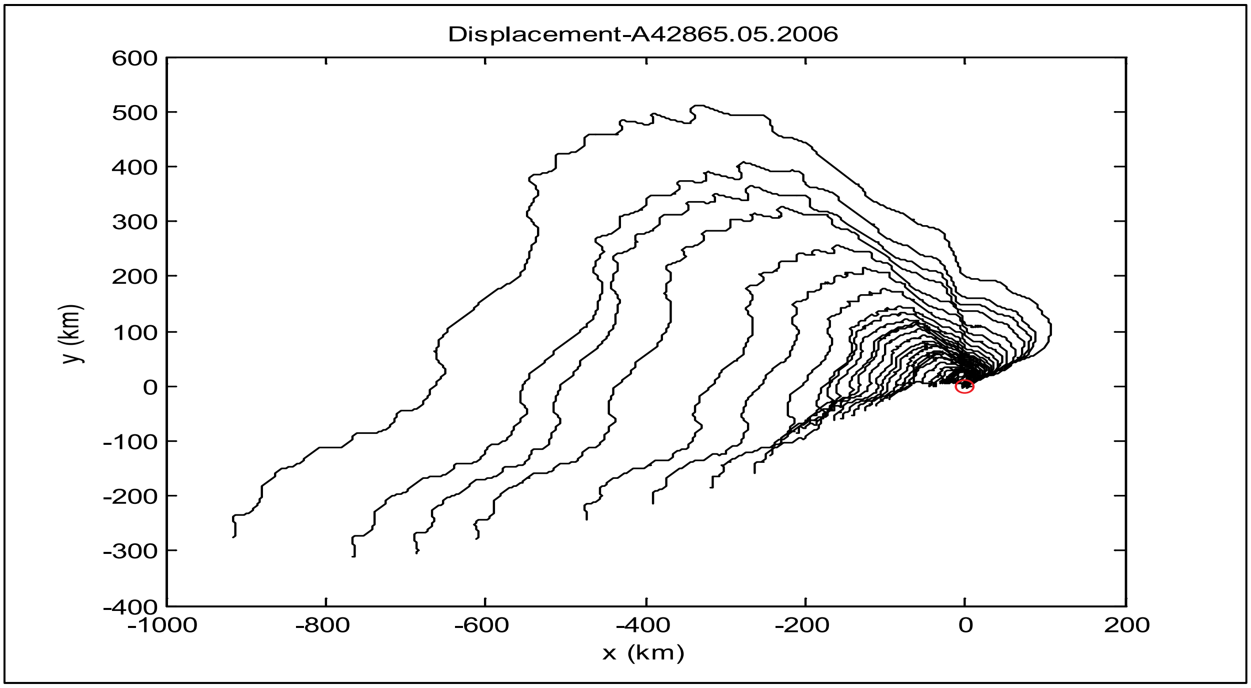

Figure 5.1.23. Progressive vector diagram at different depths for May 2006 at Station 42865.

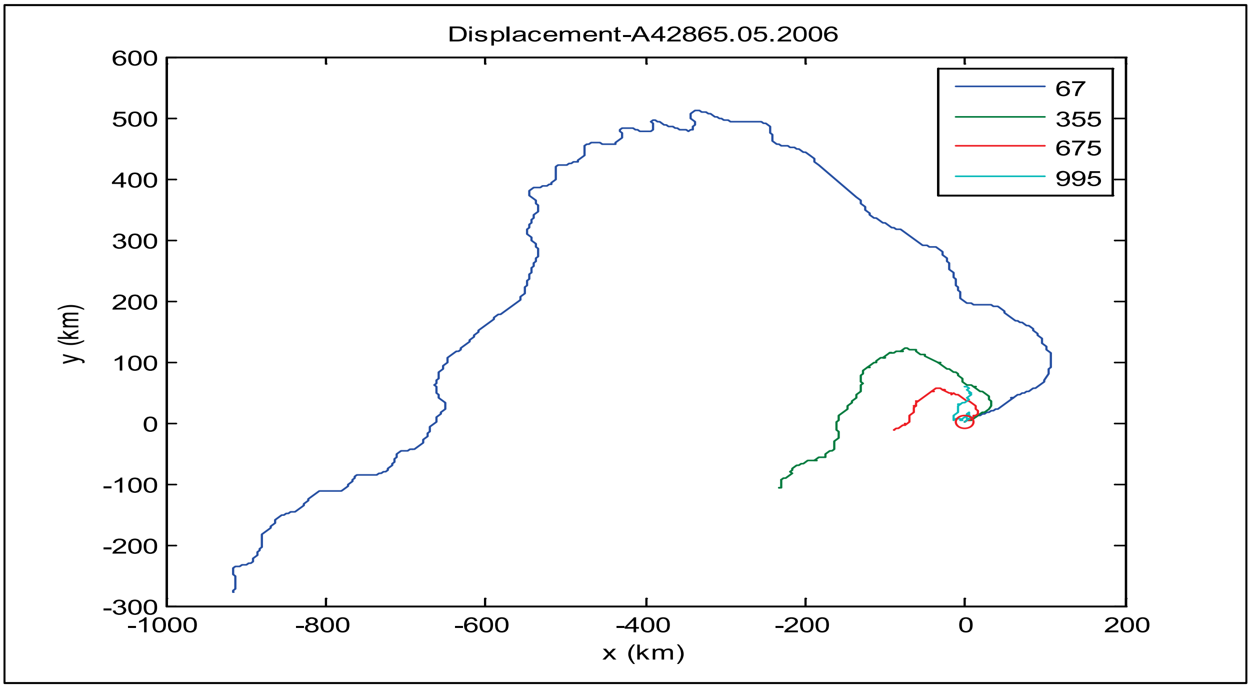

Figure 5.1.24. Progressive vector diagram at selected depths for May 2006 at Station 42865 zooming to show NIO.

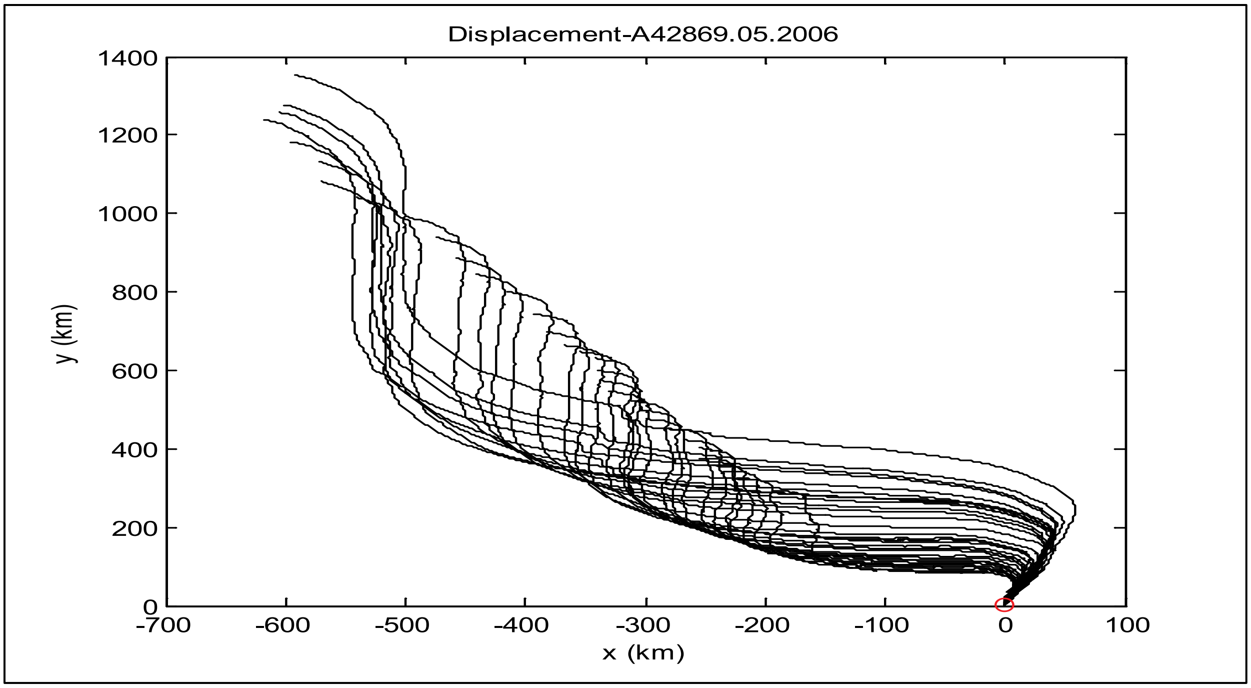

Figure 5.1.25. Progressive vector diagram at different depths for May 2006 at Station 42869.

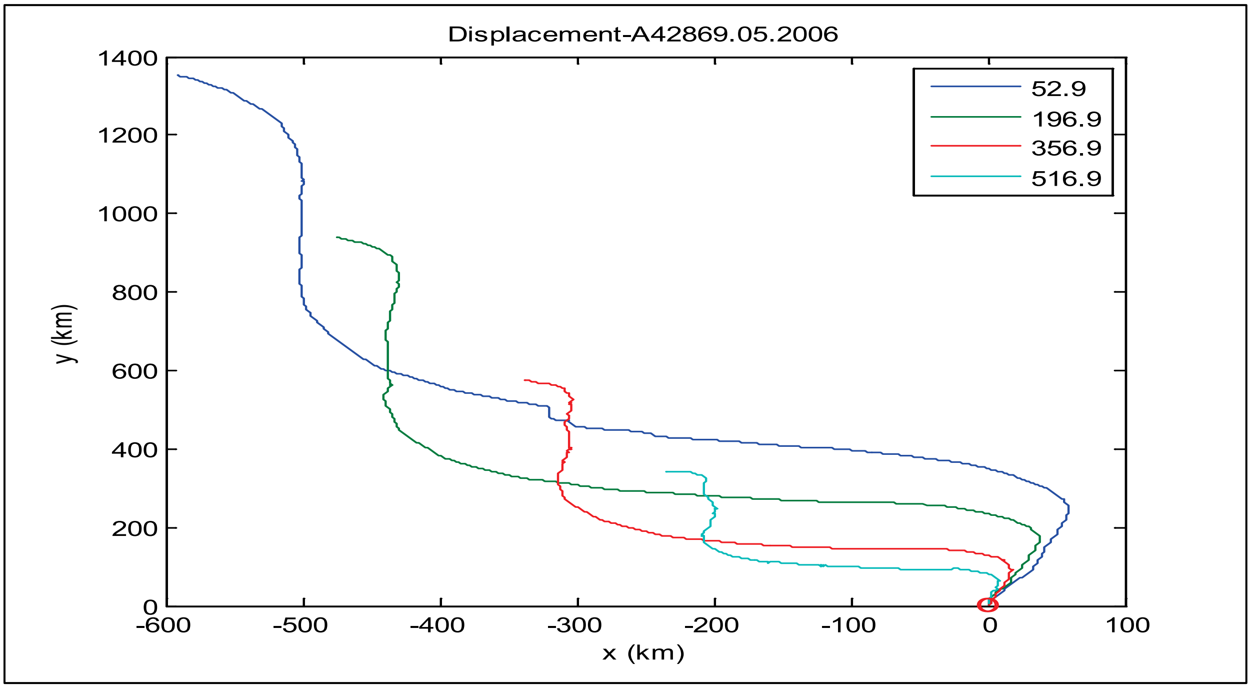

Figure 5.1.26. Progressive vector diagram at selected depths for May 2006 at Station 42869 zooming to show NIO.

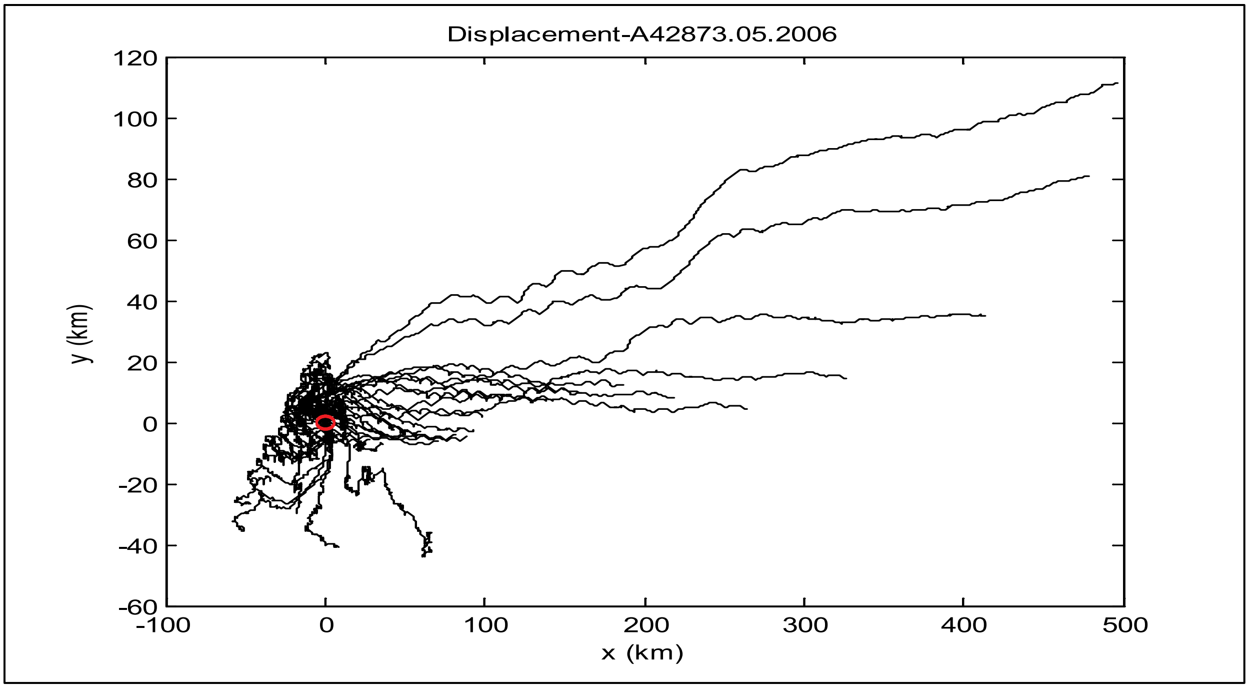

Figure 5.1.27. Progressive vector diagram at different depths for May 2006 at Station 42873.

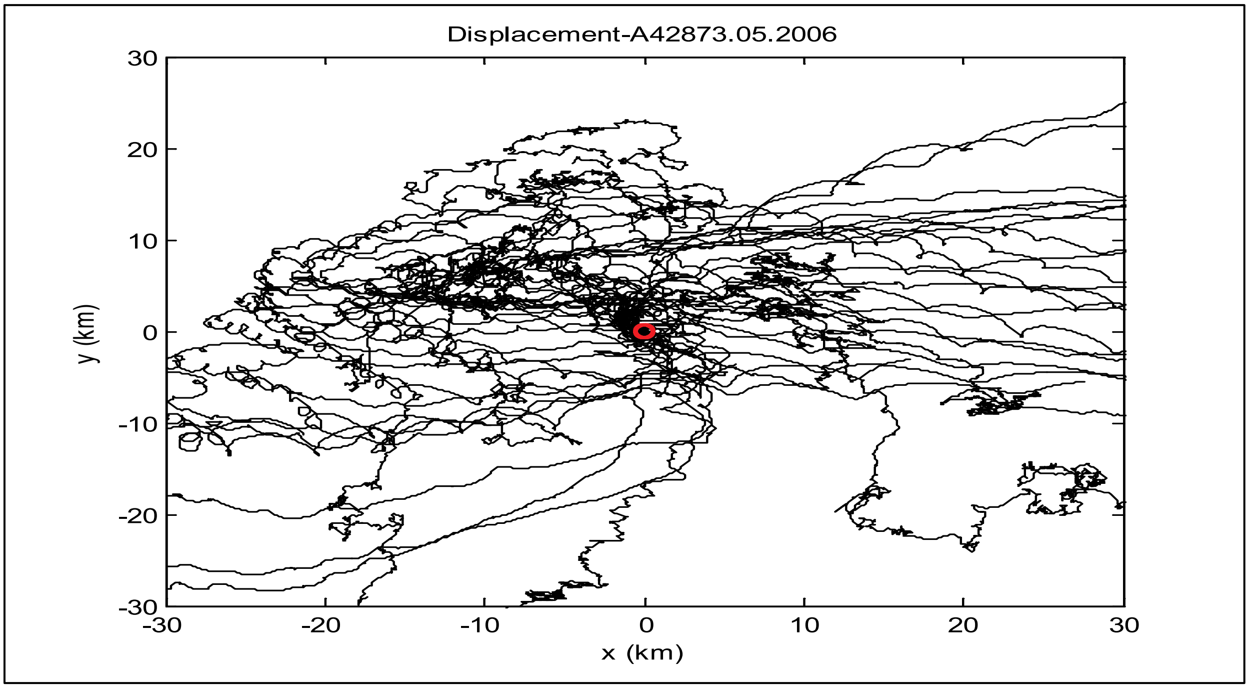

Figure 5.1.28. Progressive vector diagram enlarged at different depths for May 2006 at Station 42873.

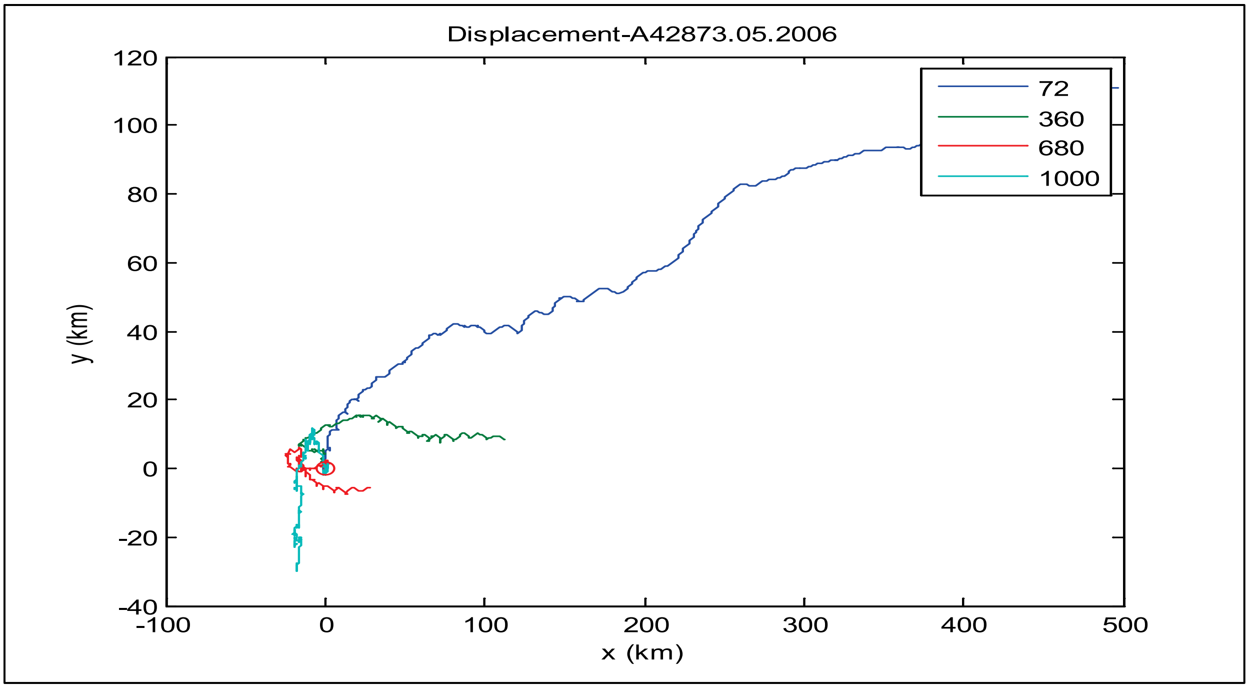

Figure 5.1.29. Progressive vector diagram at selected depths for May 2006 at Station 42873 zooming to show NIO.

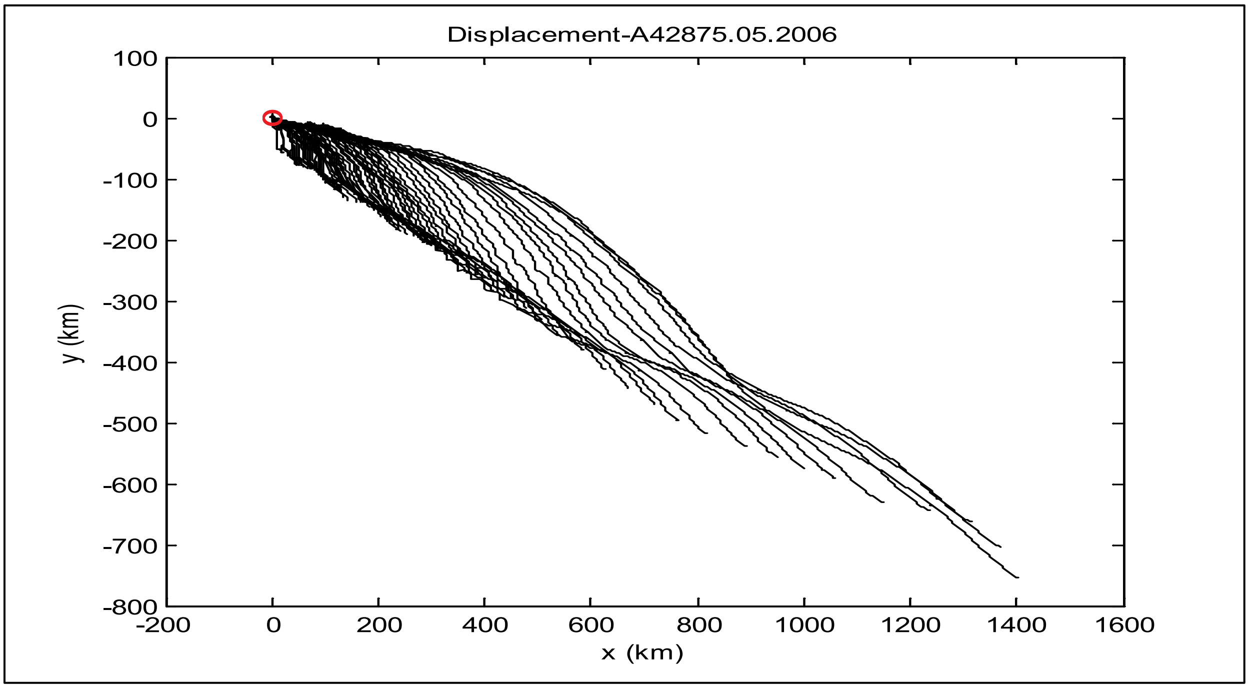

Figure 5.1.30. Progressive vector diagram at different depths for May 2006 at Station 42875.

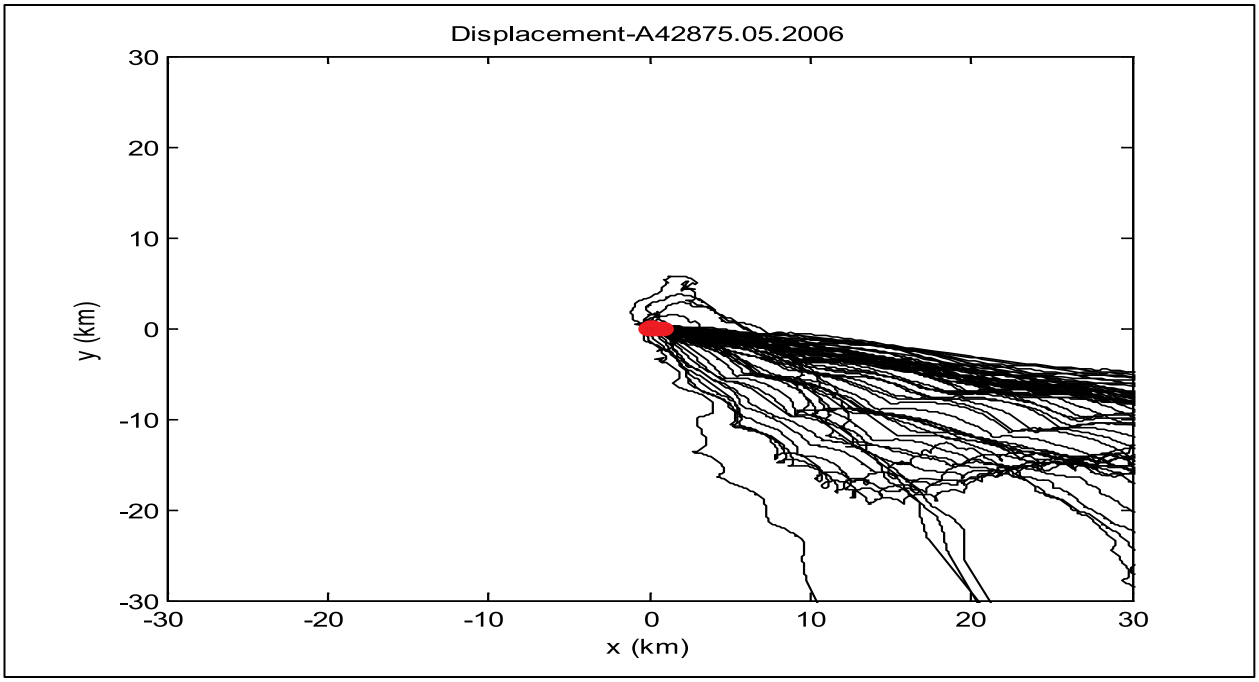

Figure 5.1.31. Enlarged progressive vector diagram at different depths for May 2006 at Station 42875.

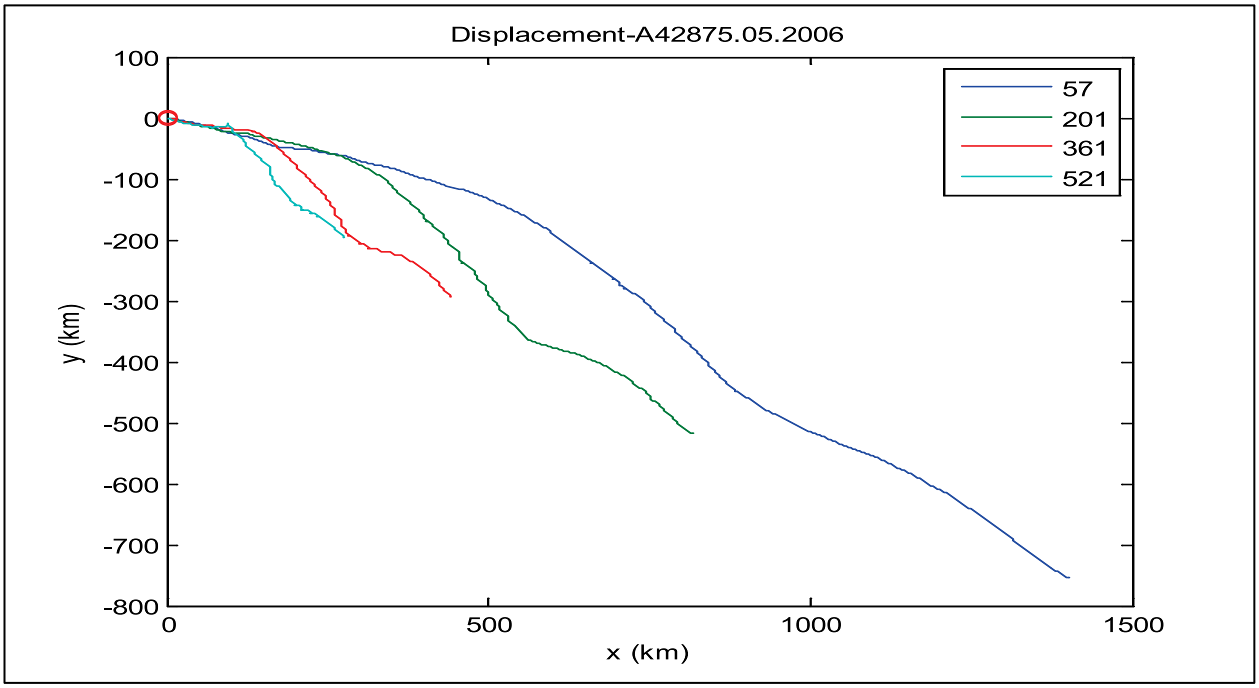

Figure 5.1.32. Progressive vector diagram at selected depths for May 2006 at Station 42875, showing the NIOs.

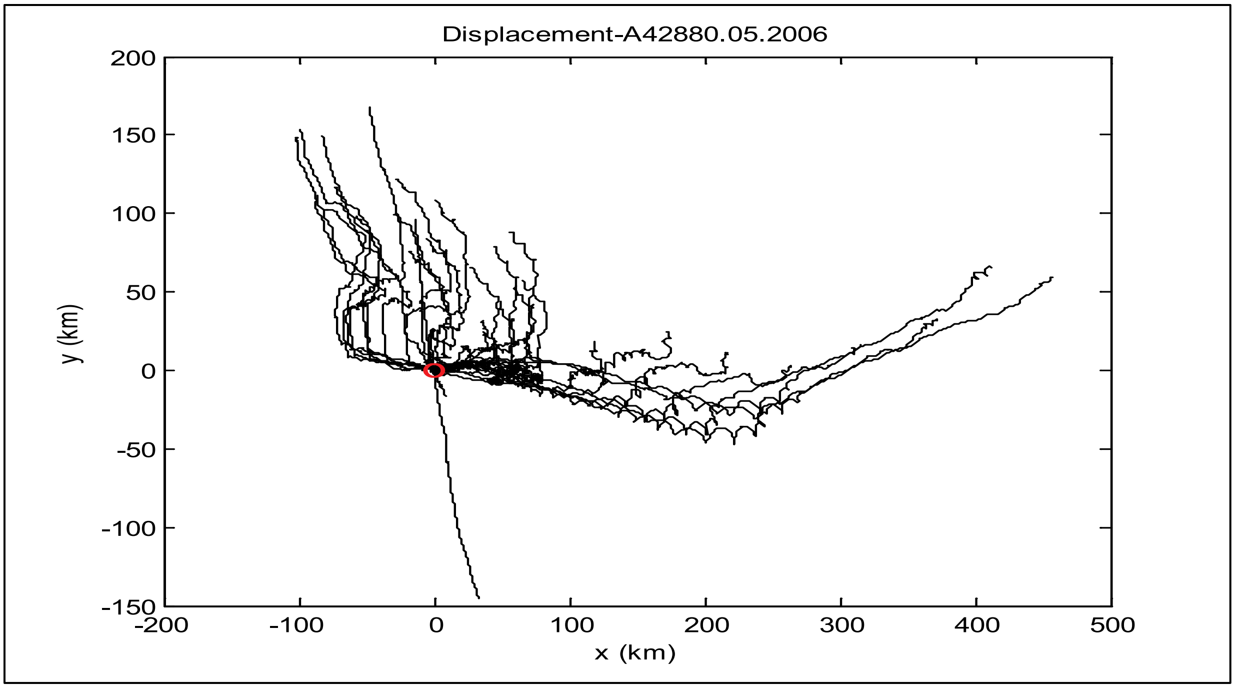

Figure 5.1.33. Progressive vector diagram at different depths for May 2006 at Station 42880.

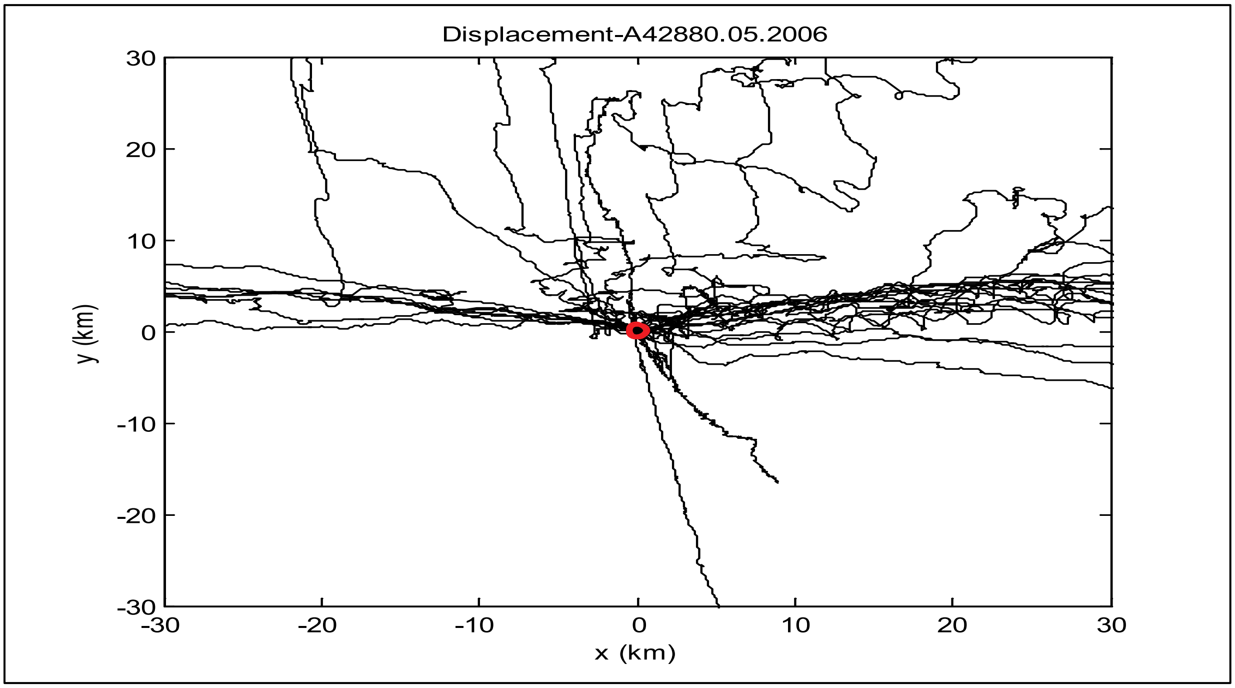

Figure 5.1.34. Enlarged progressive vector diagram at different depths for May 2006 at Station 42880 to show NIO.

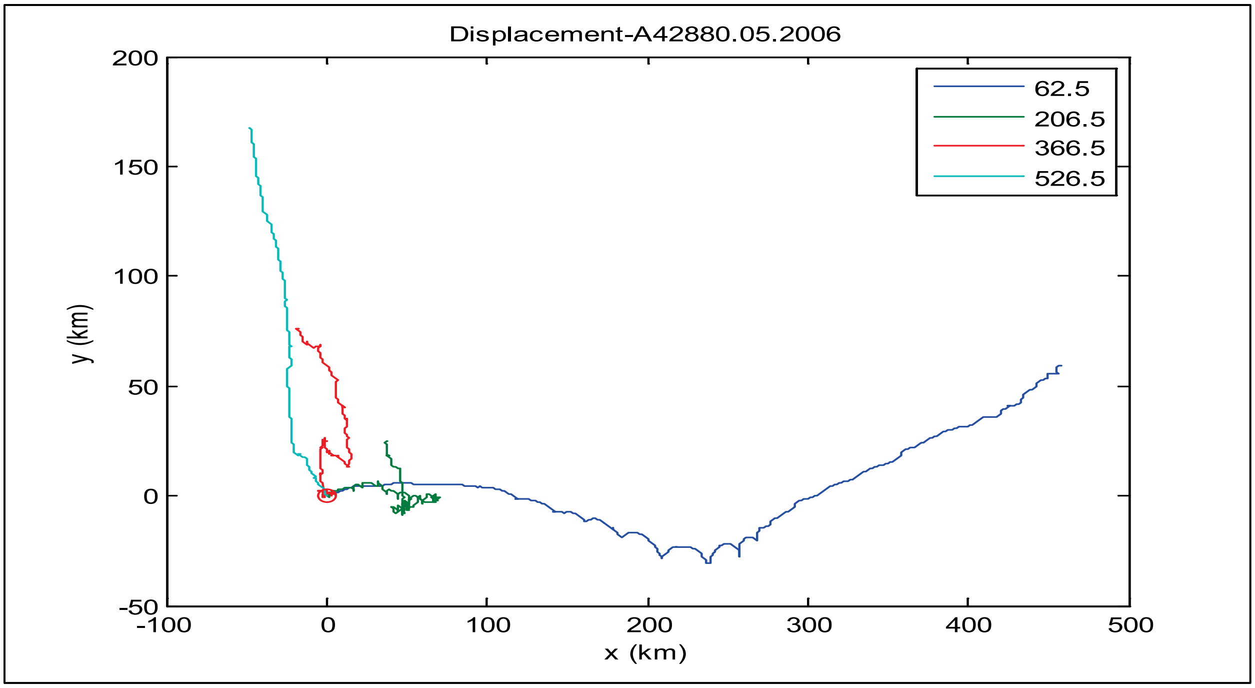

Figure 5.1.35. Enlarged progressive vector diagram at selected depths in May 2006 at Station 42880, zoomed in to show the NIOs.

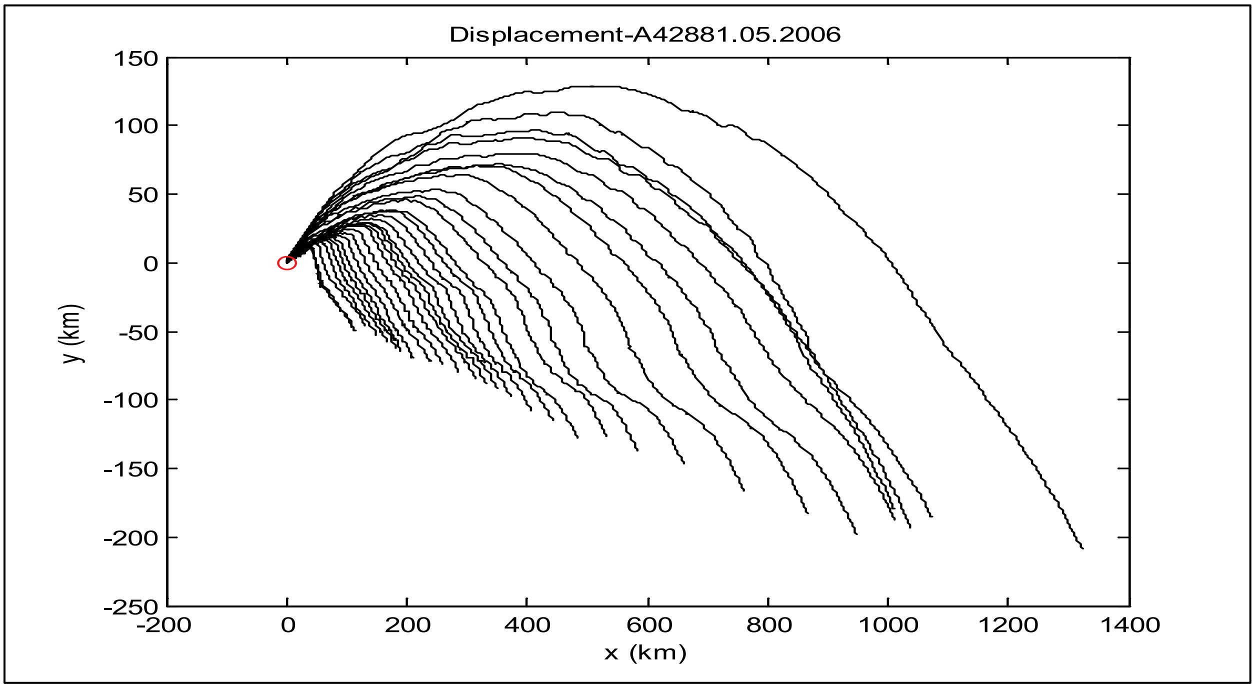

Figure 5.1.36. Progressive vector diagram at different depths for May 2006 at Station 42881.

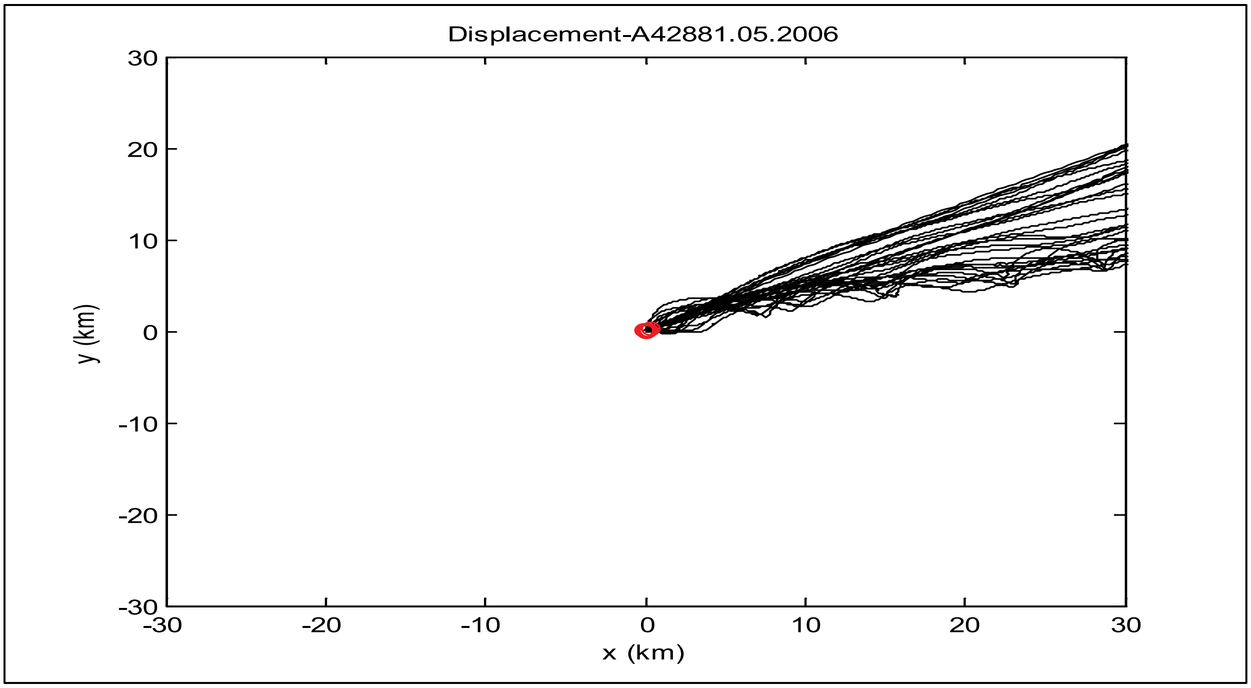

Figure 5.1.37. Enlarged progressive vector diagram at different depths for May 2006 at Station 42881.

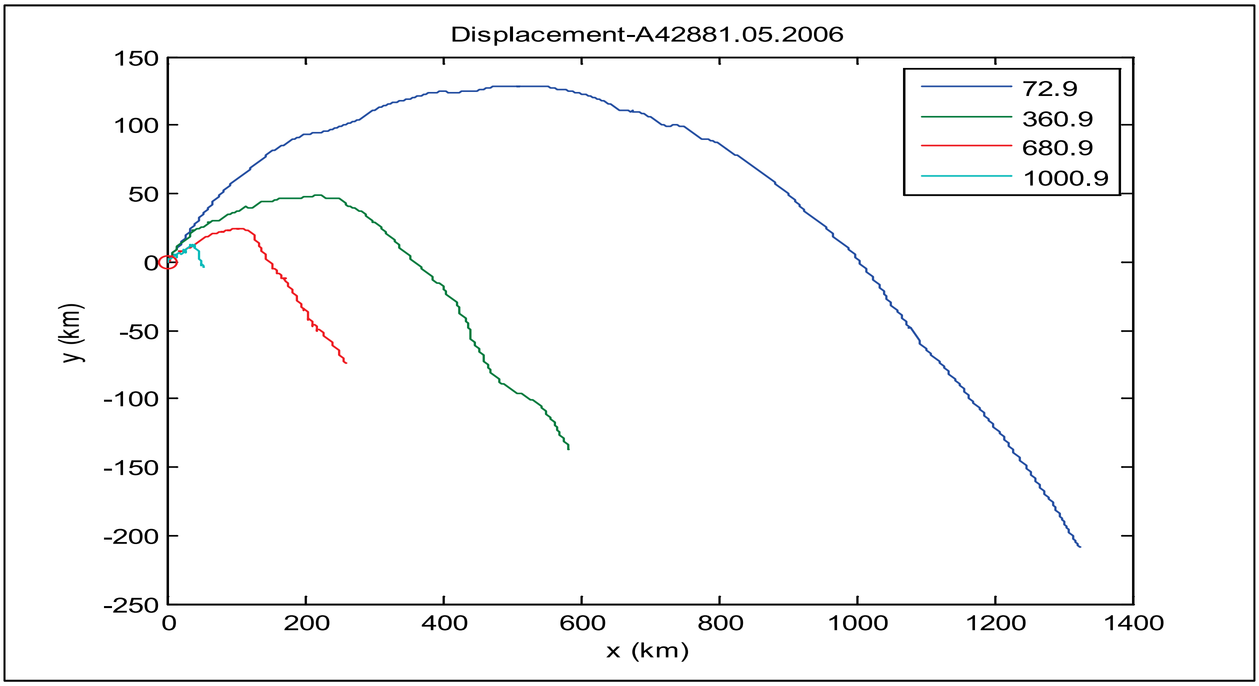

Figure 5.1.38. Enlarged progressive vector diagram at selected depths for May 2006 at Station 42881 to show NIO.

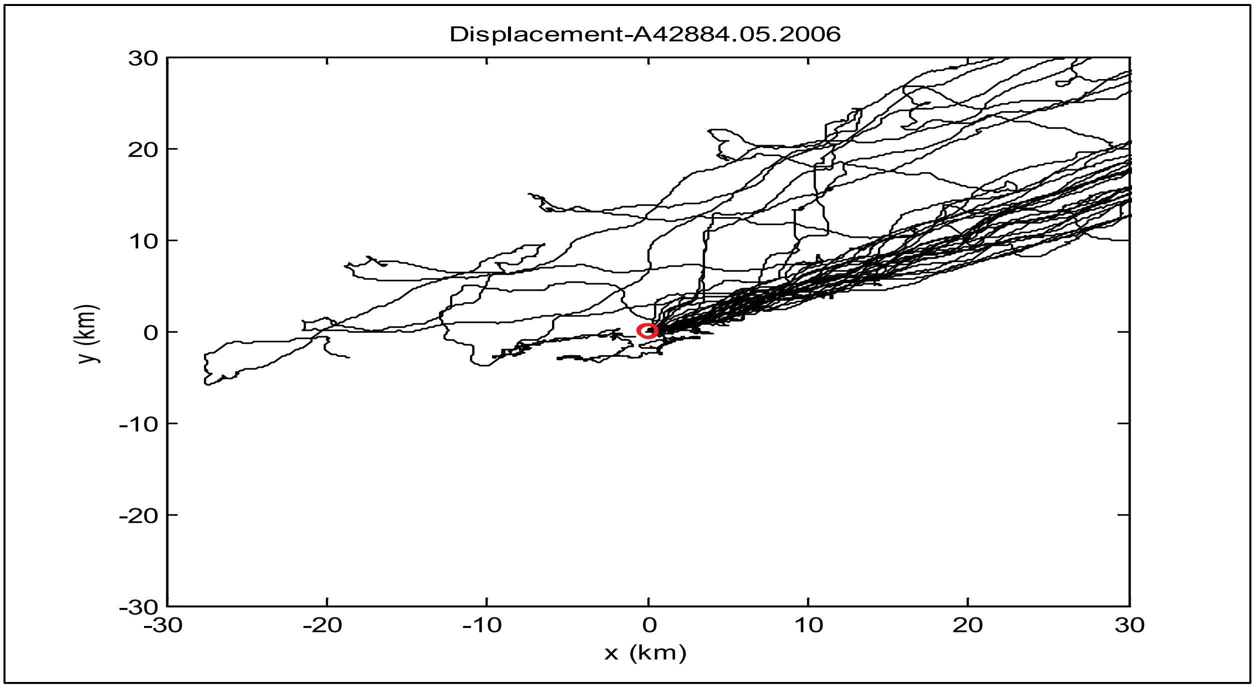

Figure 5.1.39. Progressive vector diagram at different depths for May 2006 at Station 42884.

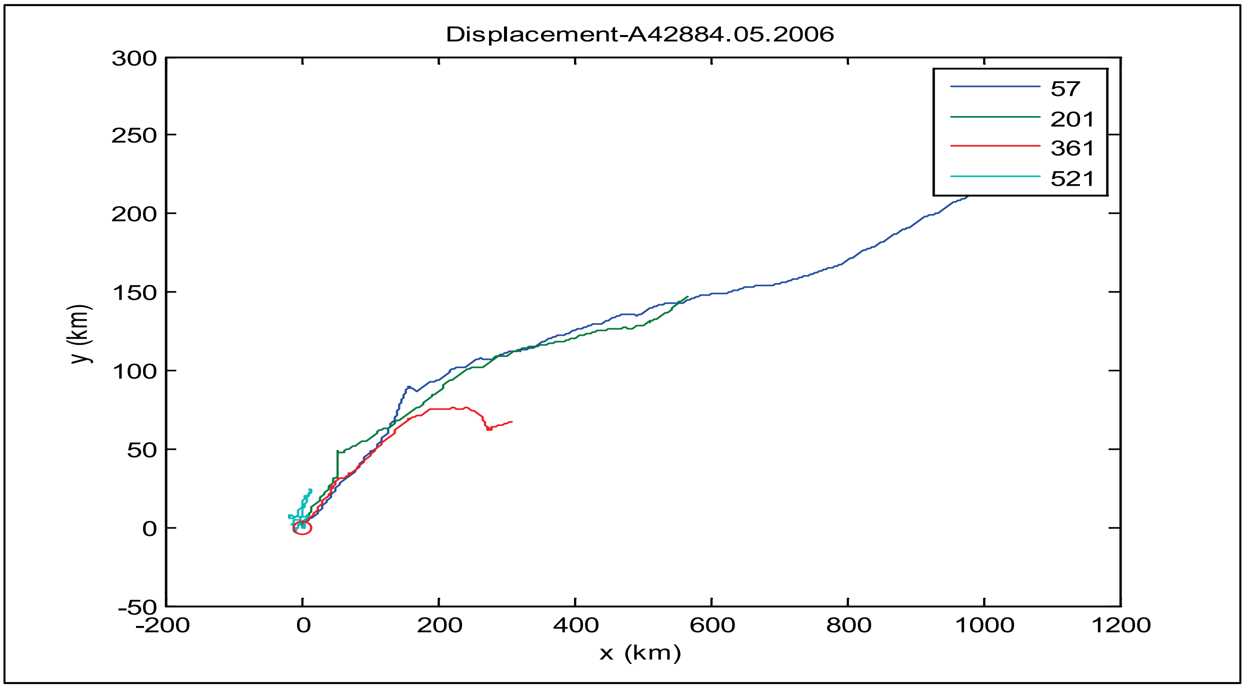

Figure 5.1.40. Enlarged progressive vector diagram at selected depths for May 2006 at Station 42884, zoom in to show the NIOs.

5.1.1 Vertical Structure and Spectrum Analysis

Vertical structures of the flow components often show signs of phase lags and vertical propagation of velocity magnitude. For example, Figures 5.1.39 and 5.1.40 are the east and north velocity component time series as functions of the vertical coordinate for Station 42361 in May 2006. In the top 300-400 m, there is an obvious upward propagation of velocity phase associated with a downward propagation of the maximum which indicate an internal wave excited from the surface.

Corresponding to the time series, the Fourier analysis of the velocity time series provides information of the major frequency band of the motion. For example, Figures 5.1.41 and 5.1.42 are the vertical profiles of the spectrum for data shown in Figures 5.1.39 and 5.1.40. There are a few features we can identify from them. First of all, it is obvious that there are a couple of bands of maximum energy around the diurnal and semi-diurnal tidal frequencies. Tides in this deep area are rather weak and the inertial oscillation frequency is very close to that of diurnal tides. The maximum at one cycle per day is mainly from the NIOs, not diurnal tides. Note that it is relatively broad in range because of the modification of the relative vorticity. It is also obvious that the maximum occurs at a depth around 200 m. There is also an indication of slight increase of frequency toward deeper water.

The lowpass filtered data allows us to identify flow components excluding the tides and NIOs. Figures 5.1.43 and 5.1.44 suggest some episodic events that produce either a surface maximum above 200 m or subsurface maximum (400-700 m in these examples) for a duration of 3-7 days. The magnitude of such motion reached ~ 25 cm/s in these examples.

Figures 5.1.45 and 5.1.46 are the 800 m vertical profiles of the east and north velocity components for Station 42367 in May 2006. The data had some large gaps and the vertical propagation of the velocity phase is not obvious. There may be a downward transfer of energy but the flow maximum is almost always on the surface. The lowpass filtered or mean velocity (Figures 5.1.47 and 5.1.48) also show some surface and subsurface maximum with a reduced magnitude (compared to the earlier example). There is also an indication of observation errors and the effect of data gaps. The velocity spectrum is similar to Station 42361 but with a lack of obvious semi-diurnal tidal component (Figures 5.1.49 and 5.1.50).

Figures 5.1.51 shows more spectra of subsurface velocity components (top most bin in the vertical) at 15 stations. It can be seen that there is a large range of variability. Generally, there is a maximum at the diurnal frequency which can be a single peak or 2 or more peaks. That is a mixture of diurnal tides and NIOs. The semi-diurnal tidal components are much weaker if it can be identified.

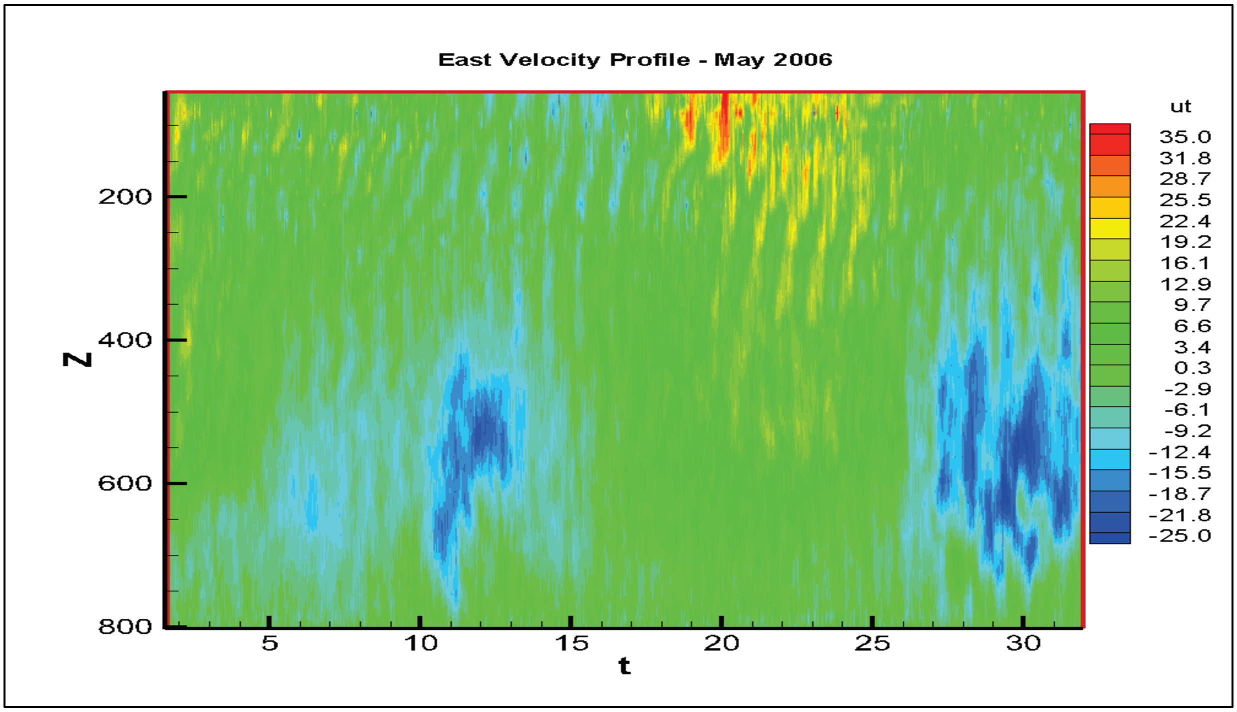

Figure 5.1.41. Hovmoller diagram for the east velocity component for Station 42361 in May 2006. The x-axis is time in days and y-axis is depth in meters.

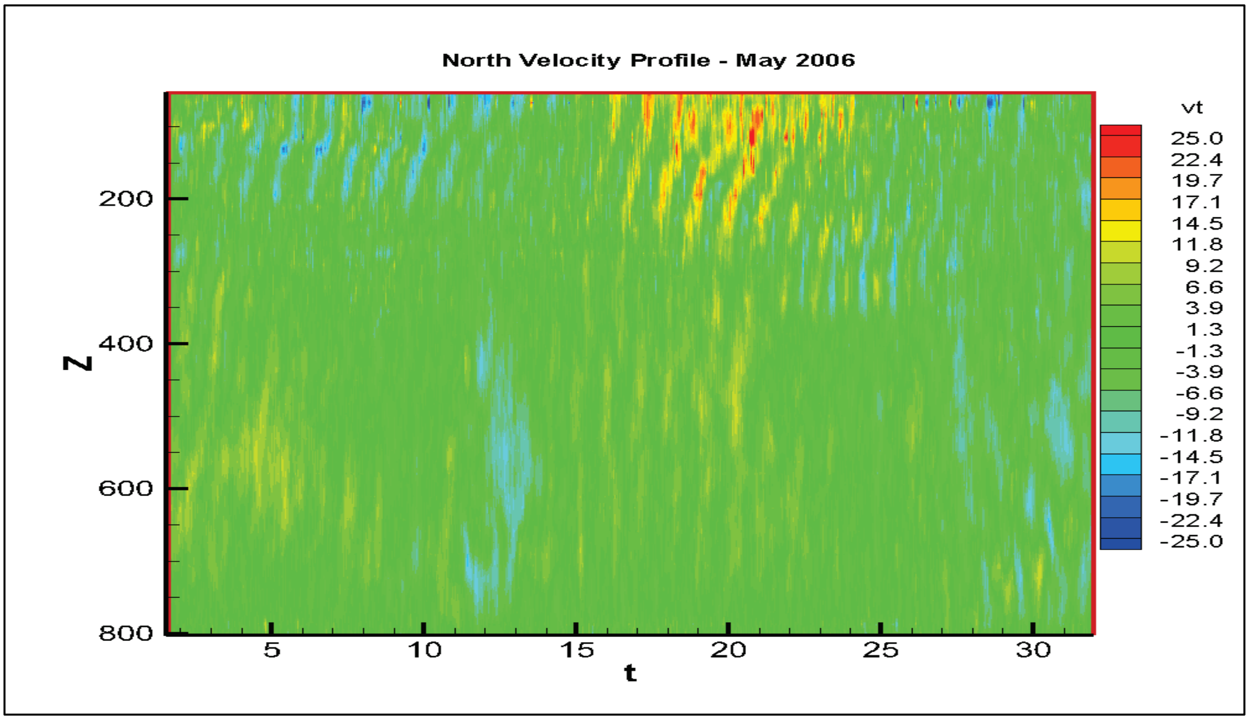

Figure 5.1.42. Hovmoller diagram for the north velocity component for Station 42361 in May 2006. The x-axis is in days and y-axis in meters.

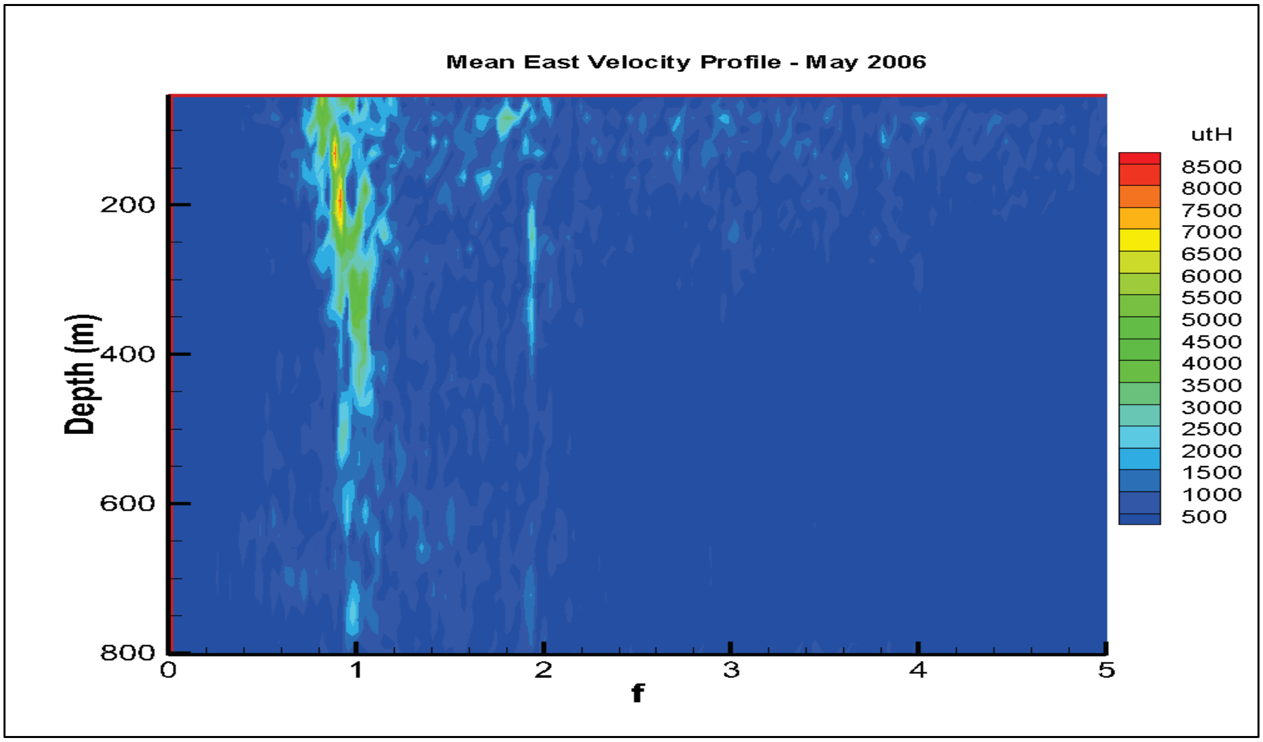

Figure 5.1.43. Spectrum and vertical profile for the east velocity component for Station 42361 in May 2006. The x-axis is for frequency (in cycle per day), y-axis in meters.

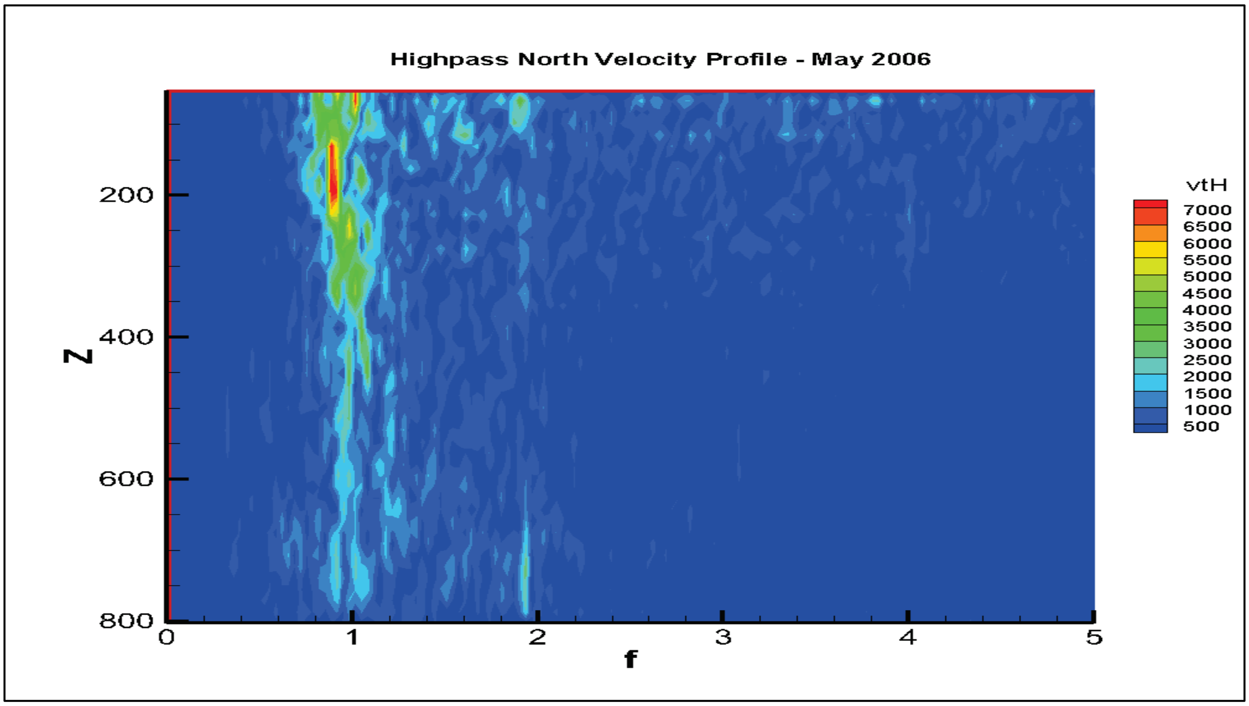

Figure 5.1.44. Spectrum and vertical profile for the north velocity component for Station 42361 in May 2006. The x-axis is for frequency (in cycle per day), y-axis in meters.

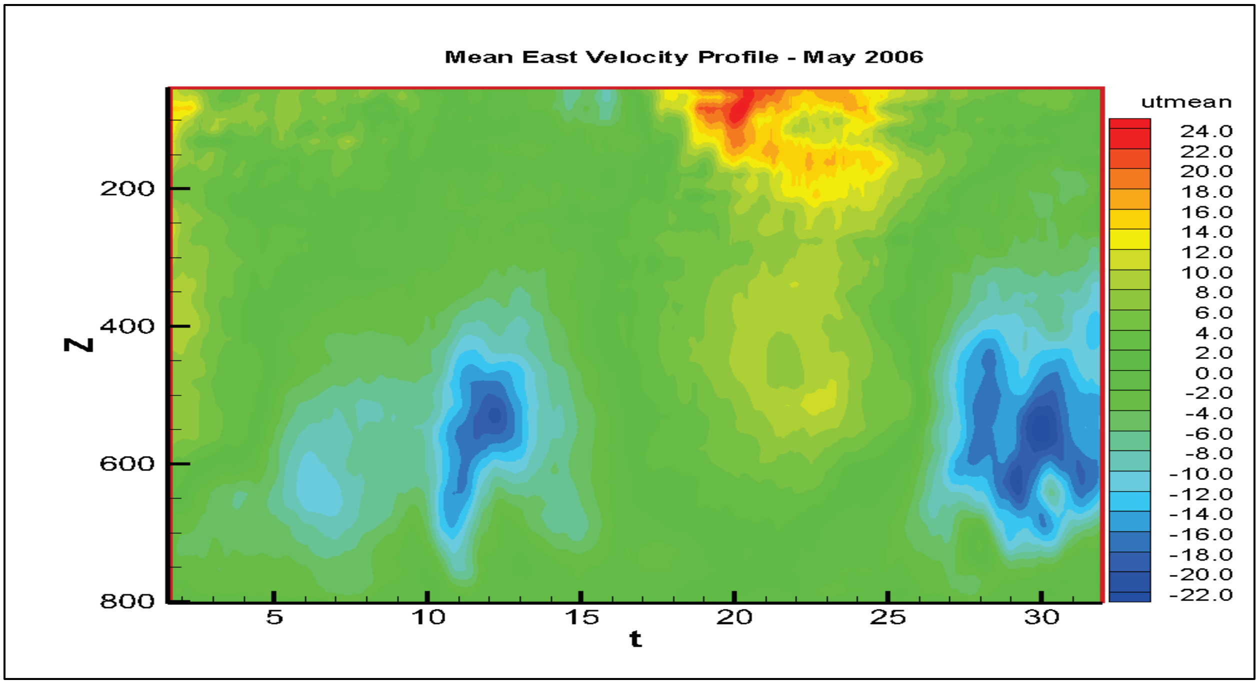

Figure 5.1.45. Low-pass filtered east velocity component for Station 42361 in May 2006. The x-axis is in days; vertical axis in meters.

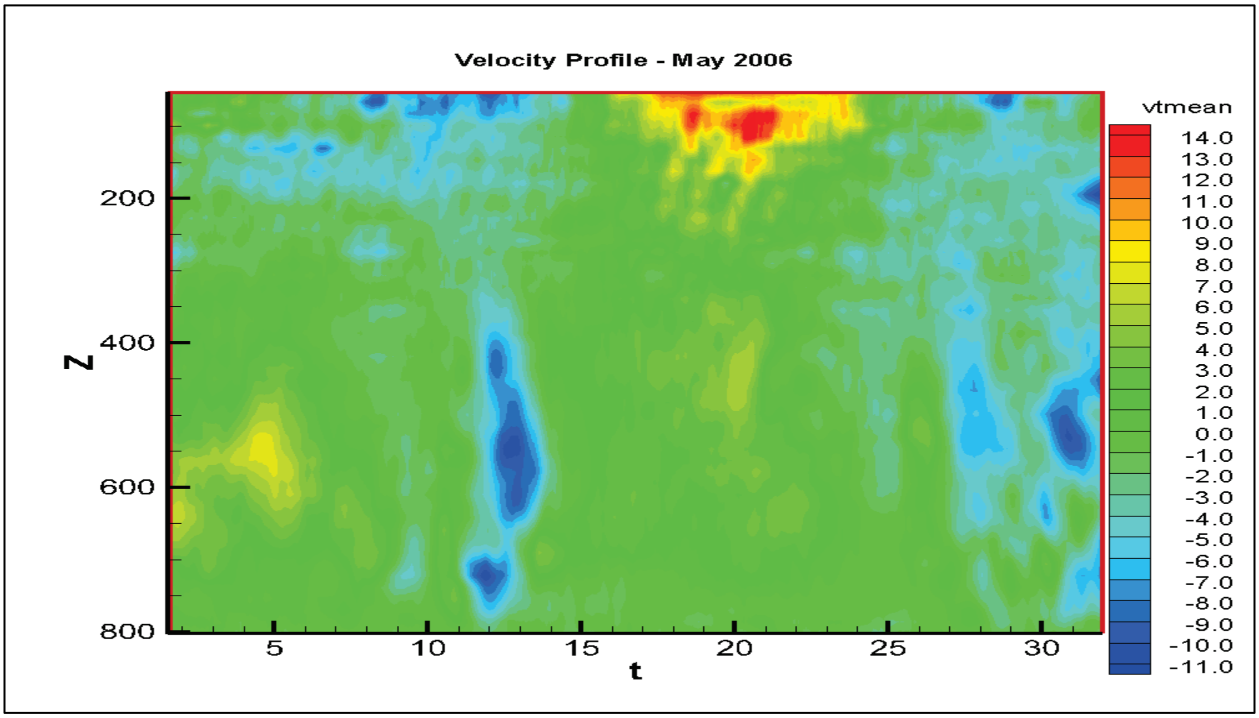

Figure 5.1.46. Low-pass filtered north velocity component for Station 42361 in May 2006. The x-axis is in days; vertical axis in meters.

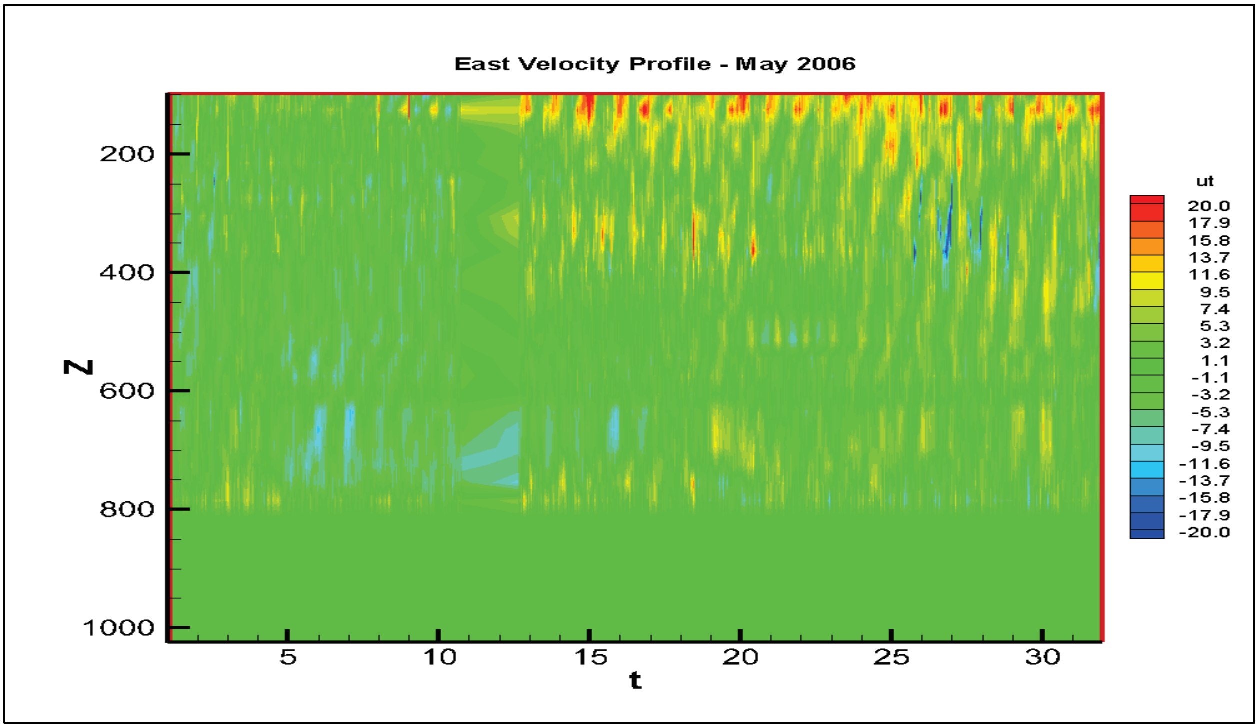

Figure 5.1.47. East velocity component for Station 42367 in May 2006. The x-axis is in days; vertical axis in meters.

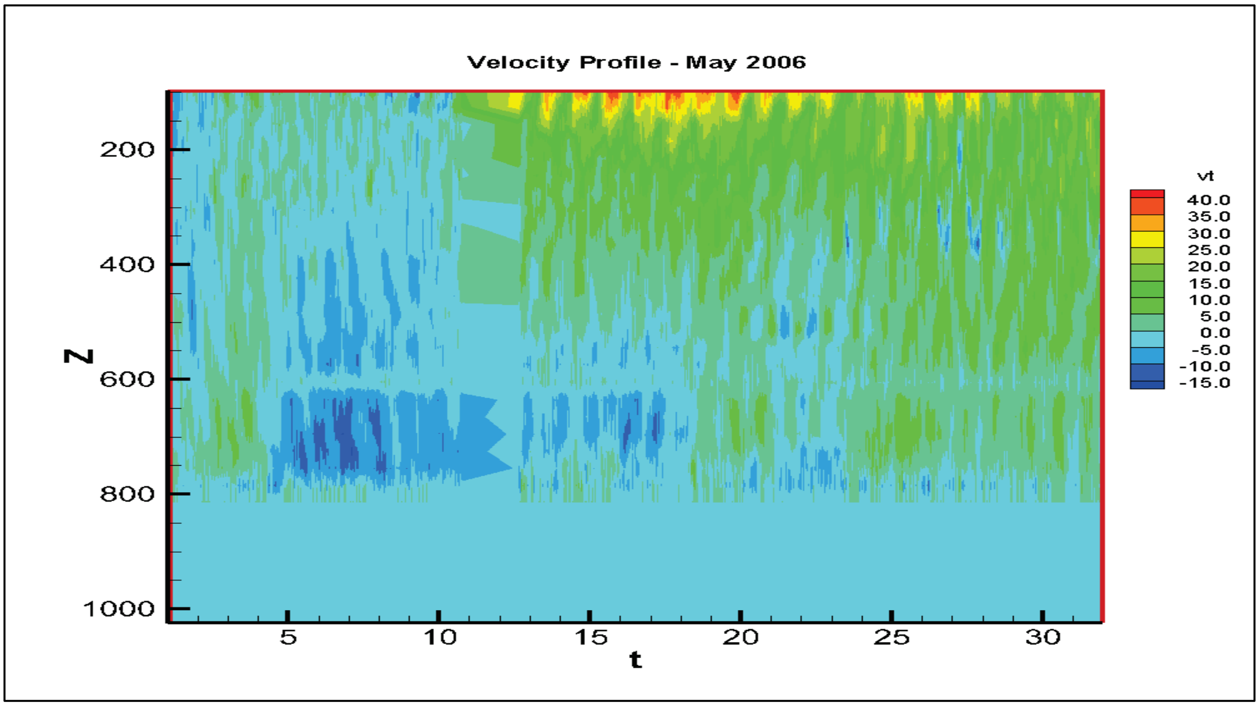

Figure 5.1.48. North velocity component for Station 42367 in May 2006. The x-axis is in days; vertical axis in meters.

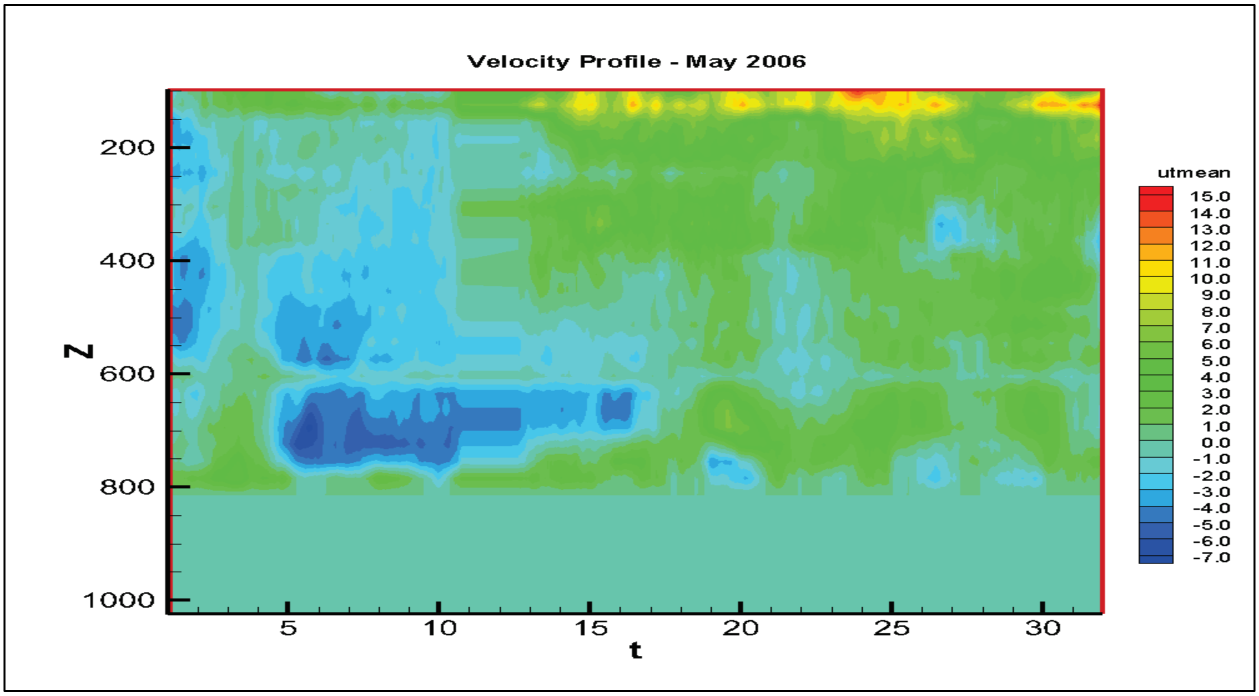

Figure 5.1.49. Mean east velocity component for Station 42367 in May 2006. The x-axis is in days; vertical axis in meters.

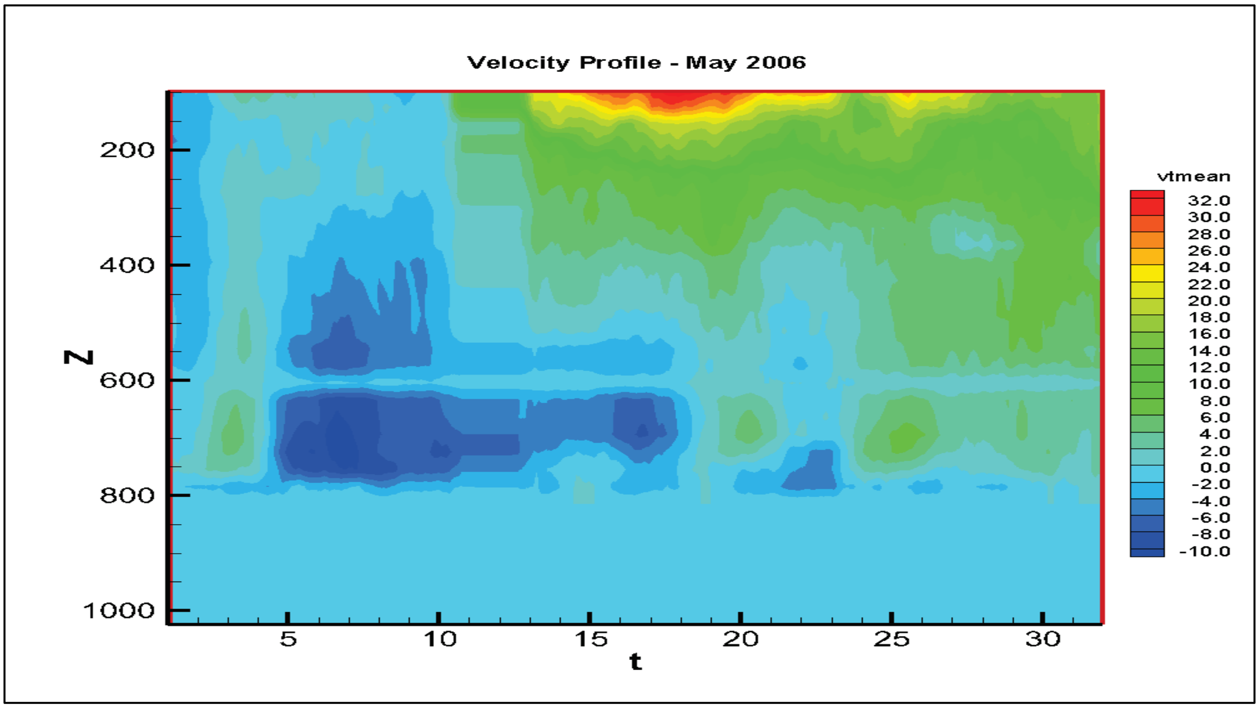

Figure 5.1.50. Mean north velocity component for Station 42367 in May 2006. The x-axis is in days; vertical axis in meters.

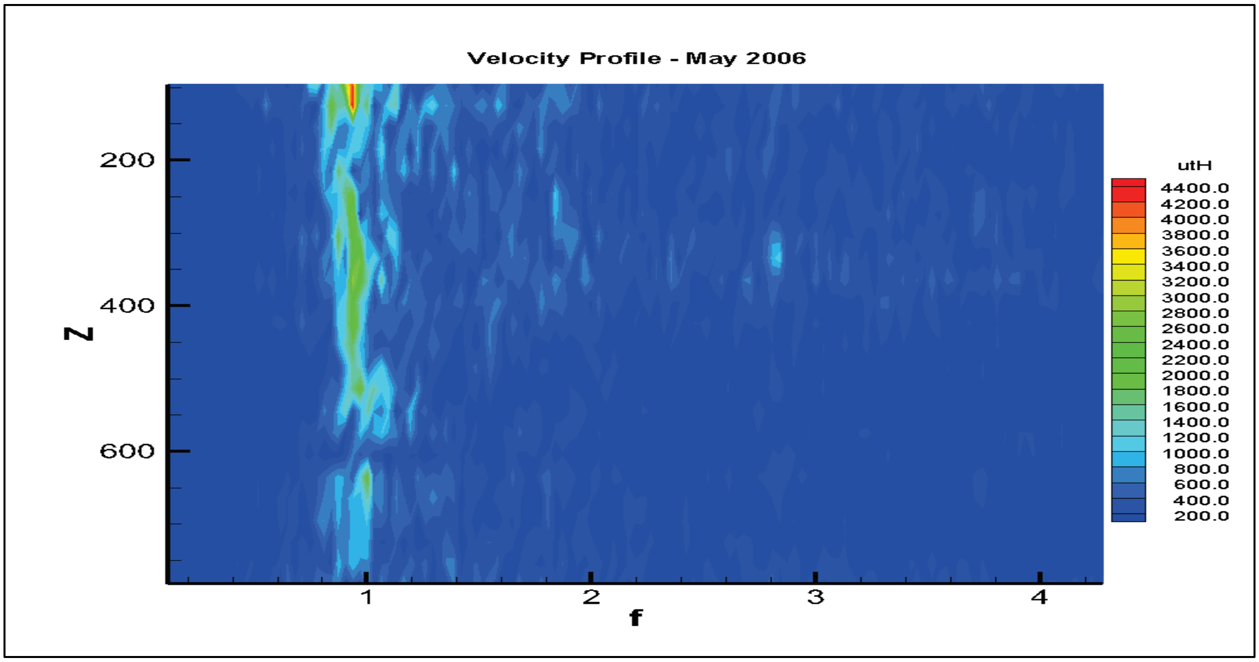

Figure 5.1.51. Spectrum for east velocity component for Station 42367 in May 2006. The x-axis is in cycles per day; vertical axis in meters.

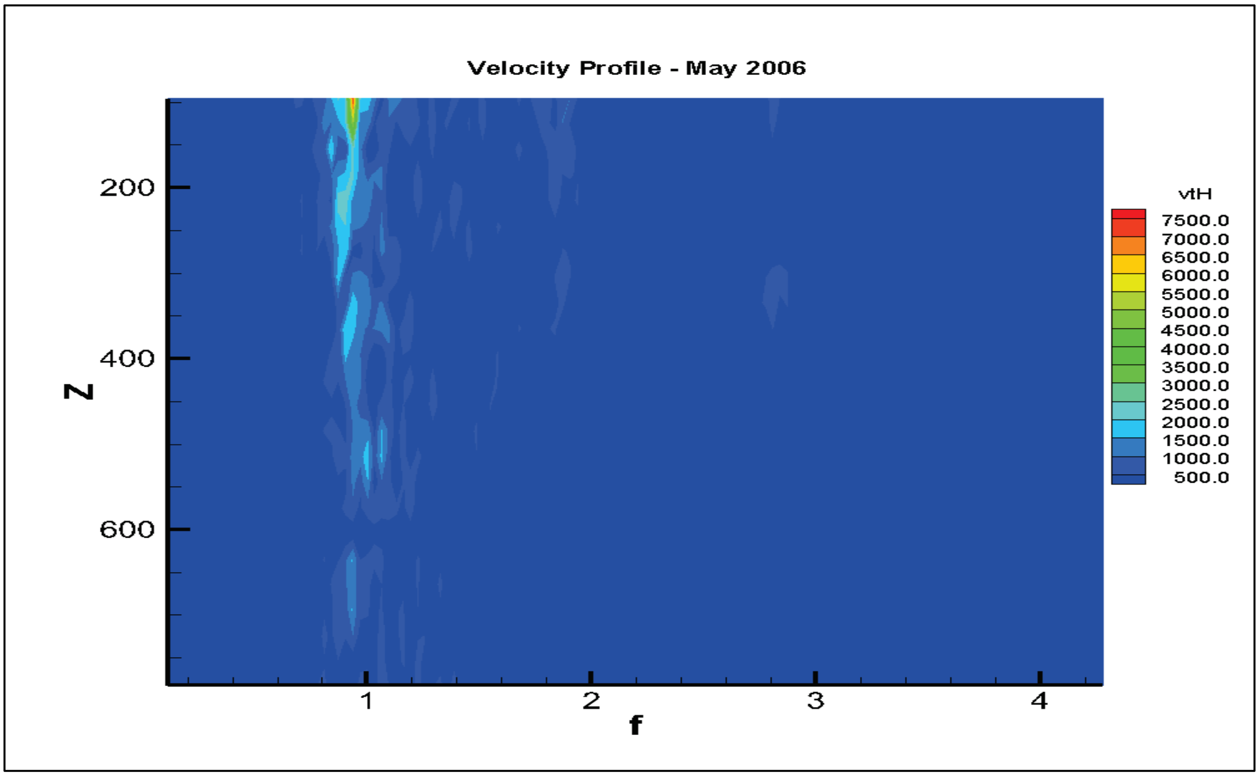

Figure 5.1.52. Spectrum for north velocity component for Station 42367 in May 2006. The x-axis is in cycles per day; vertical axis in meters.

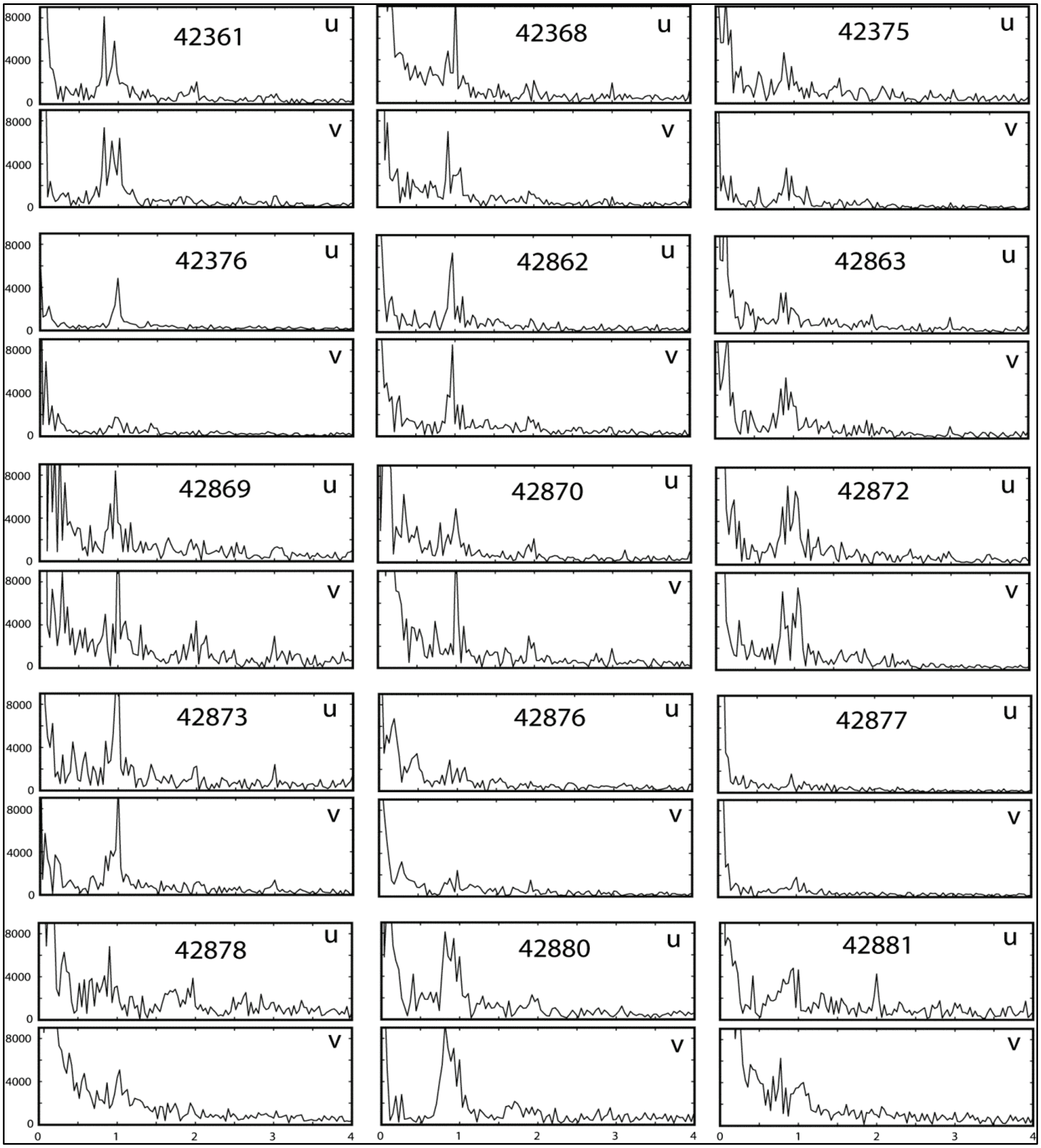

Figure 5.1.53. Spectra of velocity components for various stations in May 2006. The x-axis is in cycles per day; vertical axis in spectrum energy unit.

5.2 HURRICANE EVENTS AND INERTIAL OSCILLATIONS

Severe weather such as typhoons and hurricanes can produce strong near inertial oscillations (e.g. Lai and Sanford, 1986; Maeda et al., 1996; Zheng et al., 2006). According to the National Hurricane Center, the year 2005 was most active for Atlantic hurricanes in recorded history. At least three of the seven strong hurricanes that made landfall along the U.S. Gulf of Mexico coast caused serious damages (Knabb et al., 2005): Hurricanes Katrina, Rita, and Wilma. Hurricanes Dennis and Emily also caused significant destructions but here we will only focus on the study of the NIOs caused by Katrina (e.g. Pardue et al., 2005; Fritz, 2007; Suedel et al., 2007), Rita (Rego and Li, 2009a,b,c), and Wilma, as they present rather continuous records within about a two-month period. The tracks of these three hurricanes are shown in Figure 5.2.1. They made landfall at three distinctly different places: Katrina on the central coast of the northern Gulf of Mexico, west of the Birdfoot Delta; Rita more than 400 km to the west of Katrina's landing point; and Wilma about 900 km to the southeast of the Birdfoot Delta on southwest Florida near Cape Romano (Figure 5.2.1).

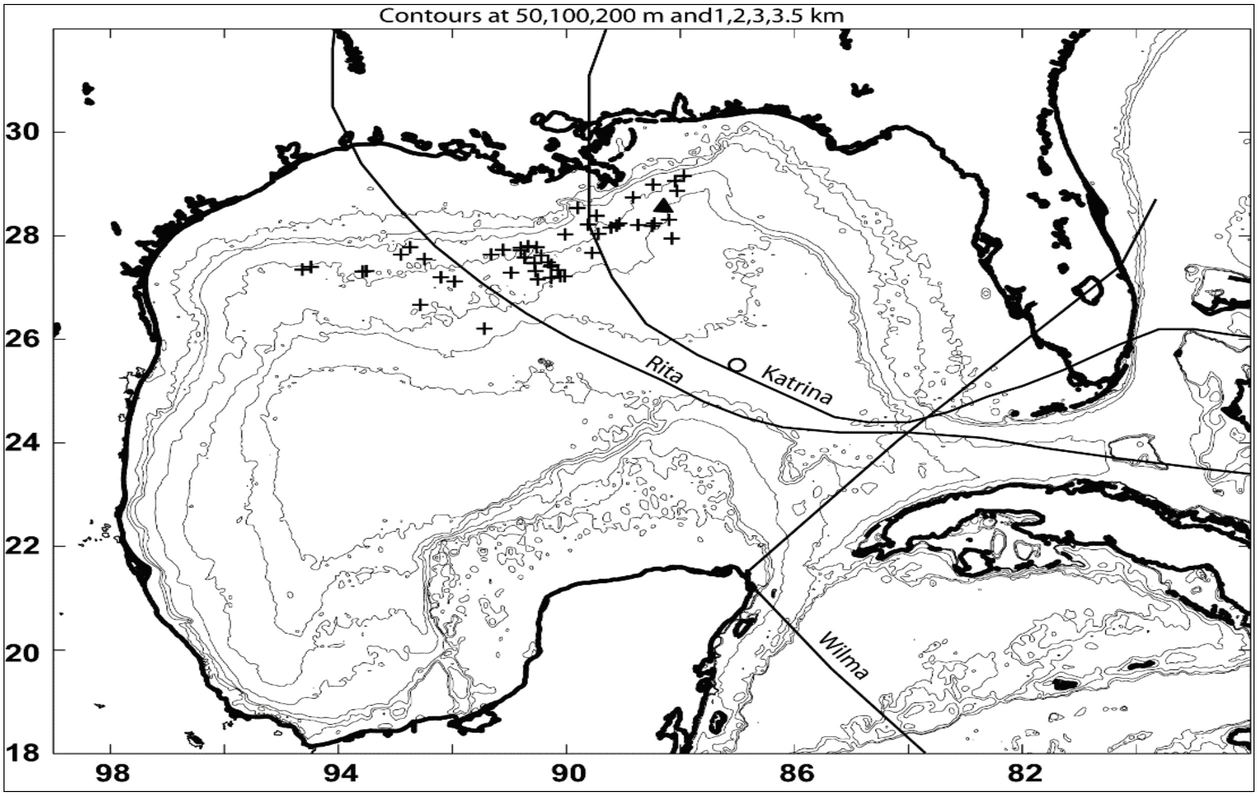

Figure 5.2.1. Study area and the tracks of Hurricanes Katrina, Rita, and Wilma, the oil and gas platforms equipped with ADCPs (crosses), and the only platform (station 42375) with an ADCP recording throughout all three hurricanes (triangle).

Figure 5.2.2 shows the wind vector time series recorded at weather station 42040 (29°12'19" N 88°12'19" W), a station closest to the platform station 42375 (Figure 5.2.1), which recorded the ADCP data discussed. Since the center of Hurricane Katrina came very close to this weather station, while the centers of Hurricanes Rita and Wilma were far from it, the wind vector plots show a strong clockwise rotating vector time series during Hurricane Katrina, a much weaker clockwise rotating vector time series during Rita, and a counter-clockwise rotating vector time series during Wilma. The wind before and after Katrina appeared to be relatively weak; while it remained relatively strong after Rita and Wilma (Figure 5.2.2).

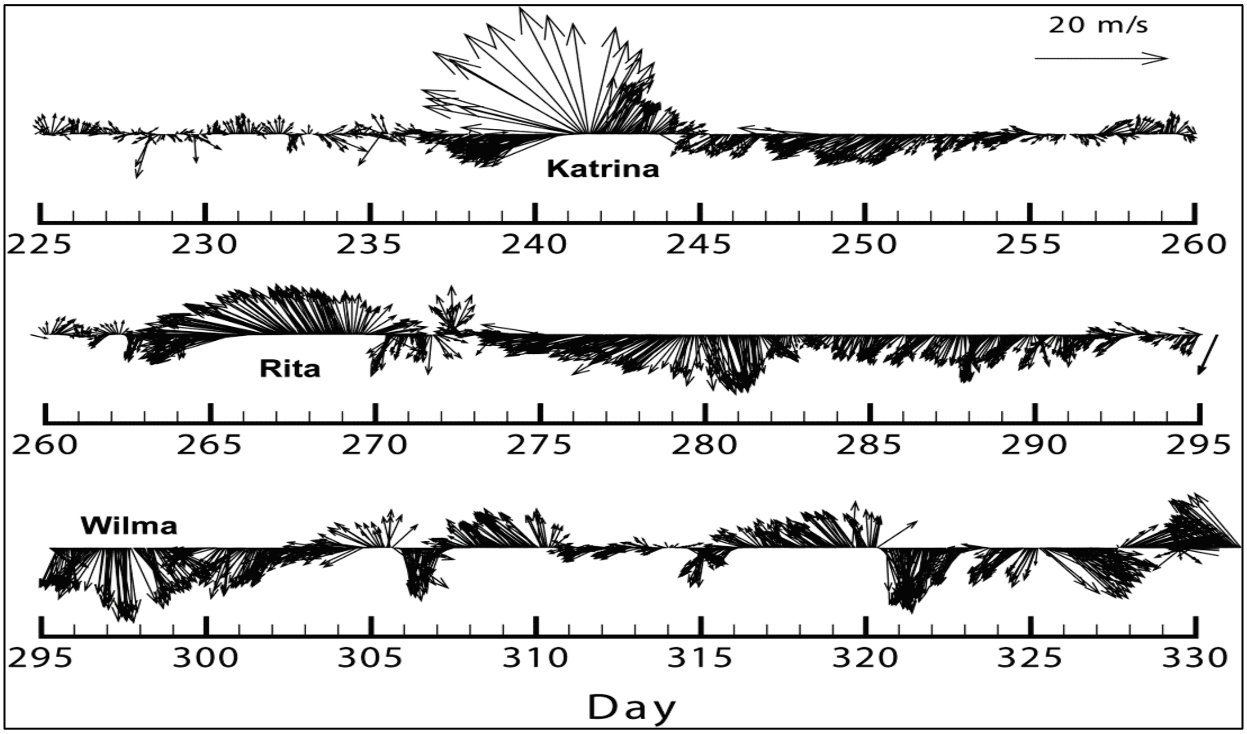

Figure 5.2.2. Wind vectors from Station 42040 (29°12'19" N; 88°12'19" W), located ~ 118 km South of Dauphin Island, AL, and ~76 km north of platform 42375 (triangle in Figure 5.2.1).

The velocity data from station 42375 show strong clockwise oscillations immediately after each of the three hurricanes as shown by the progressive velocity vector plot (Figure 5.2.3). These clockwise oscillations are excited as soon as the hurricane influenced the area and during each hurricane event, the oscillation lasted for about 10 days. It is obvious that they are NIOs caused by the weather events. To better visualize the vertical structure of the NIOs caused by the hurricanes, a 6th order Butterworth filter is implemented with a cutoff frequency of 0.6 cycle/day or 40-hour filter. The high-pass and low-pass vertical profiles of the east and north components of the velocity during Hurricane Katrina are shown in Figures 5.2.4 – 5.2.7. The vertical profiles for Hurricanes Rita and Wilma are similar and are omitted here. A few points follow immediately by an examination of Figures 5.2.4-5.2.7: 1) There is a significant NIO throughout the entire water column between 1450 m and 1920 m; 2) the NIO occurred immediately after the passage of Hurricane Katrina (same for Rita and Wilma); 3) the NIO lasted for more than 10-days after the passage of the hurricane and decreased slowly over the 10-day period; 4) there were apparently oscillations at lower frequencies – roughly 2-4 day periods.

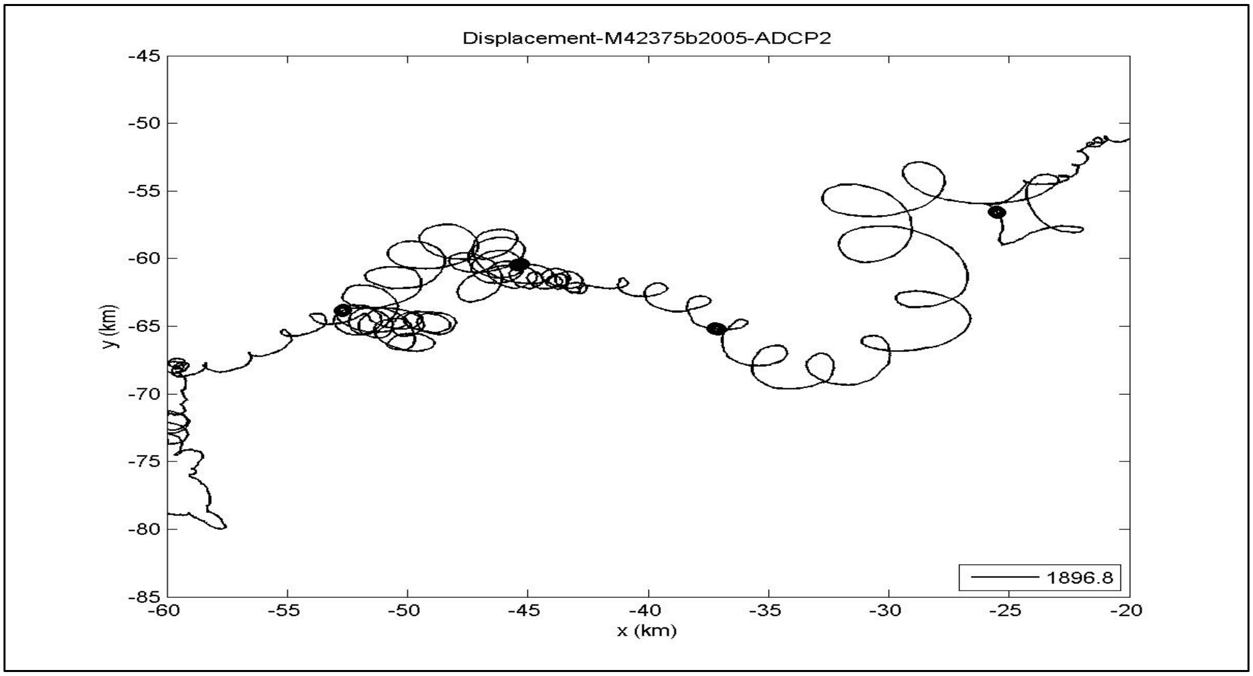

Figure 5.2.3. Progressive vector diagram showing the NIOs during Hurricanes Katrina and Rita in August and September of 2005 at station 42375.

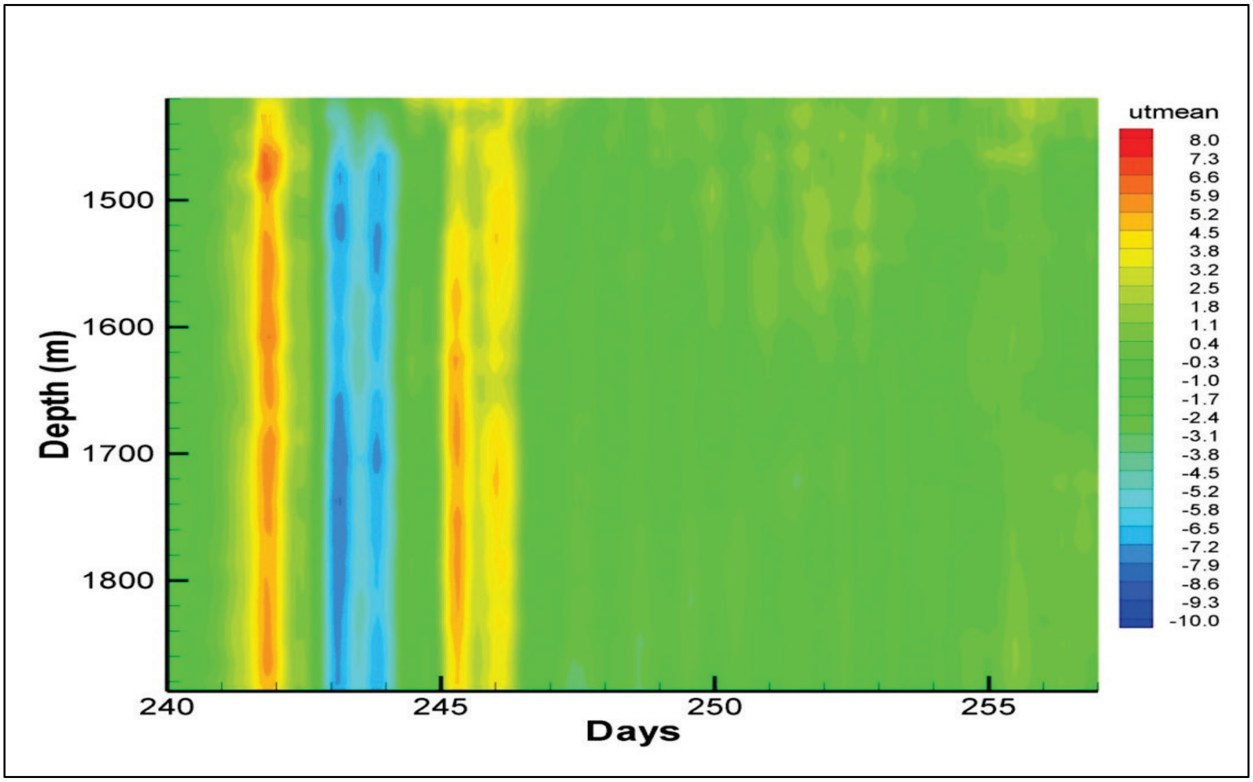

Figure 5.2.4. Time-depth plots of low-pass filtered east velocity at station 42375 during Hurricane Katrina. Speed scale in cm/s.

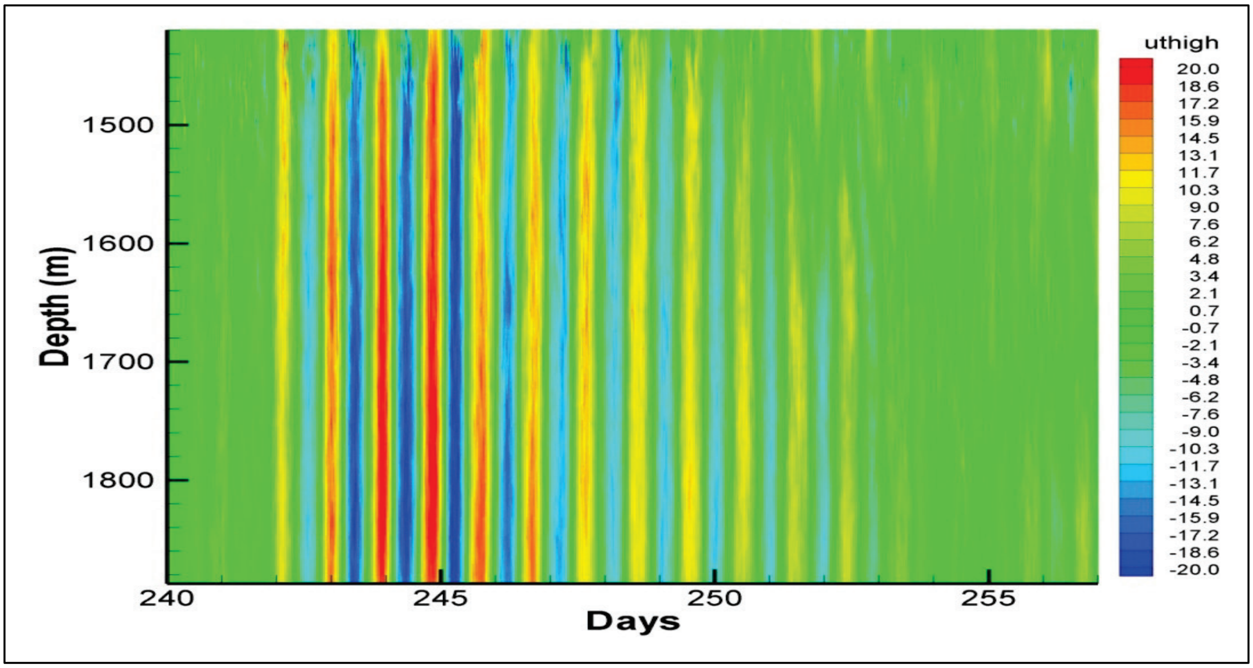

Figure 5.2.5. Time-depth plots of high-pass filtered east velocity at station 42375 during Hurricane Katrina. Speed scale in cm/s.

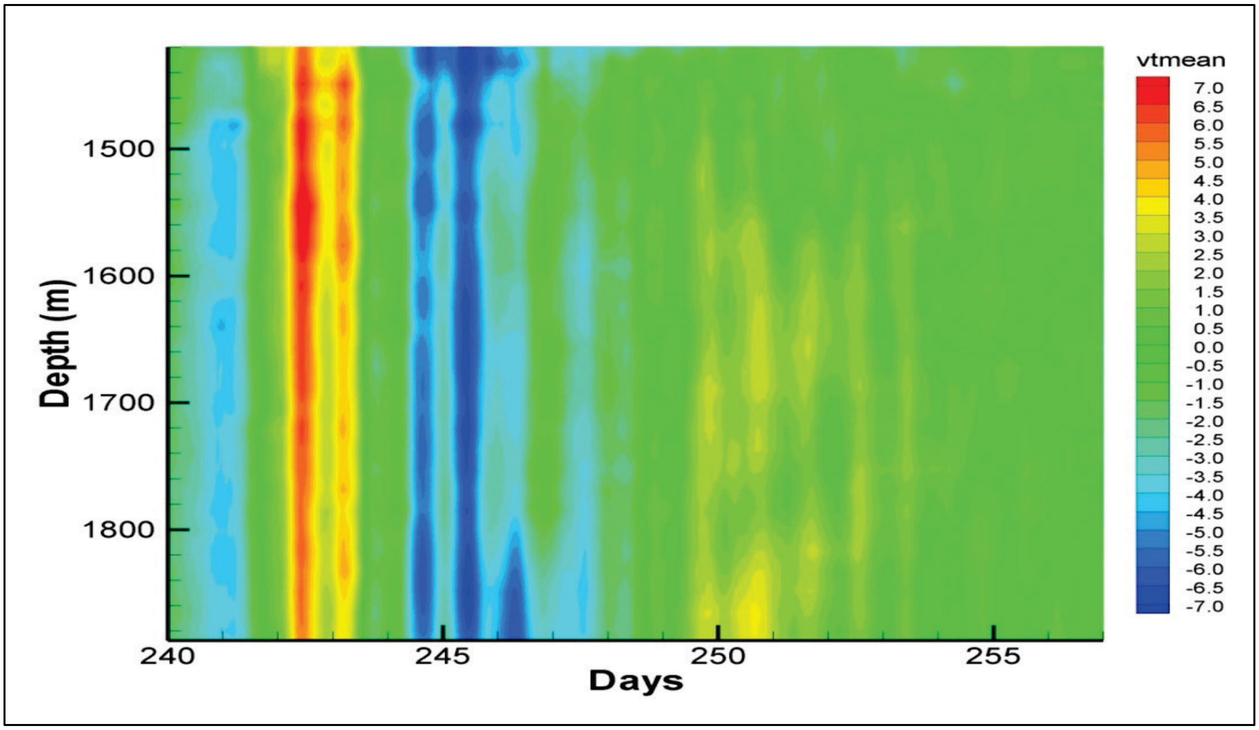

Figure 5.2.6. Time-depth plots of low-pass filtered north velocity at station 42375 during Hurricane Katrina. Speed scale in cm/s.

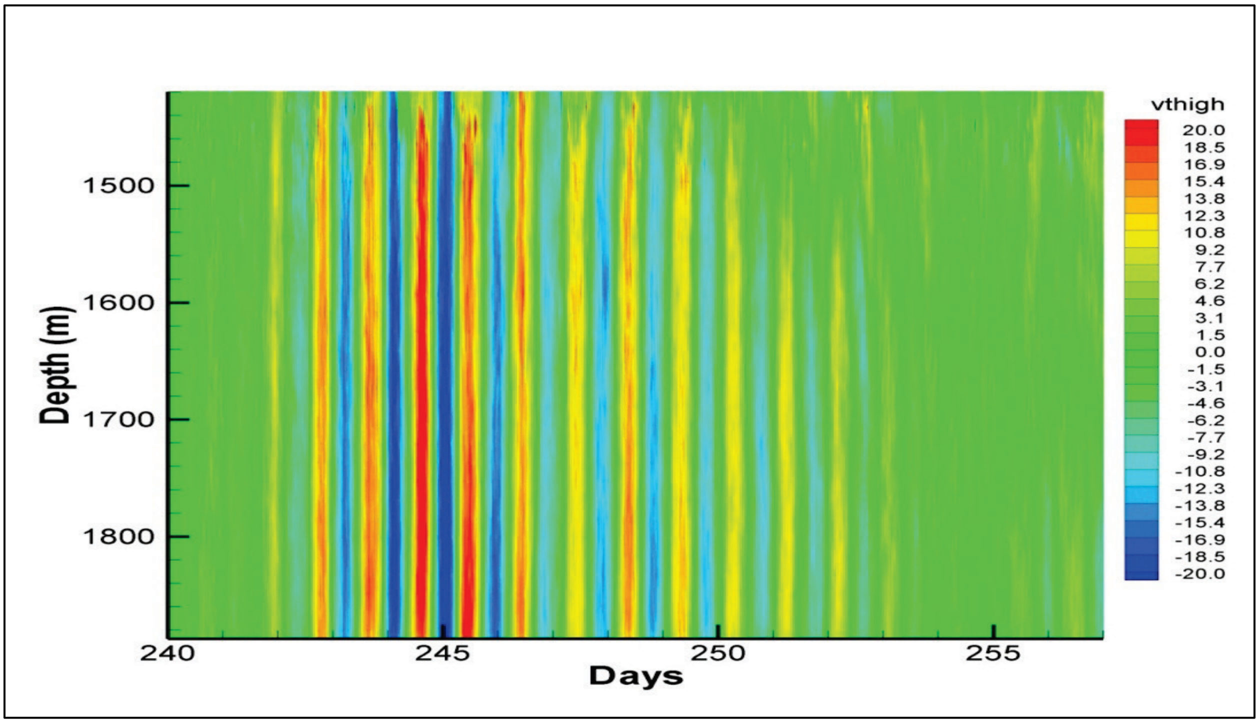

Figure 5.2.7. Time-depth plots of high-pass filtered north velocity at station 42375 during Hurricane Katrina. Speed scale in cm/s.

To further analyze the oscillations caused by the three hurricanes, we separated the records into six segments and calculated the depth averaged velocity (Figure 5.2.8). Flow speed is employed to analyze the kinetic energy changes caused by hurricanes. Segment 1, Figure 5.2.8a, covers day 225 to day 240, before Hurricane Katrina. This period has the lowest speed (max speed less than 5 cm/s), with some oscillations similar to NIOs. Since the NIOs frequencies in this area are close to those of diurnal tides, these measured oscillations may contain some background tidal currents. The data also indicate that tidal currents in this deep water area should not exceed 5 cm/s. This is very important to note as these small tidal current will not significantly interfere with the much stronger NIOs caused by the hurricanes. Segment 2, Figure 5.2.8b, shows the averaged speed from day 242 to day 252, 10-days after Katrina. This period shows the strongest speed of the record discussed, with the maximum flow reaching 25 cm/s and clear NIOs caused by the atmospheric forcing. It first ramped up within three days and then decreased almost linearly within 8-9 days. Segment 3, Figure 5.2.8c, shows the average speed from day 253 to 263, a period after the impact of Katrina and before Rita. This is a period of low speed (max ~ 6 cm/s) and less defined NIO. Segment 4, Figure 5.2.8d, shows the average speed which includes Rita and two weeks afterwards. The NIO is seen to have ramped up again, within 4-5 days, followed by a steady decrease within 10 days. The maximum speed is 15 cm/s. Segment 5, Figure 5.2.8e, shows the average speed after the impact of Rita and before Wilma. Again, this is similar to segment 3, with a small speed (up to 5 cm/s) and less defined NIO. Segment 6, Figure 5.2.8f, shows the average speed for two weeks with Wilma's influence, which shows once more increased depth averaged speed of up to 11 cm/s. The ramp-up period was about 2-3 days, followed by a 5-day drop. From these observations, we see that Hurricane Katrina caused the NIOs to be at least a factor of 5.6 times larger than before the hurricane when wind was very weak. Among this increase in the magnitude of NIO, the high-pass velocity (with a 6th order 40-hr Butterworth filter) increased by a factor of 4. This implies an increase of total kinetic energy by about a factor of 30, and high-pass kinetic energy by a factor of 16. The effects of Hurricanes Rita and Wilma on the NIOs are an increase of velocity amplitudes by about a factor of 3.3 and 2.4, respectively, than before the hurricanes.

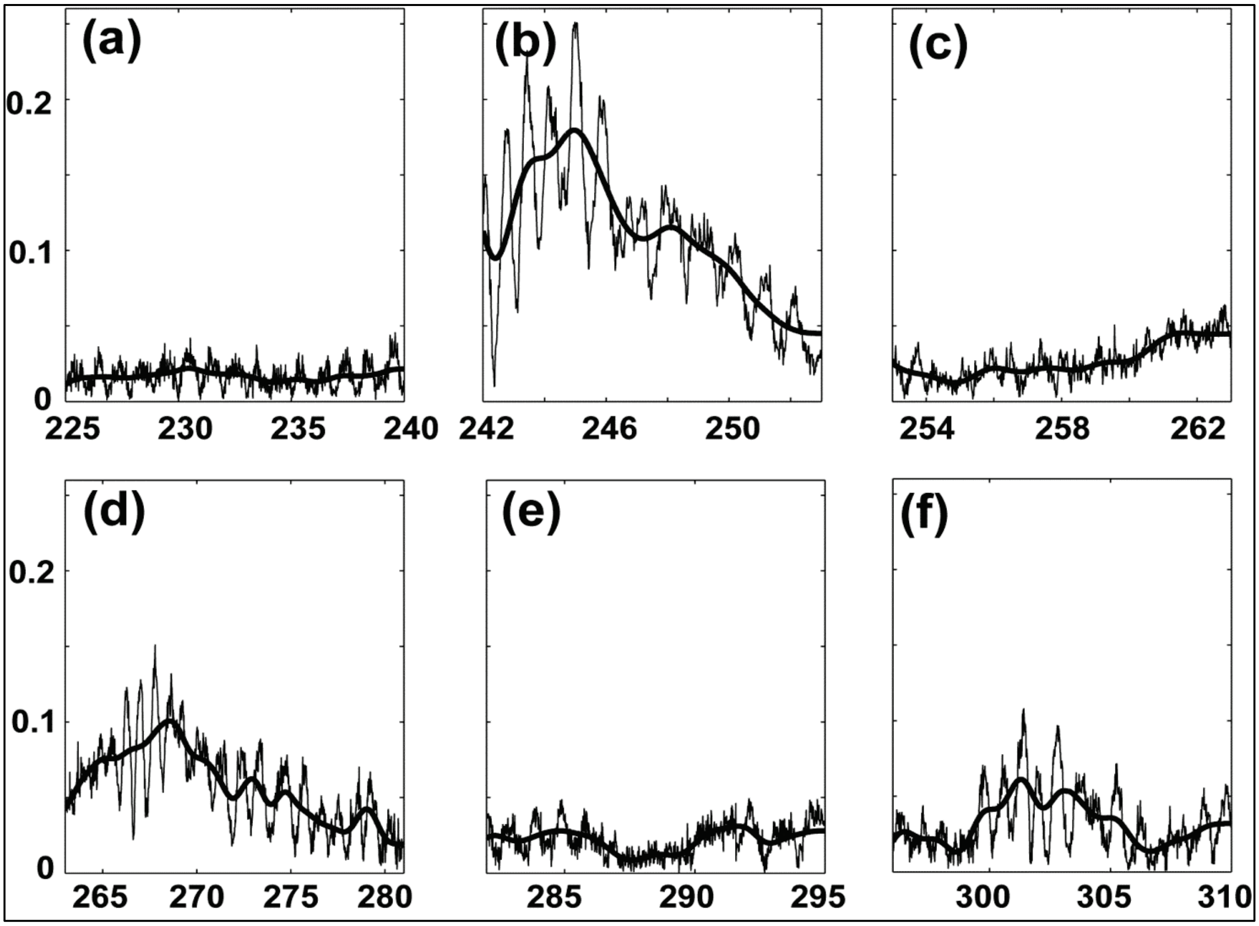

Figure 5.2.8. Depth-averaged speeds (a) before Hurricane Katrina, (b) during and after Katrina, (c) between Katrina and Rita, (d) during and after Rita, (e) between Rita and Wilma, and (f) during and after Wilma. Y-axis units are cm/s.

The increased depth-averaged flow speeds during segments 2, 4, and 6 apparently are caused by Hurricanes Katrina, Rita, and Wilma, respectively. The increased kinetic energy contains both clockwise (CW) and counter-clockwise (CC) motions. To examine how much of the motion is CW or CC, we conducted a rotary spectra analysis (e.g., O'Brien and Pillsbury, 1974). Figure 5.2.9 shows the rotary spectra for the CW rotating component (thick lines) and CC rotating component (thin lines) for the six different time periods as in Figure 5.2.8. Because the vertical axis of Figure 5.2.9 is a logarithmic scale, the differences between peak values are much larger than what they appear. Figure 5.2.9 shows that 1) the CW component is generally much larger than the CC component; 2) the peak of the CW component is centered around the local inertial period (about 24 hours); 3) there is a spread of NIO periods, mostly between 22 and 26 hours; 4) Hurricane Katrina caused the strongest NIO, followed by Rita, and then Wilma; 5) the NIO around the local inertial period seemed to have a broader peak during and after the hurricanes than during non-hurricane periods.

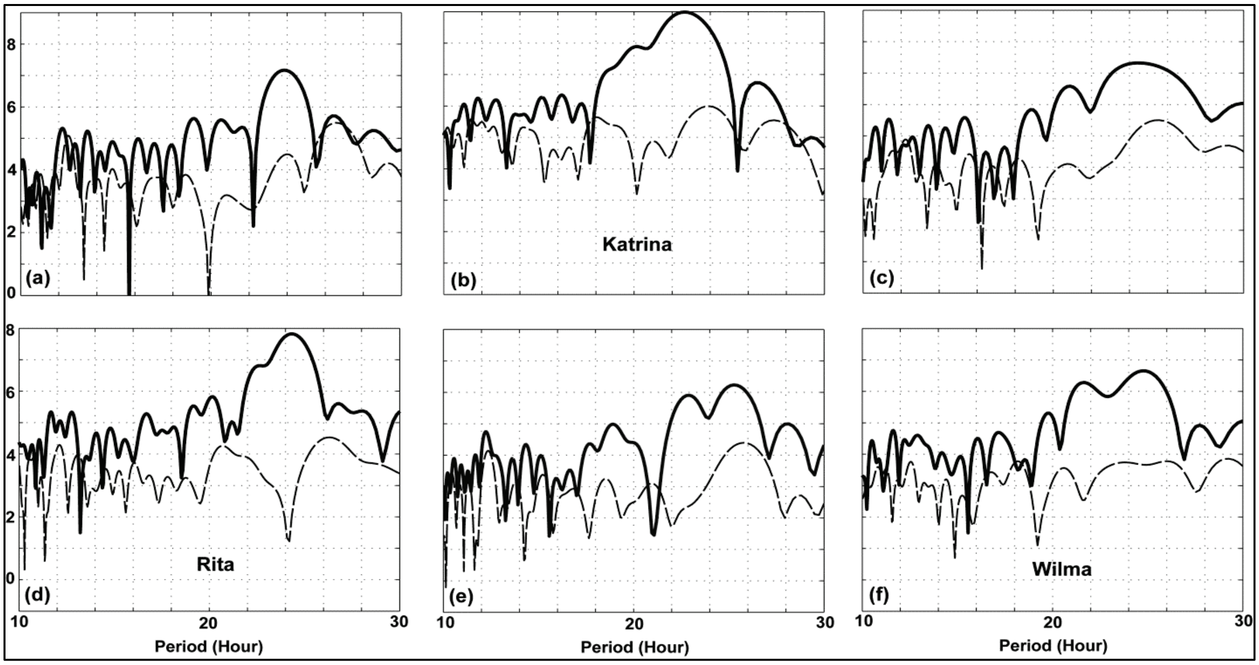

Figure 5.2.9. Rotary spectra for the depth-averaged velocity (u, v) in log-scale (a) before Hurricane Katrina, (b) during and after Katrina, (c) between Katrina and Rita, (d) during and after Rita, (e) between Rita and Wilma, and (f) during and after Wilma. The thick lines represent the clockwise rotating component and the thin lines represent the counter-clockwise rotating component.

Figure 5.2.10 plots the relative fraction of CW and CC components. It reiterates that most of the kinetic energy is in the CW component, whether with or without the influence of hurricanes. The frequency band with the least CC component is around the local inertial period, where the CW and CC components are almost 100% and 0%, respectively. This means that the east and north velocity components are almost equal in magnitude and the clockwise particle trajectories are almost circular as shown in Figure 5.2.3. As we noted earlier, the baroclinic process cannot be used to explain an almost instantaneous NIO at deep-ocean after the passage of a hurricane and a rigid-lid approximation will suppress barotropic oscillations. In this chapter, one of the points that we emphasize is that there is often an almost instantaneous barotropic NIO response in deep-ocean after a hurricane and using a Laplace Transform, we can solve the barotropic problem to quantify such a barotropic response. To that purpose, in the next section, the atmospheric forcing-induced inertial motion is examined with the depth-averaged momentum equations using a rotary function approach and the Laplace Transform.

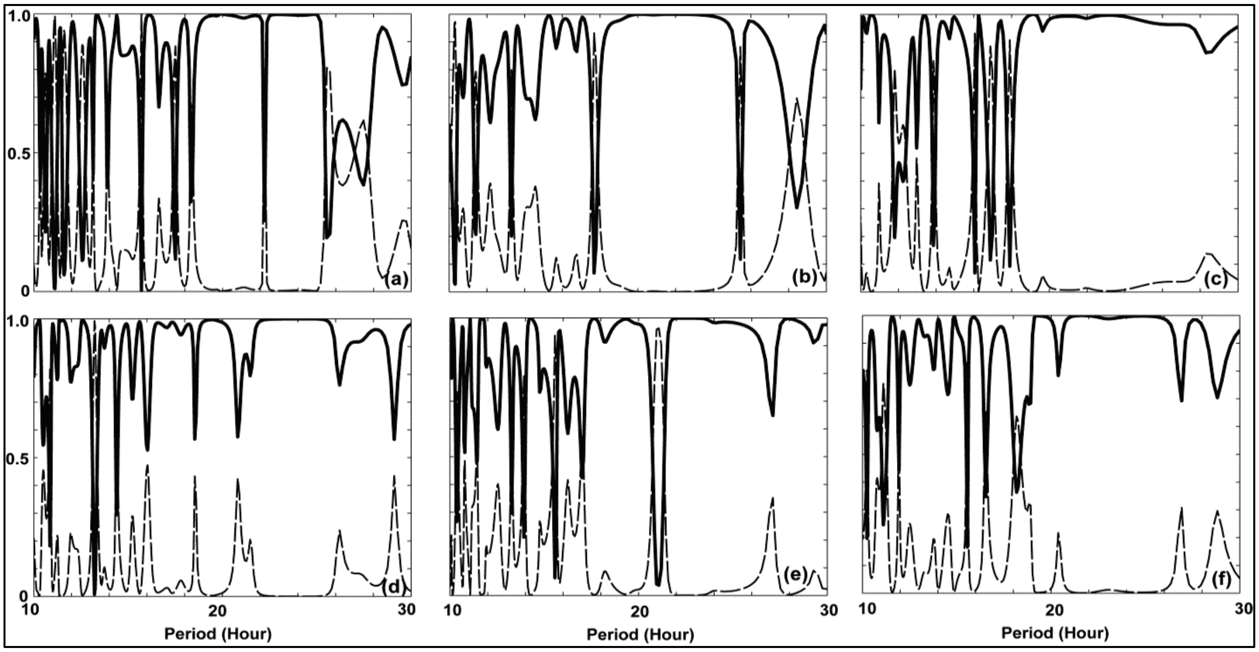

Figure 5.2.10. Fraction of energy from rotary spectra for the depth-averaged speeds (a) before Hurricane Katrina, (b) during and after Katrina, (c) between Katrina and Rita, (d) during and after Rita, (e) between Rita and Wilma, and (f) during and after Wilma. The thick lines represent the clockwise rotating component and the thin lines the counter-clockwise rotating component.

5.2.1 The Rotary Function Approach Using Laplace Transform

Since the water depth in the Gulf of Mexico is less than 4 km while the width is roughly 1000 km by 1600 km, the aspect ratio is very small, O(10^{-3}), the Gulf can be treated as "shallow water." Therefore, the overall response of the depth-averaged velocity to wind stress and pressure gradient can be examined. For the barotropic component only, we can use the depth-averaged momentum and continuity equations. Although the NIO in the upper layer of the ocean often involves baroclinic processes, here the equation is integrated vertically and only the barotropic processes are examined. It should be noted that this approach is rather different from most recent studies in which stratification is considered. Our selection of a barotropic model is based on the following reasons: 1) although the upper ocean (e.g. maximum 800 m and above) is often stratified, the deep ocean (e.g. > 800 m) is rather uniform and barotropic in motion (e.g. Welsh, et al., 2009). 2) For motions forced by severe weather such as hurricanes, the barotropic motion is the first order quantity, rather than a secondary addition to a baroclinic motion. 3) The barotropic model used in past studies use the rigid lid approximations which filter out all gravity waves and eliminates any effect of pressure gradient, while NIOs are a special kind of Poincare Waves under the influence of both earth rotation and gravity. 4) We lack information about what is the effect of pressure gradients from both the atmosphere and the surface of the ocean in the generation of NIOs in different waters (shallow and deep). A barotropic model will allow us to examine the effect of pressure gradient, water depth, and bottom friction from a holistic point of view. The majority of the Gulf's circulation consists of Loop Current and Loop Current Eddies as well as NIOs caused or influenced by meteorological forcing factors. The linearized equations of motion, assuming a constant water depth for simplicity, are

$$\frac{\partial u}{\partial t} - fv = -g\frac{\partial \zeta}{\partial x} + \frac{\tau_{ax}}{\rho h} - \frac{\beta}{h}u - \frac{1}{\rho}\frac{\partial p_a}{\partial x} \tag{1}$$

$$\frac{\partial v}{\partial t} + fu = -g\frac{\partial \zeta}{\partial y} + \frac{\tau_{ay}}{\rho h} - \frac{\beta}{h}v - \frac{1}{\rho}\frac{\partial p_a}{\partial y} \tag{2}$$

$$\frac{\partial \zeta}{\partial t} + h\left(\frac{\partial u}{\partial x} + \frac{\partial v}{\partial y}\right) = 0, \tag{3}$$

in which u, v, ζ, f, g, h, x, y, t, ρ, β, τ_{ax}, τ_{ay}, and p_a are the east and north velocity, surface elevation, Coriolis parameter, gravitational acceleration, depth, east and north coordinates, time, water density, bottom friction coefficient, east and north wind stress components, and atmospheric pressure, respectively.

Applying the Laplace Transform (e.g. Riley et al., 2006) to the first two equations and assuming that initially all fields are zero, yields,

$$\left(p + \frac{\beta}{h}\right)\tilde{u} - f\tilde{v} = -g\frac{\partial \tilde{\zeta}}{\partial x} + \frac{\tilde{\tau}_{ax}}{\rho h} - \frac{1}{\rho}\frac{\partial \tilde{p}_a}{\partial x} \tag{4}$$

$$\left(p + \frac{\beta}{h}\right)\tilde{v} + f\tilde{u} = -g\frac{\partial \tilde{\zeta}}{\partial y} + \frac{\tilde{\tau}_{ay}}{\rho h} - \frac{1}{\rho}\frac{\partial \tilde{p}_a}{\partial y} \tag{5}$$

in which p is the Laplace Transform parameter and the tildes are those after the Laplace Transform. The above equations can be rewritten as

$$\tilde{u} = \frac{-\frac{f}{\rho}\frac{\partial \tilde{p}_a}{\partial y} - \left(p+\frac{\beta}{h}\right)\frac{1}{\rho}\frac{\partial \tilde{p}_a}{\partial x} + f\frac{\tilde{\tau}_{ay}}{\rho h} + \left(p+\frac{\beta}{h}\right)\frac{\tilde{\tau}_{ax}}{\rho h} - fg\frac{\partial \tilde{\zeta}}{\partial y} - g\left(p+\frac{\beta}{h}\right)\frac{\partial \tilde{\zeta}}{\partial x}}{f^2 + \left(p+\frac{\beta}{h}\right)^2} \tag{6}$$

$$\tilde{v} = \frac{-\left(p+\frac{\beta}{h}\right)\frac{1}{\rho}\frac{\partial \tilde{p}_a}{\partial y} + \frac{f}{\rho}\frac{\partial \tilde{p}_a}{\partial x} + \left(p+\frac{\beta}{h}\right)\frac{\tilde{\tau}_{ay}}{\rho h} - f\frac{\tilde{\tau}_{ax}}{\rho h} + fg\frac{\partial \tilde{\zeta}}{\partial x} - g\left(p+\frac{\beta}{h}\right)\frac{\partial \tilde{\zeta}}{\partial y}}{f^2 + \left(p+\frac{\beta}{h}\right)^2} \tag{7}$$

The Inverse Laplace Transform of the equations (6) and (7) gives the following

$$u = F_1(t) + F_2(t) + F_3(t) + F_4(t) + F_5(t) + F_6(t) \tag{8}$$

$$v = G_1(t) + G_2(t) + G_3(t) + G_4(t) + G_5(t) + G_6(t) \tag{9}$$

where

$$F_1(t) = f_2(t) \otimes \frac{\tau_{ay}}{\rho h} = \int_0^t f_2(\tau)\frac{\tau_{ay}(t-\tau)}{\rho h}d\tau \tag{10}$$

$$F_2(t) = f_1(t) \otimes \frac{\tau_{ax}}{\rho h} = \int_0^t f_1(\tau)\frac{\tau_{ax}(t-\tau)}{\rho h}d\tau \tag{11}$$

$$F_3(t) = -f_2(t) \otimes g \frac{\partial \zeta}{\partial y} = -g \int_0^t f_2(\tau) \frac{\partial \zeta(t-\tau)}{\partial y} d\tau \tag{12}$$

$$F_4(t) = -f_1(t) \otimes g \frac{\partial \zeta}{\partial x} = -g \int_0^t f_1(\tau) \frac{\partial \zeta(t-\tau)}{\partial x} d\tau \tag{13}$$

$$F_5(t) = f_2(t) \otimes \frac{-1}{\rho} \frac{\partial p_a}{\partial y} = \frac{-1}{\rho} \int_0^t f_2(\tau) \frac{\partial p_a(t-\tau)}{\partial y} d\tau \tag{14}$$

$$F_6(t) = f_1(t) \otimes \frac{-1}{\rho} \frac{\partial p_a}{\partial x} = \frac{-1}{\rho} \int_0^t f_1(\tau) \frac{\partial p_a(t-\tau)}{\partial x} d\tau \tag{15}$$

$$G_1(t) = f_1(t) \otimes \frac{\tau_{ay}}{\rho h} = \int_0^t f_1(\tau) \frac{\tau_{ay}(t-\tau)}{\rho h} d\tau \tag{16}$$

$$G_2(t) = -f_2(t) \otimes \frac{\tau_{ax}}{\rho h} = -\int_0^t f_2(\tau) \frac{\tau_{ax}(t-\tau)}{\rho h} d\tau \tag{17}$$

$$G_3(t) = f_2(t) \otimes g \frac{\partial \zeta}{\partial x} = g \int_0^t f_2(\tau) \frac{\partial \zeta(t-\tau)}{\partial x} d\tau \tag{18}$$

$$G_4(t) = -f_1(t) \otimes g \frac{\partial \zeta}{\partial y} = -g \int_0^t f_1(\tau) \frac{\partial \zeta(t-\tau)}{\partial y} d\tau \tag{19}$$

$$G_5(t) = f_2(t) \otimes \frac{1}{\rho} \frac{\partial p_a}{\partial x} = \frac{1}{\rho} \int_0^t f_2(\tau) \frac{\partial p_a(t-\tau)}{\partial x} d\tau \tag{20}$$

$$G_6(t) = -f_1(t) \otimes \frac{1}{\rho} \frac{\partial p_a}{\partial y} = \frac{-1}{\rho} \int_0^t f_1(\tau) \frac{\partial p_a(t-\tau)}{\partial y} d\tau \tag{21}$$

$$f_1(t) = e^{-\frac{\beta}{h}t} \cos(ft) \tag{22}$$

$$f_2(t) = e^{-\frac{\beta}{h}t} \sin(ft) \tag{23}$$

In the above equations, the symbol ⊗ indicates convolution, which involves either (22) or (23). The frequency, f, which is originally the Coriolis parameter, can also be understood as the "effective inertial frequency", f_e, as discussed earlier in section 5.1. The functions f_1(t) and f_2(t) defined by (22) and (23) can be called the Frictional Inertial Functions (FIF) because the exponential term is simply the frictional decay factor. Equations (8) and (9) show that both u and v are given by six terms. The first two terms are contributed by wind stress, the third and fourth terms by the surface pressure gradient, while the last two terms by the atmospheric pressure gradient. Note that the continuity equation is not used here. A general procedure for solving this kind of problem is using all three equations, and initial and boundary conditions to solve for u, v, and ζ, treating the pressure gradient as unknowns. Equations (8) and (9) show relationships between u, v, wind stress, and the pressure gradient. The general properties of the solution will be examined next, without seeking an accurate solution of a specific boundary value problem.

5.2.2 Rotary Functions

The common feature of the expression of the solution given above is that all the terms are convolved with the frictional inertial functions (FIFs) which have a frequency of the Coriolis force f (or a modified NIO frequency, f_e , by a few percent of difference from the local Coriolis parameter f). The convolution essentially serves as a natural filter that limits the results to be in some frequency bands, in this case, the inertial frequency band, particularly in deep water (see below). To be an inertial or near inertial oscillation, the velocity vector must be rotating clockwise (counterclockwise) in the northern (southern) hemisphere. This can be examined by defining a Rotary Flow Velocity as [O'Brien and Pillsbury, 1974]

$$Z_R = u + iv \tag{24}$$

Likewise, for convenience, we also define the "Rotary Wind Stress", "Rotary Pressure Gradient", and "Rotary Atmospheric Pressure Gradient" to be, respectively,

$$\tau_R = \tau_{ax} + i\tau_{ay} \tag{25}$$

$$D_R = -g\left(\frac{\partial\zeta}{\partial x} + i\frac{\partial\zeta}{\partial y}\right) \tag{26}$$

$$P_R = -\frac{1}{\rho}\left(\frac{\partial p_a}{\partial x} + i\frac{\partial p_a}{\partial y}\right) \tag{27}$$

The reason for the use of equations (24)-(27) is simply because these complex variables can be used to describe the corresponding vectors' sense of rotation when their respective time series are evaluated. Using the above results, equation (24) can be expressed as, using (8) and (9)

$$Z_R = u + iv = (f_1 - if_2)\otimes\frac{\tau_R}{\rho h} + (f_1 - if_2)\otimes D_R + (f_1 - if_2)\otimes P_R \tag{28}$$

in which the function $f_1 - i f_2$ is:

$$F(t) = f_1 - if_2 = e^{-\frac{\beta}{h}t}e^{-ift} \tag{29}$$

It is easy to see that this is a clockwise rotating complex function of time t, affected by the frictional decay factor. For this reason, it will be called the "Frictional Rotary Inertial Function (FRIF)". Examining the results so far, equation (28) states that the rotary water velocity (Z_R) has three components: the first is a convolution of the FRIF and the rotary wind stress per unit mass ($\frac{\tau_R}{\rho h}$), the second is the convolution of the FRIF and the rotary pressure gradient (D_R), and the third is the convolution of the FRIF and the rotary atmospheric pressure gradient (P_R).

To further examine the effect of the convolution of Rotary Wind Stress on the Rotary Flow Velocity, it is assumed that the Rotary Wind Stress force per unit mass can be expressed by its Fourier series in exponential format:

$$\frac{\tau_R}{\rho h} = \sum\left(Ae^{i\omega t} + Be^{-i\omega t}\right) \qquad (30)$$

Now look at a component of wind forcing with arbitrary frequency ω, the counter-clockwise part will produce a Rotary Flow Velocity determined by

$$I = F(t) \otimes \frac{\tau_R}{\rho h} = Ae^{-\frac{\beta}{h}t}e^{-ift} \otimes e^{i\omega t} = \frac{\mathrm{A}}{\frac{\beta}{h}+i(f+\omega)}\left[e^{i\omega t} - e^{-(\frac{\beta}{h}+if)t}\right] \qquad (31)$$

Similarly, the clockwise part will produce a Rotary Flow Velocity determined by

$$J = F(t) \otimes \frac{\tau_R}{\rho h} = Be^{-\frac{\beta}{h}t}e^{-ift} \otimes e^{-i\omega t} = \frac{\mathrm{B}}{\frac{\beta}{h}+i(f-\omega)}\left[e^{-i\omega t} - e^{-(\frac{\beta}{h}+if)t}\right] \qquad (32)$$

Obviously, (31) and (32) indicate that for either the clockwise or counter-clockwise rotating wind forcing, the flow will have the original frequency, ω, of the same sense of rotation plus an inertial oscillation decaying with time, rotating clockwise (in northern hemisphere). Further, these oscillations are multiplied by a frequency dependent factor (the gain): for the counter-clockwise, and clockwise components, with the following magnitudes, respectively,

$$\mathrm{H}_1 = \left|\frac{1}{\frac{\beta}{h}+i(f+\omega)}\right| = \frac{1}{\sqrt{\left(\frac{\beta}{h}\right)^2+(f+\omega)^2}} \qquad (33)$$

$$\mathrm{H}_2 = \left|\frac{1}{\frac{\beta}{h}+i(f-\omega)}\right| = \frac{1}{\sqrt{\left(\frac{\beta}{h}\right)^2+(f-\omega)^2}} \qquad (34)$$

Figure 5.2.11 shows the "gain" expressed in (33) and (34) in log-scale for latitude 28.52°, the same latitude as station 42375. The curves are for water with large depth (1900 m) and small depth (30 m) with various bottom drag coefficient values (varying from 0.001 to 0.002). For different latitudes, the results are similar, and are thus omitted. From these gain functions, it is found that 1) there is a sharp peak at the NIO frequencies (which is also close to the diurnal tidal frequencies in this case) in deep water for the clockwise rotating component; 2) this peak for clockwise rotating component is much reduced in shallow water; 3) the change in bottom drag coefficient has a more significant impact on the peak for the clockwise component in shallow water than in deep water (the variation in deep water are barely visible such that only one curve is visible – it actually is multiple curves almost all on top of each other as the differences are very small); 4) the much reduced peak in shallow water also has a shift toward shorter period or higher frequency (which corresponds to a "blue shift"); 5) the counter-clockwise component does not have the peak oscillation; 6) the counter-clockwise component has a much reduced magnitude; and 7) the counter-clockwise component does not have a strong dependency on depth. The parameter β is a simplified (linearized) bottom friction coefficient and it depends on water depth and flow condition at the bottom.

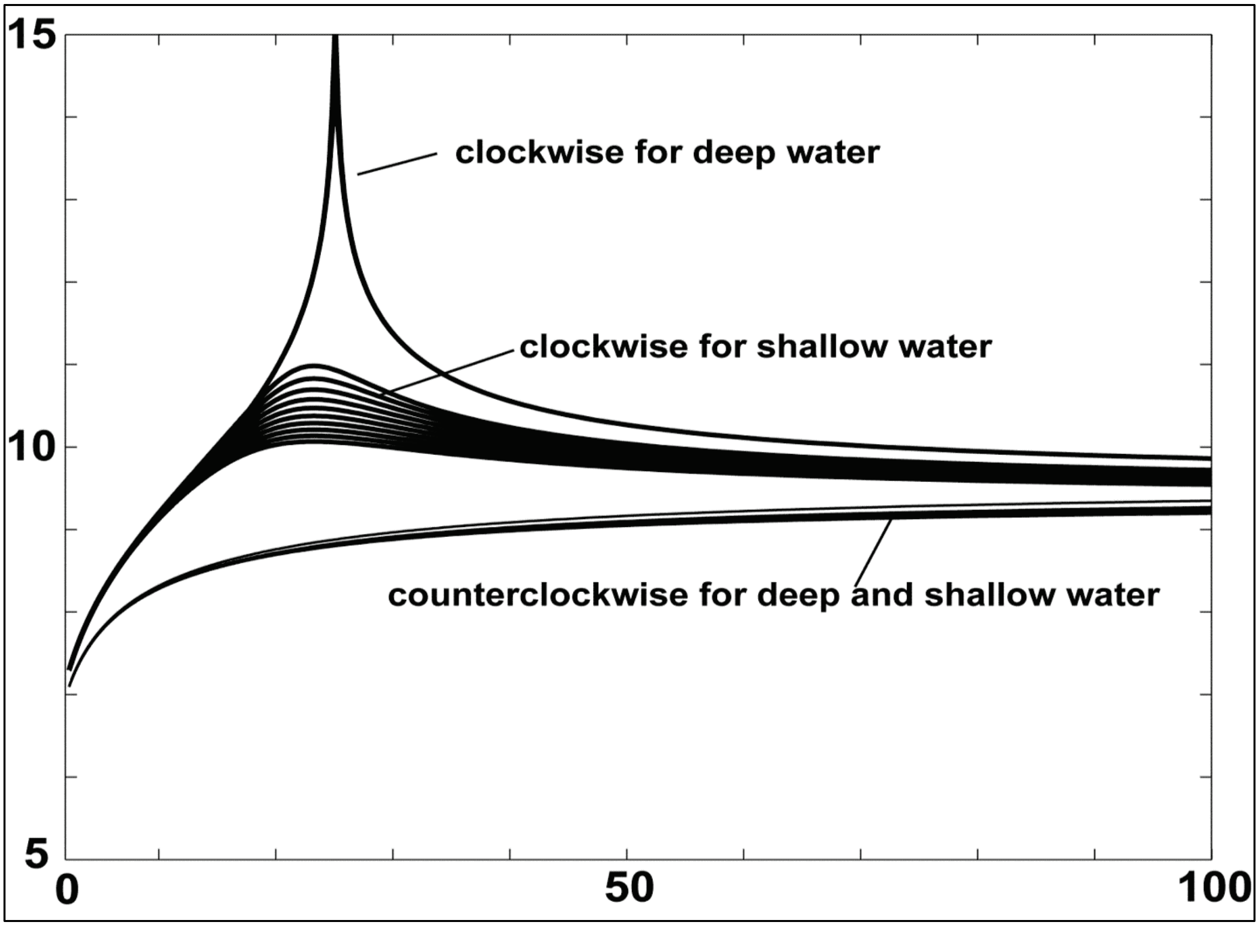

Figure 5.2.11. Theoretical response curve for clockwise rotating velocity component in deep (~ 1900 m) and shallow (30 m) waters. The results for counter-clockwise component for both deep and shallow waters are not sensitive to the depth and there is no peak in those response curves.

The important finding from this simple model is that the earth rotation serves as a “filter” which favors the inertial frequency component, such that the NIOs tend to have a higher peak in deep water. In shallow waters, the bottom friction significantly reduces the effectiveness of this “filter”. Therefore, whenever the “forcing” (wind stress or pressure gradient) contains an inertial frequency, this natural filter will tend to pick it out while reducing all other components at different frequencies.

5.3. CONCLUSIONS

Here we proposed a method using the Frictional Rotary Inertial Function and a Laplace Transform to the barotropic shallow water equations, aimed at obtaining the temporal evolution of the NIOs. We have found that the NIOs as results of the atmospheric forcing depend on water depth and bottom friction in a dramatic manner: the mathematical solution is a convolution of the frictional rotary function with the input signal (i.e. the forcing); and this is effectively a “band-pass filter” that passes the NIOs and damps all the rest. The model predicts no peaks for counter-clockwise rotating components in both shallow and deep waters. This "filter" is more efficient in deeper waters than in shallower waters. This is in contrast to the tidal currents which is minimum in deep waters and amplified in coastal waters. In this chapter, we also argue that the atmospheric forcing contributes to pressure gradient which in turn contributes to NIOs through a barotropic process. This makes it appropriate to use a baotropic rather than a baroclinic model for a secondary quantity (the baroclinic response). With a baroclinic model, it would have a rigid-lid and the effect of the atmospheric pressure gradient would be suppressed. All baroclinic model shows that it takes a much longer time for the NIOs to propagate to the bottom of a deep ocean (e.g. > 1000m), while the barotropic model allows the pressure gradient effect to be instantaneous.

With some unique observational data, we have also analyzed the barotropic NIOs during hurricane periods and non-hurricane periods. Strong NIOs initiated by Hurricanes Katrina, Rita, and Wilma in August, September, and October of 2005, respectively, in deep water between 1400 and 1900 m below the surface in the Gulf of Mexico are demonstrated using an ADCP equipped on a platform. Apparently, the observed NIOs started immediately after the passage of the hurricanes, with an additional ramping period of 2-3 days and a 7-10 day decay thereafter. The ramping process may have been caused by the vertical propagation of the baroclinic NIOs (e.g. Gill, 1984) on top of the barotropic NIOs. The NIOs appeared to be vertically uniform and in phase, lasting for about 10 days after each hurricane. These instantaneously generated NIOs at depth may be explained by a barotropic forcing provided by the wind stress, atmospheric pressure gradient, and related surface pressure gradient.

6. SUMMARY

In summary, we have analyzed a large set of time series of acoustic Doppler current profiler data from the Gulf of Mexico collected from oil and gas platforms. Data are recorded in waters with a total depth deeper than 400 m at 10-20 minute intervals from near surface (~ 30 m) to ~ 500-1000 m. At places where water depth was greater than 1100 m, two ADCPs may be used. These data are often quite continuous but contains gaps of a few weeks to a few months. Our analysis started by filling the small gaps using interpolation, but left the large gaps intact. This is particularly useful and needed for spectrum analysis because, otherwise, the frequency peaks can be distorted. Our analysis focused mainly on the period of 2005-2007. We included some analysis for 2008 data, but this time is largely ignored because of the large data volume. Also, we focused mainly on the fixed platform data, thus ADCP data from the movable drilling units were not analyzed as extensively. Our data files are in MATLAB format and therefore can be used easily for further analysis.

We completed basic statistical analysis. In the ADCP data files, we used a field called "Percentage Good" to QA/QC and select the "good data" before doing the analysis. The "Percentage Good" is an indication of the data quality. We use 75% with this field as our criteria of data selection: we reject any data point that has a Percentage Good value lower than 75%. As we stated earlier, when this value is below 75%, it is mostly much lower than 75%. Most of the data either has relatively high Percentage Good (such as 100%) or a very low value. Therefore, a cut off at 75% separates the good and bad data very well.

The number of data points is highly dependent on the depth of the point of interest. The data points dropped dramatically going into deeper water. Comparing the years with more than 4 million data points, we found that the mean speed and standard deviation did not vary much from year to year and are about 12-14 cm/s and the standard deviations vary between 12 and 16 cm/s. Comparing the different vertical locations, it is found that the mean velocity is largest near the surface and decreases with depth until a depth of about 1000 m where the velocity, while exhibiting some variations, remains relatively constant. Some of the near-bottom velocity increased substantially. This near-bottom increase may be an artificial result because of a lack of backscatter at these depths and the flow could be biased toward large velocities.

We examined the flow direction statistics. It is found that there are several types of variations: uni-modal, bi-modal, multi-modal, and omnidirectional. This result can be misleading as direction does not necessarily has a strong relation with the dynamics. For specific times, this can be true though: for example, if the Near Inertial Oscillation is particularly strong, the flow experiences all directions almost equally (unless there is a strong background mean flow), it will then be shown as omnidirectional. For the same NIO, if the background mean flow is very strong in one direction, then this NIO may appear as a uni-modal with background smaller counts of omnidirectional feature.

The temporal variation of the velocity is as large as the vertical variation. These temporal variations have two major components: one with a daily oscillation – the Near-Inertial Oscillation, and one with a much longer time scale of a few months.

We have plotted all the velocity vectors at all depths as functions of time for all stations for the years 2005 to 2007. These plots provide rich information about the NIOs, Loop Current, Loop Current frontal eddies, and the impact of Loop Current and eddies to nearby areas. The results show that NIOs are ubiquitous in the Gulf of Mexico. NIOs wax and wane but their dependence on wind or weather is investigated only for some case studies of hurricane-induced NIOs. It is clearly shown that major hurricanes such as Hurricanes Katrina and Rita produced large NIOs. Some less intensive hurricanes did not produce large NIOs partly because of the relative position of the hurricane track to the locations of the stations – if they are on the left of the tracks, the NIOs are usually not as large and as obvious.

In the analysis to hurricane induced NIOs, we proposed a method using the Frictional Rotary Inertial Function and a Laplace Transform to the barotropic shallow water equations. We have found that the NIOs as results of the atmospheric forcing depend on water depth and bottom friction in a dramatic manner: the mathematical solution is a convolution of the frictional rotary function with the input signal (i.e. the forcing); and this is effectively a "band-pass filter" that passes the NIOs and damps all the rest. The model predicts no peaks for counter-clockwise rotating components in both shallow and deep waters. This "filter" is more efficient in deeper waters than in shallower waters. This is in contrast to the tidal currents which is minimum in deep waters and amplified in coastal waters. We also argue that the atmospheric forcing contributes to pressure gradient which in turn contributes to NIOs through a barotropic process. This makes it appropriate to use a barotropic rather than a baroclinic model for a secondary quantity (the baroclinic response). With a baroclinic model, it would have a rigid-lid and the effect of the atmospheric pressure gradient would be suppressed. All baroclinic model shows that it takes a much longer time for the NIOs to propagate to the bottom of a deep ocean (e.g. > 1000m), while the barotropic model allows the pressure gradient effect to be instantaneous.

It should be noted that the analysis completed are of a preliminary nature and not exhaustive. This large dataset is a rich resource that can be used by the scientific community for years to come in studies of the dynamics of the Gulf of Mexico.

In summary, the major findings of this work include the following:

(1) Statistically, the central northern Gulf of Mexico region has larger flow velocity than that of the western area. A variation in flow magnitude in the central area appears to propagate to the west, possibly as an integrated impact from mesoscale eddies or Loop Current Eddies.

(2) NIOs are one of the dominant motions in the GoM. The other important component is strong low-frequency flows controlled mainly by the Loop Current and Loop Current Eddies, and possibly to some extent by significant large scale weather systems, which when added together can overwhelm the NIOs by a few times.

(3) The top 300-400 m are seen to have vertical variations of the NIOs, indicating internal wave effect due to vertical stratification. The NIO's phase and energy are seen to propagate vertically quite frequently. The bottom layer (e.g. below 1000 m), however, does not demonstrate such vertical propagation. This highlights the need to examine the

NIOs with barotropic, rather than baroclinic, mode in mind (the work and finding in (5) below).

(4) Hurricanes produce significant and almost instantaneous NIOs at ~1 mile below the surface. Our analysis of NIOs induced by the 2005 hurricanes suggested an increase of kinetic energy of ~30 times of the background tidal oscillations at 1450 m to 1900 m below the surface. The time scale of these NIOs is on the order of 10 days.

(5) Based on the above observations, we examined the dynamical response of NIOs caused by the barotropic surface pressure gradient and wind stress. This is in contrast to the baroclinic NIO responses that required stratification which mostly occur in the surface layer, rather than in the deep bottom layer. Our analysis gives remarkable results which indicate that the Coriolis force and the barotropic forcing from the pressure gradient and wind stress can work together to produce resonance modulated by the water depth, such that external forcing tends to excite NIOs at deep water. The response is less important for NIOs as water becomes shallower. This is in contrast to tidal oscillations which are small in deep-ocean but get amplified in shallow waters. This theoretical conclusion supported by data is the most interesting result.

7. LITERATURE CITED

Apel, J.R., 1988, Principles of Ocean Physics, Academic Press, p 634.

Berger, T.J., P. Hamilton, J.J. Singer, E. Waddell, J. H. Churchill, R.R. Leben, T.N. Lee, W. Sturges, 2000a, DeSoto Canyon Eddy Intrusion Study, Vol. I: Executive Summary, U.S. Dept. Interior, MMS, p41.

Berger, T.J., P. Hamilton, J.J. Singer, E. Waddell, J. H. Churchill, R.R. Leben, T.N. Lee, W. Sturges, 2000b, DeSoto Canyon Eddy Intrusion Study, Vol. II: Technical Report, U.S. Dept. Interior, MMS, p275.

Brooks, D.A., 1983, The wake of Hurricane Allen in the Western Gulf of Mexico, Journal of Physical Oceanography, 13: 117-129.

Chen, C., R.O. Reid, and W.D. Nowlin, Jr., 1996, Near-inertial oscillations over the Texas-Louisiana shelf, Journal of Geophysical Research, 101: 3509-3524.

D'Asaro, E. A., C.C. Eriksen, M.D. Levine, P. Niiler, C.A. Paulson, and P.V. Meurs, 1995, Upper-ocean inertial currents forced by a strong storm, Part I: data and comparisons with linear theory, Journal of Physical Oceanography, 25: 2909-2936.

D'Asaro, E. A., 1995, Upper-ocean inertial currents forced by a strong storm, Part II: modeling, Journal of Physical Oceanography, 25: 2937-2952.

DiMarco, S.F., M.K. Howard, W.D. Nowlin Jr., and R.O. Reid. 2004. Subsurface, high-speed current jets in the deepwater region of the Gulf of Mexico. U.S. Dept. of the Interior, Minerals Management Service, Gulf of Mexico OCS Region, New Orleans, LA. OCS Study MMS 2004-022. p.98

Dimas, A.A., and G.S. Triantafyllou, Baroclinic-barotropic instabilities of the Gulf Stream extension, *J. PHYS. OCEANOGR.*, 25: 825-834, 1995.

Fritz H.M., Bloom C., Sokoloski R., Singleton J., Fuggle A., McAdoo B.G., Moore A., Grass C., and Tate B., 2007. Hurricane Katrina storm surge distribution and field observations on the Mississippi barrier islands. *Estuarine, Coastal and Shelf Science* 74, 12-20.

Frolov, S.A., G.D. Rowe, L.M. Rothstein, and I. Ginis. 2004a. Cross-shelf exchange processes and the deepwater circulation of the Gulf of Mexico: Dynamical effects of submarine canyons and the interactions of Loop Current eddies with topography; final report. U.S. Dept. of the Interior, Minerals Mgmt. Service, Gulf of Mexico OCS Region, New Orleans, LA. OCS Study MMS 2004-017 149 pp.

Frolov, S.A., G.G. Sutyrin, G.D. Rowe, L.M. Rothstein, 2004b, Loop current eddy interaction with the Western Boundary in the Gulf of Mexico, JPO, vol. 34: 2223-2237.

Gill, A.E., 1982, Atmospheric-Ocean Dynamics, Academic Press, p. 662.

Gill, A.E., 1984, On the behavior of internal waves in the wakes of storms, Journal of Physical Oceanography, 14: 1129-1151.

Hamilton, P. 1990. Deep currents in the Gulf of Mexico. J. Phys. Oceanogr. 20:1087-1104.

Hamilton, P., G. S. Fargion, and D. C. Biggs, 1999: Loop Current eddy paths in the western Gulf of Mexico. *J. Phys. Oceanogr.,* 29, 1180–1207.

Hamilton, P. and A. Lugo-Fernandez. 2001. Observations of high-speed deep currents in the northern Gulf of Mexico. *Geophys. Res. Lett*, 28: 2867-2870.

Hamilton, P., J.J. Singer, E. Waddell, and K. Donohue. 2003. Deepwater Observations in the Northern Gulf of Mexico from In-Situ Current Meters and PIES. Final Report. Volume I: Executive Summary. U.S. Dept. of the Interior, Minerals Management Service, Gulf of Mexico OCS Region, New Orleans, LA. OCS Study MMS 2003-048. 14 pp.

Hart, J. E., Baroclinic instability over a slope. Part 1. Linear theory, *J. Phys. Oceanogr.* Vol. 5, no. 4, 625-633. 1975.

Hogg, N. G., Evidence for baroclinic instability in the Gulf Stream recirculation, ESSAYS ON OCEANOGRAPHY: A TRIBUTE TO JOHN SWALLOW., *PROG. OCEANOGR.*, vol. 14, 209-229, 1985.

Kirwan, A., J. Lewis, P. Reinersman, and I. Quintero, 1988: Observed and simulated kinematic properties of Loop Current rings. *J. Geophys. Res.,* 93**,** 1189–1198.

Knabb, R. D., J. R. Rhome, D.P. Brown, 2005, Tropical Cyclone Report: Hurricane Katrina: 23-30 August 2005, National Hurricane Center, pp 43.

Kroll, J., 1975, The propagation of wind-generated inertial oscillations from the surface into the deep ocean, Journal of Marine Research, 33: 15-51.

Kunze, E., 1985, Near-inertial wave propagation in geostrophic shear, Journal of Physical Oceanography, 15: 544-565.

Lai, D.Y., and T.B. Sanford, 1986, Observations of Hurricane-generated, near-inertial slope modes, Journal of Physical Oceanography, 16: 657-666.

Lewis, J. K., A. D. Kirwan Jr., and G. Z. Forristall, 1989: Evolution of a warm-core ring in the Gulf of Mexico: Lagrangian observations. *J. Geophys. Res.,* 94**,** 8163–8178.

Lozier, M.S., M.S.G. Reed, and G.G. Gawarkiewicz, Instability of a Shelfbreak Front, *J. Phys. Oceanogr.*, 32: 924-944, 2002.

Maeda, A., Uejima, K., Yamashiro, T., Sakurai, M., Ichikawa, H., & Chaen, M. et al. (1996). Near internal motion excited by wind change in a margin of the typhoon 9019. *Journal of Oceanography.Tokyo, 52*(3), 375-388.

Meacham, S., Non-modal baroclinic instability, *Dyn. Atmos. Oceans*, 12: 19-45, 1988.

Meacham, S.P. and J.C. Stephens, Instabilities of Gravity Currents along a Slope, *J. Phys. Oceanogr.*, 31: 30-53. 2001.

Mooers, C.N.K., 1975, Several effects of a baroclinic current on the cross-stream propagation of inertial-internal waves, Geophysical Fluid Dynamics, 6: 245-275.

Nowlin, W.D., A.E. Jochens, S.F. DiMarco, R.O. Reid, M.K. Howard, 2004, Deepwater Physical oceanography Reanalysis and Synthesis of Historical Data, MMS Report 2001-064.

O’Brien, J.J., and R.D. Pillsbury, 1974, Rotary wind spectra in a sea breeze regime, Journal of Applied Meteorology, 13: 820-825.

Olascoaga, M.J., Deep ocean influence on upper ocean baroclinic instability, *J. Geophys. Res.*, 106: 26,863-26,877, 2001.

Pardue, J.H., W.M. Moe, D. McInnis, L.J. Thibodeaux, K. T. Valsaraj, E. Maciasz, I. Van Heerden, N. Korevec, Q. Z. Yuan, 2005, Chemical and Microbiological Parameters in New Orleans Floodwater Following Hurricane Katrina, Environmental Science & Technology, 39: 8591-8599.

Pedlosky, J., On secondary baroclinic instability and the meridional scale of motion in the ocean, *J. Phys. Oceanogr.*, 5: 603-607, 1975.

Perkins, H., 1972, Inertial oscillations in the Mediterranean, Deep-Sea Research, 19: 289-296.

Perkins, H., 1976, Observed effect of an eddy on inertial oscillations, Deep-Sea Research, 23: 1037-1042.

Pollard, R.T., 1970, On the generation by winds of inertial waves in the ocean, Deep-Sea Research, 17: 795-812.

Pollard, R.T., and R.C. Millard, Jr., 1970, Comparison between observed and simulated wind-generated inertial oscillations, Deep-Sea Research, 17: 813-821.

Qi, H., R.A. de Szoeke, and C.A. Paulson, 1995, The structure of near-inertial waves during ocean storms, JPO, 25: 2853-2871.

Qiu, Bo; Imasato, N; Awaji, T, Baroclinic instability of buoyancy-driven coastal density current, *J. Geophys. Res.,* **93**: 5037-5050, 1988.

Rego, J.L., and C. Li. 2009a, On the importance of the forward speed of hurricanes in storm surge forecasting: A numerical study, Geophysical Research Letters, 36, L07609, doi:10.1029/2008GL036953.

Rego, J.L. and C. Li, 2009b, On the receding of storm surge along Louisiana's low-lying coast. Journal of Coastal Research SI 56(2), 1045-1049.

Rego, J.L. and C. Li, 2009c, The effect of tides and shelf geometry on storm surge: Numerical model experiments for Hurricane Rita, submitted to Journal of Geophysical Research - Oceans.

Riley, K.F., M.P. Hobson, S.J. Bence, 2006, Mathematical Methods for Physics and Engineering, Cambridge University Press, 1333 pp.

Schott, F., 1970, Spatial structure of inertial-period motions in a two-layered sea, based on observations, Journal of Marine Research, 29: 85-102.

Robinson, A.R. and J.C. McWilliams, The baroclinic instability of the open ocean, *J. Phys. Oceanogr.*, 4: 281-294, 1974.

Suedel, B.C., J.A. Steevens, A. J. Kennedy, S.M. Brasfield, and G.L. Ray, 2007, Environmental consequences of water pumped from Greater New Orleans following Hurricane Katrina: chemical, toxicological, and infaunal analysis, Environ. Sci. Technol., 41: 2594-2601.

Tanaka, K., and K. Alkitomo, Baroclinic instability of density current along a sloping bottom and the associated transport process, *J. Geophys. Res.*, 106: 2621-2638, 2001.

Tang, C.-M., Baroclinic instability of stratified shear flows in the ocean and atmospheres, *J. Geophys. Res.*, 80(9), 1168-1175, 1975.

Tintore, J., D.-P. Wang, E. Garcia, A. Viudez, 1995, Near-inertial motions in the coastal ocean, Journal of Marine Systems, 6L 301-312.

Veronis, G., 1956, Partition of energy between geostrophic and non-geostrophic oceanic motions, Deep-Sea Research, 3: 157-177.

Vidal, V. M. V., F. V. Vidal, and J. M. Pe´rez-Molero, 1992: Collision of a Loop Current anticyclonic ring against the continental shelf slope of the western Gulf of Mexico. *J. Geophys. Res.,* 97, 2155–2172.

Vukovich, F., and B. Crissman, 1986, Aspects of warm rings in the Gulf of Mexico. *J. Geophys. Res.,* 91**,** 2645–2660.

Vukovich, F., and E. Waddel, 1991: Interaction of a warm ring with the western slope in the Gulf of Mexico. *J. Phys. Oceanogr.,* 21**,** 1062–1074.

Walker, A, and J. Pedlosky, Instability of Meridional Baroclinic Currents, *J. Phys. Oceanogr.*, 32: 1075-1093, 2002.

Weller, R.A., 1982, The relation of near-inertial motions observed in the mixed layer during the JASIN (1978) experiments to the local wind stress and to the quasi-geostrophic flow field, Journal of Physical Oceanography, 12: 1122-1136.

Welsh, S.E., and M. Inoue, 2000, Loop current rings and the deep circulation in the Gulf of Mexico, Journal of Geophys. Res., vol. 105: 16,951 – 16, 959.

Welsh, S. E., Inoue, M., Rouse, L.J. and Weeks, E. 2009: Observation of the Deepwater Manifestation of the Loop Current and Loop Current Rings in the Eastern Gulf of Mexico. OCS Study MMS, 50. 110 pp.

Xing, J, and A.M. Davies, 2004a, Model studies of near-inertial motion on the continental shelf off northeast Spain: a three-dimensional/two-dimensional/one-dimensional model comparison study, Journal of Geophysical Research, vol. 109: C01017, doi: 10.1029/2003JC001822.

Xing, J, and A.M. Davies, 2004b, On the influence of a surface front on near-inertial wind-induced internal wave generation, Journal of Geophysical Research, vol. 109: C01023, doi: 10.1029/2003JC001794.

Xing, J, and A.M. Davies, 2005, Nonlinear interaction between wind-forced currents and near-inertial oscillations and internal waves in nearshore frontal regions, Journal of Geophysical Research, vol. 110: C05003, doi: 10.1029/2004JC002579.

Zheng, Q., R. J. L., N. E. Huang, J. Pan, and W.T. Liu, 2006, Observation of ocean current response to 1998 Hurricane Georges in the Gulf of Mexico, Acta Oceanologica Sinica, vol. 25(1): 1-15.

The Department of the Interior Mission

As the Nation's principal conservation agency, the Department of the Interior has responsibility for most of our nationally owned public lands and natural resources. This includes fostering the sound use of our land and water resources; protecting our fish, wildlife, and biological diversity; preserving the environmental and cultural values of our national parks and historical places; and providing for the enjoyment of life through outdoor recreation. The Department assesses our energy and mineral resources and works to ensure that their development is in the best interests of all our people by encouraging stewardship and citizen participation in their care. The Department also has a major responsibility for American Indian reservation communities and for people who live in island communities.

The Bureau of Ocean Energy Management Mission

The Bureau of Ocean Energy Management (BOEM) works to manage the exploration and development of the nation's offshore resources in a way that appropriately balances economic development, energy independence, and environmental protection through oil and gas leases, renewable energy development and environmental reviews and studies.